ELECTRON TRANSPORTATION SIMULATION IN GEANT4 CONDENSED MATTER PHYSICS SIMULATION

A Thesis

by

IMAN ATAEE LANGROUDY

Submitted to the Graduate and Professional School of
Texas A&M University
in partial fulfillment of the requirements for the degree of

DOCTOR OF PHILOSOPHY

Chair of Committee,	Prof. David Toback
Committee Members,	Prof. Bhaskar Dutta
	Prof. Mahmoud El-Halwagi
	Prof. Ricardo Eusebi
Head of Department,	Prof. Grigory V. Rogachev

December 2025

Major Subject: Physics

ABSTRACT

High-quality electron transport modeling in low-temperature, single-crystal silicon and germanium is central for understanding particle detectors dedicated to the first observation of an interaction from the dark matter that fills the universe. A deposit of even a few eV of energy into the detector can instigate billions of microphysical processes. Interpreting the data from such devices requires an accurate understanding of the quantum mechanical effects on how charge carriers propagate through anisotropic semiconductor crystals under voltage and how their interactions with the crystal generate vibrations that are subsequently measured at the detector surfaces. In this thesis, we present a modeling framework for electron transport in single-crystal semiconductors, starting from the quantum mechanical description of electrons in periodic potentials and deriving a particle-like, semiclassical model suitable for detector-scale simulations. This model captures the essential effects of crystal anisotropy and various charge interactions with the crystal, and is implemented within both a toy simulation where individual processes can be turned on and off to help build intuition about the dominant processes, as well as the full Geant4 Condensed Matter Physics (G4CMP) simulation framework. We present comparisons of the simulation results to published experimental data, demonstrating qualitative agreement and highlighting areas for further improvements.

DEDICATION

To my wife, Bita.

ACKNOWLEDGMENTS

This work builds upon the efforts of many previous and current members of the Super Cryogenic Dark Matter Search (SuperCDMS) collaboration, as well as the developers and contributors to the Geant4 Condensed Matter Physics (G4CMP) software. I am deeply grateful to everyone who has contributed to these collaborations and whose work made this thesis possible.

First and foremost, I want to thank my family. Their unconditional love, sacrifice, and support gave me the freedom and strength to follow my passions and dreams. My parents worked tirelessly throughout their lives to support me, and I can never thank them enough for everything they have done. My brother and sister were always there to encourage me and remind me to keep going when things were difficult. Above all, I am endlessly grateful to my wife, Bita, who left everything behind to join me in the United States and stood by my side through both my best and worst days.

There is no one from whom I have learned more, respected more, or owe more to than my advisor, Prof. David Toback. His patience, guidance, and unconditional care for my future shaped not only my research but also who I am as a person. He invested countless hours helping me strengthen my weaknesses, always with kindness and understanding, and never once made me feel discouraged. I always describe him as the wisest person I have ever met, and I feel incredibly fortunate to have had him as my advisor. His belief in me pushed me to become both a better scientist and a better human being, and my gratitude to him is immeasurable.

I would also like to thank Dr. Mike Kelsey, the package manager for both the SuperCDMS simulation software and G4CMP. He is one of the most knowledgeable people I have ever worked with, and I owe much of what I know about G4CMP to his mentorship. He spent countless hours teaching me, discussing ideas, and offering guidance far beyond what was ever required of him. Without his support, this work would not have been possible. I consider him a tremendous asset to the scientific community, and I feel extremely fortunate to have learned from him.

Finally, I want to thank my fellow members of the Toback Research Group. In particular, I am deeply grateful to Elham Azadbakht, my former group member and classmate, who supported me

unconditionally and treated me like family. She has been a role model whom I greatly admire.

CONTRIBUTORS AND FUNDING SOURCES

Contributors

This work was supported by a dissertation committee consisting of Professors David Toback [advisor], Bhaskar Dutta, and Ricardo Eusebi, members of the Department of Physics and Astronomy and the Mitchell Institute for Fundamental Physics and Astronomy, as well as Professor Mahmoud El-Halwagi of the Department of Chemical Engineering. All work for the dissertation was completed by the student, under the advisement of Prof. David Toback of the Department of Physics and Astronomy, and in collaboration with the members of the SuperCDMS Experiment.

Funding Sources

This work was supported by the U.S. Department of Energy (DOE), through a research grant for the SuperCDMS Experiment and, in part, by the Mitchell Institute for Fundamental Physics and Astronomy, as well as a Teaching Assistantship from Texas A&M University. Additionally, portions of this research were conducted with the advanced computing resources provided by Texas A&M High Performance Research Computing.

TABLE OF CONTENTS

Page

LIST OF FIGURES

LIST OF TABLES

TABLE Page

1. INTRODUCTION

One of the most important open questions in modern particle physics, cosmology, and astrophysics is the nature of the unseen mass that dominates the matter content of the universe. In the absence of a detailed understanding, this component has come to be known as dark matter. The "matter" portion of the name comes from the observations that, like other matter in the universe, it influences the motion of stars, galaxies, and galaxy clusters through gravity [1]. The "dark" portion comes from the fact that we can't "see" it directly, said differently it is non-luminous and has not been directly observed through electromagnetic interactions [2]. For reasons we will describe, there is good reason to believe that while this mass is constituted of enormous amounts of particles, the current standard model of particle physics has no explanation for their existence [3, 4]. If this is the case, then detecting its interactions with ordinary matter would provide critical insight into physics beyond the standard model [5]. To date, there has been no recorded evidence of an interaction between a dark matter particle other than gravitationally. Such interactions are expected to be exceedingly rare and deposit extremely small amounts of energy in a detector [6]. This motivates the development of highly sensitive experiments that rely on cutting-edge technology, often with materials that are only partially understood [7]. In this case, modeling the microscopic detector response, such as charge carriers' behavior within it, may prove crucial in their use for discovery.

Many of the major advances in our understanding of fundamental physics have been enabled by improved knowledge of how particles interact with matter. From early developments in optics that made microscopes and telescopes possible, to the discovery and control of electrical conduction in solids, progress in experimental physics has often depended on a deeper understanding of the materials. In particle physics, experiments often rely on detectors whose performance is governed by the microscopic behavior of charge carriers inside the detector material. As experiments push toward being able to measure smaller energy deposits and rarer interactions, accurately modeling how particles move through matter becomes essential for both interpreting data and designing future technologies [7]. History is replete with examples where advances developed for fundamental

physics have had a huge impact on fields outside them, including electricity, lasers, transistors, and superconductors.

In this thesis, we describe our advances in the quantitative modeling of electron transport in low-temperature semiconductor devices for use in the search for dark matter with the Super Cryogenic Dark Matter Search (SuperCDMS) experiment. This experiment has evolved over many years to provide better sensitivity to dark matter interactions [8]. The primary method of the experiment is to use single-crystal detectors at milliKelvin temperatures to record low-energy deposits in the eV range [7]. The expectation is that when a dark matter or standard model particle interacts with the detector, it frees electrons inside the crystal lattice. The motion of the electrons in the lattice in response can be measured with very sensitive sensors on the surface of the detector. If we want to be able to provide evidence of dark matter interactions, we need to demonstrate a quality understanding of the crystal response. One of the most powerful ways to do so is to put our best understanding of the myriad interactions the electrons undergo before being collected into a highly sophisticated simulation. This work summarizes our results and the state of the art of single-charge transport modeling in semiconductor crystals.

In this chapter, we give a high-level overview of both the motivation for this work and what is coming in the thesis. In Section 1.1, we provide an overview of some of the simplest and most compelling evidence for dark matter, as well as some clues that point to it being a particle in nature. In Section 1.2, we discuss dark matter detection methods, with a focus on the SuperCDMS experiment and its use of a semiconductor crystal as a detector, and why a detailed understanding of the detector response is essential for an effective data analysis. In Section 1.3, we discuss charge transport within a semiconductor crystal, with a focus on how it influences the detector response and how we can gain intuitive understanding by using simulations of the billions of microphysical interactions. In Section 1.4, we provide an overview of the thesis with its focus on the physics and simulation of electron transport in single-crystal solids to assist with our experiments.

1.1 The Mystery of Dark Matter

In this section, we describe some of the evidence for dark matter and why the current best explanation is that it is a particle. In the first paragraph, we describe the discrepancy between the expected and observed stellar velocities around the center of galaxies and how it provides indirect evidence for the existence of dark matter. In the second paragraph, we overview complementary evidence that comes from the bending of light as it passes through curved spacetime near a massive object. In the third paragraph, we discuss the remnants of two colliding galaxy clusters, the Bullet Cluster, and how the spatial separation between the observable atomic mass and the estimate of the center of mass provides evidence for the particle nature of dark matter.

The discrepancy between the expected and observed stellar velocities around the center of galaxies provides indirect evidence for the existence of dark matter. Example data, shown in Figure 1.1, indicates that there is a large amount of mass in galaxies that we can't see directly, as the expected stellar velocities calculated from observed mass (stars and gas) don't match the observed velocities [9]. The most successful theories of gravity suggest that the orbital motion of stars in spiral galaxies is governed by the gravitational potential generated by all enclosed mass. If the contributions from the visible stellar population and interstellar gas are considered, Newtonian dynamics predicts that the rotational velocity should decrease with radius once most of the luminous matter has been enclosed. Instead, measurements consistently show that the velocity profile, even at the largest distances from the galaxy center, rises at a slow rate. This behavior implies that the visible matter, which participates in electromagnetic interactions, accounts for only a small fraction of the total gravitational potential. On the other hand, the velocity distribution can be readily explained if there is a contribution from an additional, non-luminous component of mass, which does not participate in electromagnetic interactions, and dominates the total mass at large radii [1]. This type of motion has been observed independent of which galaxy we are analyzing. The explanation of the motion as being due to a non-luminous mass component that contributes significantly to the gravitational potential is one of the most readily understood and widely cited pieces of evidence for the existence of dark matter.

Additional evidence for dark matter comes from the bending of light as it passes through curved spacetime near a massive object, known as gravitational lensing [10]. According to general relativity, mass and energy curve spacetime, and light follows these curved paths rather than traveling in straight lines. As a result, light emitted from a distant galaxy can be deflected by the gravitational influence of an intermediate galaxy or galaxy cluster, producing distorted, magnified, or even multiple images of the background source. An example of this effect is shown in Figure 1.2, where the observed lensing pattern provides a direct probe of the total mass distribution along the photon path. General relativity allows for the prediction of the mass of the intermediate object based on the amount of light path bending due to lensing. As with the orbital velocities of stars in galaxies, observations of lensing around galaxies consistently indicate that there must be far more mass than is estimated from stars, gas, and dust alone [1, 11]. More detailed analysis shows consistency with the previous results from star speeds in terms of the fraction of the mass in a galaxy, as well as how it is distributed.

The remnants of two colliding galaxy clusters, the Bullet Cluster, as shown in Figure 1.3, demonstrate how the spatial separation between the observable atomic mass and the estimated center of mass provides evidence for the particle nature of dark matter. Galaxy cluster collisions provide a unique environment in which the different components of matter respond differently during the collision period because of their distinct interactions. As is the case with single galaxies, clusters of galaxies are expected to consist of large amounts of both dark matter and regular atomic matter. When two separate clusters collide, the atomic gas in each cluster is subject to powerful electromagnetic interactions, causing it to change direction and heat up upon collision. The observations show that the lensing-derived measurements of the centers of mass for the two clusters, however, are spatially displaced from the regions containing most of the ordinary matter, indicating that the bulk of the mass barely interacted during the collision [4]. This behavior is difficult to reconcile with modified gravity models. Instead, the observed separation strongly supports the interpretation of the dominant portion of the mass as being a non-relativistic particle species that experiences negligible drag during such events. The Bullet Cluster is therefore considered one

of the clearest astrophysical demonstrations that dark matter is not simply an artifact of modified gravitational dynamics but behaves as a particle component distinct from ordinary matter.

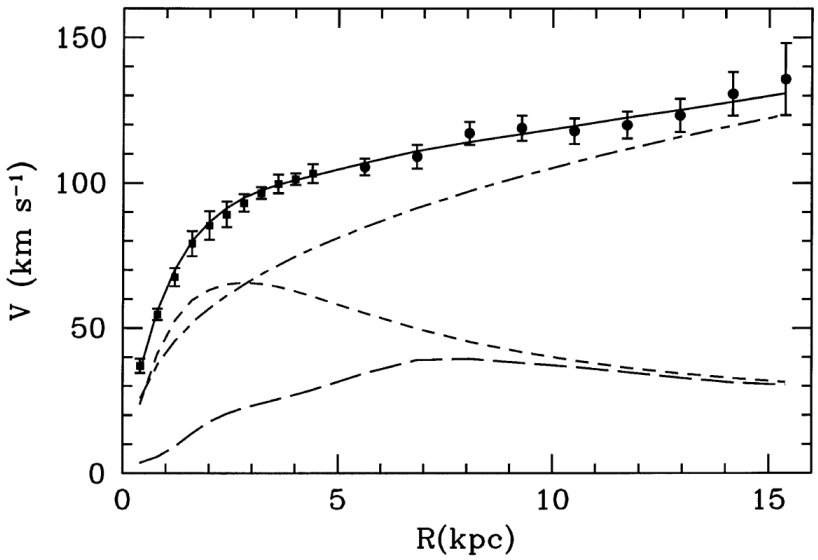

Figure 1.1: This figure shows the expected and observed velocities of the stars around the center of the spiral galaxy M33 as a function of the radial distance from the center. We show it because it is a clean observational example that provides indirect evidence for the existence of dark matter. The dashed lines show the expectations from gravitational contributions from the stellar disc (short-dashed line) and the gas contribution (long-dashed line). The points show the data, which are significantly above the predicted velocities if only visible matter is taken into account. The difference can be explained by the presence of additional matter in the galaxy that is distributed symmetrically, engulfing the atomic matter, known as the halo. The solid line is the best fit, including the dark matter particle model, which well-describes the data, with the dot-dashed line representing the dark matter-only contribution, which dominates the total mass of the galaxy. Taken from [9].

Having concluded our discussion of the evidence for the existence of dark matter and that it is likely to be a particle, we next move to the process of attempting to observe it in action. We describe different methods of directly detecting dark matter to help us understand various experimental approaches and strategies, including the SuperCDMS experiment. Doing so helps motivate our focus on the free charge carriers and and vibrations in a crystal, known as phonons, that are produced and move through the SuperCDMS detector material after an interaction. Each

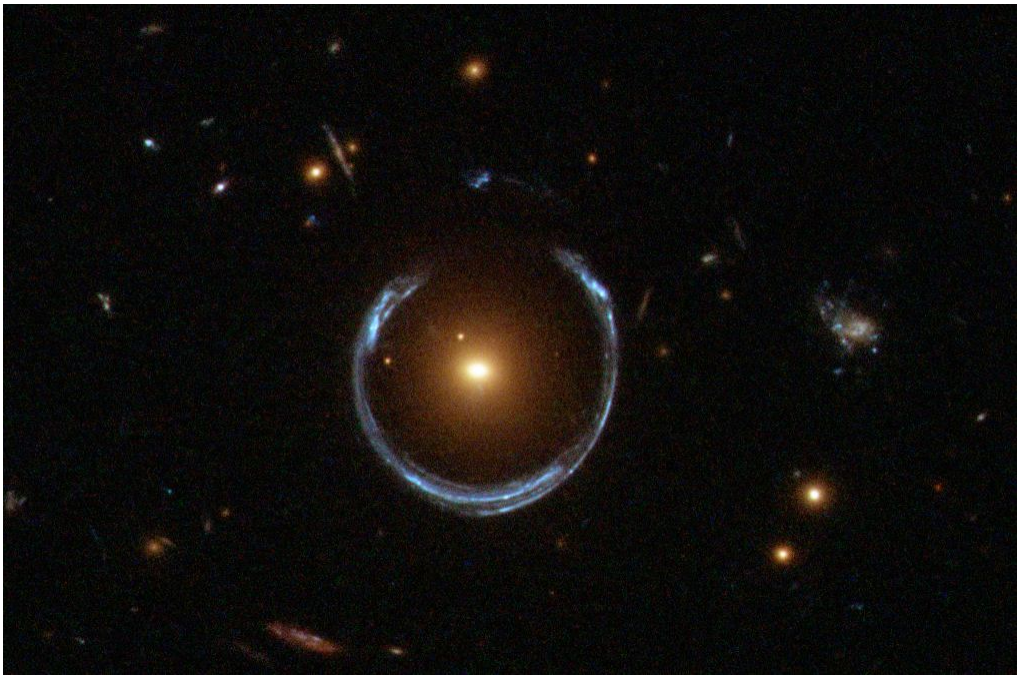

Figure 1.2: This figure shows the gravitational lensing pattern, known as an Einstein Ring, around a luminous red galaxy, where its mass distorted the light from a far-away blue galaxy behind it. We show it because the observed size of the Einstein ring is different than the expected size (not shown) estimated from the visible matter. This difference provides indirect evidence for the existence of dark matter [1, 11]. Photo credit: [12].

plays a central role in determining the detector response and the interpretation of the experimental data.

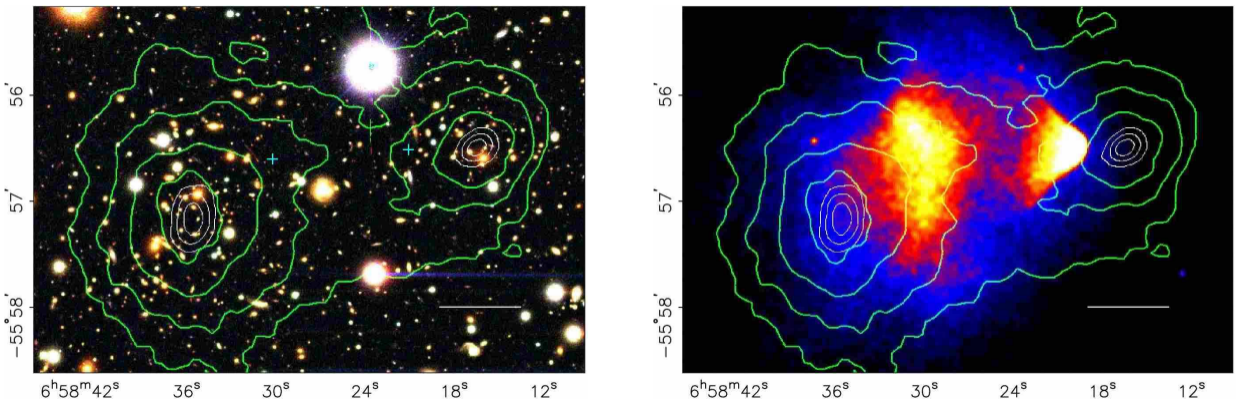

Figure 1.3: This figure shows two views of the remnants of two colliding galaxy clusters named the Bullet Cluster, which provides evidence for the particle nature of dark matter. We show it because the clear separation between the atomic mass, shown in the heat map on the right, and the full mass distribution from gravitational lensing, shown in the green contours in both, is well-explained by a description of the dark matter as a mostly non-interacting particle that simply traverses space. The left panel is an optical image of the sky, where the background shows visible light from galaxies in and around the cluster, and the superimposed green lines indicate the contours of constant density inferred from gravitational lensing. The axes indicate the coordinates on the sky, similar to longitude and latitude, for celestial positions. The right panel displays the same region in X-rays, where the colored areas represent atomic mass density (yellow/red indicates higher density, blue indicates lower density), with the green contours again added for comparison. This mismatch indicates that most of the mass is not in the visible matter and passed through the collision without slowing down [3]. Photo credit: [4].

1.2 Detecting Dark Matter and the SuperCDMS Experiment

In this section, we discuss methods for observing a dark matter particle interaction, with a focus on the direct detection SuperCDMS experiment, which uses single-crystal semiconductor detectors. The design of such experiments and the analysis of the data from them are highly interrelated and need to take into account how both dark matter and other particles are expected to interact with a detector. The better the detector design and understanding of the detection mechanisms, the better the expected sensitivity.

Before beginning the description of our method of choice, a single-crystal detector kept at milliKelvin temperatures, we overview the different methods of dark matter detection to motivate the primary components of a direct approach. There are three main categories of experiments, including collider, indirect, and direct methods, as shown in Figure 1.4 [13]. The direct detection method is based on the hypothesis that the dark matter particles that fill the Milky Way should be traversing the Earth at any moment in time. With an appropriate device we should, in principle, be able to detect a single particle interaction using the method shown at the bottom of the Figure 1.4; more details about the other methods are given in the figure caption.

For direct detection experiments, as we will see, single-crystal semiconductor detectors offer significant benefits, but taking advantage of them requires a deep understanding of how the crystal responds to particle interactions. To illustrate this, we start with an overview of the reasons behind the choice of these crystals and how they are used in the SuperCDMS experiment. This also highlights why detailed simulations of the underlying physical processes may prove crucial for any potential discovery.

In Subsection 1.2.1, we overview some of the most important components of detector design and data analysis in direct detection methods. In Subsection 1.2.2, we describe the role that semiconductor crystals play in the SuperCDMS detectors, as shown in Figure 1.5. In Subsection 1.2.3, we discuss the recorded data after all the processes have completed, and provide an overview of how it is analyzed to motivate the value of high-quality simulations.

1.2.1 Dark Matter Direct Detection Methods

In this section, we overview some of the most important components of detector design and data analysis in direct detection methods. This helps explain why this work focuses on the understanding of charge transport in semiconductors. Since the design of the detector and the analysis of the data it produces are inseparable, for pedagogical reasons, we start by describing the end-stage of analysis and work our way backwards. The detectors record information about an interaction, with each primary interaction referred to as an event. The typical analysis of the data examines both individual events recorded by the detector to see if they can be considered dark matter candidates, and ensembles of events to determine if there is a dark matter contribution to the ensemble. In the first paragraph, we discuss the primary requirements that make a material suitable for use in direct detection experiments. In the second paragraph, we describe the requirements that extend beyond simply recording small energy deposits and focus on how detector design and data analysis must cope with the wide range of possible detector responses to different particles and interaction locations within the device.

The primary requirements that make a material suitable for use in direct detection experiments include its ability to respond to very small energy deposits from dark matter, the ability to transfer that energy to sensors, and ideally, allow for methods that prevent or otherwise allow us to identify and reject interactions that can mimic a dark matter signal. Direct detection experiments must measure extremely small energy depositions, often at the scale of a few electronvolts [13]. While there are many potential ways to accomplish these goals, one of the most common and powerful is a detector medium where an interaction can ionize electrons within the medium, or cause the medium to vibrate in a measurable way [14]. In the case of solids, this means that it is advantageous if the amount of energy required to liberate an electron from the stationary atoms is small. It is also beneficial if the material allows any ionized electrons or atomic vibrations to propagate so that sensors can accurately record their energy, position, and time of arrival. On the other hand, to help distinguish between small energy deposits and measurement noise, the population of already existing conduction electrons and atomic vibrations in a solid must be minimized, so as not to mix

them with the ones caused by an energy deposit. In principle, detectors that can produce distinct signatures in both the total charge collected, phonon production, and timing information have an even greater possibility of distinguishing between dark matter and other interaction types.

Beyond the ability to record small energy deposits, direct detection experiments must account for the wide range of detector responses arising from different particles, interaction locations, and instrumental effects, which complicates the identification of rare dark matter interactions. There can be a large variation in the types of underlying processes that produce a response in a detector, and the detector typically records them all. Most events arise from standard model particles that interact with the detector material through well-understood mechanisms. On the other hand, environmental and instrumental effects, including electronic noise and non-uniformity of the detector response and configuration, can produce events where the observed response is different from expected or only a fraction of the response is observed. This can result in events where the full set of properties of the original interaction is misreconstructed. As a result, only a very small subset of interactions, if present at all, would be expected to originate from dark matter [15] and be well-measured. Therefore, the analysis of the data must account for the full spectrum of possible event types and distinguish those that are consistent with dark matter from those that mimic it from backgrounds or detector artifacts. The ability to correctly interpret these mixed populations is a central challenge in direct detection searches.

Having concluded an overview of the primary direct detection detector requirements and the big picture of how the events collected will be analyzed, we next describe why semiconductor crystals are used in the SuperCDMS experiment. As we will see, semiconductors can serve as a powerful component of a detector, but have many complex properties that must be taken into account in order to fully utilize their advantages. This discussion helps motivate a high-quality understanding of charge transport, which directly relates to improvements in interpreting the data for use in analysis, and how simulations can assist.

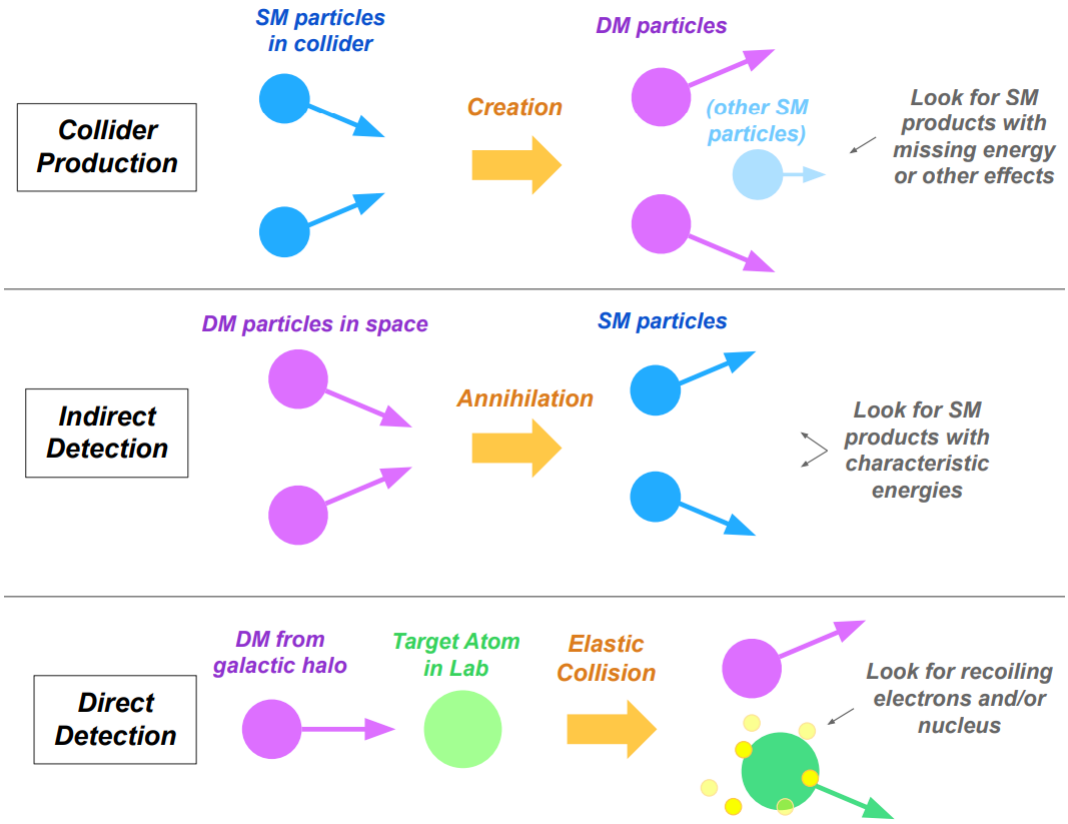

Figure 1.4: This figure shows a cartoon of the three primary experimental approaches to observe an interaction of the hypothesized dark matter (DM) particle. We show it because the work in this thesis is designed to assist in the understanding of the detectors used in direct detection experiments (bottom row). The top row shows an experiment where two standard model (SM) particles collide with enough energy to produce dark matter particles. Typically, a large detector surrounds the collisions and compares observations to the hypothesis of standard model-only interactions [16]. The middle row shows the indirect detection method in which dark matter particles collide in outer space, annihilate, and produce high-energy final-state particles. Telescopes and other detectors compare observations of particle energies with predictions made only from the standard model [17]. The bottom row shows the direct detection method in which a dark matter particle interacts with standard model particles in a detector. Custom sensors on the detector volume compare observations from the hypotheses both with and without dark matter interactions [15, 18]. Figure taken from [19].

1.2.2 Using a Semiconductor Crystal as a Detector in SuperCDMS

In this section, we describe the role that semiconductor crystals play in the SuperCDMS detectors, as shown in Figure 1.5. We note at the beginning that there are a number of complex, non-intuitive processes involved in the detector response, many of which are governed by the ways that charges propagate in the semiconductor. While we will describe them in more detail in Chapter 2, for pedagogical reasons we will foreshadow a number of terms in our overview. In the first paragraph, we introduce the SuperCDMS experiment and the two different types of detectors, silicon and germanium. In the second paragraph, we describe how particle interactions ionize atoms in the detector, effectively creating an electron-hole pair in the crystal lattice. In the third paragraph, we discuss the movement of charges and phonons, and describe the most important differences between an electron in a crystal and one in a vacuum, and how adding a voltage across the detector provides signal (number of phonons) amplification. In the fourth paragraph, we overview how the charge and phonon sensors, shown in Figures 1.6 and 1.7, provide measurement information for use in analysis.

The two different types of detectors, shown in Figures 1.6 and 1.7, used in the SuperCDMS experiment allow it to compare low-energy interactions across different target materials, improving both the ability to estimate the rates and energies of various background sources and the overall sensitivity to different dark matter models. To satisfy the requirements discussed in Subsection 1.2.1, the detectors are operated at milliKelvin temperatures to minimize the amount of atomic vibrations and free charges. This particular pair of semiconductors are chosen because each requires only a few eV of energy deposit to liberate an electron from its atom (referred to as having a small bandgap for reasons described in more detail in Chapter 2), as well as have well-understood crystal structures and allowed energy levels (energy bands) [7].

Particle interactions in the detector ionize atoms in the crystal lattice, creating electron–hole pairs, as illustrated in Figure 1.5. While Chapter 2 will provide more detail, we summarize the primary set of processes. When a particle deposits enough energy in a semiconductor crystal to ionize an atom, the electron becomes free to move throughout the material (referred to as being

in the conduction band). On the other hand, this process leaves behind an empty spot in the atomic lattice, and electrons from neighboring atoms can move into it. This process can repeat multiple times, acting like the propagation of a positively charged electron and referred to as a hole. Each charge from an electron–hole pair can propagate through a semiconductor crystal. The number of pairs created depends on the total deposited energy and the bandgap of the material, making semiconductor detectors with charge sensors both highly sensitive to small interactions and capable of providing an estimate of the energy of the interaction [14].

Once charges are liberated, they propagate through the crystal under the combined potential of the crystal lattice structure and any applied electric field, but do so in a way where quantum mechanical effects must be considered. For reasons we will describe in more detail in Chapter 2, electrons are particularly affected as both their acceleration and speed are governed by the direction they move within the crystal, which makes their motion very unlike that in a vacuum. Both types of charges can also scatter within the crystal and produce phonons [20].[1] These phonons can carry away energy and propagate in the crystal. Understanding and simulating these processes are the main focus of this thesis.

The charge and phonon sensors shown in Figures 1.6 and 1.7 provide the measured information used to reconstruct particle interactions in the SuperCDMS detectors [8]. The charge sensors collect the location of each charge that makes it to the surface, which provides some information about the original amount of energy deposited, where the interaction occurred, and some indications of whether the event is well-measured. These sensors contain electrodes that additionally provide the voltage across the crystal, which accelerates the charges, which in turn produce phonons. The phonons typically can travel for up to a few microseconds before they are absorbed by the phonon sensors. This information can be used independently or in conjunction with the collected charge information in the analysis of the data if available. The ability to work backwards from the measured quantities forms the sensitivity to dark matter interactions. Unfortunately, many processes

[1] While we will describe this more in Chapter 2, we note that the charges can scatter on other charges or phonons that happen to be present, although this is expected to be negligible at the low temperatures employed for the SuperCDMS detectors.

can alter the observed quantities from their simple expectations. For example, non-uniformities in the electric field affect charge trajectories and their rate of energy gain. Additionally, depending on the location of an interaction, some fraction of the charges can reach the sidewalls and be absorbed. This would affect both the number of charges collected as well as the number of phonons produced. Without an understanding of the full set of effects in the detector, the ability to reconstruct the original interaction can be severely compromised. Typically, these events need to be identified and either rejected or corrected, which requires a good understanding of each effect's contribution. With only qualitative understanding or averaged responses, the search might miss a signal, or misidentify poorly-measured events as being due to dark matter interactions.

Having concluded our introduction to semiconductor detectors of the SuperCDMS experiment and overviewed the complexity of their response to the particle interactions, we next move to talk about how to understand the detector response for use in analysis, which motivates the role of simulation.

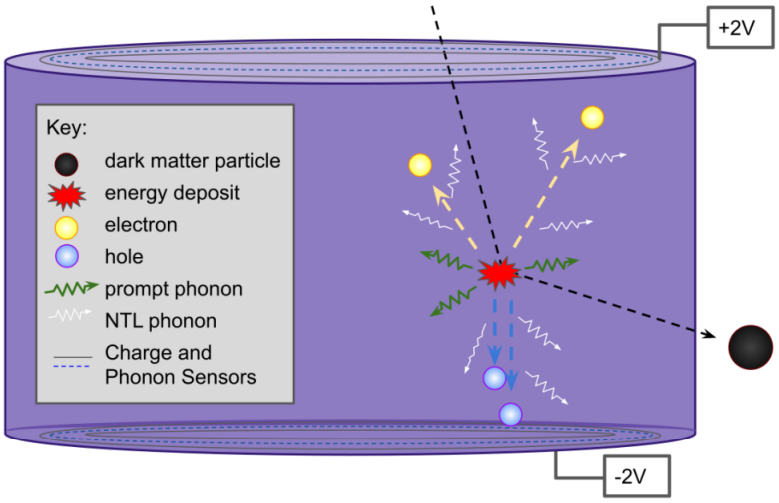

Figure 1.5: This figure shows a cartoon of an interaction of a dark matter particle impinging on a semiconductor detector and the motion of the resulting charges and phonons before collection. We show it to illustrate the early-stage response of a particle interacting with the detector and depositing its energy, which produces electron-hole pairs and phonons. As the charges travel through the detector, they produce more phonons. Both the phonons and charges propagate until each gets absorbed at the top or bottom surface of the detector, where their energy is recorded. These measurements give us an estimate of the energy and interaction position of the incident particle for comparisons to expectations. Taken from [19].

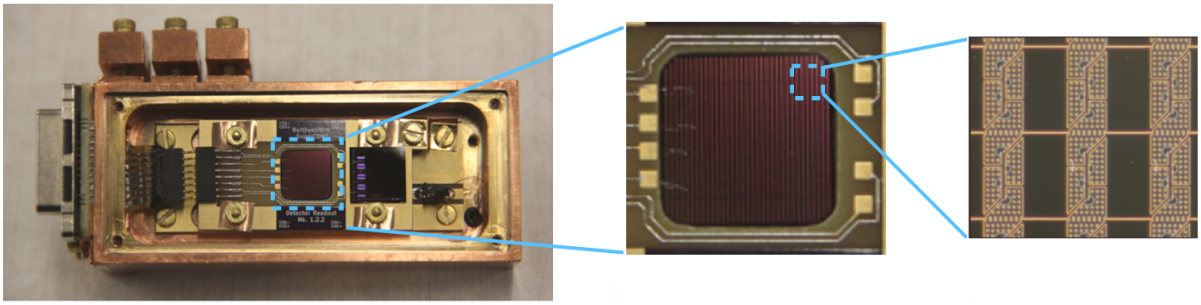

Figure 1.6: This figure shows three views of a silicon version of a SuperCDMS detector with a high voltage across it, known as an HVeV detector, and used as a test device at the NEXUS facility. We show it because it illustrates the detector layout used for our simulations to study electron transport in silicon crystals. The detector has a $10\ \mathrm{mm} \times 10\ \mathrm{mm} \times 4\ \mathrm{mm}$ silicon crystal mounted in the middle of its housing and is operated at $50\ \mathrm{mK}$. The phonon sensors populate the surface, and the middle and right versions of the plot show zoomed-in versions to provide detail. Taken from [21, 22]

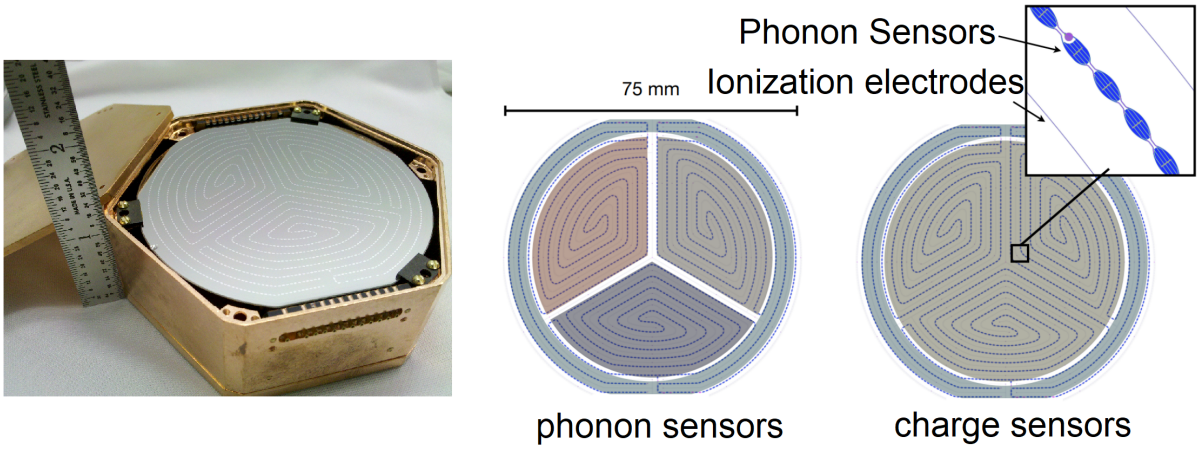

Figure 1.7: This figure shows a germanium version of a SuperCDMS detector with a few volts of potential across it, known as an iZIP detector, and used during the Soudan data collection period: a photo on the left and a cartoon of the charge and phonon sensor layout on the surface on the middle and right. We show it because the circular layout is similar to what will be used in the SNOLAB experiment moving forward [8], and will be used in our simulations to study electron transportation in the germanium crystals. The crystal is $76\ \mathrm{mm}$ in diameter with a $25.4\ \mathrm{mm}$ thickness, operating at $50\ \mathrm{mK}$, but with phonon and charge sensors on both the top and bottom surfaces. On the right, the blue dotted lines that are also visible in the physical form of the detector are the phonon sensors, and the charge sensors are the thin lines between them, which are visible if we zoom in. The colored regions in the middle are the three different phonon sensor groupings, while the colored regions on the right are the different charge sensor groupings (inner and outer). Both are used to help determine the energy and position of the incident particle. Pictures taken from [22, 23].

1.2.3 Understanding Detector Response for Effective Data Analysis

In this section, we discuss the recorded data after all the processes in Figure 1.5 have completed, and provide an overview of how it is analyzed to motivate the value high-quality simulations. An oversimplified way of thinking about the analysis is that it has three steps: First, determining a best-estimate reconstruction of the properties of each event, second, rejecting the subset of events that are readily identified as not being due to well-measured dark matter interactions, and third, analyzing the remaining set of events as being to see if it is a combination of both backgrounds and dark matter, or just backgrounds. In an ideal detector, the time, position, and energy of each charge and phonon produced are perfectly recorded. In the real detectors, we have only a small number of sensors, each of which only reports the combined time and energy of all charges or phonons that reach them. Our focus will be on the first stage of the analysis, which is the process of looking at the outputs from the sensors and working backwards to infer what we can about the original interaction. This process is referred to as reconstruction. Said differently, reconstruction is the process of using the outputs from the sensors in Figures 1.6 and 1.7 to determine what the properties are of the incoming particle in Figure 1.5. Since enormous numbers of microphysical interactions occur between the original energy deposit and when the charges and phonons hit the sensors, the interpretation of their readout is highly non-trivial; the better our understanding of the processes, the higher fidelity our reconstruction will be. In the first paragraph, we highlight some of the primary goals of the reconstruction methods. In the second paragraph, we motivate the use of simulations as a guide for the reconstruction methods.

In principle, the ideal reconstruction could identify both the incident particle (dark matter or standard model) and all of the relevant information about it, such as position and energy. In practice, a primary focus is on rejecting poorly-measured events, such as those that occur in locations in the detectors where not all the charges or phonons make it to the sensors, or where the charges fail to traverse the full voltage drop. In such cases, the readout information does not reflect the expected response for a well-measured event, so if we misinterpret the readout information as being due to a well-measured interaction, we misclassify the event. For example, we may systemati-

cally underestimate the energy of the interaction. This can introduce biases into our final analysis, particularly in statistical fits that rely on modeling the full energy distributions of signal and background events [15]. The closer we can get to a precise reconstruction on an event-by-event basis, the better the experiment sensitivity for ensembles of events.

Simulations can be used as a guide for the reconstruction methods. Following the lead of previous particle physics experiments, we simulate the full set of microscopic charge and phonon physics processes, from the initial particle interaction to the sensor response [24, 25]. By running many simulation events, we can effectively build a mapping between input interaction configurations and their resulting sensor signals. The reconstruction of an event using an inversion of this mapping assists in the identification of poorly-measured events and allows for an estimate of the original interaction properties from the observed sensor data. In addition, simulations allow us to quantitatively assess reconstruction performance and compare various reconstruction procedures as part of an analysis optimization process. Fortunately, by including both charge and phonon transport in a single simulation framework, we can generate consistent sensor-level expectations, enabling a unified and physically grounded reconstruction strategy.

Having motivated the value of both high-quality reconstruction and the potential for using simulations to help, we stop to note that the fidelity of any reconstruction based on simulation is only as good as the quality of the simulation. A proper simulation must model the complex trajectories of charge carriers and the scattering and propagation of phonons, taking into account the dominant effects. In the next section, we provide an overview of the physics of charge transport with an eye towards how it will be implemented in the simulation.

1.3 Charge Transport in Condensed Matter and its Simulation

In this section, we overview the large number of complex processes that govern charge transport within a semiconductor crystal and how they influence the detector response. Our focus will be on the electron transport. We note in advance that electrons' motion will be very different than that in free space, and both electrons and holes can produce multiple phonons. We also note that the description of hole transport can be described as a simplified version of the electron propagation.

The primary influences on the charge transport are the periodic potential provided by the structure of the crystal, the magnitude of the electric field, and interactions with individual atoms of the lattice. As we will see, when quantum mechanical effects are taken into account, the potential imposes a set of allowed energies which are direction dependent, as shown in Figure 1.8. In the presence of an additional electric field, as shown in Figures 1.9 and 1.10, the charges accelerate in non-intuitive ways, drift, and generate phonons as they scatter, ultimately producing a complex arrival pattern on the detector surface. Since the sensors reside at the surfaces of the detector, accurately predicting the distribution of the charge arrival positions and the number and energy of the phonons produced becomes important for reproducing observables such as the incident particle's position, time, and energy.

In Subsection 1.3.1, we discuss charge transportation in a semiconductor crystal, how the structure of atoms in a crystal (band structure) affects it, and how the electric field affects charge trajectories and phonon production. In Subsection 1.3.2, we provide an overview of the modeling and simulation of the charge transport and phonon production and describe how they fit into the overall SuperCDMS simulation framework.

1.3.1 Charge Transportation in a Semiconductor Crystal

In this subsection, we describe the dominant parts of charge transportation in a crystal lattice, as they can differ significantly from a charge moving through a vacuum. We note that here we are previewing the results presented in detail in Chapter 2 as the quantum mechanical calculations can be complex. In the first paragraph, we describe how the structure of atoms in a crystal imposes

multiple constraints on the motion of electrons within it. In the second paragraph, we overview the very different effect an electric field has on the acceleration and trajectories of charges in a crystal as shown in Figure 1.9. In the third paragraph, we describe the low-energy interactions charges can have with the crystal, which are the main source of phonon production; we will refer to them as intravalley scatterings. In the fourth paragraph, we describe the charge interactions with impurities in the atomic structure and high-energy interactions with the crystal, which we will refer to as intervalley scatterings.

The structure of atoms in a crystal imposes multiple constraints on the motion of electrons within it. This includes the electrons' usual state (attached to a lattice site), what can cause them to get detached and be able to move throughout the crystal, and the difference between motion in the crystal and in a vacuum. The periodic arrangement of atoms in a semiconductor crystal imposes a repeating potential that, when taking quantum mechanical effects into account, restricts electrons to a discrete set of allowed energies, forming direction-dependent energy bands separated by forbidden regions [26], as shown in Figure 1.8 and referred to as a valley. At low temperatures, while most electrons will remain with a single atom, an electron can be excited into one of the allowed energy bands, for example, by an external particle energy deposit. When this occurs, the electron is allowed to move. However, as the allowed energies are direction-dependent, the curvature of the energy–momentum relation determines how they move through the lattice [27]. Ultimately, the anisotropic band structure in a crystal results in velocities and accelerations that are in sharp contrast to the isotropic motion expected for free charges in a vacuum and plays a central role in determining both how they propagate and where they are ultimately measured. We note in advance that while the band structure can have an impact on hole propagation, it is especially important for electrons; for our purposes, a hole can be effectively thought of as a charge in a vacuum with a mass that is slightly different than that of an electron.

When an electric field is added, the accelerations and trajectories become even more different. The response of a charge carrier to an applied electric field is, again, affected by the periodic potential of the crystal lattice structure, which affects the curvature of the associated energy bands [27].

While holes can again be effectively thought of as free in an electric field, the acceleration and trajectories of electrons are even more complicated, as shown in Figure 1.9. Of particular note is that the electron's acceleration is not necessarily aligned with the electric field. Electrons are constrained to be in the valleys shown in Figure 1.8. This implies that a set of electrons with identical locations and speed magnitudes will experience different acceleration even under the same applied field due to the direction of the charge relative to the orientation of the lattice. This anisotropic behavior has important consequences for charge transport, as it breaks the symmetry present in isotropic media and leads to different characteristic patterns in the arrival positions for electrons and holes at the crystal surfaces. Understanding how the electric field interacts with the band structure is, therefore, essential for accurately modeling the motion of charges in semiconductor detectors.

The dominant interaction process for both electrons and holes as they drift through a semiconductor is to scatter off atoms and produce phonons, as shown in Figure 1.10. These are typically low-energy interactions such that the charge will remain in the same direction-dependent energy band (valley); for this reason this process, typically referred to as Luke scattering [20], is also often referred to as intravalley scattering.[2] In an electric field, this can be the primary source of phonons[3] as well as a large influencer on the trajectories. As each scattering transfers kinetic energy from the charge carrier to the atomic structure, the charge will typically remain in the low-energy regime and remain in the same energy band, which means that its overall path direction is essentially the same, but with a small zigzag component of motion, as shown in Figure 1.9. Repeated scattering events produce a significant population of phonons along the drift path, adding to the overall available phonon population that can be measured by the detector. As the charge transport, as well as the rate and energy of the phonon emissions, depend on both the band curvature and the applied electric field, proper modeling of intravalley scattering is important for using semiconductor-based dark matter detectors.

[2]Note that even though holes can scatter from the lattice and produce phonons, since they only have one valley, the term intravalley can be thought of as a bit of a tautology. For simplicity, we use the same term for both electrons and holes.

[3]Also known as Luke phonons.

A charge can also interact with impurities in the atomic structure or have high-energy interactions with the crystal, which we will refer to as intervalley scattering. The name comes from the fact that an electron can scatter such that it transitions into a different valley.[4] Unlike intravalley scattering, any interaction that changes the valley of an electron requires a large change in charge momentum and therefore typically involves either an elastic scattering due to impurities in the crystal's atomic structure or the emission of a high-energy phonon [28, 29]. These interactions are comparatively rare at low energies but become increasingly relevant as the electron gains momentum under an applied electric field. Intervalley scattering, therefore, plays an important role in determining the overall distribution of electron arrival positions in semiconductor detectors.

Having concluded our overview of charge transportation in a semiconductor crystal, we can see how the microscopic processes can affect macroscopic observables. The microscopic issues are dominated by the quantum mechanical nature of electron interactions in a crystal lattice, which has a large impact on the macroscopic trajectories from a particle interaction point to the arrival of all the charges and phonons on the surface. While it is not hard to craft qualitative predictions, reliable quantitative predictions require more sophisticated methods, for example, those that we use in simulations. To explain how all the effects described here are simulated, we introduce the SuperCDMS simulation, which is discussed in the next subsection.

[4]While this will be discussed more in Chapter 2, we note that this name is a bit of a misnomer for holes as they cannot change valleys; holes reside only in one band maximum in our model. Holes can undergo impurity interactions, but the name intervalley is still used as it only has a noticeable effect for electrons.

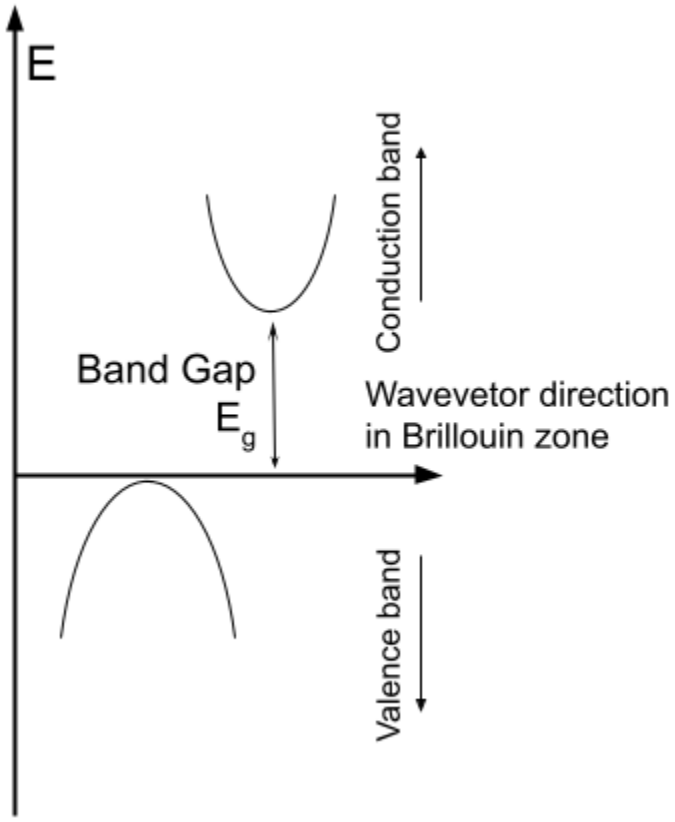

Figure 1.8: The solid curves in this figure show a simplified cartoon of the allowed energy vs. wavevector (described in more detail in Chapter 2 but for now can be thought of as being a direction) for an electron in a semiconductor with a single energy band in the conduction and valence regions. We show it because the allowed energies depend on the direction of charge propagation in the conduction band. The existence of direction-dependent energy bands causes the trajectories of electrons through a semiconductor to be different than those expected for a free electron, as shown in Figure 1.9. We also note that in the conduction band, we refer to directions in which the energy is minimum as valleys. We note that in silicon and germanium, there are multiple directions that have the same minimum energy due to the crystal symmetry, which we will explain in more detail in Chapter 2, and a more complete version of this figure will be shown in Figures 2.6 and 2.7.

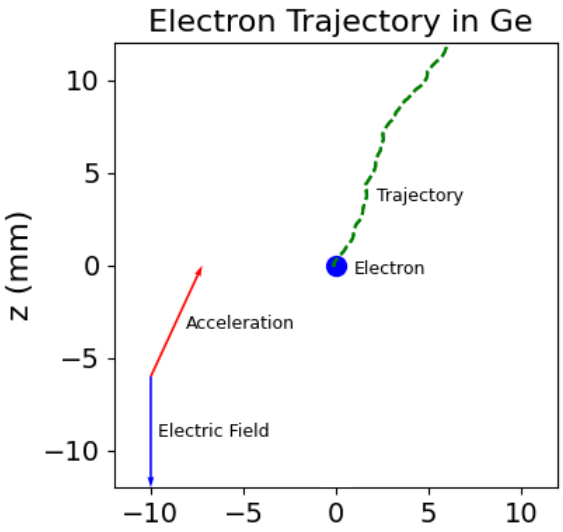

Figure 1.9: This figure shows a cartoon of how a single example electron moves in an anisotropic semiconductor crystal with an electric field like those used in the SuperCDMS detectors. We show this to illustrate the combination of the two dominant effects: under an electric field, an electron will accelerate in a direction different from the electric field [27, 30], and the zigzag motion that occurs due to scatterings along its path. The combination of the accelerations and scatterings produces a large number of phonons, as shown in Figure 1.10.

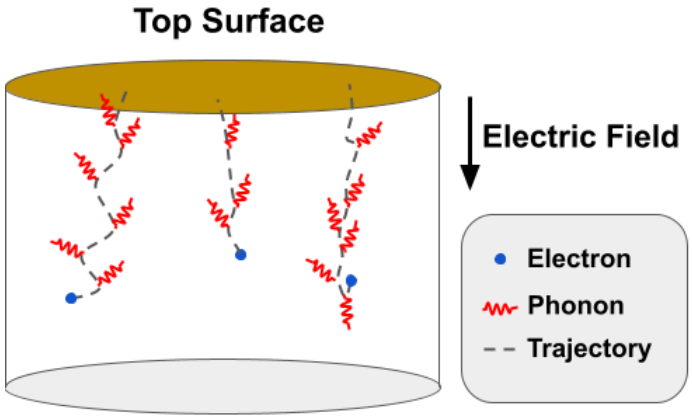

Figure 1.10: This figure shows a cartoon of phonons being emitted from electrons during propagation in an anisotropic semiconductor crystal with an applied voltage across it, like those used by SuperCDMS detectors. We show this because both electrons and holes (not shown) scatter and emit phonons. In both cases, this causes their path to have a zigzag trajectory [20], and can produce enough phonons for a measurement, especially for large voltages.

1.3.2 Charge Transportation Modeling in SuperCDMS Detector Simulation

In this section, we provide an overview of the modeling and simulation of the charge and phonon transport and describe how it fits into the overall SuperCDMS simulation framework. In the first paragraph, we provide an overview of the different parts of the SuperCDMS experiment simulation as shown in Figure 1.11. In the second paragraph, we describe the advantages and limitations of the primary simulation framework, Geant4 [31], for our work. In the third paragraph, we discuss the custom addition of the Geant4 Condensed Matter Physics, G4CMP [32], charge transportation modeling, as well as its status prior to the start of this work, as well as how we will improve it.

The SuperCDMS experiment simulation consists of different parts, as shown in Figure 1.11. The simulation is built on top of the Geant4 toolkit, which provides the geometry and infrastructure for modeling the properties and interactions of particles in different materials. Within this framework, the event generation begins with a source simulation that models the initial particles entering the detector volume. Such a source can be either a standard model particle as a background source or a dark matter particle. These events are then passed to the detector simulation stage, which incorporates several specialized modules: the crystal simulation, implemented using the G4CMP extension to model charge and phonon transport in the semiconductor, the sensor simulation, which describes the response of the readout channels, and the noise simulation, which models the electronic and thermal fluctuations present in the real experiment. The combined output of these components produces a set of data in the same format as that recorded by the physical detectors. The charge and phonon data are then processed through the reconstruction pipeline, which extracts best-fit results for quantities like position and energy and produces the final processed data used for analysis. This structure allows the simulation to replicate the full experimental chain from particle interaction to final analysis-level observables. We note that the focus of this thesis is on improvements to the crystal simulation.

The primary simulation framework, Geant4, has multiple advantages and limitations for our work. Geant4 serves as the foundation of our simulation framework because it provides a mature

and widely validated toolkit for modeling particles, their propagation and interactions, and detector geometry. Its modular design allows the integration of custom physics processes and supports complex geometries and realistic material descriptions, making it well-suited for large-scale detector simulations such as SuperCDMS. However, Geant4 represents charged particles using a classical, point-like description and does not natively support the quantum-mechanical behavior of electrons and holes in a semiconductor crystal. In particular, the anisotropic band structure, direction-dependent acceleration, and scattering processes that govern charge transport in a semiconductor are not included. To model these effects within the Geant4 infrastructure, G4CMP adopts a semi-classical, particle-like approximation for electrons and holes that captures the quantum mechanical features of their motion while remaining compatible with Geant4's trajectory-based tracking.

The G4CMP framework is extended in this work to improve its charge transport modeling by addressing limitations in its earlier implementations and incorporating a more complete semi-classical description of charge motion in semiconductor crystals. Before this work, the G4CMP framework provided only a partial implementation of the physics governing charge transport in semiconductor crystals; for example, it only included simplified assumptions about the band structure. The results of this version did not match our expectations from the theory, including energy conservation issues. The work in this thesis describes the extensions of the crystal simulation component of G4CMP to incorporate a semiclassical transport model that captures the full set of quantum mechanical effects overviewed in the previous paragraphs and described in detail in the coming chapters. These additions provide a physically motivated, direction-dependent description of charge motion compatible with the Geant4 infrastructure, enabling the detector simulation to more accurately reproduce the behavior of electrons and holes in silicon and germanium crystals that can be compared to test-bench results, and used by the experiment for the search analysis.

Having concluded our discussion of charge transportation modeling in the SuperCDMS detector simulation and our plans for enhancing it, as the main goal of the thesis, we now provide an overview of the thesis to help us understand the big picture of its different parts.

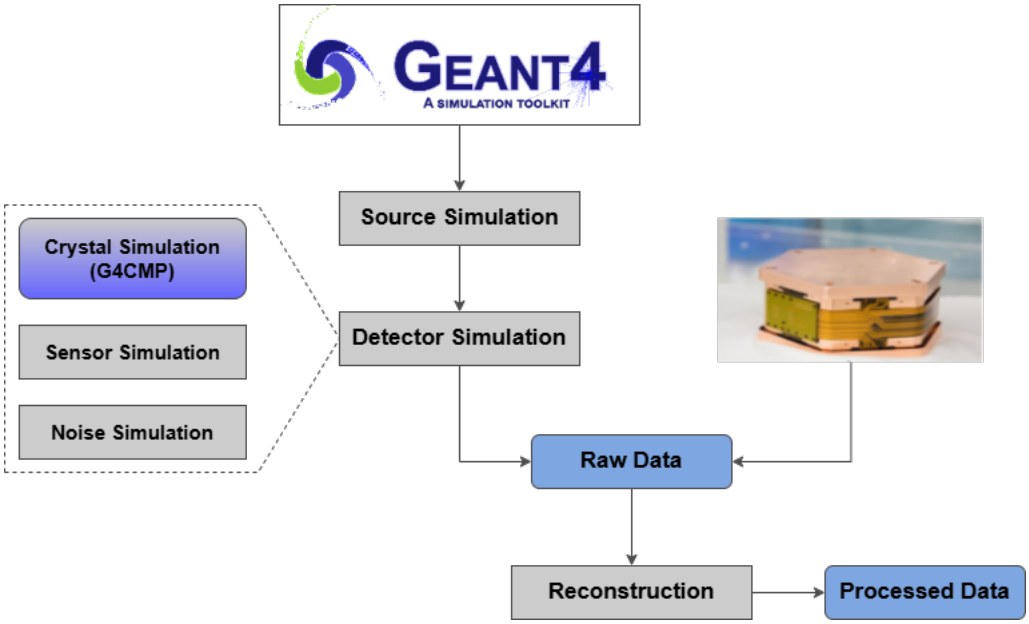

Figure 1.11: This figure shows how the custom charge and phonon transport simulations in this work, labeled Crystal Simulation, fit into the entire SuperCDMS simulation framework, which starts at the top and works its way downward. We show it because while SuperCDMS uses the Geant4 toolkit to simulate both the source (incident particles in Figure 1.5) and the detector simulation, in this work we focus on the modeling of charge transportation in anisotropic semiconductor crystal using the custom software package known as Geant4 Condensed Matter Physics (G4CMP) [32]. Note that the figure includes a number of components that come after the crystal simulation but are not used in this work. They include the sensor and noise simulation components as well as the parallel structure for data from the detector and how it is processed on the right-hand side.

1.4 Overview of the Thesis

In this thesis, we focus on the physics and simulation of electron transport in low-temperature, single-crystal solids to assist with our experiments. Our goals include building a deep understanding of the quantum mechanical behaviors, an intuitive understanding of the expectations of their effects in macroscopic observables, a working simulation that models the dominant effects, and evidence that the simulation matches our expectations. While we have covered the basics, achieving these goals will take a number of steps and a clear path forward. Since the detectors work by observing charges collected by sensors, we study what happens to free electrons that originate inside the detector and focus on the macroscopic distribution of their arrival positions on the surface. As we will see, many of the various microscopic effects will individually produce complex macroscopic outcomes. In combination, the complexity rises further. The steps towards our goal begin with a proper understanding of the quantum mechanical description of charge transport inside a crystal lattice, as well as the various interactions that a charge can have along its trajectory. We then move to providing intuition about the impact of each effect by taking advantage of the ability of simulations to allow for turning them on and off one at a time. Specifically, we can simulate a large number of electrons emitted from a point in a hypothetical detector in various configurations and record their arrival distribution. These results can be compared to both expectations as well as to a set of test-bench results, shown in Figures 1.12 and 1.13.

With our overview of the motivation, goals, and path complete, we next give a more detailed description of the rest of this document. In Chapter 2, we describe the most modern theoretical understanding of the charge transportation in crystal semiconductors, including a wave-like and particle-like description of the charge motion, the different energy levels and energy bands, and the scattering effects with an eye towards how to model the quantum mechanical nature of the charge transportation with a particle-like description. In Chapter 3, we introduce a number of physically motivated approximations to create a particle-like model for charge transport in solids, and analyze how atomic structure, electric fields, and scattering effects affect the arrival positions. In Chapter 4, we introduce a toy simulation that includes only the effects described in Chapter 3,

to help us form intuitive expectations for both the macroscopic (arrival patterns on the top surface) and microscopic (charge propagation) behaviors of electrons in both the absence and presence of each of these effects. In Chapter 5, we showcase the full SuperCDMS crystal simulation results with G4CMP after the inclusion of our modeling upgrades and compare them to both our expectations formed in Chapter 4 and the experimental data. In Chapter 6, we outline directions for improving the modeling of the scattering, how the modeling framework developed in this thesis may be applied beyond the SuperCDMS experiment for quantum computing, and we conclude the thesis by commenting on our hopes for the upcoming SuperCDMS experiment at SNOLAB.

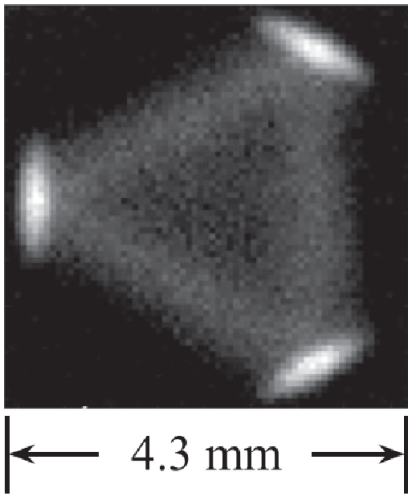

Figure 1.12: This figure shows an example set of experimental results for the arrival positions of electrons at the top surface of a $10\ \mathrm{mm} \times 10\ \mathrm{mm} \times 4\ \mathrm{mm}$ silicon crystal test device with a monoenergetic source at the center. We show this because it is an example of a result that we expect to be able to simulate and compare with. We note that in this case, the crystal has a $[111]$ orientation (more on that in Chapter 2), a temperature of $5\ \mathrm{K}$, and a $-4\ \mathrm{V}$ potential applied. Picture taken from Ref. [33].

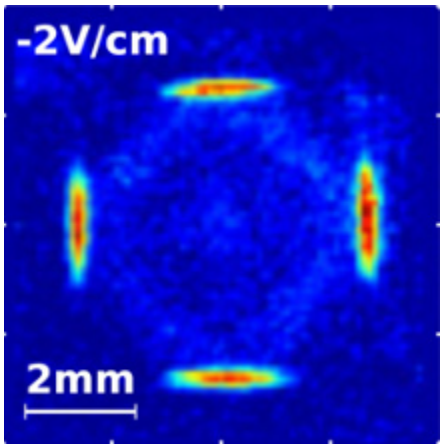

Figure 1.13: This figure shows an example set of experimental results for the arrival positions of electrons at the top surface of a $3.89\ \mathrm{mm} \times 10\ \mathrm{mm} \times 10\ \mathrm{mm}$ high-purity germanium crystal test device with a monoenergetic source at the center [34]. We show this because it is an example of a result that we expect to be able to simulate and compare with. We note that in this case, the crystal has an orientation of $[101]$, a temperature of $1\ \mathrm{K}$, and a $-2\ \mathrm{V}$ potential applied. Picture taken from Ref. [34].

2. QUANTUM MECHANICAL DESCRIPTION OF CHARGE PROPAGATION IN SEMICONDUCTOR CRYSTALS

In this chapter, we introduce the quantum mechanical description of the behavior of charge carriers in semiconductor crystals, following the discussions in Refs. [26, 27, 30, 35, 36][1]. The inclusion of the quantum effects is essential for accurately modeling and interpreting the response of semiconductor-based dark matter detectors, such as those used in the SuperCDMS experiment. Unlike classical motion in a vacuum, charge transport in a crystal must take into account the wave-like description of charges, which leads to a macroscopic description that can be significantly different from motion in free space.

The motion of charges in a semiconductor is governed by the allowed set of energies, a toy example of which is shown in Figure 1.8, featuring direction-dependent maxima and minima (known as valleys) that lead to anisotropic dynamics arising from the crystal lattice's structure. We note in advance that, since there are currently no simulation tools capable of directly modeling this wave-like behavior within the context of detector-scale particle transport, we will need descriptions that are not only well-motivated but lend themselves to an effective particle-like description, ones that retain the essential quantum features of the system. That stage of the modeling will be described in Chapter 3 and implemented in the custom Geant4 Condensed Matter Physics (G4CMP) simulation package, which is an extension of the longstanding Geant4 software framework.

As we will see, the details of the geometry of the crystal lattice lead to different valleys in materials like silicon and germanium. While most electrons will be bound to an atom in the lattice, electrons that gain enough energy will detach from their original atom and behave as a mobile negative charge, while the absence of the electron in the atom behaves like a mobile positive charge, called a hole. At low energies, the motion of electrons and holes can be separately approximated using the typical vacuum equations, but with effective direction-dependent masses around the minima and maxima of the relevant allowed energies, that reflect the symmetries of

[1] For simplicity, we will only add references for material outside the scope of those texts.

the underlying crystal. While both electrons and holes can move freely between atoms, they may also scatter off the lattice or other particles, changing their momentum and energy in ways that can produce lattice vibrations (we will refer to these as phonons because of their particle-like nature in a solid), which must be accounted for in any realistic transport model. We note in advance that many of the upcoming results are only relevant for electrons, as they are the real particles. The transport of holes can be thought of as being determined by a simplified subset of the effects; we will be explicit when results affect electrons only, and refer to charges when both are affected in similar ways.

The style of this chapter will be a combination of derivations and quoted results, with the primary goal of providing a qualitative but intuitive sense of the quantitative modeling used in later chapters. In Section 2.1, we begin by describing the most relevant aspects of the wave-particle duality of electrons to set the stage for how quantum mechanical calculations produce results that differ from classical predictions. In Section 2.2, we provide an overview of the results for the general description of charges in solids, which includes the allowed energy bands, and show the primary implications for the specific case of single crystals. In Section 2.3, we use the periodic structure of the crystal to calculate the allowed energy states. In Section 2.4, we describe how, near specific extrema, the motion of charges in these states can be approximated as particle motion with either a modified scalar effective mass or a direction-dependent mass. Finally, in Section 2.5, we outline the scattering processes that influence charge motion, which must be included in any realistic description of nature.

2.1 Wave-like Vs. Particle-like Description of Charge Motion

In this section, we begin with a simplified description of the quantum mechanical framework required for calculating the motion of charges in semiconductor crystals to illustrate the non-classical (and non-intuitive) behaviors. A proper use of the most relevant quantum mechanical terms, their meanings, and how they are related to each other through the Schrödinger wave equation that governs their motion is essential for understanding and describing how charge carriers propagate, especially in anisotropic crystals like silicon and germanium. In the first paragraph, we use the

example of the famous double-slit experiment to highlight the most important wave-like properties of particles. In the second paragraph, we bring in the Schrödinger equation for quantum behavior and explain its use for describing charges in free space. In the third paragraph, we describe how the wave-like quantum modeling can be readily used as as part of a particle-like description of electron motion in crystals.

The double-slit experiment highlights the most important wave-like properties of particles [37, 38]. It reveals that electrons, when passed one at a time through two slits, form an interference pattern characteristic of wave behavior. As shown in Figure 2.1, even though electrons are emitted and detected as discrete particles, the pattern on the detection screen shows the wave-like interference between multiple possible paths.

The Schrödinger equation can be used to describe the quantum behavior of charges in free space. The time-independent Schrödinger equation for a particle of mass m is written as:

$$H\psi(\vec{r}) = \left[-\frac{\hbar^2}{2m}\nabla^2 + V(\vec{r})\right]\psi(\vec{r}) = E\psi(\vec{r}), \tag{2.1}$$

where H is called the Hamiltonian, $\vec{r}$ is the position of the particle, $\psi(\vec{r})$ is the particle's wavefunction, $V(\vec{r})$ is the potential imposed on the particle, E is the total energy, and $\hbar$ is the reduced Planck constant. In free space, the potential $V(\vec{r})$ will be zero, and the wavefunction solution is interpreted as describing how the probability amplitude of finding the particle varies in space [39]. In this case, the solutions to this equation are plane waves, given by

$$\psi(\vec{r}) = \psi_0 e^{i\vec{k}\cdot\vec{r}}, \tag{2.2}$$

where ψ_0 is the amplitude of the wavefunction, $\vec{k}$ is the wavevector, and the corresponding energy is given by:

$$E(\vec{k}) = \frac{\hbar^2 k^2}{2m}. \tag{2.3}$$

This description allows for a direct representation of the waves' momentum through $\vec{p} = \hbar\vec{k}$, and

its direction determines the direction of wave propagation, as illustrated in Figure 2.1.

The wave-like quantum modeling can be readily used as part of a particle-like description of electron motion in crystals. Since electrons are fundamentally described by wavefunctions, we can approximate their particle-like behavior as the superposition of many plane-wave states with wavevectors clustered around a central value $\vec{k}_0$, and refer to this as a wave packet. We can associate the position and velocity of the wave packet using simple relations. Specifically, if the electron is described by a wave packet centered at wavevector $\vec{k}_0$, we can associate the electron velocity with the average group velocity, which is given by

$$\vec{v}_g = \vec{\nabla}_{\vec{k}} E(\vec{k}_0). \tag{2.4}$$

As long as the wavevector distribution of the plane waves that construct the wave packet remains narrow and do not spread significantly, the motion of the wave packet resembles that of a classical particle. This approximation forms the foundation of semiclassical transport models and remains reliable even when the potential energy terms are added to the Schrödinger equation. While the solutions are non-trivial for solids in general, the special case of the periodic atomic structure in crystals allows us to accurately model electron dynamics, using the techniques described in Chapter 3.

Having introduced the wave-particle duality and the Schrödinger equation to effectively describe the motion of electrons as a wave packet, we are now prepared to examine how periodic potentials in solids modify the energy-momentum relationship and give rise to energy bands.

2.2 Energy Bands and Electron and Hole Transport in a Solid

In this section, for pedagogical reasons, we summarize the results of the calculations that describe the allowed propagation of charges in solids before deriving them for the special case of crystals in Section 2.3.2. The primary results are that only certain energies, as shown in Figure 2.2 are allowed, referred to as energy levels, and that these allowed energy levels are direction-dependent, as shown in Figure 1.8. Both will have significant implications for charge transport and

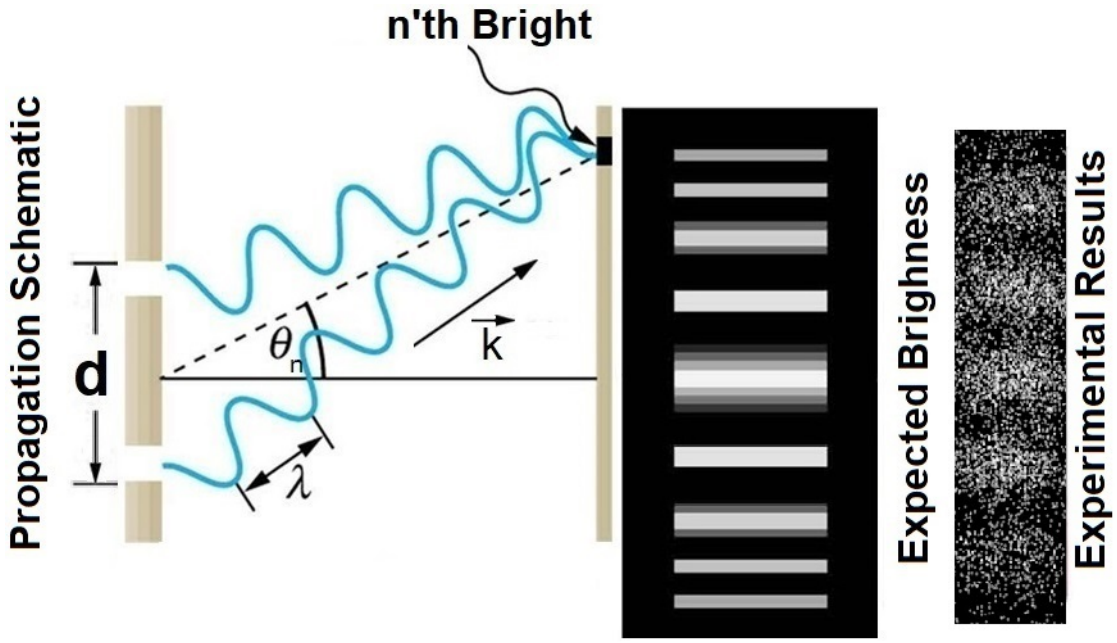

Figure 2.1: This figure shows three different views of the famous double-slit experiment, but using electrons [37, 40]. We show it to illustrate the quantities of the wave and particle-like nature of electrons. In the propagation schematic on the left, the wavevector $\vec{k}$ can be defined with the direction of electron wave propagation (same direction as $\vec{k}$ on the figure) and magnitude $|k| = \frac{2\pi}{\lambda}$ where λ is given by the de Broglie wave relation. The constructive interference peaks shown in the middle figure as bright regions occur for the cases where the path lengths corresponds to an integer number of wavelengths, which is satisfied when $\lambda = \frac{d \sin\theta_n}{n}$, where d is the distance between the two slits, n can be any integer number, and θ_n is the angle of the n'th Bright spot relative to the center of the slits. Experimental results for individual electrons are shown on the right from Ref. [41].

how solids are used in detectors.

There is value in defining a number of terms. Solids that easily allow for charge movement are referred to as conductors, those that do not allow for charge movement are known as insulators, and solids in between are known as semiconductors. The set of allowed energy levels can be closely spaced, and when this occurs, it is referred to as an energy band. Additionally, significant energy separation between different energy bands in a solid can occur, which is described as a band structure for the material, and when there is a significant energy difference between the energy bands, we refer to that as a band gap. In the first paragraph, we describe the significant differences between the allowed motion of electrons in the set of bands shown in Figure 2.2, which gives rise

to why they are referred to as the valence band and the conduction band. In the second paragraph, we describe how the magnitude of the bandgap provides a useful separation between the properties of solids and motivates their categorization into conductors, insulators, and semiconductors. In the third paragraph, we describe a useful property of semiconductors, which is that when the band gap is small, electrons in the valence band can be readily excited into the conduction band in an interaction, propagate, and scatter off the lattice, creating phonons. In the fourth paragraph, we take a moment to point out that the combination of a small bandgap and the ability of charges to move through the crystal, be guided under an electric field, and produce phonons, which can also freely propagate like a particle, is what makes them useful as detectors for experiments like SuperCDMS.

There are significant differences between the allowed motion of electrons in the set of bands shown in Figure 2.2, which gives rise to why they are referred to as the valence band and the conduction band. A solid in an equilibrium state can be thought of as a large number of electrons surrounding fixed atomic sites, where each has settled into its lowest available energy state. The lowest available electron energy states can be thought of as simply being attached to the atom; for our purposes, they can be thought of as effectively being stationary. As these electrons reside in the outer valence shell of the atom, they are referred to as being in the valence band. As individual electrons are allowed to have higher energies, and these energies can be thought of as being due to their motion through the solid, those energy states are referred to as being in the conduction band.

The magnitude of the bandgap provides a useful separation between the properties of solids and motivates their categorization into conductors, insulators, and semiconductors. In conductors, the valence and conduction bands overlap, allowing free electron flow at all times. In insulators, the band gap is large, and electrons remain bound, inhibiting conduction. Semiconductors occupy the intermediate regime where thermal or interaction energy can excite electrons from the valence band into the conduction band. The absence of an electron in the outer valence shell can be thought of as a "hole".

A useful property of semiconductors is that when the band gap is small, electrons in the va-

lence band can be readily excited into the conduction band in an interaction, propagate, and cause phonons in the atomic structure when they collide with the lattice. As the conduction band is not fully occupied, electrons can move from the conduction band of one atom to that of another atom, effectively moving in the solid, which is the basis of the charge propagation in solids. Since valence electrons can also move between atoms, this allows for the convenient description of the location of the hole left behind as the motion of a single positive charge carrier. Both charge carriers can travel through the semiconductor and propagate in ways that are significantly affected by the lattice structure. Moving to the special case where the solid consists of atoms in a single-crystal lattice structure, the energy levels and motion of the charges become simpler to describe, as both are readily described by Equation 2.1, but where the potential is periodic. The same is true for phonons, as they can be created from any type of interaction with the lattice and they can propagate through the crystal with a particle-like motion. These processes will be described in more detail in Section 2.5.

The combination of a small bandgap and the ability of charges to move through the crystal, be guided under an electric field, and produce phonons, which can also freely propagate, is what makes semiconductors useful as detectors for experiments like SuperCDMS. This is especially true when they are placed under an external voltage. When a dark matter particle or a standard model particle interacts with the detector and deposits energy, as shown in Figure 1.5, it not only excites electrons, which create a corresponding number of holes, but both will be accelerated by the external voltage, interact with the atoms, and produce phonons. By recording the energies of the final set of charges and phonons, we can make inferences about the energy and type of the incident particle.

Having introduced the concept of band structure and its general impact on charge propagation, we proceed to examine the specific geometry of the atoms in silicon and germanium crystals, which enables us to provide a quantitative description of the transport by their energy bands. We will switch to providing more of the derivations, as the calculations for solids with symmetric atomic structures can help elucidate the understanding of the details of charge transport. Since the system is more complicated than propagation in free space, we will introduce some useful concepts

based on the symmetries of the lattice for use in our calculations, for example, the concepts known as the Brillouin zone and the reciprocal lattice.

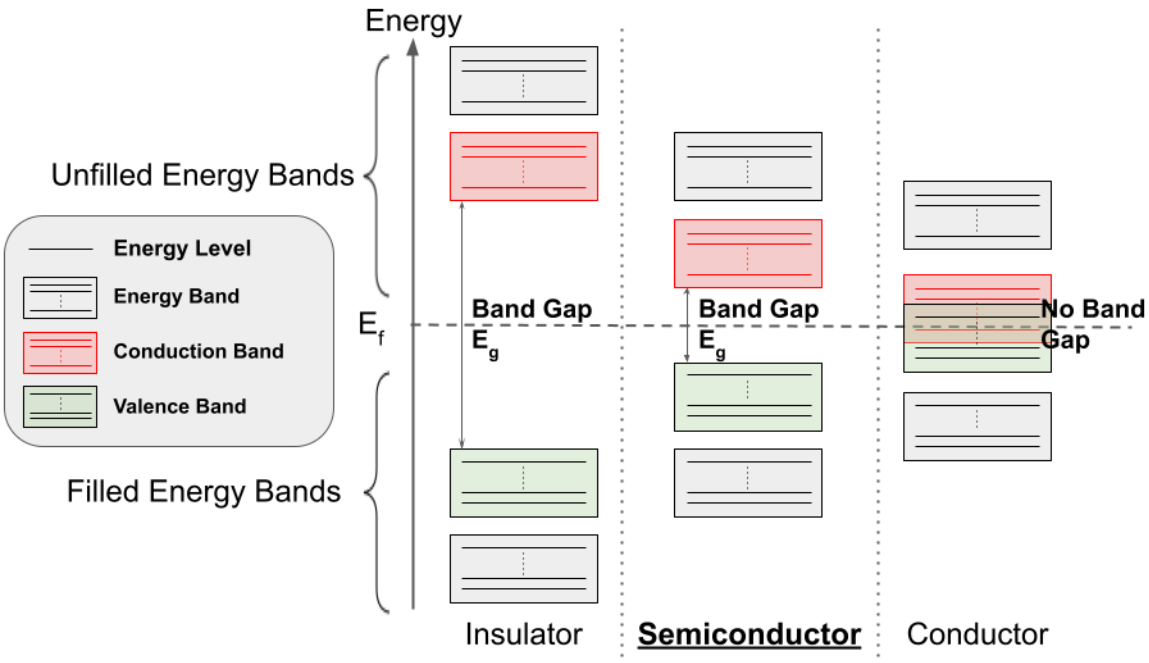

Figure 2.2: This figure shows a simplified cartoon of the allowed energy levels for electrons grouped as energy bands for three different types of solids referred to as insulators, semiconductors, and conductors. We show it because the energy determines whether an electron is attached to the lattice (valence band and below) or free to move within the solid (conduction band and above), and the energy difference between those bands can give the solid different properties. We note that in semiconductor crystals, which are the focus of this work, an external energy deposition larger than the band gap can excite an electron from the valence band into the conduction band, where it can propagate. We also note that, as shown in Figure 1.8 and in more realistic detail in Figures 2.6 and 2.7, the energy levels in semiconductors are also dependent on the direction of the charge carrier's wavevector.

2.3 Energy Band Structure in Semiconductor Crystals

In this section, we derive how the periodic structure of the atoms in a crystal determines the energy levels available to electrons and holes, and how this gives rise to the formation of complex anisotropic energy bands that are dependent on the charge's wavevector, as shown in Figure 1.8.

Understanding these energy bands is essential for particle-like modeling of charge transport at the microscopic level, which is our goal in Chapter 3. To do this, in Subsection 2.3.1, we describe the periodic atomic structure of silicon and germanium in real space and explain how this periodicity leads to a corresponding structure in wavevector space. As we will see, a description of the lattice symmetry in terms of wavevectors, a concept known as the Brillouin zone, allows us to use the geometric framework to quantitatively determine the properties of the energy bands. In Subsection 2.3.2, we use the Schrödinger equation with a periodic potential to derive the most important properties of semiconductors.

2.3.1 Crystal Lattice Structure and First Brillouin Zone

In this section, we describe the underlying crystal structure of semiconductors, such as silicon and germanium, to explain the spatial periodicity of the potential and how this periodicity leads to a corresponding structure in wavevector space. We also introduce two concepts, known as reciprocal space and the Brillouin zone, for use in calculations. In the first paragraph, we describe the periodic atomic arrangement in real space and define the crystal lattice. In the second paragraph, we illustrate how the periodic atomic arrangement of silicon and germanium leads to a spatially repeating potential that determines charge transport behavior. In the third paragraph, we define the concepts of both a reciprocal lattice and the first Brillouin zone, as well as how they are constructed, and why they are useful for describing how the symmetries of the real-space lattice can be used to describe similar symmetries in the electron's set of allowed wavevectors. In the fourth paragraph, we identify the high-symmetry directions and points within the Brillouin zone, which are useful for identifying the axes that will be most important for our discussion of charge transportation in Subsection 2.4.2.

The periodic atomic structure of semiconductors like silicon and germanium, shown as in Figure 2.3, can be used to explain the origin of their symmetry and the constraints it places on electron motion, such as the periodic potential, which is crucial to solving the Schrödinger equation discussed in Subsection 2.3.2. A useful way to describe the crystal lattice is to think of the smallest group of atoms in the lattice that reflects the overall symmetry, such that the entire lattice can be

built up by repetition in three dimensions. This group is referred to as a unit cell, where one atom is at the origin $(0, 0, 0)$. Both silicon and germanium have a unit cell that can be described as a two-atom basis face-centered cubic (FCC) structure where the second atom is located at $(\frac{1}{4}, \frac{1}{4}, \frac{1}{4})$. This structure is known as diamond cubic. Because the atomic pattern is the same in every cell, we can use the fact that the physical properties of the crystal remain the same in certain directions.

The periodic atomic arrangement of silicon and germanium leads to a spatially repeating energy potential that governs charge behavior. The particles in the atoms effectively provide an electromagnetic potential for nearby electrons. Since the crystal lattice of both silicon and germanium is periodic, some physical properties, including this potential, are also periodic. This means that if we write the potential energy as a function of position, $U(\vec{r})$, it satisfies the condition

$$U(\vec{r}) = U(\vec{r} + \vec{R}), \tag{2.5}$$

for any $\vec{R}$ that connects one lattice point to another equivalent point in the crystal, referred to as a lattice vector. In other words, the electron sees exactly the same environment whether it is near one atom or another, which governs the quantum mechanical motion of charges through the material and ultimately results in the curved valence and conduction bands shown in Figure 1.8.

For pedagogical reasons, we describe and define both the reciprocal lattice and the first Brillouin zone in advance of their use in calculations. Each will be useful for describing how the symmetries of the real-space lattice play a role in describing similar symmetries in the allowed set of electrons' wavevectors, which is essential for determining the allowed electron wavefunctions and energy bands in Subsection 2.3.2. In advance of the calculations, we note that the solutions of the wave equation in Equation 2.1 are expected to correspond to plane waves but with additional boundary conditions imposed by the periodic atomic arrangement; there will be similarities between the periodicity in the real-space crystal structure and the allowed set of wavevectors. Since one can think of the wavevectors as being a Fourier transform of the position (or Fourier space), one can define the set of wavevectors that are solutions to the periodic potential as also having a

periodic structure; this set of wavevectors is what is referred to as the reciprocal lattice. With this definition, we further define the first Brillouin zone as the region in reciprocal space that is closer to the origin than to any other reciprocal lattice point, as illustrated in Figure 2.4. As we will see in Subsection 2.3.2, while electrons can have any wavevector, all physical properties are periodic in reciprocal space, so any $\vec{k}$ outside the Brillouin zone can be translated back into it without changing the physical content of the state, which means that it contains all the physically distinct wavevectors. The same is true for holes. Thus, the symmetry of this zone is useful both in describing the symmetry of the real-space lattice as well as how the energy of any charge varies with direction.

The three-dimensional high-symmetry directions and points within the Brillouin zone, as shown in Figure 2.5, can be used to establish the axes that will be most important for our discussion of charge transportation in Subsection 2.4.2. These directions correspond to specific paths between high-symmetry points such as the center ($\Gamma = [000]$), the zone edges ($X = [001]$ in silicon), and the corners ($L = [111]$ in germanium). Later, we show that these directions determine where energy extrema, such as conduction band minima, are likely to occur.

Having defined the crystal lattice and introduced the Brillouin zone and its high-symmetry directions, we now turn to solving the Schrödinger equation for these special cases. In the next section, we show that in a periodic potential, the electron states can be written as a plane wave multiplied by a lattice-periodic function (Bloch's theorem), and how it leads directly to the formation of energy bands and valley structures in silicon and germanium.

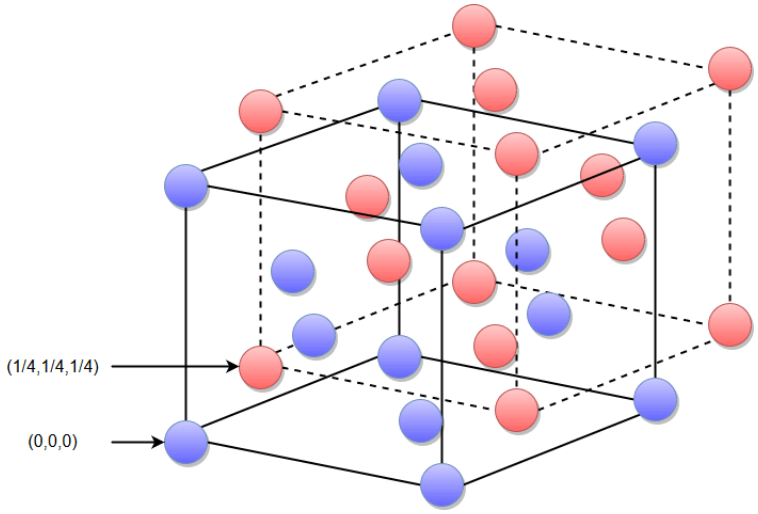

Figure 2.3: This figure shows the diamond cubic crystal structure typical of silicon and germanium. We show it because it illustrates how the crystal can be described as a face-centered cubic (FCC) lattice with a two-atom basis. The blue atoms form the FCC lattice with one atom at the origin $(0, 0, 0)$ and the red atoms form the basis, offset by $(\frac{1}{4}, \frac{1}{4}, \frac{1}{4})$. This repeating unit forms the real-space crystal lattice, which underlies the periodic potential that governs the motion of electrons. The periodic structure shown here leads directly to the definition of the reciprocal lattice and the construction of the Brillouin zone in Figures 2.4 and 2.5.

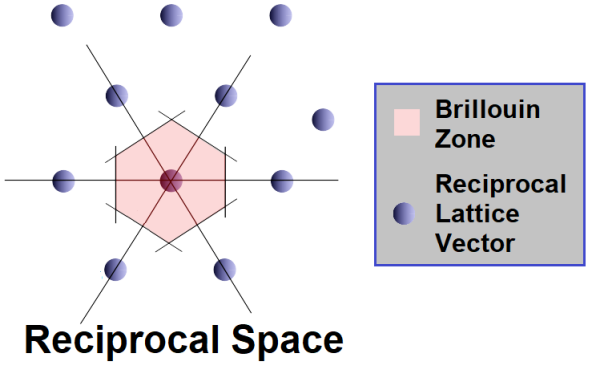

Figure 2.4: This figure shows a wavevector space where each location anywhere in the space indicates an allowed wavevector for a face-centered cubic (FCC) crystal lattice structure as shown in Figure 2.3. We show it because, with the aid of the lines and pink regions, it allows for the definition of the Brillouin zone, which can be used to specify the full set of allowed wave states and energies for both silicon and germanium crystals. The point in the center of the pink region, the origin, corresponds to the Γ point, where $\vec{k} = 0$. The points surrounding it correspond to the reciprocal lattice vectors, where their position indicates both the magnitude and direction of the corresponding wavevector $\vec{k}$ relative to the origin. The lines indicate the symmetry directions along the reciprocal lattice vectors, such as the high-symmetry paths connecting Γ to X or L. The pink region, centered on the origin and bounded by the bisector along each line to the nearest-neighbor point along the line, is known as the first Brillouin zone. Taken from [42].

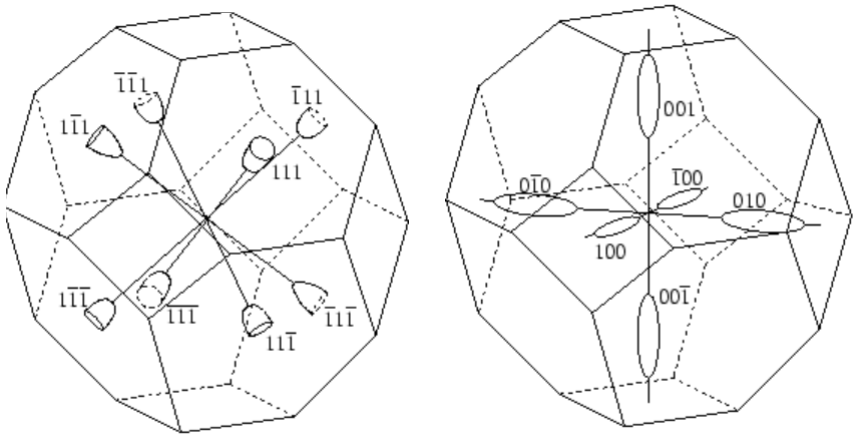

Figure 2.5: This figure shows a three-dimensional version of the same lattice in Figure 2.4, which allows us to see the full set of directional definitions. We show it because the directions defined by the Brillouin zone are useful for describing wave propagation. In the left figure, we show the directions along the edges of the Brillouin zone, which is defined as $L = [111]$ along with its variations. The directions situated along the zone boundaries are known as the $X = [001]$, and are shown along with its variations in the right figure. The center of the Brillouin zone is known as $\Gamma = [000]$. Taken from [35].

2.3.2 Solutions to the Schrödinger Equation in Semiconductor Crystals: Bloch's Theorem

In this section, we use the Schrödinger equation with a periodic potential to derive the most important properties of semiconductors. This will involve several steps, and we will proceed with a combination of derivations where useful and references for others. We start with calculations of the form of the electron wavefunction in a crystal, as it provides the fundamental result that the allowed wavefunctions are constrained by the periodicity of the lattice and can be expressed as a product of a plane wave and a lattice-periodic function. Using the concepts of the Brillouin zone, we can show that both the wavefunctions and the corresponding energy levels are periodic in wavevector space, and that the energy spectrum forms continuous bands that exhibit local extrema as shown in Figures 2.6 and 2.7 for silicon and germanium. This will have enormous implications, including a band gap between the valence and conduction bands, as well as allowing for simple transport descriptions at low energies. In the first paragraph, we show how translational symmetry in the potential imposes mathematical constraints on the electron's wavefunction. In the second paragraph, we demonstrate how these constraints result in energy bands and explain why the energy levels in a semiconductor depend on the charge's wavevector. In the third paragraph, we explain why the Brillouin zone alone can fully describe the energy bands. In the fourth paragraph, we focus on the interpretation of the valleys in the low-energy limit for silicon and germanium, as they will prove useful in describing charge transportation in our devices. In the fifth paragraph, we report quantitative numbers on the silicon and germanium band gaps, as they represent the minimum energy required to excite an electron from the valence band to the conduction band, which is a crucial concept to consider when studying how a detector responds to an incident particle.

The Schrödinger equation for an electron in a crystal can be used to show how translational symmetry in the potential leads to mathematical constraints on the electron's wavefunction. We begin by noting that the single-electron Schrödinger equation in a crystalline solid is a special case of Equation 2.1. To distinguish this special case, we can rewrite it using different notation for the

mass and potential:

$$H\psi(\vec{r}) = \left[-\frac{\hbar^2}{2m_0}\nabla^2 + U(\vec{r})\right]\psi(\vec{r}) = \epsilon\psi(\vec{r}), \tag{2.6}$$

where m_0 is the free electron mass, $U(\vec{r})$ is the periodic potential produced by the atomic lattice, and ϵ is the resulting allowed energy. As stated in Equation 2.5, the defining property of the potential is that it is invariant under lattice translations. We define the lattice translation operator $T_{\vec{R}}$, which acts on a wavefunction as

$$T_{\vec{R}}\psi(\vec{r}) = \psi(\vec{r} + \vec{R}). \tag{2.7}$$

We can see that the operator $T_{\vec{R}}$ commutes with the Hamiltonian:

$$[H, T_{\vec{R}}] = 0, \tag{2.8}$$

which implies that the eigenfunctions of H can be chosen to also satisfy

$$T_{\vec{R}}\psi(\vec{r}) = \lambda_{\vec{R}}\psi(\vec{r}), \tag{2.9}$$

where $\lambda_{\vec{R}}$ is the eigenvalue of the translation operator. We also have:

$$T_{\vec{R_1}}T_{\vec{R_2}}\psi(\vec{r}) = T_{\vec{R_2}}T_{\vec{R_1}}\psi(\vec{r}) = T_{\vec{R_1}+\vec{R_2}}\psi(\vec{r}) = \psi(\vec{r} + \vec{R_1} + \vec{R_2}). \tag{2.10}$$

Therefore, we have:

$$\lambda_{\vec{R_1}+\vec{R_2}} = \lambda_{\vec{R_1}}\lambda_{\vec{R_2}}, \tag{2.11}$$

which is true for:

$$\lambda_{\vec{R}} = e^{i\vec{k}\cdot\vec{R}}, \tag{2.12}$$

for some vector $\vec{k}$. Additionally, we have:

$$T_{\vec{R}}\psi(\vec{r}) = \psi(\vec{r}+\vec{R}) = \lambda_{\vec{R}}\psi(\vec{r}) = e^{i\vec{k}\cdot\vec{R}}\psi(\vec{r}). \tag{2.13}$$

This defines the allowed phase change under translation and introduces the wavevector $\vec{k}$ as a conserved quantum number.

For each fixed wavevector $\vec{k}$, the Schrödinger equation can be simplified to a different eigenvalue problem with a periodic wavefunction, which means the energy levels are a function of wavevector $\vec{k}$ that includes its direction. The relation

$$\psi_{\vec{k}}(\vec{r}+\vec{R}) = e^{i\vec{k}\cdot\vec{R}}\psi_{\vec{k}}(\vec{r}) \tag{2.14}$$

implies that $\psi_{\vec{k}}(\vec{r})$ cannot be periodic, but its magnitude and phase repeat modulo a phase factor. To take advantage of this we define a function $u_{\vec{k}}(\vec{r})$ by

$$\psi_{\vec{k}}(\vec{r}) = e^{i\vec{k}\cdot\vec{r}}u_{\vec{k}}(\vec{r}), \tag{2.15}$$

which allows us to write:

$$e^{i\vec{k}\cdot(\vec{r}+\vec{R})}u_{\vec{k}}(\vec{r}+\vec{R}) = \psi_{\vec{k}}(\vec{r}+\vec{R}) = e^{i\vec{k}\cdot\vec{R}}\psi_{\vec{k}}(\vec{r}) = e^{i\vec{k}\cdot(\vec{r}+\vec{R})}u_{\vec{k}}(\vec{r}), \tag{2.16}$$

which shows that $u_{\vec{k}}(\vec{r})$ is lattice-periodic

$$u_{\vec{k}}(\vec{r}+\vec{R}) = u_{\vec{k}}(\vec{r}). \tag{2.17}$$

This is Bloch's theorem: in a periodic potential, the eigenfunctions of the Hamiltonian can be written as a plane wave multiplied by a lattice-periodic function. Since each value of $\vec{k}$ corresponds to a different eigenvalue problem, by inserting Equation 2.15 into Equation 2.6 the Schrödinger

equation at fixed $\vec{k}$ becomes:

$$\left[\frac{1}{2m_0}(\hbar\vec{k}+\hat{\vec{p}})^2+U(\vec{r})\right]u_{n\vec{k}}(\vec{r})=\epsilon_n(\vec{k})u_{n\vec{k}}(\vec{r}), \tag{2.18}$$

where the $\hbar\vec{k}$ comes from applying the $\vec{\nabla}$ operator on $e^{i\vec{k}\cdot\vec{r}}$ in Equation 2.15, $\vec{p}=-i\hbar\nabla$ is the canonical momentum operator, and n labels the discrete set of solutions of the Bloch eigenvalue problem often referred to as the energy band quantum number. The solutions to each of these eigenvalue problems will give us the energy levels at that fixed $\vec{k}$, and combined with all possible values for $\vec{k}$ form the energy band structure for the semiconductor.

The set of wavevectors that are solutions to the periodic potential, known as the reciprocal lattice, simplifies the interpretation of the energy bands. This is enabled by expanding the real-space description of $u_k(\vec{r})$ in Equations 2.15 and 2.17 into a Fourier series, which allows us to see why the Brillouin zone alone can fully describe the energy bands. The exponential term $e^{i\vec{k}\cdot\vec{r}}$ in Equation 2.15 describes a plane wave with crystal momentum $\vec{k}$, while the function $u_{\vec{k}}(\vec{r})$ encodes the effect of the atomic structure on the electron's behavior as seen in Equation 2.17. Because $u_{\vec{k}}(\vec{r})$ has the same periodicity as the lattice, it can also be expanded in a Fourier series via:

$$u_{\vec{k}}(\vec{r})=\sum_{\vec{G}\in\mathbb{G}}c_{\vec{G}}e^{i\vec{G}\cdot\vec{r}}, \tag{2.19}$$

where c_G is the set of expansion coefficients, $\vec{G}$ describes a vector that is periodic under translation and readily identified as a reciprocal lattice vector, and the full set of such vectors is given by $\mathbb{G}$. For any lattice vector $\vec{R}$, we have:

$$u_{\vec{k}}(\vec{r}+\vec{R})=\sum_{\vec{G}\in\mathbb{G}}c_{\vec{G}}e^{i\vec{G}\cdot(\vec{r}+\vec{R})}=\sum_{\vec{G}\in\mathbb{G}}c_{\vec{G}}e^{i\vec{G}\cdot\vec{R}}e^{i\vec{G}\cdot\vec{r}}. \tag{2.20}$$

Due to the periodicity of $u_{\vec{k}}(\vec{r})$ shown in Equation 2.17, we have:

$$e^{i\vec{G}\cdot\vec{R}}=1, \tag{2.21}$$

which shows that $\vec{G} \cdot \vec{R} \in 2\pi\mathbb{Z}$, where $\mathbb{Z}$ is the integers group, for all reciprocal lattice vectors $\vec{G} \in \mathbb{G}$ and lattice vector $\vec{R}$. This is the defining condition of reciprocal lattice vectors in $\mathbb{G}$ as was illustrated in Figure 2.4. By adding this into the wavefunction $\psi_{\vec{k}}(\vec{r})$, we can write:

$$\psi_{\vec{k}}(\vec{r}) = \sum_{\vec{G}\in\mathbb{G}} c_{\vec{G}} e^{i(\vec{k}+\vec{G})\cdot\vec{r}}, \tag{2.22}$$

which shows that the wavefunction is a superposition of plane waves with wavevectors $\vec{k} + \vec{G}$. Shifting the wavefunction by any reciprocal lattice vector $\vec{G}_0 \in \mathbb{G}$, we have:

$$\psi_{\vec{k}+\vec{G}_0}(\vec{r}) = \sum_{\vec{G}\in\mathbb{G}} c_{\vec{G}} e^{i(\vec{k}+\vec{G}+\vec{G}_0)\cdot\vec{r}}. \tag{2.23}$$

But as $e^{i\vec{G}_0\cdot\vec{R}} = 1$ by definition of $\vec{G}_0$, for all vectors $\vec{G} \in \mathbb{G}$ we have:

$$e^{i(\vec{G}_0+\vec{G})\cdot\vec{R}} = e^{i\vec{G}_0\cdot\vec{R}} e^{i\vec{G}\cdot\vec{R}} = 1, \tag{2.24}$$

which means that the group of $\vec{G}_0 + \mathbb{G}$ is the same group as $\mathbb{G}$. This means that the wavefunctions in Equation 2.23 are just a relabeling to $\vec{G}' = \vec{G} + \vec{G}_0$ with shifted coefficients:

$$\psi_{\vec{k}+\vec{G}_0}(\vec{r}) = \sum_{\vec{G}'\in\mathbb{G}} c_{\vec{G}'-\vec{G}_0} e^{i(\vec{k}+\vec{G}')\cdot\vec{r}}. \tag{2.25}$$

Thus, the Hamiltonian matrix is periodic in $\vec{k}$-space: it has the same structure at $\vec{k}$ and $\vec{k} + \vec{G}$ for all $\vec{G} \in \mathbb{G}$, leading to the same eigenvalue spectrum when shifting by a reciprocal lattice vector. Therefore, for every eigenfunction ψ_k and reciprocal lattice vector $\vec{G} \in \mathbb{G}$, there exists an eigenfunction at $\vec{k} + \vec{G}$ with the same energy. As the set of eigenfunctions is a complete basis for the Hilbert space, we can define the eigenfunctions so that:

$$\psi_{\vec{k}+\vec{G}_0}(\vec{r}) = \psi_{\vec{k}}(\vec{r}). \tag{2.26}$$

This indicates that the wavefunctions are unique only up to a constant reciprocal lattice vector, meaning that the Brillouin zone alone can fully describe all the energy bands.

We now transition from a general description to a focus on the interpretation of the energy band in the low-energy limit for silicon and germanium, demonstrating that they exhibit extrema, which we will refer to as valleys when considering minima in the conduction band. Because the wavefunctions of electrons in a crystal obey Bloch's theorem, they are periodic in both physical space and wavevector space. Specifically, in Equation 2.26 we showed that the wave functions of a periodic potential are periodic in the reciprocal space. As a result, the energy $\epsilon(\vec{k})$ must also satisfy periodic boundary conditions in reciprocal space:

$$\epsilon(\vec{k} + \vec{G}) = \epsilon(\vec{k}). \tag{2.27}$$

As the energy bands are continuous, this periodicity implies that multiple extrema can occur within the Brillouin zone. It can be shown [26] that there are minima at high-symmetry points such as X or L as shown in Figure 2.5. In anisotropic semiconductors like silicon and germanium, the minimum appears at these high-symmetry points, forming what are referred to as valleys. In silicon, the conduction band has six equivalent minima located along the X directions, specifically at $\pm[100]$, $\pm[010]$, and $\pm[001]$, as shown in Figure 2.6. These valleys are degenerate and define the dominant transport directions at low temperature. In germanium, the valleys are located along the eight L directions, i.e., $\pm[111]$, $\pm[1\bar{1}1]$, $\pm[\bar{1}11]$, and $\pm[\bar{1}\bar{1}1]$, as shown in Figure 2.7. These valleys also form degenerate energy minima and determine the directions in which low-energy electrons propagate. The maximum, in the valence band, describes the motion of holes; while this can be thought of as a valley, that term is usually reserved for the motion of electrons in the conduction band. In both materials, the valley structure reflects the underlying crystal symmetry and strongly influences the anisotropic behavior of carriers.

Since the methods for calculating the numerical values of the energy band extrema for specific crystals are outside the scope of this work, we simply report the band gap energies. These numbers

are needed for simulation modeling as the band gap represents the minimum energy required to excite an electron from the valence band to the conduction band, which directly affects how a detector responds to an incident particle. In silicon, the band gap is temperature-dependent and can be approximated as [43]

$$E_g^{\mathrm{Si}}(T) = 1.166 - \frac{4.73 \times 10^{-4} T^2}{T + 636} \ \mathrm{eV}, \tag{2.28}$$

where T is the temperature. At cryogenic temperatures (e.g., $T = 50\ \mathrm{mK}$), the band gap is effectively $E_g^{\mathrm{Si}} \approx 1.166\ \mathrm{eV}$. Similarly, for germanium, the band gap is given by [43]

$$E_g^{\mathrm{Ge}}(T) = 0.7437 - \frac{4.77 \times 10^{-4} T^2}{T + 235} \ \mathrm{eV}, \tag{2.29}$$

which evaluates to $E_g^{\mathrm{Ge}} \approx 0.7437\ \mathrm{eV}$ at $T = 50\ \mathrm{mK}$. These values represent the minimum energy required to excite an electron from the valence band to the conduction band at the lowest-energy valley. Higher-energy valleys, such as the L or Γ points in silicon, or X and Γ in germanium, require significantly more energy (e.g., over $0.8\ \mathrm{eV}$) and are not thermally populated at cryogenic temperatures.

Having concluded our discussion of the solutions to the Schrödinger equation in semiconductor crystals using Bloch's theorem, we next introduce a pair of approximations near the energy band extrema, which provide a framework for calculating the energies of electrons and holes at low energies. These approximations lay the foundation for Chapter 3, where we utilize these results to model the transport properties of charge carriers in semiconductors in a semiclassical manner, using effective masses that approximate the quantum mechanical effects.

2.4 Approximations for Electron and Hole Energy Band Structures Near Extrema

In this section, we present two different methods for approximating solutions to Equation 2.18 near the band extrema. At low energies, all free electrons and holes are located near the band extrema, as they don't have enough energy to move to higher energies. This allows for the use

of approximations near band extrema to effectively describe charge transport at low energies. For pedagogical reasons, we begin by exploring the results for hole propagation, as even though it is not the focus of this thesis, some aspects of it help our intuition regarding electron propagation. In Subsection 2.4.1, we introduce a method to approximate solutions for holes at $\vec{k_0} = 0$, referred to as the $\vec{k} \cdot \vec{p}$ method, and then interpret the results for low energies to justify a simplistic model for the behavior of hole energy bands. In Subsection 2.4.2, as the conduction band minimums are not along the $\vec{k_0} = 0$ and are anisotropic, we use a fully mathematical Taylor series expansion technique to approximate the energy around an extremum which can be readily interpreted as an anisotropic mass tensor, which is the core of our modeling approach for electrons in Chapter 3.

2.4.1 The $\vec{k} \cdot \vec{p}$ Approximation Method for Hole Energy Bands

In this section, we describe our first approximation method and apply it to derive the wavefunction solutions for holes at their $\vec{k_0} = 0$ extrema to provide an effective mass description. In the first paragraph, we introduce a widely used method for calculating energy band structures, which can be employed for semiconductors that have a number of energy bands that intersect at an extremum at $\vec{k} = 0$. In the second paragraph, we justify our description of the hole energy bands using a simplified scalar effective mass. This will set us up well for the electron transport descriptions in Subsection 2.4.2.

Since a quantum mechanical description of the wavefunctions must take into account the superposition of the wavefunction solutions for all of them, one can think of the bands as "interacting." A useful approximation for our case is to employ a perturbation method, where we treat the multiple-band solutions from the crystal structure as a small correction to the free-charge case. Following the description of Ref. [44] and expanding the $(\hbar\vec{k} + \vec{p})^2$ term in Equation 2.18, we can rewrite the Hamiltonian in a perturbative form, to obtain:

$$H(\vec{k}) = H_0 + \frac{\hbar^2 k^2}{2m_0} + \frac{\hbar}{m_0}\vec{k} \cdot \vec{p}, \tag{2.30}$$

where we have renamed the $\frac{p^2}{2m_0}$ term as the H_0 which illustrates that it is crystal Hamiltonian at the

band extremum $\vec{k}_0 = 0$, the second collects the $\hbar^2 k^2$ terms and describes the free space solution, and the cross term placed third suffices to describe the influence of other bands and the remaining terms which are expected to be small (perturbation) due to the multiple allowed interacting bands. This is known as the $\vec{k} \cdot \vec{p}$ method. Using non-degenerate perturbation theory around the extrema shown in Figures 2.6 and 2.7 [44], the energy for band n can be written to second order as:

$$\epsilon_n(\vec{k}) = \epsilon_n(0) + \frac{\hbar^2 k^2}{2m_0} + \frac{\hbar^2}{m_0^2} \sum_{i \neq n} \frac{|\langle u_{i,0}|\vec{k} \cdot \vec{p}|u_{n,0}\rangle|^2}{\epsilon_n(0) - \epsilon_i(0)}, \tag{2.31}$$

where the second term is the kinetic energy of a free particle, while the third term accounts for the influence of neighboring bands, i, on the curvature of the energy dispersion.

While several models can describe the energy bands of holes to a certain degree of approximation, a simplified scalar effective mass can be used in our description of the hole energy bands. For our purposes, we will describe some of the complexity for use in future simulations, then proceed to the set of approximations we made and their justification. Several models have been developed using the $\vec{k} \cdot \vec{p}$ method, including Kane's model [45] and the Luttinger–Kohn model [46] to describe the hole energy bands. Following the description of these works, we report without derivation that at the Γ-point ($\vec{k} = 0$) the valence band extrema consist of three closely spaced bands. The first two bands share the same maximal energy, but have different slopes as a function of $\vec{k} = 0$. The one with a larger curvature (smaller slope) is known as the Heavy Hole (HH) band, and the other, where the energy decreases more rapidly away from $\vec{k} = 0$, is known as the Light Hole (LH) band. The third is energetically inaccessible at low temperatures and is known as the Spin-Orbit or Split-Off (SO) band; for completeness, we note that the SO band lies approximately $\Delta = 44\ \mathrm{meV}$ below in silicon and $\Delta = 290\ \mathrm{meV}$ below in germanium [36]. Since both the HH and LH bands are anisotropic around $\vec{k} = 0$, a more proper description of their equienergetic surfaces is given by [47]:

$$\epsilon = ak^2(1 \pm g(\theta, \phi)), \tag{2.32}$$

where a is a constant, θ and ϕ are the polar and azimuthal angles of wavevector $\vec{k}$ using the same

frame as shown in Figure 2.5, and $g(\theta, \phi)$ is given by Refs [48, 49]; this description is why the bands are referred to as having warped surfaces in the literature, and in general, the HH band is much more anisotropic than the LH band. Luckily, for a hole with energy ϵ, in the limits of $\epsilon \ll \Delta$ and $\epsilon \gg \Delta$, all valence bands are effectively parabolic [49]. Because of the scattering effects that we will discuss in Section 2.5.1, at $T = 50\,\mathrm{mK}$, in which SuperCDMS-like detectors operate, the thermal energy $k_B T \approx 4.3\,\mu\mathrm{eV}$ and the hole energies at all times can be considered to be extremely small compared to the HH–SO and LH–SO energy splitting. As a result, in this work, we only consider the $\epsilon \ll \Delta$ regime, where only the very top of the valence band is populated [50], and the valence bands are parabolic. The parabolic nature suggests that, to a reasonable degree of approximation, we can combine the two terms in Equation 2.31 to get:

$$\epsilon_c(\vec{k}) \approx \epsilon_c(0) + \frac{\hbar^2 k^2}{2m^*}, \tag{2.33}$$

where m^* is the particle's effective mass. Following Ref. [51, 52] we take the hole effective mass of $m_h^* = 0.35 m_e$ in germanium and $m_h^* = 0.5 m_e$ in silicon, where $m_e = 0.511$ MeV/c^2 is the electron's mass. We note that while these assumptions are not fully validated in the literature, we do not expect them to significantly affect the results in this work.

While more precise modeling of hole transportation could improve the accuracy of the SuperCDMS detector simulation, it is unclear whether a better description would enhance the experiment's sensitivity. We next move to the approximations for electron transportation, as they are the focus of this work. In this case, the anisotropies of the valleys are important, so we will use a Taylor series expansion to show that the low-energy conduction bands are well-modeled using a semiclassical description with a diagonalized mass tensor formalism.

2.4.2 Describing Electron Transport in a Semiconductor Crystal as Occurring in "Valleys"

In this section, we focus on the allowed energy minima in the conduction bands as shown in Figures 2.6 and 2.7. As the electron valleys are fast-changing, anisotropic, and not centered at $\vec{k} = 0$, the methods described in Subsection 2.4.1 are not easily applicable, but do help point a way

forward. For electrons at low energies, we use a Taylor series expansion around the valley minima. In this case, instead of getting a single effective mass, we will have a three-dimensional tensor. In the first paragraph, we describe the Taylor series expansion for electrons near an extremum and introduce a mass tensor notation, which will be useful for our semiclassical modeling in Chapter 3. In the second paragraph, we use the mass tensor for the case of the minima of the conduction bands to elucidate the particle-like modeling for electron transport at low energies.

The Taylor series expansion for electrons near an extremum illustrates the utility of incorporating a mass tensor notation, which will be central for our semiclassical modeling in Chapter 3. It provides a purely mathematical description of how a function (such as energy) changes near an extremum by using local derivatives. Bloch's theorem ensures that $\epsilon_n(\vec{k})$ is a smooth function within the Brillouin zone. Therefore, near a local extremum $\vec{k}_0$, we can expand the band energy in a Taylor series where the first two terms are given by:

$$\epsilon_n(\vec{k}) \approx \epsilon_n(\vec{k}_0) + \frac{1}{2}\sum_{\alpha,\beta} \left.\frac{\partial^2 \epsilon_n}{\partial k_\alpha \partial k_\beta}\right|_{\vec{k}_0} (k_\alpha - k_{0\alpha})(k_\beta - k_{0\beta}) = \epsilon_n(\vec{k}_0) + \frac{\hbar^2}{2}\langle k|\mathcal{M}_n^{-1}|k\rangle, \quad (2.34)$$

where α and β are the indices for the directions (which are arbitrary at this point), and the definition of the tensor $\mathcal{M}$ is given by:

$$\left(\mathcal{M}_n^{-1}\right)_{\alpha\beta} = \frac{1}{\hbar^2} \left.\frac{\partial^2 \epsilon_n(\vec{k})}{\partial k_\alpha \partial k_\beta}\right|_{\vec{k}_0}. \quad (2.35)$$

Given its role, we refer to it from here on as the mass tensor.

Focusing on the example of an electron in a cryogenic setting that has approximately the energy of the lowest energy valley, the mass tensor can be written in terms of the directions where the axes of the tensor are aligned with direction of the $\vec{k}$ at the minimum, (referred to as the longitudinal direction, and indicated with an L subscript) and those perpendicular (referred to as the transverse directions, and indicated with the T or $T1$ and $T2$ subscripts) to it. For both the silicon and germanium cases, we find that near each conduction band minimum, the energy dispersion is approximately ellipsoidal and can be expressed in a locally aligned coordinate system. In the valley frame, where the x axis is aligned with the valley direction, the mass tensor takes a diagonal

form with only two different constants, where we suggestively label them as m_L and m_T:

$$\mathcal{M}_n = \begin{bmatrix} m_L & 0 & 0 \\ 0 & m_T & 0 \\ 0 & 0 & m_T \end{bmatrix}. \tag{2.36}$$

For the wavevector $\vec{k} = (k_L, k_{T1}, k_{T2})$, rewriting Equation 2.34 the energy takes the form

$$\epsilon(\vec{k}) = \epsilon_0 + \frac{\hbar^2 k_L^2}{2m_L} + \frac{\hbar^2}{2m_T}(k_{T1}^2 + k_{T2}^2), \tag{2.37}$$

where m_L is the longitudinal mass along the valley axis, and m_T is the transverse mass perpendicular to it. These values are determined from experiment, in silicon $m_L = 0.92m_e$ and $m_T = 0.19m_e$, and in germanium $m_L = 1.588m_e$ and $m_T = 0.082m_e$ [26, 51, 52]. This formulation enables us to create particle-like modeling. Since we are describing low-energy electrons, we can safely work with the assumption that each conduction band electron resides within a uniquely labeled valley, and its motion is governed by the anisotropic mass tensor associated with that valley. The mass tensor in the lab frame is obtained by rotating this diagonal form into the global crystal coordinate system. This formalism is readily expandable to include additional potential energy sources in the Hamiltonian, such as an external voltage, and allows for a direction-dependent acceleration, which is necessary for accurate modeling of arrival patterns on the detector surface. We will revisit this in more detail in Chapter 3.

Having concluded our introduction of the modeling we will use for the energy bands of both electrons and holes, we turn to the various mechanisms by which charge trajectories can be altered through scattering. In the next section, we describe how scatterings can alter the energy and momentum of charges, including both cases where the electron ends up in the same valley or a different one after scattering, which are referred to as intravalley and intervalley scattering, respectively.

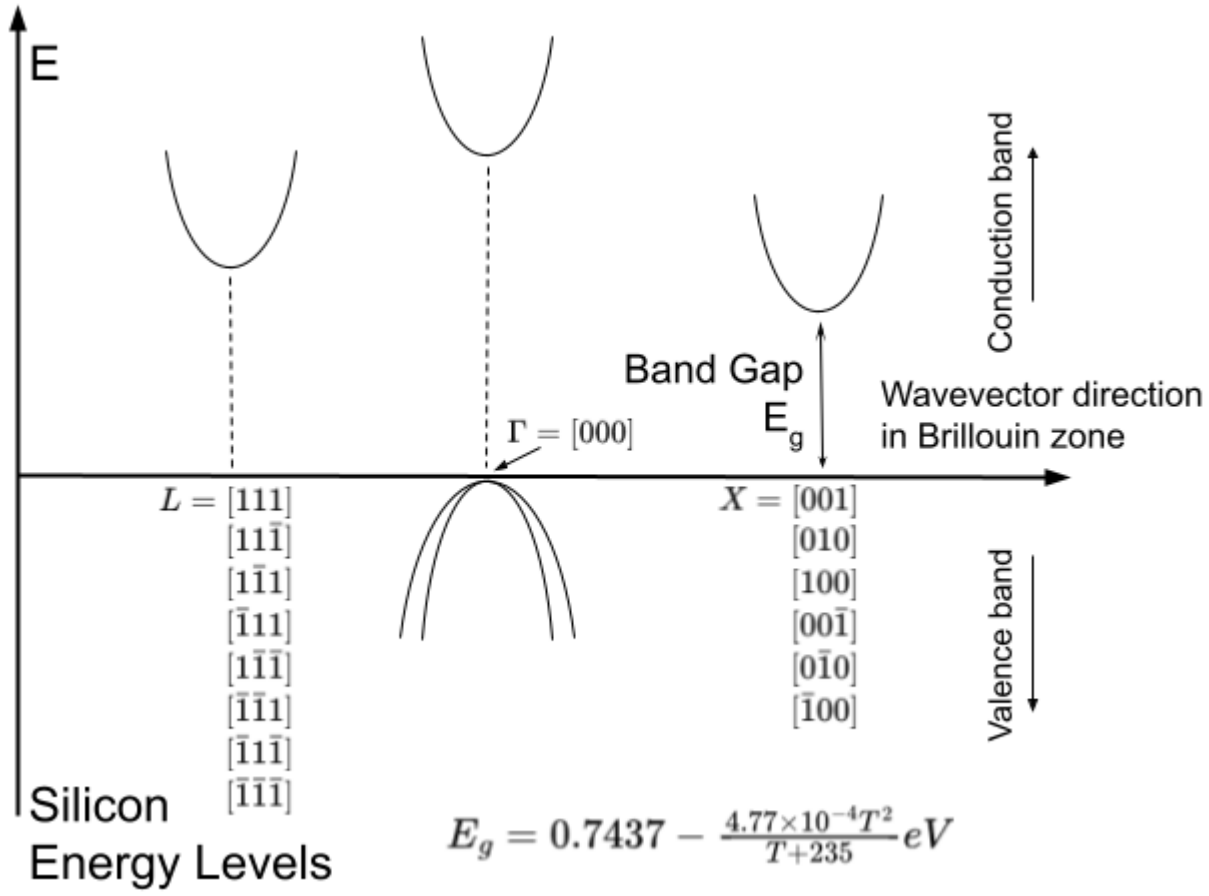

Figure 2.6: This figure shows the energy vs. wavevector for the allowed energy levels in a silicon crystal separated by electron direction zone. We show it because the allowed energy levels are dependent on the direction of propagation of the charge in the conduction band, and they minimize around the L, Γ (which indicates that the electron is essentially stationary), and X directions in the wavevector space as shown in Figure 2.5. For this reason, they are referred to as valleys. Note that the y-axis is left arbitrary as quantitative descriptions are temperature dependent. One of the implications of this result is that the minimum energy needed to excite an electron to the conduction band from the valence band is different for an electron with a wavevector direction along each of the six X directions (which, for low-energy electrons, becomes the most common direction of wavevector) shown in the right hand side of Figure 2.5. Similar results for germanium are shown in Figure 2.7.

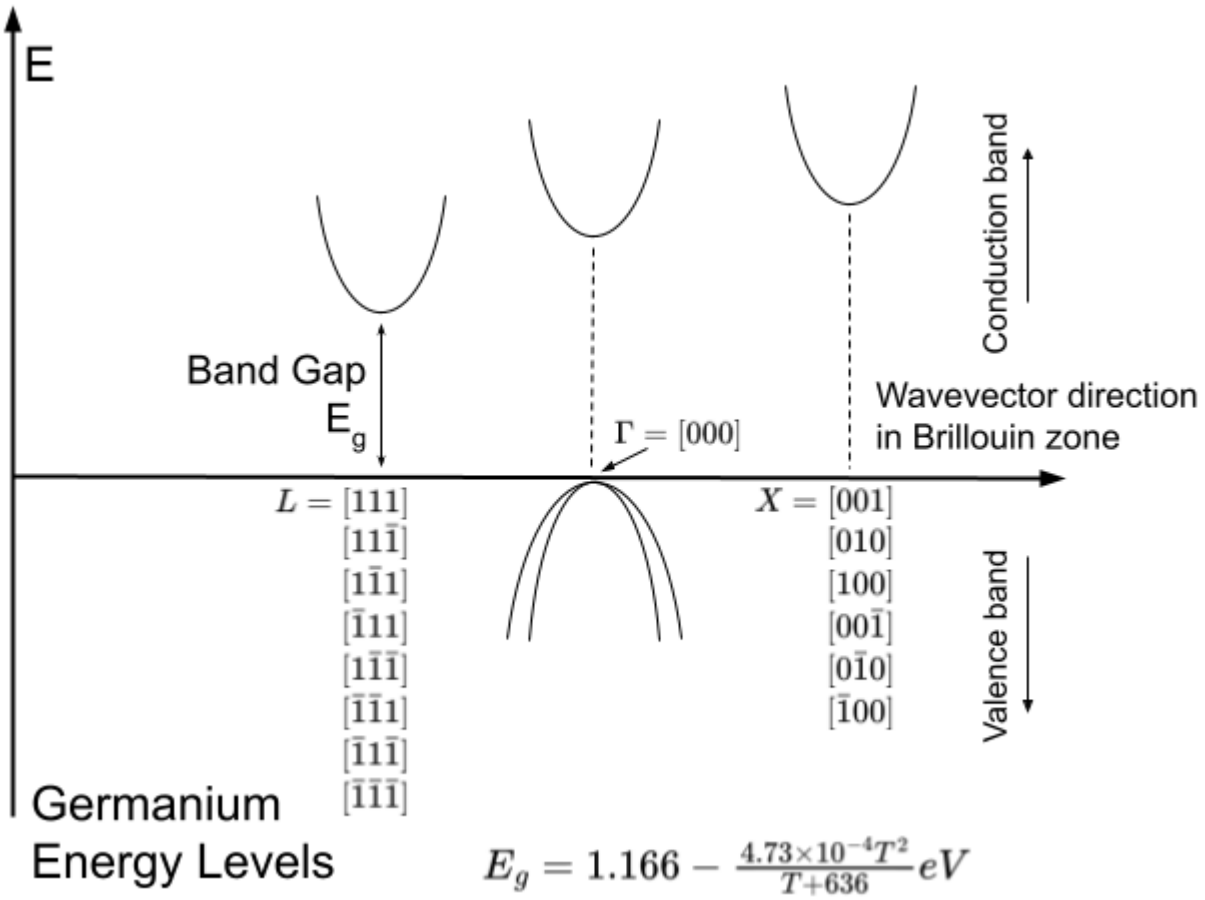

Figure 2.7: This figure shows the same energy levels vs. wavevector as in Figure 2.6, but for germanium. We show it because while the same valleys appear in germanium, the minimum energy needed to excite an electron to the conduction band from the valence band is for an electron with a wavevector direction along each of the eight L directions shown in the left hand side of Figure 2.5.

2.5 Scattering Effects in a Semiconductor Crystal

In this section, we describe the scattering processes, shown in Figure 2.8, that charges undergo as they propagate through a semiconductor crystal, as well as our simplified methods to model them in the simulations, as shown in Figure 2.9. A full description of charge scattering in a semiconductor crystal, in general, is complicated [47]. Our previous discussions of the transport have mostly assumed a fixed and uniform lattice, and that there are no other particles present to interact with. In a real crystal, charges can interact with the lattice in ways such that both are affected; they can interact with non-uniformities in the lattice (which we will refer to as crystal impurities), and they can interact with other particles, such as free charges or phonons. Each of these has the potential to change the momentum and energy of the charge as well as produce phonons. We note at the outset that the methods used in our simulations will be based on approximations and simplifications that are applicable at cryogenic temperatures and low-energy regimes.

Before describing our simplified modeling, we quickly comment on the notation used in this work. While holes can be described as a form of electron transport in the valence band valley, for our purposes, it only has a single valley that cannot change. For this reason, we will only refer to electrons as having a valley, and that only electrons can change valleys. With this in mind, our modeling will be done as two separate processes:

- Inelastic scatterings that emit a phonon, but don't change the charge's valley. These will be referred to as intravalley scattering, or Luke scatterings, and are shown on the left side of Figure 2.9.

- Elastic scatterings that do not emit a phonon but change the charge's valley. These will be referred to as intervalley scattering and are shown on the right side of Figure 2.9. We note that while holes can have elastic scatterings, when we are describing intervalley scatterings, we are referring to electrons only.

While both electrons and holes can scatter, we focus on the electron scattering, as we can describe hole scattering by considering a subset of electron scattering, as only the first category (intravalley

scattering) is useful in describing holes.

One can think of the dominant effects at cryogenic temperatures and low energies as being described by models in which the charge causes the atoms in the lattice to vibrate or the charge changes its trajectory because it encounters a local change in the potential. The former process can be modeled as the charge motion causing atoms to move within the lattice using what is known as deformation potential theory [26, 53]. The local motion of a lattice site will cause motion in the neighboring sites and propagate away as a wave, which is our phonon. This is the process in the top left of Figure 2.8. If the atoms within the basis of a unit cell move in phase or out of phase with each other, the outgoing phonon is referred to as an acoustic or optical phonon, respectively. The processes are referred to as acoustic or optical phonon emission scattering, and, as we will see, these phonons are low and high-energy, respectively. Typically, for kinematic reasons, low-energy phonon emission is not correlated with a change in the valley of the electron, but it can be with a high-energy emission. Switching to the case in which an electron encounters a crystal impurity, which is a local change in the potential, shown in the bottom right of Figure 2.8, the process is typically elastic, with different interaction rates depending on whether the impurity is neutral or charged. Since no phonon is produced, the electron can readily switch valleys.

A main motivation behind our simplified models comes from the expected interaction rates. Following the results presented in Ref. [28], Figure 2.10 shows the scattering rates for the various processes in the low-energy regime. A number of notes are in order. The first is that due to low free-charge and phonon population in the crystal, especially at low temperatures, the interaction rates for the processes in the top right and bottom left of Figure 2.8 are so small as to be considered negligible. The second is that the optical phonon emissions can only happen on the rare occasions where the electrons have an energy above the optical phonon emission threshold (quantitative detail below); this makes optical phonon emission processes rare in our settings. A further simplification is that since any high-energy phonon produced in optical phonon emission will quickly downconvert [52, 54], any phonon emission can effectively be thought of as just the production of lots of low-energy phonons. Thus, while imperfect, for electrons our modeling can

be reduced to the processes shown in Figure 2.9; we can effectively categorize any scattering as an intravalley scattering process with no change in electron valley, but with a phonon produced, and intervalley scattering, with no change in the electron's energy, but with a change in the electron's valley. For completeness, we again note that we model holes so that they participate in the former but not the latter processes.

In the first subsection, we describe our model of intravalley scattering, in which a charge emits a phonon but remains within its original valley, as shown on the left side of Figure 2.9; In the second subsection, we describe our simplified model of intervalley scattering, an electron-only process, as shown on the right side of Figure 2.9, where the electron changes valley without any change in its energy; holes don't undergo intervalley scattering, as they lack multiple symmetry-equivalent energy bands.

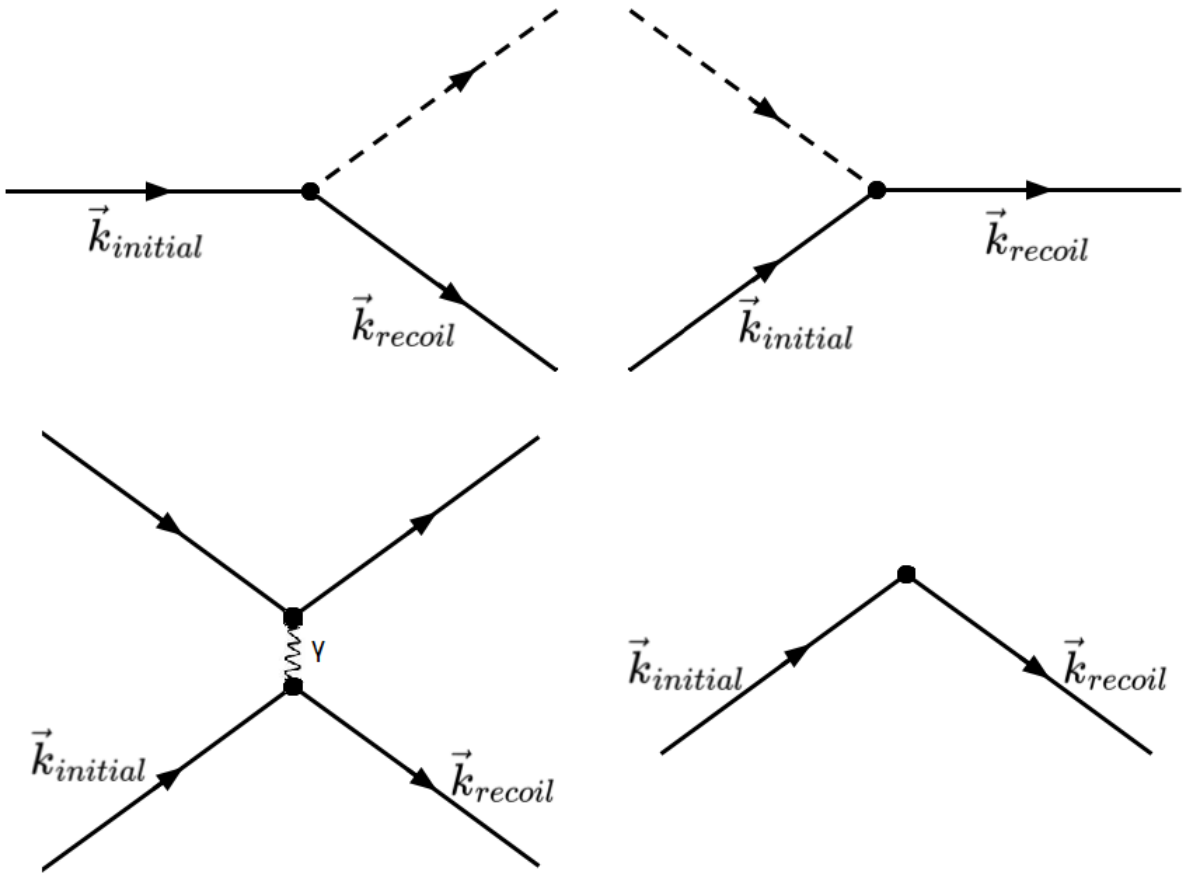

Figure 2.8: In this figure, we show Feynman diagrams of four different scattering processes. We show them to describe some of the most important types of scattering in a semiconductor crystal. In the top row, we show two inelastic scatterings. On the left, a charged particle interacts with a lattice site and emits a phonon, both changing directions and losing energy. On the right-hand side, a charged particle absorbs a phonon and scatters. On the bottom left, a charge interacts with another charge, transfers some energy, and scatters. On the bottom right, a charge interacts with a crystal impurity and scatters elastically without losing or gaining kinetic energy. It's important to note that in the low temperature, low energy regime, as shown in Figure 2.10 and discussed in the text, the only important scattering types are the phonon emission (top left) and impurity scattering (bottom right).

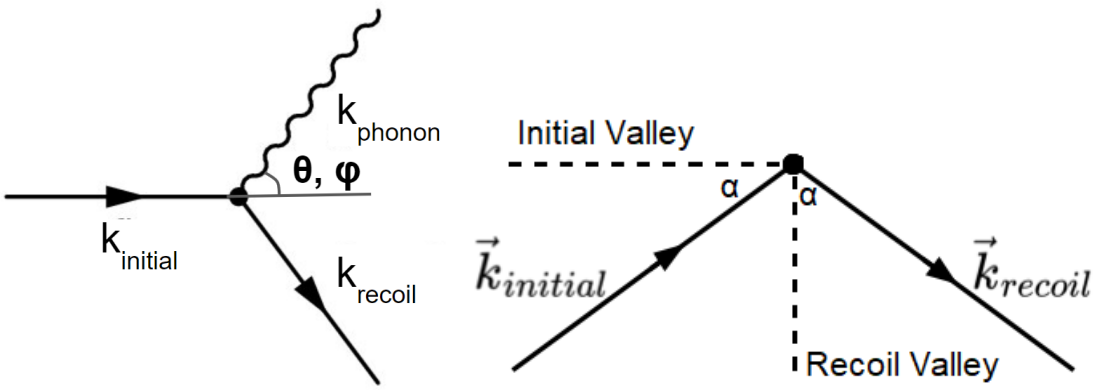

Figure 2.9: In this figure, we show the diagrams of the dominant pair of processes used in our simulations to model the more complete set of scattering processes shown in Figure 2.8. We show it to describe how we model changes in electron energy, momentum, and valley. For the reasons described in the text, all intervalley scattering processes (electrons and holes) are modeled using the left figure, where a charge emits an acoustic phonon without changing its valley, and all the intervalley scatterings (electron only) are modeled using the right figure, where an electron changes its valley while preserving the angle between its momentum and its valley without emitting a phonon.

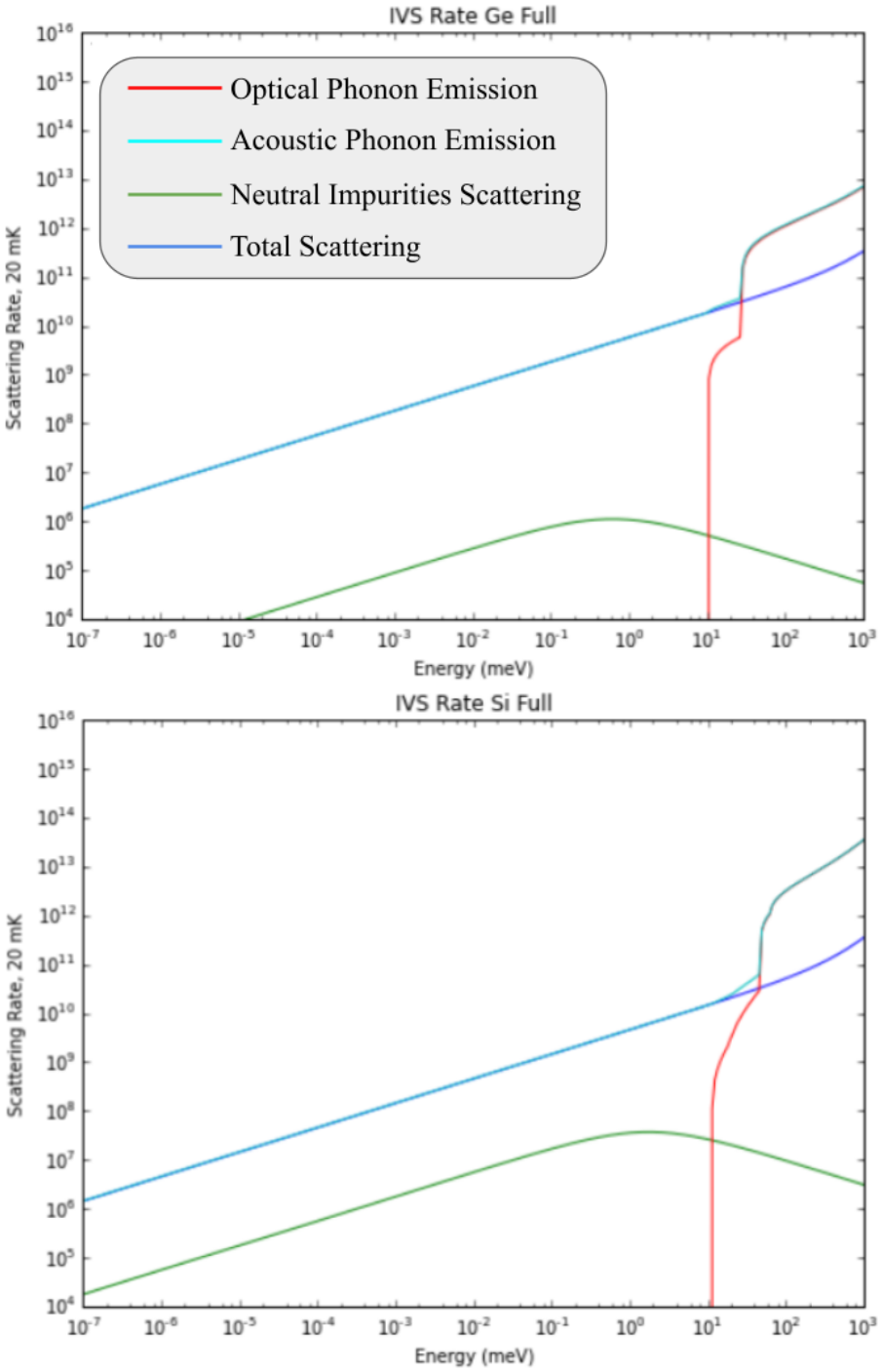

Figure 2.10: In this figure, we show the scattering rates of charges as a function of energy for both germanium and silicon. We show it to demonstrate the dominant scatterings at low energies, which helps justify the choice of processes shown in Figure 2.9. At the lowest energies, the scattering rate is dominated by acoustic phonon emission, which is entirely intravalley scattering; intervalley scatterings are rare but can occur and are dominated by interactions with impurities. At around $10\ \mathrm{meV}$, the scattering rate becomes dominated by optical phonon scattering, which emits a high-energy optical phonon. This energy is referred to as the optical phonon scattering threshold. Figures taken from Ref. [28].

2.5.1 Interactions Between Charges and the Lattice that Produce Phonons: Intravalley Scattering (Luke Scattering)

In this subsection, we describe our modeling of intravalley scattering as shown in the top left of Figure 2.8 or the left-hand side of Figure 2.9. We focus on the context of a crystal under an applied electric field, where a charge accelerates and gains energy, such that it can quickly scatter from a lattice site, emit a phonon, shedding some of its kinetic energy while remaining in the same valley [20, 55]. For the reasons mentioned above, we focus on the electron case where it remains within its initial conduction band valley, and this process is known both as intravalley and Luke scattering [52]; at low energies, a hole resides in a single valley, and so the same descriptions apply. In the first paragraph, we provide a general description of the phonon emission scattering kinematics in a crystal. In the second paragraph, we summarize the quantitative methods for estimating the scattering rates for optical and acoustic phonon production used in Figure 2.10. In the third and fourth paragraphs, we provide some of the quantitative methods used in the creation of Figure 2.10, which helps justify our simplifying assumptions.

We first provide a general description of the phonon emission scattering kinematics in a crystal. Since the interaction must conserve energy and momentum, as well as result in an allowed energy state of the charge, we can write:

$$\vec{k} = \vec{k'} + \vec{q}, \quad \epsilon = \epsilon' + \hbar\omega, \tag{2.38}$$

where $\vec{k}$ and ϵ are the initial wavevector and energy of the charge, $\vec{k'}$ and ϵ' are the final wavevector and energy of the change, and ω, $\vec{q}$ and $\hbar\omega$ are the frequency, momentum and energy of the emitted phonon, respectively. Note that we have changed the notation from Figure 2.9 from $\vec{k}_{initial}$ to just $\vec{k}$, and $\vec{k}_{recoil}$ to just $\vec{k'}$. The phonons emitted during this process are called Neganov-Luke phonons, and in principle can be acoustic or optical.

The quantitative methods from Refs. [28, 51] provide an estimate of the scattering rates for optical and acoustic phonon production used in Figure 2.10, which we use later. Following the

calculation of the scattering probabilities $P(k, k')$ per unit time done in Ref. [47], one can calculate the scattering rates $\frac{1}{\tau_{ac}}$ and $\frac{1}{\tau_{op}}$ for acoustic and optical phonon emission scattering respectively where τ_{ac} and τ_{op} are the mean free time between acoustic and optical scattering events. Before quoting the results from the derivations in Refs. [28, 51] in a parabolic band, we note that conservation of energy places limits on the minimum magnitude of the charge wavevector before a scattering, $\vec{k}$; the effective limits are referred to as k_{ac} and k_{op}, respectively. With this in mind, we quote the acoustic phonon emission scattering rate, which takes the form of:

$$\frac{1}{\tau_{ac}} = \frac{1}{3}\frac{\hbar k^2}{m l_0 k_{ac}}\left[1 - \frac{k_{ac}}{|\vec{k}|}\right]^3, \tag{2.39}$$

where $\vec{k}$ is the charge's wavevector, m is the charge's mass, the effective threshold wavevector k_{ac} is given by

$$k_{ac} = m|\vec{v}_{ac}|, \tag{2.40}$$

corresponding to a longitudinal acoustic phonon with phase velocity of $\vec{v}_{ac}$ and frequency of $\omega = |\vec{v}_{ac}||\vec{q}|$, $\vec{q}$ is the phonon wavevector, and l_0 is a characteristic length defined as:

$$l_0 = \frac{\pi\hbar^4\rho}{2m^3 C_{ac}^2}, \tag{2.41}$$

where ρ is the crystal mass density, while C_{ac} is the acoustic deformation potential constant, which quantifies how electronic energy bands shift due to lattice vibrations or strain in a crystal [56, 57]. Following the derivation of Ref [28], the optical phonon emission scattering rate τ_{op} takes the form of:

$$\frac{1}{\tau_{op}} = \frac{C_{op}^2}{\pi\rho}\sqrt{\frac{2m^5}{\hbar^5\omega_{op}}}\frac{|\vec{k}|}{k_{op}}\left[1 - \frac{k_{op}^2}{k^2}\right]^{1/2}, \tag{2.42}$$

where $\hbar\omega_{op}$ is the optical phonon's energy, C_{op} is a deformation potential constant, and k_{op} is defined as:

$$k_{op} = \sqrt{\frac{2m\omega_{op}}{\hbar}}, \tag{2.43}$$

and can be thought of as the threshold electron wavevector at which the electron has just enough kinetic energy to emit an optical phonon of frequency ω_{op} in a parabolic band.

A more quantitative description of the acoustic and optical phonon emission scatterings explains why we refer to them as high and low energy processes, and justifies our focus on the acoustic phonon emission scatterings for the rest of the work. Focusing on the last terms in Equations 2.39 and 2.42, one can see that acoustic and optical phonon emission scatterings can only proceed when the charge wavevector $\vec{k}$ magnitude is bigger than k_{ac} and k_{op}. This is shown quantitatively in Figure 2.10; optical phonon emission scattering becomes allowed at a higher energy, around $10\ \mathrm{meV}$ for both silicon and germanium[28]. The acoustic phonon emission, however, can happen at high rates even in the $1\ \mathrm{meV}$ regime due to k_{ac}, depending on the low phonon phase velocity v_{ac} as described in Equation 2.40. For the case where there is an external electric field, it is useful to compare the path length for scattering as a function of energy to the voltage drop over the same path. For low temperatures, given that acoustic scattering processes dominate at the lowest energy, if the voltage drop over the path length for an acoustic interaction is small compared to $10\ \mathrm{meV}$, then the charge will likely scatter before it ever gains enough energy to have an optical scattering. This is referred to as the low-field strength regime. In principle, while there are scenarios with high-enough field strengths for the optical phonon emission scattering to become important, as discussed in Subsection 2.4.1, we are focusing on the μeV regime ($\epsilon \ll \Delta$), and therefore, we only consider the acoustic phonon scattering. In Chapter 3, we will discuss the methods we used to calculate the probabilities of the post-scattering charge angles shown in Figure 2.9.

We now provide a more detailed understanding of why intravalley processes are dominant at cryogenic temperatures, as shown in Figure 2.10. Starting with the top right and bottom left diagrams in Figure 2.8, we note that at cryogenic temperatures, charges and phonons in silicon or germanium have extremely low thermal energy, on the order of a few $\mu\mathrm{eV}$. As such, any charge that interacts with them will remain confined to the lowest-energy portion of a valley and cannot reach the high momentum required to transition between valleys. In the case of impurity scatterings, shown in the bottom right of Figure 2.8, the rates, as shown in Figure 2.10, are considerable but

two or three orders of magnitude lower than the acoustic phonon emissions; therefore, we consider impurity scatterings negligible for intravalley scattering, but important for intervalley scattering, which we will discuss separately. The bottom line is that most scattering events are intravalley and can be modeled as phonon emission within a single band extrema.

Having concluded our discussion of intravalley scattering and how it produces phonons, we now describe a second, lower rate, type of process which is only available to electrons and, in the case of a high-momentum transfer, changes electrons' valley: intervalley scattering.

2.5.2 Impact on the Transport When a Charge Changes Valleys: Intervalley Scattering

In this subsection, we describe the dominant processes that can cause intervalley scattering, as shown in Figures 2.8, as well as the justification for our simplified modeling shown in Figure 2.9. In the first paragraph, we define the processes that can produce intervalley scattering, as well as the constraints that limit the rate at which it occurs. In the second paragraph, we provide justifications for the macroscopic modeling of the intervalley scattering as shown on the right side of the Figure 2.9. In the third paragraph, we describe how intervalley scattering is modeled within G4CMP, and we introduce the functional forms used to parameterize the scattering rate for silicon and germanium.

As described before, we refer to intervalley scattering as any process in which an electron transitions from one conduction band valley to another, that is, its wavevector changes significantly to a different location in $\vec{k}$-space corresponding to an allowed symmetry-equivalent energy minimum. Because valleys are separated by large momentum differences (e.g., from $[001]$ to $[100]$ in silicon), any interaction responsible for the transition must provide a correspondingly large momentum transfer. In principle, an intervalley scattering process can proceed with a phonon being emitted or absorbed, or transferring energy and momentum to another electron. In practice, the rate at which these cases can occur is limited by the number of phonons and charges available for interactions, as well as the kinematic constraints for switching between allowed symmetry-equivalent energy bands. In impurity scattering, on the other hand, the impurity in the atomic structure of the crystal changes the potential in the Schrödinger equation locally, causing the particle to scatter

elastically, resulting in only a momentum change but conserved energy [58]. The impurity site can be caused by either unionized or ionized atoms, respectively called neutral and charged impurity scattering. The derivation of this type of scattering is beyond the scope of this work and can be found in Refs. [28, 58]. While holes can participate in impurity scattering, given that there are no constraints on their outgoing momentum, we simply assume this contribution to hole scattering is negligible and fully described by the intravalley scattering. For the purposes of this work, we will use the terms intervalley scattering and impurity scattering interchangeably for simplicity.

We use a macroscopic modeling of the intervalley scattering as shown on the right side of the Figure 2.9. While, as described in Section 2.5, optical phonon emission (top left of Figure 2.8) can change the valley while emitting a high-energy phonon, from a macroscopic view, since the phonon would quickly downconvert, the final state would essentially be an electron in a different valley and multiple low-energy phonons. This is essentially indistinguishable from the combination of an impurity scattering and multiple acoustic phonon scatterings. For this reason, we can model optical phonon emission as having two separate components: an intervalley scattering without a phonon, and several intravalley scatterings which produce acoustic phonons. For the case of electrons in an electric field, given enough time, the high number of acoustic phonon emissions effectively randomizes electrons' momentum direction within a valley, rendering the change in momentum-valley angle difference in the intervalley scattering insignificant. For these reasons, we simplify our modeling of intervalley scattering to only include the change of valleys while preserving the angle between its wavevector and its valley, and leave the production of phonons to be approximated by intervalley processes; this is exemplified in right side of Figure 2.9 where momentum is readily conserved by the mass of the full lattice.

We are now ready to describe how intervalley scattering is modeled within G4CMP and introduce the functional forms used to parameterize the scattering rate for silicon and germanium. For simplicity, we model all intervalley scattering as an elastic interaction (no phonons produced) and as having low but non-zero rates [59]. While the interaction rate is expected to be determined at

the microscopic level as a function of energy[2], as discussed in Refs. [32], the current state of the art is to model the intervalley scattering rate ν_{IV} in G4CMP probabilistically, with the rate being dependent on the local electric field strength using parameterizations fit from data for each crystal. These include both a quadratic form discussed in Ref [60]:

$$\nu_{\mathrm{IV}} = A\left(E_0^2 + |\vec{E}|^2\right)^{\alpha_{quadratic}/2}, \tag{2.44}$$

and a linear form discussed in Ref [28]:

$$\nu_{\mathrm{IV}} = b + m|\vec{E}|^{\alpha_{linear}} \tag{2.45}$$

where $\vec{E}$ is the electric field vector, and the parameters $\vec{E}_0$ (often referred to as the minimum field), A and m are coefficients, b is a constant term, and $\alpha_{quadratic}$ and α_{linear} are exponent terms [32]. For our purposes, we note that while these parameters might have physical meaning for this work, we treat them only as simple mathematical parameters. We will use the former equation for germanium and the latter for silicon.

Having laid out the theoretical foundation for wave-like charge transport and scattering in semiconductors, we next turn to the development of a particle-based modeling framework suitable for numerical simulation. While this chapter described the quantum mechanical nature of electron behavior in a periodic potential, including Bloch wave solutions, our goal in the next chapter is to reformulate this understanding into a semiclassical picture that allows efficient simulation of charge propagation. This transition from wave-based to particle-like descriptions enables us to incorporate complex effects such as anisotropic acceleration, scattering events, and electric field responses in a computationally tractable manner, allowing for the simulations discussed in later chapters.

[2]Work on these functions is in progress by collaborators.

3. PARTICLE-LIKE MODELING OF CHARGE TRANSPORT IN SEMICONDUCTORS FOR USE IN SIMULATION

In this chapter, we build a theoretical framework for describing charge transport in semiconductor crystals using a particle-like approximation. While the underlying physics of charge carriers is governed by quantum mechanics, the goal is to reduce the complexity by developing a classical-like description where carriers follow trajectories governed by velocity and acceleration, as in Newtonian mechanics, but modified to account for the crystal's anisotropic and periodic structure, as well as the various forms of scattering. This modeling approach is especially useful for implementation in simulation software, such as the Geant4 Condensed Matter Physics (G4CMP) package, which assumes a particle-based framework and naturally allows for deterministic propagation in the presence of electric fields as well as for probabilistic scattering interactions. The central result from Chapter 2 is that, for low-energy electrons near the conduction band minimum, the quantum mechanical effects can be absorbed into a direction-dependent effective mass tensor. This allows us to treat the motion of charges in semiconductors in a particle-like manner while preserving the key features of the band structure.

Because Geant4 tracks particles along discrete paths, we require an effective description in which the quantum wave behavior described in Chapter 2 can be approximated by the motion of particles as wave packets. In the semiclassical picture, a charge carrier is represented as a localized wave packet constructed from the quantum mechanical wavefunction. By analyzing how such a packet evolves within a periodic crystal potential, we can define effective particle-like properties—such as energy, wavevector, group velocity, and acceleration—that govern its dynamics. As described in Section 2.4.2, the effects of the anisotropic band curvature near energy minima are well-described by replacing the scalar mass in the classical form by an effective mass tensor. Since this mass tensor is typically anisotropic and position-independent in the absence of fields, modeling scattering processes (Section 2.5) requires a transformation to a coordinate frame where the tensor becomes isotropic. This same transformation also defines a geometric space in which

pseudo-relativistic corrections can be applied in a mathematically consistent way, allowing us to better integrate the resulting motion and interactions with Geant4's relativistic particle tracking system.

In Section 3.1, we describe a semiclassical description of charge transport in semiconductors in the absence of both external electric fields and scattering. In Section 3.2, we include the effect of an external electric field and describe how charges accelerate in a direction not aligned with the electric field, due to the tensor nature of the mass. In Section 3.3, we extend the semiclassical modeling framework to include the effects of scattering on charge carrier trajectories in semiconductors by using scattering theory results for isotropic energy bands combined with a coordinate transformation that allows those results to be used in an anisotropic energy band structure. In Section 3.4, we show how the energy, momentum, and velocity relations can be reformulated using a pseudo-relativistic framework with anisotropic mass tensors, which provides a unified formalism that maintains consistency with special relativity while preserving the anisotropic dynamics captured by the effective mass tensor. In Section 3.5, we outline some of the methods used in our simulation to model the full trajectory of charge carriers, beginning from their initial creation to their propagation and subsequent scattering interactions.

Having introduced the motivation, derivation, and utility of a particle-like model for electron motion, we next proceed to lay out this formalism by applying it to the case of charge transport without an electric field or scattering, and analyze the anisotropic velocity distributions that emerge in this limit.

3.1 Charge Transport in the Absence of an Electric Field Without Scattering Effects

In this section, we describe our semiclassical model of charge transport in semiconductors in the absence of both external electric fields and scattering. The goal is to reformulate the quantum mechanical description of charge carriers into a particle-like framework that is compatible with Geant4's trajectory-based simulation architecture. In the first paragraph, we introduce the particle-like modeling by deriving the group velocity of a charge carrier starting from first principles using Bloch's theorem. In the second paragraph, we reformulate our results using the effective mass and

mass tensor approximations for holes and electrons. Lastly, in the third paragraph, we illustrate the implications of anisotropic motion for electrons with the same energy in a semiconductor by analyzing the dependence of the velocity magnitude on the electrons' propagation direction.

We first introduce the particle-like modeling by deriving the group velocity of a charge carrier starting from first principles using Bloch's theorem. While a large number of mathematical steps are involved, there is value in laying out the relationship between the wavefunction description of charges and a particle-like notion of motion. Since the group velocity is defined as the expectation value of the momentum divided by the carrier mass, by writing out the full set of steps, following the discussion in Section 2.3.2, we find the velocity in the n'th energy band of the charge given by:

$$\begin{aligned}
\vec{v}_n(\vec{k}) &= \frac{\langle p \rangle}{m} \\
&= \frac{1}{m}\langle \psi_{nk}|\hat{p}|\psi_{nk}\rangle \\
&= \frac{1}{m}\langle \psi_{nk}| - i\hbar\vec{\nabla}|\psi_{nk}\rangle \\
&= \frac{1}{m}\langle u_{nk}| - i\hbar e^{i\vec{k}\cdot\vec{r}}\vec{\nabla}|e^{-i\vec{k}\cdot\vec{r}}u_{nk}\rangle \\
&= \frac{-i\hbar}{m}\langle u_{nk}|(e^{i\vec{k}\cdot\vec{r}}\vec{\nabla}e^{-i\vec{k}\cdot\vec{r}} + e^{i\vec{k}\cdot\vec{r}}e^{-i\vec{k}\cdot\vec{r}}\vec{\nabla})|u_{nk}\rangle \\
&= \frac{\hbar\vec{k}}{m} - \frac{i\hbar}{m}\langle u_{nk}|\vec{\nabla}|u_{nk}\rangle.
\end{aligned} \tag{3.1}$$

The first term is the same as that of a free charge, while the second term shows the effect of the crystal periodic potential on the group velocity. To evaluate the second term, we start from Bloch's Schrödinger equation, described in Equation 2.18, and expand the kinetic energy term:

$$\left[-\frac{\hbar^2}{2m}\nabla^2 - i\frac{\hbar^2}{m}\vec{k}\cdot\vec{\nabla} + \frac{\hbar^2k^2}{2m} + U(\vec{r})\right]|u_{nk}\rangle = \epsilon_{nk}|u_{nk}\rangle. \tag{3.2}$$

To understand the behavior of the energy band near the the $\langle u_{nk}|$ state, we multiply both sides with $\langle u_{n'k'}|$, where n' and k' are the quantum number and wavevector of a secondary state, and find:

$$\langle u_{n'k'}| - \frac{\hbar^2}{2m}\nabla^2 - i\frac{\hbar^2}{m}\vec{k}\cdot\vec{\nabla}|u_{nk}\rangle = \left(\epsilon_{nk} - \frac{\hbar^2k^2}{2m}\right)\langle u_{n'k'}|u_{nk}\rangle - \langle u_{n'k'}|U(\vec{r})|u_{nk}\rangle. \tag{3.3}$$

Recognizing that both $i\vec{\nabla}$ and ∇^2 are Hermitian (ie. $(\nabla^2)^\dagger = \nabla^2$), and using the periodic boundary condition and Gauss's theorem [61], we write:

$$\langle u_{nk}|i\vec{\nabla}|u_{n'k'}\rangle = \langle u_{n'k'}|i\vec{\nabla}|u_{nk}\rangle^* \quad \text{and} \quad \langle u_{nk}|\nabla^2|u_{n'k'}\rangle = \langle u_{n'k'}|\nabla^2|u_{nk}\rangle^*. \tag{3.4}$$

Using this feature and subtracting the Hermitian conjugate of Equation 3.3 from itself, the right side of the equation can be simplified via:

$$\begin{aligned}
&\langle u_{n'k'}| - \frac{\hbar^2}{2m}\nabla^2 - i\frac{\hbar^2}{m}\vec{k}\cdot\vec{\nabla}|u_{nk}\rangle - \langle u_{nk}| - \frac{\hbar^2}{2m}\nabla^2 - i\frac{\hbar^2}{m}\vec{k'}\cdot\vec{\nabla}|u_{n'k'}\rangle^* \\
&= \langle u_{n'k'}| - \frac{\hbar^2}{2m}\nabla^2 - i\frac{\hbar^2}{m}\vec{k}\cdot\vec{\nabla}|u_{nk}\rangle - \langle u_{n'k'}| - \frac{\hbar^2}{2m}\nabla^2 - i\frac{\hbar^2}{m}\vec{k'}\cdot\vec{\nabla}|u_{nk}\rangle \\
&= \langle u_{n'k'}| - \frac{\hbar^2}{2m}\nabla^2 - i\frac{\hbar^2}{m}\vec{k}\cdot\vec{\nabla} + \frac{\hbar^2}{2m}\nabla^2 + i\frac{\hbar^2}{m}\vec{k'}\cdot\vec{\nabla}|u_{nk}\rangle \\
&= \langle u_{n'k'}| - i\frac{\hbar^2}{m}\vec{k}\cdot\vec{\nabla} + i\frac{\hbar^2}{m}\vec{k'}\cdot\vec{\nabla}|u_{nk}\rangle,
\end{aligned} \tag{3.5}$$

which results in a simple relationship between two states of nk and $n'k'$:

$$\langle u_{n'k'}| - i\frac{\hbar^2}{m}(\vec{k}-\vec{k'})\cdot\vec{\nabla}|u_{nk}\rangle = \left(\epsilon_{nk} - \epsilon_{n'k'} - \frac{\hbar^2}{2m}(k^2 - k'^2)\right)\langle u_{n'k'}|u_{nk}\rangle. \tag{3.6}$$

As explained in Chapter 2, at low temperatures, most charges reside around the extremums (valleys for electrons). This means for charges in the same band $n = n'$, we will have $|\vec{k'}| \to |\vec{k}|$ and $\epsilon_n(\vec{k}) \to \epsilon_{n'}(\vec{k'})$, which allows us to use the Taylor expansions for both the wavevector and energy to make the following approximation:

$$\epsilon_n(\vec{k}) - \epsilon_n(\vec{k'}) \approx (\vec{k}-\vec{k'})\cdot\vec{\nabla}_k\epsilon_n(\vec{k}), \quad k^2 - k'^2 \approx 2\vec{k}\cdot(\vec{k}-\vec{k'}). \tag{3.7}$$

By applying these approximations to the Equation 3.6, we can further simplify it for the charges in the same band at low temperatures:

$$-i\frac{\hbar^2}{m}\langle u_{nk}|(\vec{k}-\vec{k'})\cdot\vec{\nabla}|u_{nk}\rangle = (\vec{k}-\vec{k'})\cdot\left(\vec{\nabla}_k\epsilon_n(\vec{k}) - \frac{\hbar^2\vec{k}}{m}\right). \tag{3.8}$$

As this is true for every $|\vec{k'}| \to |\vec{k}|$, we can finally get the important equation:

$$\frac{-i\hbar}{m}\langle u_{nk}|\vec{\nabla}|u_{nk}\rangle = \frac{1}{\hbar}\vec{\nabla}_k\epsilon_n(\vec{k}) - \frac{\hbar\vec{k}}{m}. \tag{3.9}$$

Substituting into Equation 3.1, we obtain the final simple expression for the group velocity:

$$\vec{v}_n(\vec{k}) = \frac{1}{\hbar}\vec{\nabla}_k\epsilon_n(\vec{k}). \tag{3.10}$$

One might find this result either exciting or uninteresting, as it is the same definition we have for free-charge group velocity; however, in this case, the energy is given by Equation 2.34. Using this result, we approximate the trajectory of the charge as that of a particle with a definite velocity and position, which was our goal in the particle-like description.

This allows us to reformulate our results using the effective mass and mass tensor approximations for holes and electrons. This is necessary for simulation purposes because Geant4 propagates particles using classical dynamics, which must be adjusted to reflect the anisotropic band structure of semiconductors. For holes near the band exterma at low energies ($\epsilon \ll 42\ \mathrm{meV}$ for silicon and $\epsilon \ll 290\ \mathrm{meV}$ for germanium), using the approximation made in Equation 2.33, we get:

$$\vec{v}_n(\vec{k}) = \frac{\hbar\vec{k}}{m^*}, \tag{3.11}$$

where m^* is the hole effective mass. Additionally, the energy in terms of velocity takes the form of:

$$\epsilon_n(\vec{v}) = \epsilon_n(\vec{v}_0) + \frac{1}{2}m^*v^2, \tag{3.12}$$

which is the same as the classical form, just with an effective mass instead of a bare mass. For electrons near a valley minimum, replacing energy with Equation 2.34, the velocity takes the form of:

$$\vec{v}_n(\vec{k}) = \hbar\mathcal{M}_n^{-1}\vec{k} = \mathcal{M}_n^{-1}\vec{p}. \tag{3.13}$$

This relation indicates that the velocity vector is not generally aligned with the momentum, and the proportionality is governed by the inverse mass tensor $\mathcal{M}_n^{-1}$. Rewriting the energy in terms of the velocity gives:

$$\epsilon_n(\vec{v}) = \epsilon_n(\vec{v}_0) + \frac{1}{2}\langle\vec{v}|\mathcal{M}_n|\vec{v}\rangle. \tag{3.14}$$

This expression enables us to define a consistent notion of velocity and kinetic energy, even when the effective mass is anisotropic.

The implications of anisotropic motion for electrons with the same energy in a semiconductor can be illustrated by analyzing the dependence of the velocity magnitude on the electrons' propagation direction, with examples shown in Figures 3.1 and 3.2. Based on the approximations introduced in Section 2.4.2, we work in the valley-aligned frame and use Equation 2.36 to express the energy as a function of the velocity components. For a velocity vector $\vec{v} = (v_L, v_{T_1}, v_{T_2})$, where v_L is the longitudinal component, along the valley axes, and v_{T_1}, v_{T_2} are the components in the transverse directions, the energy is given by:

$$\epsilon_n(\vec{v}) = \epsilon_n(\vec{v}_0) + \left[\frac{1}{2}m_L v_L^2 + \frac{1}{2}m_T(v_{T_1}^2 + v_{T_2}^2)\right]. \tag{3.15}$$

An important consequence of this is that electrons with the same total energy can exhibit different speeds depending on their direction of motion. Specifically, an electron moving purely in the longitudinal direction (i.e., along the valley axis) with energy ϵ has a speed $|\vec{v}_1| = \sqrt{2\epsilon/m_L}$, while one moving purely in a transverse direction has speed $|\vec{v}_2| = \sqrt{2\epsilon/m_T}$. Since $m_L > m_T$ for both silicon and germanium (see Section 2.4.2), we have $|\vec{v}_1| < |\vec{v}_2|$, implying that electrons traveling closer to the valley axis move more slowly than those moving away from it, even at identical energy as visualized in Figure 3.1. Another way to visualize this is to consider the case of an electron emitted from a location and examine the speeds and arrival times at a constant surface above it. As shown in Figure 3.2 for silicon, we observe that the velocity magnitude varies with direction due to the anisotropic band curvature governed by the mass tensor.

Having concluded our discussion of the charge transport in the absence of both scattering and

external electric fields, we have established the foundation for modeling charge motion using a particle-like framework. This semiclassical formalism enables us to model charges with defined positions and velocities, accounting for the inherently anisotropic nature of their motion. In the next section, we extend this model to incorporate the influence of an electric field, while continuing to neglect scattering until Section 3.3, to describe how carriers accelerate and curve through the crystal under the action of external forces.

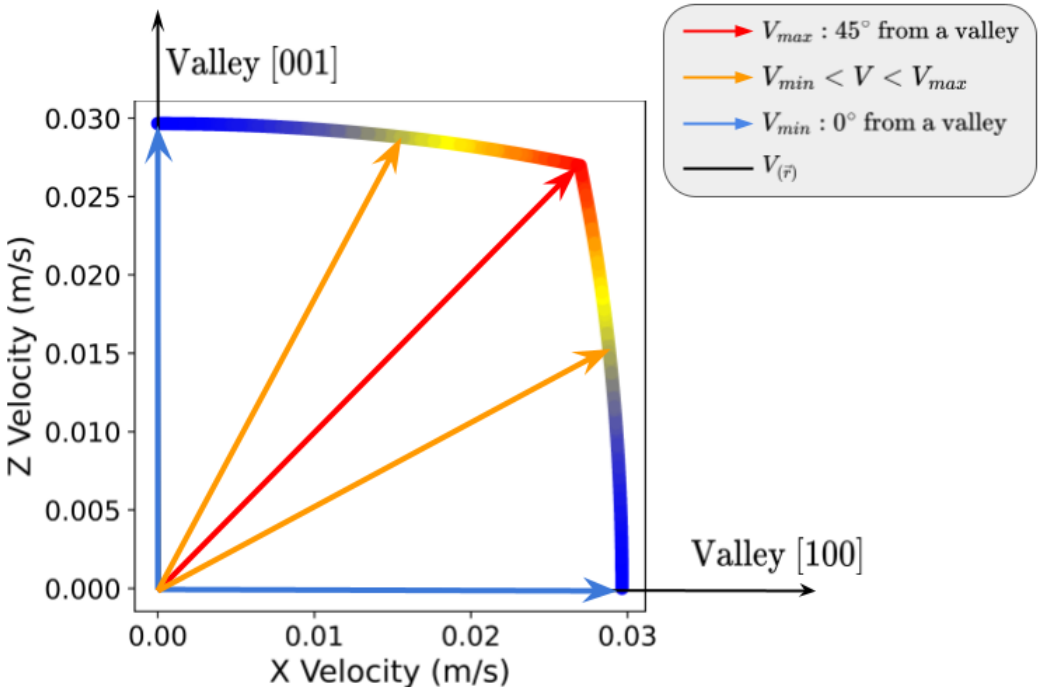

Figure 3.1: This figure shows the relationship between the electron velocity vectors and the angle relative to the valleys for a constant energy in silicon; the color in the band is a heat map of the speed of the same energy electrons, and the arrows show a few specific examples. We show it because the speed of an electron in a semiconductor minimizes in the direction of the valley and gets bigger as the directions move away from it. In this case, the directions are between the [001] and [100] valleys, and we are only showing a quarter of the sphere in two dimensions.

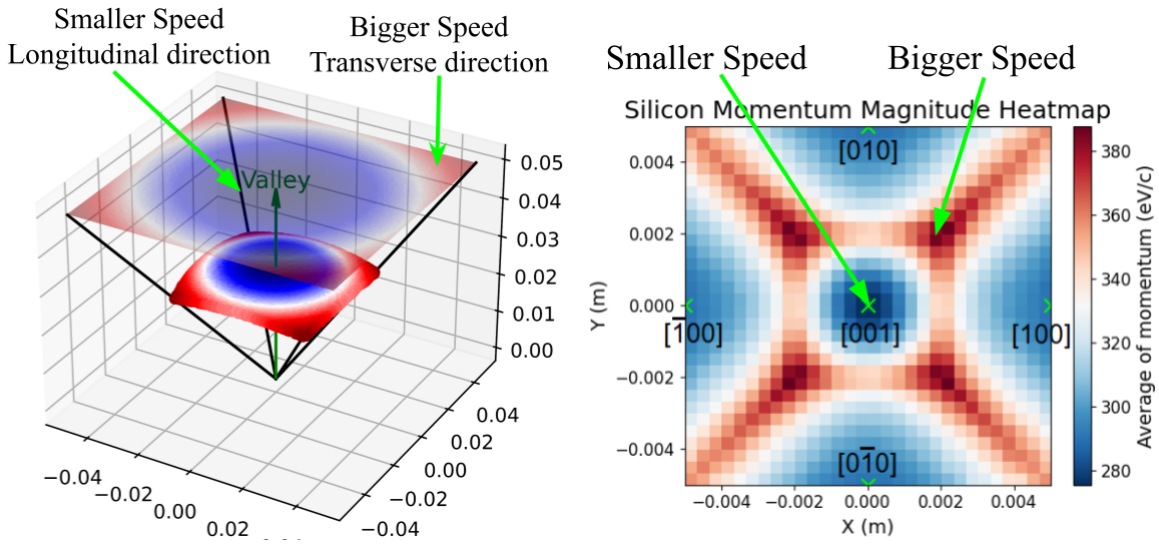

Figure 3.2: This figure shows two different views of the relationship between the direction of an electron and its momentum in silicon. We show it to indicate how the semiconductor energy band structure impacts the speed as it propagates due to the tensor nature of the mass. On the left, we indicate the speed of electrons that start at the origin with the same energy and arrive at a surface in the xy plane, where the crystal is oriented such that the [001] valley is in the z direction. In the absence of an electric field, these electrons continue through the medium with a constant velocity but eventually hit the surface with a time of arrival indicated by the colors. In the right figure, we only consider the two-dimensional projection on the top surface but with a much-expanded region (or smaller distance from the source) that encompasses the full range of directions, which allows us to project both the 3-dimensional valley structure and the trajectories onto a 2-dimensional plane. This type of projection will be very helpful as we move to more complicated scenarios later in the text.

3.2 Charge Transport Under an Electric Field Without Scattering Effects

In this section, we derive the semiclassical equations of motion for electrons and holes in a semiconductor under an external electric field while neglecting scattering effects. Again, our goal is to construct a particle-like description of transport and derive equations of motion in which charges accelerate under a force within a band structure. While holes have their acceleration magnitude modified by the effective mass, the electrons will need to be described by a direction-dependent acceleration due to the curvature of the electronic band structure, which is captured via the mass tensor description. In the first paragraph, we derive the semiclassical expression for the acceleration of a charge carrier under an external force in a periodic potential using the semiclassical velocity relations. In the second paragraph, we apply the general acceleration formula to the specific case of low energy, using the effective mass approximations introduced in Section 2.4. In the third paragraph, we shift our focus to the implications for electrons in our devices and describe how, in the presence of an electric field, electrons in different valleys accelerate differently, resulting in distinct spatial patterns on the detector surface when considering scenarios like those shown in Figure 3.2.

We use the semiclassical velocity relations to derive the semiclassical expression for the acceleration of a charge carrier under an external force in a periodic potential. Starting from the definition of acceleration as the time derivative of velocity, we get:

$$\vec{a}_n(\vec{k}) = \frac{\mathrm{d}\vec{v}_n(\vec{k})}{\mathrm{d}t} = \frac{\mathrm{d}}{\mathrm{d}t}\left(\frac{1}{\hbar}\vec{\nabla}_k\epsilon_n(\vec{k})\right) = \frac{1}{\hbar}\vec{\nabla}_k\frac{\mathrm{d}\epsilon_n(\vec{k})}{\mathrm{d}t}. \tag{3.16}$$

As the energy is a function of wavevector, the time derivative of the energy can be rewritten using the chain rule:

$$\frac{\mathrm{d}\epsilon_n(\vec{k})}{\mathrm{d}t} = \frac{\mathrm{d}\vec{k}}{\mathrm{d}t}\cdot\vec{\nabla}_k\epsilon_n(\vec{k}). \tag{3.17}$$

Using the definition of the external force $\vec{F}$ as the rate of change of the crystal momentum $\hbar\vec{k}$, we

have:

$$\vec{F} = \hbar \frac{\mathrm{d}\vec{k}}{\mathrm{d}t}. \tag{3.18}$$

Substituting this into the acceleration expression allows us to write:

$$\vec{a}_n(\vec{k}) = \frac{1}{\hbar^2}\vec{\nabla}_k \left(\vec{F} \cdot \vec{\nabla}_k \epsilon_n(\vec{k})\right) = \frac{1}{\hbar^2}\left[(\vec{\nabla}_k \vec{F}) \cdot \vec{\nabla}_k \epsilon_n(\vec{k}) + \vec{F} \cdot \vec{\nabla}_k (\vec{\nabla}_k \epsilon_n(\vec{k}))\right]. \tag{3.19}$$

For a charge in an electromagnetic field, the $\vec{\nabla}_k \vec{F}$ term takes the following form:

$$\begin{aligned} \vec{F} &= -q\vec{E} - q\vec{v}_n(\vec{k}) \times \vec{B} = -\frac{q}{\hbar}\vec{\nabla}_k \epsilon_n(\vec{k}) \times \vec{B} \\ \Rightarrow \vec{\nabla}_k \vec{F} &= -q\vec{\nabla}_k \vec{E} - \frac{q}{\hbar}\vec{\nabla}_k \left(\vec{\nabla}_k \epsilon_n(\vec{k}) \times \vec{B}\right) \\ &= -q\vec{\nabla}_k \vec{E} - \frac{q}{\hbar}\vec{\nabla}_k \left(\vec{\nabla}_k \epsilon_n(\vec{k})\right) \times \vec{B} - \frac{q}{\hbar}\vec{\nabla}_k \epsilon_n(\vec{k}) \times \vec{\nabla}_k \vec{B}. \end{aligned} \tag{3.20}$$

Since electric and magnetic fields are defined in the real space and $\vec{\nabla}_k \vec{E} = \vec{\nabla}_k \vec{B} = 0$, for an electromagnetic field, this reduces to:

$$\vec{\nabla}_k \vec{F} = -\frac{q}{\hbar}\vec{\nabla}_k \left(\vec{\nabla}_k \epsilon_n(\vec{k})\right) \times \vec{B}. \tag{3.21}$$

As a result, in the case of no magnetic field, this term goes to zero, and Equation 3.19 further reduces to:

$$\vec{a}_n(\vec{k}) = \sum_{\alpha,\beta} \left(\frac{1}{\hbar^2}\frac{\partial^2 \epsilon_n(\vec{k})}{\partial k_\alpha \partial k_\beta} F_\beta\right) \hat{\alpha}, \tag{3.22}$$

where α and β are Cartesian coordinates, and $\hat{\alpha}$ denotes the unit vector in the α-direction. This result expresses the acceleration in terms of the curvature of the band structure, which naturally leads to the appearance of an inverse mass tensor in anisotropic crystals, which we will study next.

To rewrite the general acceleration formula from an external field to a specific case of low energy, one can use the effective mass approximations introduced in Sections 2.4.1 and 2.4.2. Starting with holes, the valence band maximum at low energies, using the approximation made in

Equation 2.33, we have

$$\frac{\partial^2 \epsilon_n(\vec{k})}{\partial k_\alpha \partial k_\beta} = \frac{1}{m_h^*}\delta_{\alpha\beta}, \tag{3.23}$$

where $\delta_{\alpha\beta}$ is the Kronecker delta ($\delta_{\alpha\beta} = 0$ when $\alpha \neq \beta$ and $\delta_{\alpha\beta} = 1$ when $\alpha = \beta$). Substituting this into Equation 3.22, the acceleration becomes:

$$\vec{a}_n = \sum_{\alpha,\beta} \frac{1}{m_h^*}\delta_{\alpha\beta} F_\beta \hat{\beta} = \frac{1}{m_h^*}\sum_{\alpha} F_\alpha \hat{\alpha} = \frac{\vec{F}}{m_h^*}. \tag{3.24}$$

This is consistent with the modeling of a hole motion using Newton's second law with the bare mass replaced by the effective hole mass. For electrons near the bottom of the conduction band, the curvature is generally anisotropic, and the second derivative of the energy defines the inverse mass tensor. Using the mass tensor defined in Equation 2.35, the acceleration takes the form:

$$\vec{a} = \mathcal{M}_n^{-1}\vec{F}. \tag{3.25}$$

As in the case of velocity, this result emphasizes that the acceleration vector is not generally aligned with the external force. Instead, its direction and magnitude are governed by the anisotropic structure of the band through the inverse mass tensor $\mathcal{M}_n^{-1}$. Together with the velocity relation derived in Section 3.1, these equations form the foundation for semiclassical particle-like modeling in anisotropic crystals.

We now shift our focus to the implications for electrons that start inside our devices but can propagate and reach a surface, as shown in Figure 3.2. In the presence of an electric field, electrons in different valleys accelerate differently, resulting in a set of groupings of arrival positions on the detector surface. Using the approximations from Section 2.4.2, the mass tensor becomes diagonal in the valley-aligned frame. For a general external force $\vec{F} = (F_L, F_{T_1}, F_{T_2})$, where F_L is the longitudinal component, along the valley axis, and F_{T_1}, F_{T_2} are transverse components, the acceleration becomes:

$$\vec{a}_n = \left(\frac{F_L}{m_L}, \frac{F_{T_1}}{m_T}, \frac{F_{T_2}}{m_T}\right), \tag{3.26}$$

expressed in the valley-aligned coordinate system. As introduced in Section 2.3.2, silicon and germanium have six and eight symmetry-equivalent conduction band minima, respectively, located at the X and L points in the Brillouin Zone. In the low energy regime, electrons populate these valleys, and the orientation of the mass tensor, and hence the acceleration response, depends on which valley the electron resides in. For example, for the case of an external force $\vec{F} = [0, 0, F_z]$. Electrons in the $[001]$ valley will accelerate as $\vec{a}_n = (0, 0, F_z/m_L)$, whereas those in the $[100]$ or $[010]$ valleys will experience $\vec{a}_n = (0, 0, F_z/m_T)$ in the crystal frame. This leads to a difference in acceleration magnitudes between electrons in different valleys. More generally, since the valley axis is not always aligned with the applied field or perpendicular to it, the resulting acceleration vector may also point in a different direction than the force. This anisotropic response is illustrated in Figure 3.3 for the case of germanium, where electrons get accelerated in a direction different than the force. These direction and magnitude-dependent responses cause electrons from different valleys to arrive at different regions on the detector surface, forming multiple spatial clusters. This phenomenon is clearly observed in experimental results shown in Figures 1.12 and 1.13. In Chapter 4, we will reproduce and analyze these arrival patterns using simulation tools to further understand the consequences of valley anisotropy.

Having concluded our derivation of the particle-like equations of motion in an applied electric field, we move to include scattering processes. Since this process can be complicated, we introduce a mathematical technique that enables a transformation from the lab frame to one where scattering processes are more readily performed, known as the Herring-Vogt transformation [62]. This will help bridge the gap between band structure theory and Geant4-compatible modeling, allowing Monte Carlo techniques play a crucial role in predicting the complete trajectory, including scattering.

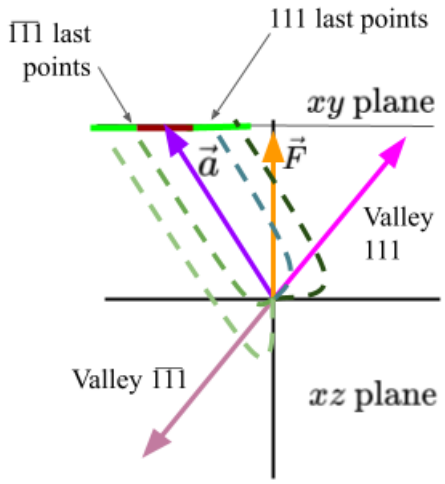

Figure 3.3: This figure shows a cartoon of a set of electron trajectories inside a germanium crystal with valleys that are aligned in the $[\pm 1, \pm 1, \pm 1]$ directions and an electric field that is applied in the z direction. We show it because it illustrates that the motion of a charge in a certain valley gets accelerated in a direction that is not necessarily aligned with either the external force or the valley direction. The trajectories, illustrated as the dashed lines, are emitted from the center like in Figure 3.2, and encounter a surface. Note that in this case, we have again oriented the z direction as being up and the electric field in the z direction, but the valley direction aligns with neither of the two. For valleys on the same axis but in opposite directions, the electrons in both valleys will have the same acceleration and will end up in a similar location on the surface (assuming the surface is far enough from the electrons' origin relative to the electrons' initial energy).

3.3 Trajectories when Scattering Effects are Included

In this section, we extend the semiclassical modeling framework to include the effects of scattering on charge carrier trajectories in semiconductors. While previous sections described smooth, deterministic motion under an applied electric field using anisotropic mass tensors, real charge transport is interrupted by scattering events that alter both the energy and direction of carriers, as illustrated in Figure 1.9. To ensure physical accuracy, these processes must be modeled in a way that respects the underlying anisotropic band structure while remaining compatible with the scattering theory introduced in Section 2.5. However, the derivation in that section assumes isotropic energy bands. To address this challenge, we present a mathematical framework that maps anisotropic energy bands into isotropic ones, allowing the isotropic scattering results to be applied to the anisotropic case; holes are readily approximated as already being isotropic, which means that the same mathematical framework can be trivially applied. In the first paragraph, we introduce the concept of constant energy surfaces and their value in modeling charge transport in semiconductors. In the second paragraph, we explain how both the group velocity and acceleration of a charge carrier relate geometrically to the constant energy surface in $\vec{k}$-space, which facilitates a useful visualization of some of the differences between charge transport in isotropic and anisotropic media. In the third paragraph, we introduce a mathematical technique that transforms the anisotropic wavevector space, where constant energy surfaces are ellipsoidal, into a coordinate system in which these surfaces become spherical, referred to as the Herring-Vogt transformation, which allows for isotropic treatment of scattering effects in semiconductors. In the fourth paragraph, we describe how we model the scattering process and how we calculate the post-scattering charge and phonon states. In the fifth paragraph, we describe how the scattering interactions affect the trajectory of the charges.

We first introduce the concept of constant energy surfaces and their role in modeling charge transport in semiconductors. A constant energy surface is defined as the set of all wavevectors $\vec{k}$ for which the energy $\epsilon_n(\vec{k})$ remains fixed; an example for an isotropic medium like vacuum is shown in Figure 3.4. These surfaces characterize how the energy depends on both the magnitude and

direction of $\vec{k}$, and they enable a geometric determination of the direction of the group velocity and acceleration. In an isotropic medium, the energy follows the relation $\epsilon(\vec{k}) = \epsilon_0 + \frac{\hbar^2 k^2}{2m}$, where m is the effective mass of the charge carrier. This leads to spherical constant energy surfaces in $\vec{k}$-space. By contrast, semiconductor crystals such as silicon and germanium exhibit direction-dependent energy curvature due to their anisotropic band structure. In the special case of low-energy electrons near a valley minimum, as discussed in Section 2.4.2, we can transform into a valley-aligned frame in which the mass tensor becomes diagonal. The energy in this regime and this frame is given by Equation 2.37, revealing that the constant energy surfaces become ellipsoidal. A cartoon of an anisotropic constant energy surface is shown in Figure 3.5, where the ellipsoidal shape reflects the different longitudinal and transverse effective masses of the electron.

The group velocity and acceleration of a charge carrier relate geometrically to the constant energy surface in $\vec{k}$-space, which facilitates a useful visualization of some of the differences between the charge transport in isotropic and anisotropic media. As discussed in Section 3.1, the group velocity of a charge carrier in band n is given by $\vec{v}_n = \frac{1}{\hbar}\vec{\nabla}_{\vec{k}}\epsilon_n(\vec{k})$, which is always perpendicular to the constant energy surface at the point $\vec{k}$. Moreover, because these surfaces are continuous, we can always find a wavevector $\vec{k}'$ such that $\epsilon_n(\vec{k}') = \epsilon_n(\vec{k})$ and $\vec{k}'$ is aligned with the applied force $\vec{F}$. A feature of this construction is that it allows us to define a velocity $\vec{v}' = \mathcal{M}_n^{-1}\vec{k}'$, and relate it to the acceleration $\vec{a}_n = \mathcal{M}_n^{-1}\vec{F}$ through the following chain of equalities:

$$\begin{aligned} \vec{a}_n = \mathcal{M}_n^{-1}\vec{F} \Rightarrow \frac{|\vec{k}'|}{|\vec{F}|}\vec{a}_n = \mathcal{M}_n^{-1}\vec{k}' = \vec{v}' = \frac{1}{\hbar}\vec{\nabla}_{\vec{k}'}\epsilon_n(\vec{k}') \\ \Rightarrow \hat{a} = \frac{|\vec{F}||\vec{a}|}{\hbar|\vec{k}'|}\vec{\nabla}_{\vec{k}'}\epsilon_n(\vec{k}'), \end{aligned} \tag{3.27}$$

which shows that the acceleration vector $\vec{a}_n$ is also perpendicular to the constant energy surface at the point where the applied force intersects it. Since this conclusion applies to both isotropic and anisotropic crystals, the geometric relationships between velocity, acceleration, and the constant energy surface can be easily visualized as illustrated in Figures 3.6 and 3.7 for an isotropic and an anisotropic medium, respectively. The isotropic case becomes trivial to solve as the mass tensor

reduces to a scalar by setting $\mathcal{M} = m\mathcal{I}$, where $\mathcal{I}$ is the identity tensor and m is the scalar effective mass.

To transform the anisotropic wavevector space, where constant energy surfaces are ellipsoidal, into a coordinate system in which these surfaces become spherical, we introduce a mathematical technique referred to as the Herring-Vogt transformation, $\mathcal{H}$ [62]. This transformation allows for an isotropic treatment of scattering effects in semiconductors. In the valley-aligned frame, where the mass tensor is diagonalized as $\mathcal{M}_n = \mathrm{diag}(m_L, m_T, m_T)$, this transformation is defined by

$$|k\rangle = \mathcal{H}|k'\rangle, \quad \text{with} \quad \mathcal{H} = \sqrt{\frac{\mathcal{M}_n}{m_0}}, \tag{3.28}$$

where m_0 is a reference mass that scales the radius of the spherical constant energy surfaces by $\sqrt{m_0}$. Since $\mathcal{M}_n$ is real and diagonal in this frame, we can simplify the quadratic form:

$$\langle k|\mathcal{M}_n^{-1}|k\rangle = \frac{1}{m_0}\langle k'|k'\rangle = \frac{|\vec{k}'|^2}{m_0}. \tag{3.29}$$

Thus, Equation 2.34 becomes

$$\epsilon_n(\vec{k}) = \frac{\hbar^2}{2}\langle k|\mathcal{M}_n^{-1}|k\rangle = \frac{\hbar^2|\vec{k}'|^2}{2m_0}, \tag{3.30}$$

which describes a spherically symmetric constant energy surface in the transformed space. Note that this transformation is on the reciprocal lattice, which means it only makes the constant energy surfaces spherical in the reciprocal space. In Section 3.4, we will discuss a metric transformation that acts on both reciprocal and real lattices. The primary advantage of the Herring-Vogt transformation arises in modeling scattering processes. Since scattering is treated as an instantaneous event in our simulations, where the charge position remains unchanged, we can transform to the isotropic Herring-Vogt frame, apply the scattering process more easily, and then transform the resulting wavevector back to the original anisotropic frame. This approach allows us to treat anisotropic scattering dynamics using isotropic models while preserving physical correctness.

We are now ready to describe how we model the scattering process and how we calculate the post-scattering charge and phonon states. To apply the isotropic scattering theory developed in Section 2.5 to the anisotropic band structure of materials like silicon and germanium, we first apply the Herring-Vogt transformation to the reciprocal lattice, enabling us to perform the scattering processes in an isotropic frame. Once the transformation is applied, we model each intravalley scattering event using a differential probability distribution derived from deformation potential theory [26, 53]. The angular probability density function (PDF) for an acoustic phonon to be emitted at angle θ, measured with respect to the charge carrier's initial wavevector $\vec{k}$, is given by:

$$P(k,\theta)\,\mathrm{d}\theta = \frac{\hbar k^2}{m l_0 k_{ac}} \left(\cos\theta - \frac{k_{ac}}{k}\right)^2 \sin\theta\,\mathrm{d}\theta, \tag{3.31}$$

where θ in the left-hand side of Figure 2.9 and other symbols are defined in Section 2.5.1, and $0 \leq \theta \leq \cos^{-1}\left(\frac{k_{ac}}{k}\right) \leq \pi/2$. This distribution ensures both energy and momentum conservation and enforces forward-directed emission. Given a value of θ, the rest of the kinematics are uniquely determined; the kinetic energy of the charge is reduced, and the updated charge and phonon states are transformed back into the anisotropic crystal frame. In the simpler case of intervalley scattering described in Section 2.5.2, which we model as the right-hand side of Figure 2.9, there are no phonons, so the process is simply the electron changing its valley while the electron's wavevector preserves its angle with the new valley.

Lastly, it's important to describe how the scattering events affect the trajectory of the charges. In the absence of scattering, as discussed in Section 3.2, the path of a charge carrier evolves smoothly under the influence of a valley-dependent acceleration. However, once intravalley scattering is included, each event alters the direction of motion while simultaneously reducing the kinetic energy of the charge. Over time, as multiple phonons are emitted, the information about the original velocity is essentially washed away and what remains becomes dominated by the direction of the anisotropic acceleration vector $\vec{a}_n = \mathcal{M}_n^{-1}\vec{F}$. This phenomenon produces a focusing effect, where the trajectory is drawn into alignment with the acceleration direction. Figure 3.8 illustrates this

behavior by comparing charge trajectories in the presence and absence of intravalley scattering as shown in Figure 3.3. In contrast, intervalley scattering changes the identity of the valley altogether, rotating the charge's direction into a new valley-aligned frame while preserving its angle relative to the valley axis. This process causes electrons to deviate from the principal focusing axes and land between the primary impact zones, as seen in the arrival patterns in the real experiment results shown in Figures 1.12, and 1.13. The combined influence of repeated intravalley and occasional intervalley scattering leads to distinct clustering and spread in arrival distributions, which we will investigate in greater detail in Chapter 4 using Monte Carlo simulations.

Having concluded our description of the expectations for the trajectories of charges in an anisotropic crystal with an external field, and including scattering, we now turn to a pseudo-relativistic formulation of charge transport. In the next section, we provide motivation for expressing energy, momentum, and velocity using a pseudo-relativistic framework built upon an anisotropic mass tensor. The formalism we introduce converges to standard special relativity in the vacuum limit while preserving the anisotropic dynamics of semiconductors in the low-energy regime.

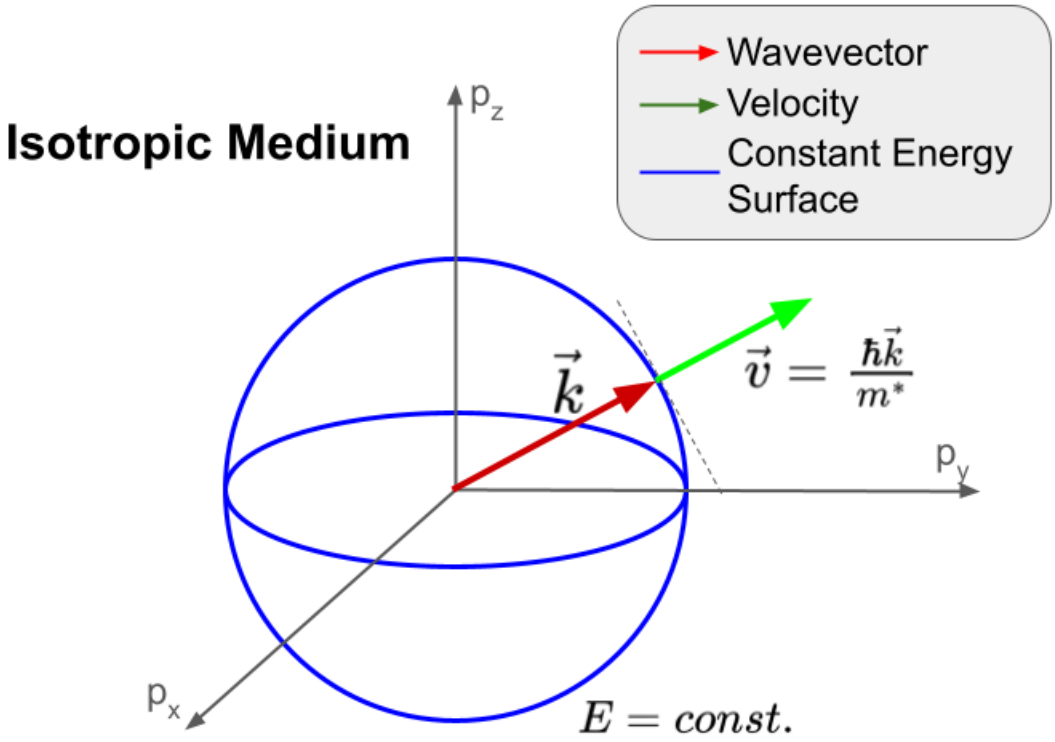

Figure 3.4: This figure shows the simple relationship between the kinetic energy of a particle in an isotropic medium and its wavevector by indicating all the same energy points in wavevector space, known as a constant energy surface. We show it because, in an isotropic medium, the constant energy surface is spherical, leading to a perfect alignment between velocity and wavevector direction, where both are normal to the constant energy surface due to $\vec{v} = \frac{1}{\hbar}\vec{\nabla}_{\vec{k}}\epsilon(\vec{k})$. Note that in the velocity description, we have used the effective mass, m^*, which, in the limit of vacuum, turns into the rest mass of the charge.

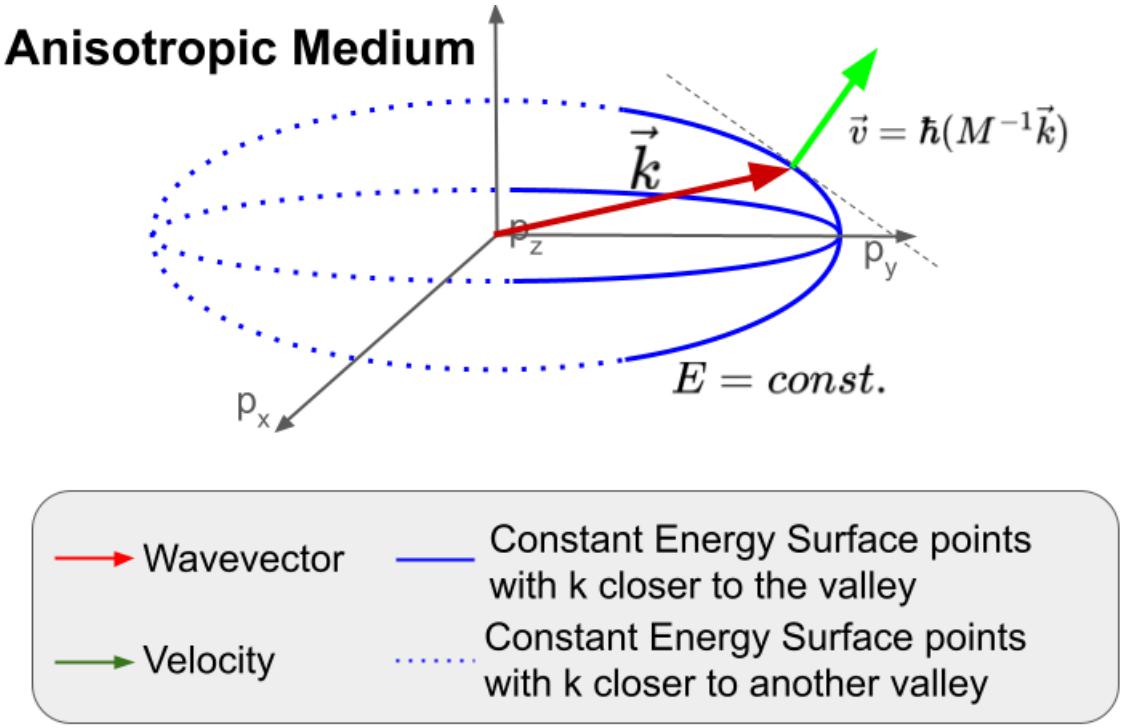

Figure 3.5: This figure shows the same diagram as in Figure 3.4 but for a anisotropic crystal. We show it because in a semiconductor crystal, like silicon, the constant energy surfaces have an ellipsoidal shape due to the semiconductor energy band structure. Note that we are no longer using the effective mass in the velocity but a tensor $\mathcal{M}$ that is defined so that the effective mass and directions are correct.

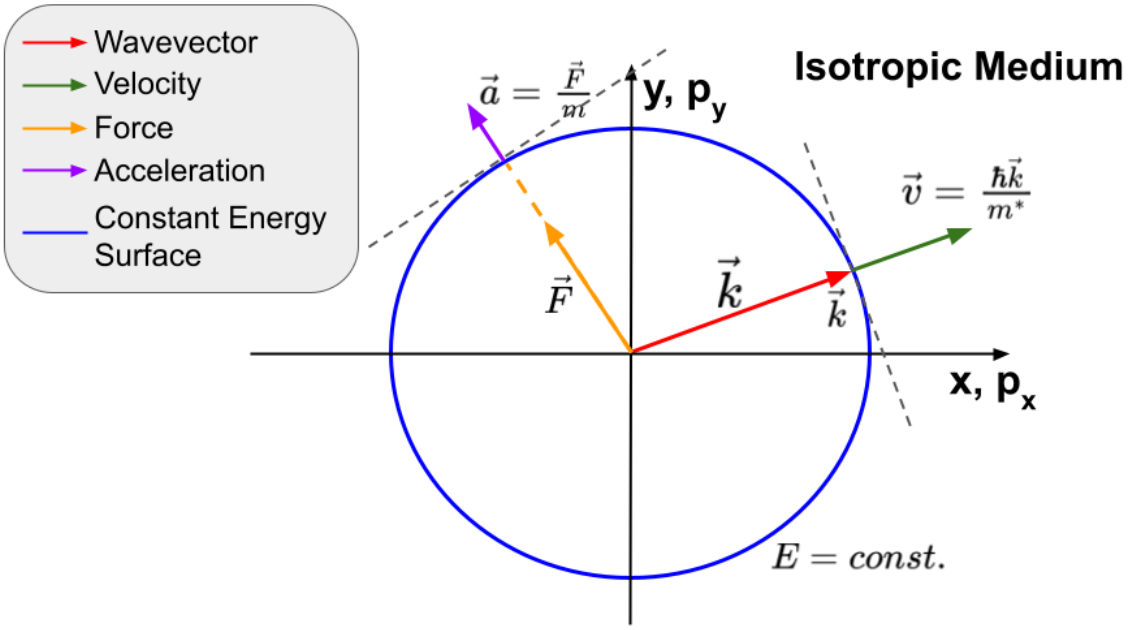

Figure 3.6: In this figure, we show a two-dimensional view of Figure 3.4, but where we have added in the acceleration for the case where there is a force. We show this because, in this case, an external force causes the particle to accelerate in a direction that is aligned with the force. What is important is that while the velocity and acceleration point in the same direction in this simple case, the alignment is really normal to the tangent to the surface of constant energy, which will be different in the anisotropic medium.

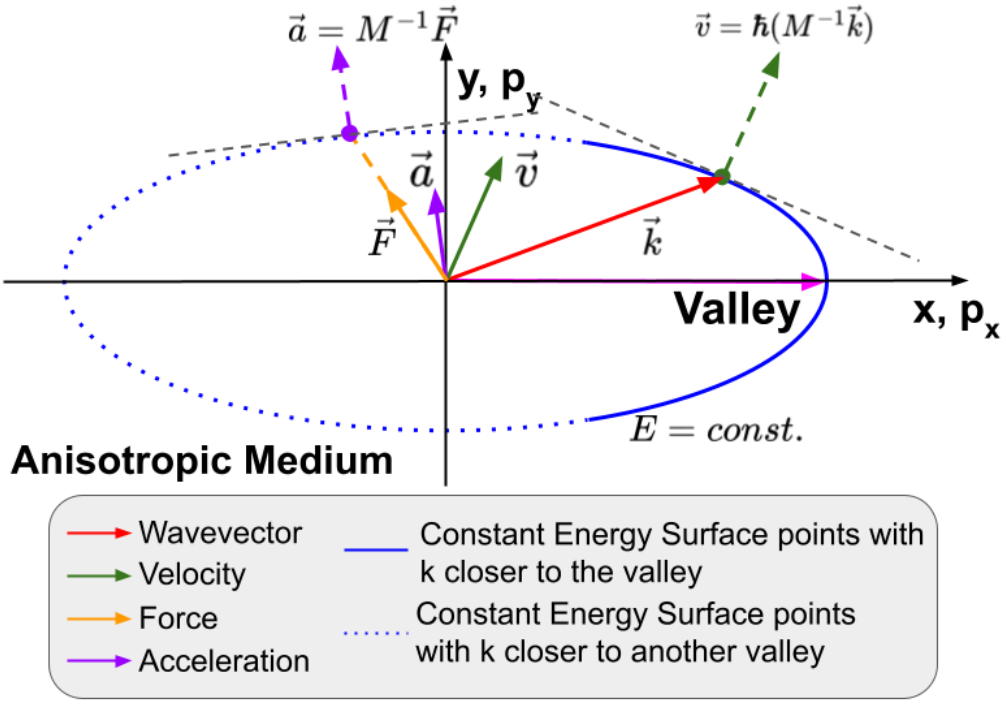

Figure 3.7: This figure shows the same quantities shown in Figure 3.6 but for the silicon case shown in Figure 3.5. We show this because, in a semiconductor, in the same way that the velocity and wavevector are no longer in the same direction, an external force causes the particle to accelerate in a direction that is not aligned with the force but governed by the same mass tensor $\mathcal{M}$. These behaviors result in phenomena such as varying charge velocity magnitudes for the same energy but different directions, as shown in Figure 3.2.

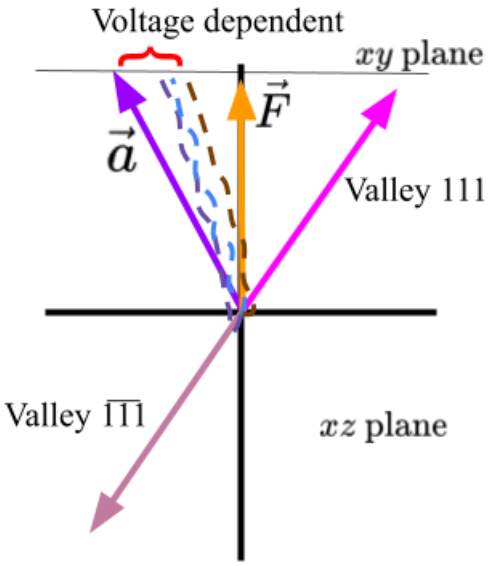

Figure 3.8: This figure shows the same case as described in Figure 3.3, but where intravalley scattering is included. We show it because with intravalley scattering, all the charges in the same valley axis (both valley and anti-valley charges) end up in a small region between the acceleration direction and the valley due to their energy loss as they propagate.

3.4 A Pseudo-Relativistic Framework for Carrier Dynamics in Anisotropic Crystals

In this section, we extend our semiclassical model of charge transport by introducing a pseudo-relativistic geometric framework that incorporates the effects of the anisotropic band structure. While the calculations in the previous sections were done with non-relativistic quantum mechanics, and our modeling is based on the low-energy assumption, a pseudo-relativistic formulation becomes useful as the Geant4 simulation infrastructure relies on relativistic relationships between energy and momentum when propagating, scattering, and decaying particles. Additionally, it also adds the advantage of allowing us to think of the anisotropic medium as an analogy of the curved space-time geometry of general relativity. In the first paragraph, we construct a generalized spacetime geometry that enables us to incorporate pseudo-relativistic corrections into the non-relativistic equations in a way that retains their essence. In the second paragraph, we extend the pseudo-relativistic formalism we have developed to define both the covariant and contravariant four-momenta, which, by using its spatial part, allows us to describe both the wave-like description of the charge (through the wavevector) and the particle-like modeling of it, consistent with the crystal band structure.

A generalized pseudo-relativistic spacetime geometry can be constructed to enable us to use our non-relativistic results with minor corrections. To develop a consistent, real-space description, especially one that smoothly reduces to the semiclassical equations derived in previous sections, we introduce a Minkowski-like geometry with a modified spatial metric determined by the mass tensor. We define a pseudo-Minkowski metric $g_{\mu\nu}$ in the valley-aligned coordinate frame as:

$$g_{\mu\nu} = \begin{bmatrix} 1 & 0 \\ 0 & -\mathcal{H}^2 \end{bmatrix}, \quad \text{where} \quad \mathcal{H}^2 = \frac{\mathcal{M}_n}{m_0}, \tag{3.32}$$

where we have used the same definitions as in Equation 3.28. As a check, we note that in a vacuum, this geometry reduces to the Minkowski geometry, which matches the special relativity

results. This metric allows us to define an invariant spacetime interval as:

$$\mathrm{d}s^2 = c^2\,\mathrm{d}t^2 - \langle\vec{x}|\frac{\mathcal{M}_n}{m_0}|\vec{x}\rangle, \tag{3.33}$$

which generalizes the flat spacetime structure of special relativity to incorporate anisotropic crystal dynamics. Dividing by c^2, we express this interval in the form of proper time $\mathrm{d}\tau$:

$$\mathrm{d}\tau^2 = \mathrm{d}t^2 - \langle\vec{x}|\frac{\mathcal{M}_n}{m_0c^2}|\vec{x}\rangle, \tag{3.34}$$

leading to a generalized Lorentz factor:

$$\gamma = \frac{1}{\sqrt{1 - \langle\vec{v}|\frac{\mathcal{M}_n}{m_0c^2}|\vec{v}\rangle}}. \tag{3.35}$$

Using this, we define the four-velocity U^μ of a charge carrier as:

$$U^\mu = (c\gamma, \gamma\vec{v})\,, \tag{3.36}$$

where the spatial component $\vec{v} = \mathrm{d}\vec{x}/\mathrm{d}t$ is the physical velocity in the lab frame. The total pseudo-relativistic energy is then expressed as:

$$\epsilon(\vec{v}) = \gamma m_0c^2 = \frac{m_0c^2}{\sqrt{1 - \langle\vec{v}|\frac{\mathcal{M}_n}{m_0c^2}|\vec{v}\rangle}}. \tag{3.37}$$

In the classical (non-relativistic) limit where $v/c \ll 1$, to the second degree, this expression expands to:

$$\epsilon(\vec{v}) \approx m_0c^2 + \frac{1}{2}\langle\vec{v}|\mathcal{M}_n|\vec{v}\rangle = \epsilon_0 + \frac{1}{2}\langle\vec{v}|\mathcal{M}_n|\vec{v}\rangle, \tag{3.38}$$

recovering the semiclassical formulation previously derived in Section 3.1.

We extend our pseudo-relativistic formalism to define both the covariant and contravariant four-momenta, which, by using its spatial part, allows us to describe both the wave-like description of

the charge (through the wavevector) and the particle-like modeling of it, consistent with the crystal band structure. As shown in Section 2.3.2, the wavevector $\vec{k}$ enters the wavefunction through the phase factor $\vec{k} \cdot \vec{r}$, as in Equation 2.15, which is also used in our particle like modeling in Equation 3.1. Since the position $\vec{r}$ transforms as a contravariant vector under coordinate changes, the wavevector $\vec{k}$, which forms a scalar product with it, must transform as a covariant vector. This guarantees that the phase $\vec{k} \cdot \vec{r}$ remains invariant under coordinate transformations. To formalize this, we define the covariant four-momentum P_μ and its components $\vec{P}_0$ and $\vec{P}_{\text{quasi}}$, where the term quasi-momentum is used to describe the charge momentum in an anisotropic crystal. We determine the values by lowering the index of the contravariant four-velocity U^μ using the generalized anisotropic metric $g_{\mu\nu}$ introduced in the previous paragraph:

$$P_\mu = m_0 U_\mu = \sum_\nu m_0 g_{\mu\nu} U^\nu = \gamma m_0 \begin{bmatrix} 1 & 0 \\ 0 & -\mathcal{H}^2 \end{bmatrix} \begin{bmatrix} c \\ \vec{v} \end{bmatrix} = \gamma \begin{bmatrix} m_0 c \\ -\mathcal{M}_n \vec{v} \end{bmatrix} = \begin{bmatrix} \vec{P}_0 \\ -\vec{P}_{\text{quasi}} \end{bmatrix}. \quad (3.39)$$

This form of the covariant momentum ensures that the spatial components encode the anisotropic inertial response of the charge carrier, as described by the band structure near the valley minimum. To extract the physical wavevector, we interpret the spatial part of the covariant four-momentum (the quasi-momentum) $\vec{P}_{\text{quasi}}$ as:

$$\vec{P}_{\text{quasi}} = \gamma \mathcal{M}_n \vec{v} = \hbar \vec{k}. \quad (3.40)$$

This expression generalizes the classical relation between wavevector and velocity by including both the anisotropic mass tensor and the pseudo-relativistic Lorentz factor γ. In the non-relativistic limit where $\gamma \to 1$, we recover the semiclassical particle model introduced in Section 3.1:

$$\vec{k} = \frac{1}{\hbar} \mathcal{M}_n \vec{v}. \quad (3.41)$$

The Lorentz factor in terms of the spatial part of the covariant four-momentum can be calculated

as:

$$\begin{aligned}\gamma &= \frac{1}{\sqrt{1-\frac{1}{\gamma^2}\langle\vec{P}_{\text{quasi}}|\frac{\mathcal{M}_n^{-1}}{m_0c^2}|\vec{P}_{\text{quasi}}\rangle}} \\ \Rightarrow \gamma^2 &= 1+\langle\vec{P}_{\text{quasi}}|\frac{\mathcal{M}_n^{-1}}{m_0c^2}|\vec{P}_{\text{quasi}}\rangle \\ \Rightarrow \gamma &= \sqrt{1+\langle\vec{P}_{\text{quasi}}|\frac{\mathcal{M}_n^{-1}}{m_0c^2}|\vec{P}_{\text{quasi}}\rangle}.\end{aligned} \tag{3.42}$$

Combining it with Equation 3.40, we get:

$$\gamma = \sqrt{1+\hbar^2\langle\vec{k}|\frac{\mathcal{M}_n^{-1}}{m_0c^2}|\vec{k}\rangle} \tag{3.43}$$

which can be compared to Equation 3.35. Now we can rewrite the energy-wavevector relationship as:

$$\begin{aligned}\epsilon(\vec{v}) &= \gamma m_0c^2 \\ &= m_0c^2\sqrt{1+\langle\vec{P}_{\text{quasi}}|\frac{\mathcal{M}_n^{-1}}{m_0c^2}|\vec{P}_{\text{quasi}}\rangle} \\ &= m_0c^2\sqrt{1+\hbar^2\langle\vec{k}|\frac{\mathcal{M}_n^{-1}}{m_0c^2}|\vec{k}\rangle},\end{aligned} \tag{3.44}$$

where in the non-relativistic limit, we recover the Equation 2.34:

$$\epsilon(\vec{k}) \approx m_0c^2+\frac{1}{2}\hbar^2\langle\vec{k}|\mathcal{M}_n^{-1}|\vec{k}\rangle = \epsilon_0+\frac{1}{2}\hbar^2\langle\vec{k}|\mathcal{M}_n^{-1}|\vec{k}\rangle. \tag{3.45}$$

Since it will be useful in our simulations, we note that we can introduce the contravariant four-momentum, where we have suggestively labeled the spatial part of the contravariant momentum the transport momentum or $\vec{P}^{\text{tr}}$:

$$P^\mu = m_0U^\mu = \gamma m_0\begin{bmatrix}c\\ \vec{v}\end{bmatrix} = \begin{bmatrix}\vec{P}^0\\ \vec{P}^{\text{tr}}\end{bmatrix}, \tag{3.46}$$

where

$$\vec{P}^{\mathrm{tr}} = \gamma m_0 \vec{v}. \tag{3.47}$$

The most useful property of this quantity is that it is related to the velocity linearly and can fully describe the charge's movement in real space. It also allows us to calculate the Lorentz factor γ and hence energy $\epsilon = \gamma m_0 c^2$, in terms of the transport momentum by inserting Equation 3.47 into Equation 3.35:

$$\begin{aligned} \gamma &= \frac{1}{\sqrt{1 - \frac{1}{\gamma^2}\left\langle \vec{P}^{\mathrm{tr}} \left| \frac{\mathcal{M}_n}{m_c^3 c^2} \right| \vec{P}^{\mathrm{tr}} \right\rangle}} \\ \Rightarrow \gamma &= \sqrt{1 + \left\langle \vec{P}^{\mathrm{tr}} \left| \frac{\mathcal{M}_n}{m_c^3 c^2} \right| \vec{P}^{\mathrm{tr}} \right\rangle}, \end{aligned} \tag{3.48}$$

and therefore, the energy can be written in terms of the transport momentum as:

$$\epsilon(\vec{P}^{\mathrm{tr}}) = \gamma m_0 c^2 = \sqrt{m_0^2 c^4 + \left\langle \vec{P}^{\mathrm{tr}} \left| \frac{\mathcal{M}_n c^2}{m_0} \right| \vec{P}^{\mathrm{tr}} \right\rangle}. \tag{3.49}$$

Finally, we can relate the quasi-momentum and transport momentum using Equation 3.40:

$$\vec{P}^{\mathrm{tr}} = \gamma m_0 \vec{v} = m_0 \mathcal{M}_n^{-1} \vec{P}_{\mathrm{quasi}} = \hbar m_0 \mathcal{M}_n^{-1} \vec{k}. \tag{3.50}$$

Having established a pseudo-relativistic framework for modeling charge transport in anisotropic semiconductors, we next use it to address some of the technical issues surrounding the implementation of our model within a simulation. The particle-like description and the scattering models discussed throughout this chapter must be incorporated into a computational framework that accurately combines the deterministic and probabilistic behaviors of charge carriers. In the next section, we describe the Monte Carlo simulation techniques used to implement and execute these models, including the generation of charges, their propagation, and the probability of scattering interactions within the context of Geant4.

3.5 Technical Notes about Some of the Monte Carlo Methods used in our Simulations

In this section, we outline some of the methods used in our simulation to model the full trajectory of charge carriers. Like most simulation programs, the implementation is accomplished by stitching together a series of steps, beginning from the initial particle creation and proceeding through their propagation and subsequent scattering events. While Geant4 is an incredibly powerful and flexible tool that can simulate both the deterministic aspects of charge transport, as well as the probabilistic nature of the scattering and decaying processes, utilizing Monte Carlo techniques, it makes a number of simplifying assumptions about the relationships between many of the kinematic variables that aren't compatible with trajectories within anisotropic media. For this reason, it is interfaced with the custom G4CMP framework, which allows for custom handling of momentum, energy, and direction to ensure physical accuracy within anisotropic media. While the simulation has many moving parts, we focus on three main ones that are most relevant to this work:

- Event creation in which a charge is generated following an energy deposition, where electrons and holes are initialized with specific valley assignments and energies as determined by a chosen set of probability distributions (Monte Carlo methods).
- Charge propagation between scattering events, where the motion of particles is governed by the deterministic equations of motion described in this chapter.
- Scattering events, where transitions between valleys or directions occur due to elastic interactions or interactions that emit phonons, are determined probabilistically.

In the first paragraph, we describe the Monte Carlo methods used to generate the initial charge carriers in our Monte Carlo simulation to form the start of an event. In the second paragraph, we describe the processes Geant4 uses for the deterministic portions of the charge trajectories. In the third paragraph, we briefly comment on which of the calculations can effectively set $\gamma = 1$ and which cannot. In the fourth paragraph, we derive the equations that G4CMP uses to determine the

physical quantities passed to Geant4 before and after a particle's trajectory segment. In the fifth paragraph, we spell out the calculations and Monte Carlo methods used to incorporate scattering into the simulation between the free-propagation segments. In the sixth paragraph, we dive deep into the mathematical work used in our modeling of intervalley scattering.

Monte Carlo methods are used to generate the initial charge carriers in the simulation to form the start of an event. Following an energy deposition, the simulation spends all the energy to create electron-hole pairs and prompt phonons. All electrons and holes created have the same initial total energy, approximately three times the bandgap, to prevent them from recombining [63]. Each generated charge is assigned a random direction uniformly sampled over the unit sphere. The simulation then determines which valley this direction most closely aligns with by calculating the angle between the selected direction and each of the valley directions, and assigning the charge to the valley that yields the smallest angle. This initialization ensures that subsequent charge dynamics begin in a physically consistent valley-specific frame.

The processes Geant4 uses for the deterministic portions of the charge trajectories only require the initial momentum, mass, and net force for its calculations. Since there is no unique method to calculate the trajectories, Geant4 utilizes variables based on the spacetime interval, $\mathrm{d}s$, so the input information it requires and the set of assumptions it makes for calculations must be taken into consideration when applying them to our purposes. We note that:

- The input variable versions Geant4 uses to determine its equations of motion can be thought of as the initial direction of motion, $\frac{\mathrm{d}\vec{r}}{ds}$, an effective force which is the derivative of the momentum vector with respect to the path length, $\vec{f} = \frac{\mathrm{d}\vec{P}}{\mathrm{d}s}$, and the effective lab time of flight given by the derivative of the time of flight with respect to the path length, $t_{\mathrm{tof}} = \frac{\mathrm{d}t}{\mathrm{d}s}$.

- As Geant4 uses momentum in the real space for transport, its momentum would be the contravariant momentum or transport momentum, $\vec{P}^{\mathrm{tr}}$, introduced in Equation 3.47.

- Since the calculations for the trajectory over time of a step are done as a geometrical problem using $\mathrm{d}s$ instead of $\mathrm{d}t$, all results are independent of mass and charge, but assumes that that

both $\vec{f}$ and t_{tof} are constant during a step. For a variable field or mass, this means the steps must be small.

- After each propagation step, Geant4 returns the charge's updated position, but only stores the updated transport momentum, since it assumes all relevant quantities can be deduced from them, such as energy using $\epsilon^2 = m_{\text{charge}}^2 c^4 + |\vec{P}^{\text{tr}}|^2 c^2$.

With these assumptions in mind, we note that since there are significant differences between Geant4's variables and the methods and equations used in Section 3.1, G4CMP provides custom handling of variables both before and after the trajectory step. Specifically:

- Before the calculation of the trajectories, Geant4 must be sent the momentum direction, $\vec{f}$ and t_{tof}. In isotropic media, these are just the standard definitions of the momentum unit vector direction, force over velocity $\frac{\vec{F}}{|\vec{v}|}$, and inverse velocity $\frac{1}{|\vec{v}|}$. However, for anisotropic media, we need to assign custom values for each of these such that a charge will end up in the right location according to the equations of motion, i.e., values based on the quantities from Equations 3.13, 3.14, and 3.25.

- For isotropic media, the standard kinematic results can be directly interpreted and used for any next step in the simulation. However, given the inputs above, while the magnitude and direction of the transport momentum in Equation 3.47 will be correct, the remaining kinematics will not be what is expected in Equations 3.48, 3.49, and 3.50 as Geant4 uses the given scalar mass of the charge mass to deduce the Lorentz factor, energy, velocity, and wavevector from transport momentum. For this reason, we replace the value of the mass stored in Geant4 (not used in calculating the trajectory) with an effective mass, m_{eff}, that provides the correct energy before any further steps are taken as other processes use the Geant4 energy, and calculate the velocity and wavevector using Equation 3.40 whenever we need them.

It's useful to briefly comment on which of the calculations can effectively set $\gamma = 1$ and which cannot. At low energies, it is often valid to assume $\gamma \approx 1$ for calculating the $\vec{f}$ and t_{tof}, as the

relative error on the final position and momentum remains of order $\mathcal{O}\left(\frac{|\vec{v}|^2}{c^2}\right)$. To see that, in a simplistic scenario of n steps of s_0 length, each with a $\frac{\Delta s_0}{s_0}$ error, the total error for the whole path of ns would be $\frac{\Delta s}{s} \leq \frac{n\Delta s_0}{ns_0} = \frac{\Delta s_0}{s_0}$, which means the error would remain negligible. However, for energy calculations, Geant4 consistently applies the relativistic energy-momentum relation $\epsilon^2 = m_{\text{eff}}^2 c^4 + |\vec{P}^{\text{tr}}|^2 c^2$ so setting $\gamma = 1$ in Equation 3.47 would mean using the energy from Equation 3.38 instead of Equation 3.37. This would introduce a systematic error in scenarios where m_{eff} is used, particularly in scattering events that produce a phonon. For example, in a phonon emission scattering, using Equation 3.38 to calculate the charge energy before and the charge and phonon energy after would show a mismatch. While the bias scales as $\frac{\Delta\epsilon}{\epsilon} \approx 10^{-7}$ per scattering interaction in principle, the weight of each error caused by each step varies based on the energy of the step. In our setting, due to energy gains from the electric field and energy loss from intravalley scatterings, the total energy remains relatively constant, resulting in each error having the same weight in the total error. Ultimately, since all the errors are in the same direction, the total error scales linearly with the number of steps in the form of $\frac{n\Delta\epsilon}{\epsilon}$, where n is the number of steps. Since there can be large numbers of interactions, these small conservation of energy errors accumulate over time to yield observably incorrect results. To eliminate this issue, we adopt the pseudo-relativistic formalism introduced in Section 3.4 for determining m_{eff} consistently with Geant4's energy calculation. Specifically, since Geant4 returns the correct value of the the transport momentum $\vec{P}^{\text{tr}}$ we use Equation 3.49 in our calculation of m_{eff}.

The quantities passed to Geant4 before and after a particle's trajectory segment, the effective force $\vec{f}$, the lab time-of-flight t_{tof}, and the effective mass m_{eff}, are calculated in G4CMP. Each is a function of the transport momentum $\vec{P}^{\text{tr}}$. Using the definition of $\vec{P}^{\text{tr}}$ from Equation 3.47 and assuming $\gamma = 1$, we take:

$$t_{\text{tof}} = \frac{\mathrm{d}t}{\mathrm{d}s} = \frac{1}{|\vec{v}|} = \frac{1}{m_c|\vec{P}^{\text{tr}}|}. \tag{3.51}$$

For the effective force $\vec{f}$, we again assume $\gamma = 1$, and differentiate the transport momentum leading

to:

$$\vec{f} = \frac{\mathrm{d}(\vec{P}^{\mathrm{tr}})}{\mathrm{d}s} = \frac{\mathrm{d}t}{\mathrm{d}s}\frac{\mathrm{d}(m_c\vec{v})}{\mathrm{d}t} = \frac{1}{|\vec{v}|}m_c\vec{a} = \frac{1}{|\vec{v}|}m_c\mathcal{M}^{-1}\vec{F}, \tag{3.52}$$

where $\vec{F}$ is the electric force acting on the charge and $\mathcal{M}$ is the mass tensor. Because $\mathcal{M}$ depends on the direction of motion, small simulation step sizes are enforced to preserve accuracy. To ensure Geant4 calculates the correct kinetic energy based on $\vec{P}^{\mathrm{tr}}$, and Equation 3.49 we calculate m_{eff} via:

$$\begin{aligned} \epsilon_{\mathrm{kin}} &= \sqrt{m_{\mathrm{eff}}^2c^4 + |\vec{P}^{\mathrm{tr}}|^2c^2} - m_{\mathrm{eff}}c^2, \quad \text{where} \quad \epsilon_{\mathrm{kin}} = \epsilon(\vec{P}^{\mathrm{tr}}) - m_cc^2, \\ \Rightarrow m_{\mathrm{eff}} &= \frac{1}{2c^2}\cdot\frac{|\vec{P}_{\mathrm{tr}}|^2c^2 - \epsilon_{\mathrm{kin}}^2}{\epsilon_{\mathrm{kin}}} = \frac{1}{2c^2}\cdot\frac{|\vec{P}^{\mathrm{tr}}|^2c^2 - \left[\epsilon(\vec{P}^{\mathrm{tr}}) - m_cc^2\right]^2}{\epsilon(\vec{P}^{\mathrm{tr}}) - m_cc^2}. \end{aligned} \tag{3.53}$$

Since we anticipate that future developers of G4CMP will find it useful, we spell out the calculations and Monte Carlo methods used to incorporate scattering into the simulation between the free-propagation segments. Scattering events are treated as instantaneous transitions, during which the direction and energy of the charge carrier may change, and phonons may be emitted. We note that G4CMP handles the process fully, which means, unlike the propagation process discussed earlier, we don't need custom handling of the input variables. Intravalley and intervalley scattering are considered separately, and the scattering rate calculations in Section 2.5 are used with Monte Carlo methods to calculate when they occur as the series of trajectories progress. The two mechanisms also affect the charge trajectory differently, as discussed in Section 3.3. As described in Section 2.5.2 in this work, we assume intervalley scattering randomly reassigns the charge to a new valley of the same type, preserving the angle between the charge's wavevector and the valley axis during the transition. This is implemented by rotating the charge's state into the frame of the new valley, while maintaining the original angle. The implementation of intravalley scattering is done on a microscopic level and therefore requires more mathematical work as described below.

The calculations for intervalley scattering are all modeled as acoustic phonon emission and use the Herring-Vogt transformation to switch from the lab frame to the spherical frame, determining the final-state kinematics probabilistically using standard tools, and then transforming back again. Using conservation of energy and momentum in this frame, the emitted phonon wavevector $\vec{q}_{\mathrm{hv}}$

can be given by:

$$|\vec{q}_{\rm hv}| = 2(|\vec{k}_{\rm hv}|\cos\theta - k_{ac}), \tag{3.54}$$

where $\vec{k}_{\rm hv}$ is the initial charge wavevector in the Herring-Vogt frame, k_{ac} is the effective threshold wavevector defined in Equation 2.40, and θ is the emission angle and is sampled according to a differential probability distribution derived from the interaction physics. Each scattering interaction is implemented using a Monte Carlo method based on the corresponding angular distribution of the emitted phonon in the spherically symmetric reference frame (after the Herring-Vogt transformation). For completeness, we note that to sample the emission angle θ, we begin by integrating the probability distribution function $P(k,\theta)$ in Equation 3.31, to obtain the cumulative distribution function (CDF) u:

$$\begin{aligned} u &= \int_0^\theta P(k_{\rm hv},\theta')\,{\rm d}\theta' \\ &= \frac{\hbar k_{ac}}{ml_0}\left(\frac{k_{\rm hv}}{k_{ac}}\right)^2 \int_0^\theta \left(\cos\theta' - \frac{k_{ac}}{k_{\rm hv}}\right)^2 \sin\theta'\,{\rm d}\theta' \\ &= -\frac{\hbar k_{ac}}{3ml_0}\left(\frac{k_{\rm hv}}{k_{ac}}\right)^2 \left[\cos^3\theta - 3\left(\frac{k_{ac}}{k_{\rm hv}}\right)\cos^2\theta + 3\left(\frac{k_{ac}}{k_{\rm hv}}\right)^2\cos\theta\right], \end{aligned} \tag{3.55}$$

where l_0 is the characteristic length as defined in Equation 2.41 and m is the charge mass. To sample θ, we invert the above expression by solving for $\cos\theta$ as a function of u:

$$\theta = \cos^{-1}\left[\sqrt[3]{-\left(\frac{k_{ac}}{k_{\rm hv}}\right)^2\left(\frac{k_{ac}}{k_{\rm hv}} + 3\frac{ml_0}{\hbar k_{ac}}u\right)} + \frac{k_{ac}}{k_{\rm hv}}\right]. \tag{3.56}$$

We define the valid domain for sampling by evaluating the CDF at its extrema:

$$\begin{aligned} &\theta_{min} = 0 \Rightarrow u_{\rm max} = -\frac{\hbar k_{ac}}{3ml_0}\left(\frac{k_{\rm hv}}{k_{ac}}\right)^2\left(1 - 3\frac{k_{ac}}{k_{\rm hv}} + 3\left(\frac{k_{ac}}{k_{\rm hv}}\right)^2\right), \\ &\theta_{max} = \cos^{-1}\left(\frac{k_{ac}}{k_{\rm hv}}\right) \Rightarrow u_{\rm min} = -\frac{\hbar k_{ac}}{3ml_0}\left(\frac{k_{\rm hv}}{k_{ac}}\right)^2\left(\frac{k_{ac}}{k_{\rm hv}}\right)^3 = -\frac{\hbar k_{ac}}{3ml_0}\left(\frac{k_{ac}}{k_{\rm hv}}\right). \end{aligned} \tag{3.57}$$

To facilitate uniform sampling, we define a normalized random variable $u^* \in [0,1]$ by linearly

mapping $u \in [u_{\min}, u_{\max}]$:

$$\begin{aligned} u^* &= \frac{u - u_{\min}}{u_{\max} - u_{\min}} \\ &= \frac{u + \frac{\hbar k_{ac}}{3ml_0}\frac{k_{ac}}{k_{\text{hv}}}}{-\frac{\hbar k_{ac}}{3ml_0}\left(\frac{k_{\text{hv}}}{k_{ac}}\right)^2\left(1 - \frac{k_{ac}}{k_{\text{hv}}}\right)^3} \\ &= -\left(\frac{k_{ac}}{k_{\text{hv}}}\right)^2\left(\frac{k_{ac}}{k_{\text{hv}}} + 3\frac{ml_0}{\hbar k_{ac}}u\right)\left(1 - \frac{k_{ac}}{k_{\text{hv}}}\right)^{-3}. \end{aligned} \tag{3.58}$$

Substituting u^* into Equation 3.56, we obtain the expression:

$$\theta = \cos^{-1}\left[\sqrt[3]{u^*\left(1 - \frac{k_{ac}}{k_{\text{hv}}}\right)^3} + \frac{k_{ac}}{k_{\text{hv}}}\right]. \tag{3.59}$$

To ensure monotonicity (i.e., increasing u yields increasing θ), we define a reflected variable $u^{**} = 1 - u^*$, yielding the final sampling formula:

$$\theta = \cos^{-1}\left[\sqrt[3]{(1 - u^{**})\left(1 - \frac{k_{ac}}{k_{\text{hv}}}\right)^3} + \frac{k_{ac}}{k_{\text{hv}}}\right], \quad 0 \le u^{**} \le 1. \tag{3.60}$$

This expression provides an efficient and accurate way to sample the phonon emission angle θ consistent with the angular distribution. To complete the remaining direction components, the azimuthal angle $\varphi \in [0, 2\pi)$ is sampled uniformly, and the pair (θ, φ) specifies the direction of the emitted phonon in the Herring-Vogt frame. Together with energy conservation, this direction uniquely determines the post-scattering kinematics of the charge and phonon in the Herring-Vogt frame. Lastly, by an inverse Herring-Vogt transformation, the process is completed, and we update m_{eff} as the energy of the charge is now changed.

Having established our particle-like modeling and the foundational components of our Monte Carlo simulation, we are now ready to simulate how these mechanisms collectively shape charge transport at a larger scale. Before presenting the full G4CMP results, we build physical intuition and isolate the dominant effects contributing to observable behavior by constructing a simplified

simulation that implements the core transport principles developed in this chapter, which we will refer to as a "toy" simulation. This approach enables us to visualize and analyze the macroscopic consequences of microscopic processes, without the full complexity of the SuperCDMS detector simulation. In the next chapter, we present this toy simulation framework and demonstrate its effectiveness in capturing the essential features of charge transport relevant to our experimental context.

4. SIMULATING THE DOMINANT EFFECTS WITH A TOY SIMULATION

In this chapter, we present our simplified simulation framework, toy model, designed to isolate and visualize the dominant effects that shape the motion of electrons in semiconductor crystals as described in previous chapters. While the full simulation described in Chapter 5 incorporates a comprehensive set of physical processes, including phonon tracking, boundary interactions, and realistic device geometry, here we focus on pedagogy. Our goal is to get an intuitive sense of how each of the microscopic processes and effects, such as anisotropic band structure, electric field, and scattering processes, influences the trajectories, final positions, and arrival time distribution of the charge carriers. By stripping away complicating effects and running simulations in simple geometries, where effects can be turned on and off, we can build intuition about the core dynamics governing electron transport in materials like silicon and germanium.

The toy model focuses on electrons with fixed energy emitted from a point source, as shown in Figure 3.2, at the center of a rectangular detector volume. We create several datasets, listed in Table 4.1, with different configurations. We vary the underlying band structure (from isotropic to anisotropic), the presence of an applied electric field, and whether intravalley and intervalley scattering mechanisms are enabled to simulate the macroscopic result of the microscopic behaviors shown in Figures 3.1, 3.3, and 3.8. This allows us to compare them side by side and directly observe how each effect modifies the electrons' spatial paths and arrival distributions at the detector surface. These results serve as a qualitative benchmark for interpreting the more complex and quantitative simulation results presented in the next chapter.

We start by describing the setup of the toy simulation and specifying the configurations we used to generate the results. All simulations are performed assuming a simple rectangular crystal with dimensions $80 \times 80 \times 24\ \mathrm{mm}^3$, as listed in Table 4.2 with each electron starting at the geometric center of the crystal ($x = y = z = 0$) with a fixed energy and emitted uniformly in all directions. This ensures that any features of the trajectories or surface arrival distributions arise entirely from the physical modeling rather than initial conditions. The valley orientation of each crystal is chosen

to highlight the specific transport behaviors we aim to study. For example, in silicon, we select a configuration in which the valley axes are either parallel or perpendicular to the electric field, ensuring that all electrons accelerate along the same axis but with different magnitudes depending on their valley. For germanium, we orient the crystal so that all valleys make the same angle with the field, leading to equal acceleration magnitudes but different directions. These specific choices enable us to test the different consequences of anisotropy in a controlled manner.

The set of simulations produced for our studies is organized in a hierarchical structure, as listed in Table 4.1. To build intuition, we begin with the simplest possible configuration, an isotropic crystal with no electric field and no scattering. In this case, electrons move in straight lines at constant speed, as predicted by the modeling in Section 3.1. We then incrementally introduce one physical effect at a time before moving to the anisotropic crystal simulation. First, we analyze how the electric field and intravalley scattering affect the electron propagation[1]. Then we change the crystal to an anisotropic one, but without any effects, to observe the impact of an anisotropic crystal on the electron velocity as described in Section 3.1. After that, we enable an external electric field and observe its impact on acceleration, as described in Section 3.2. Next, we include intravalley scattering, which introduces energy emission in the form of phonons and direction changes due to phonon emission, as modeled in Section 3.3. Then we add intervalley scattering without including intravalley scattering, which causes charges to transition between valleys without energy loss, changing their effective mass and acceleration characteristics. Finally, we simulate the combined effects of electric fields and both types of scattering. This incremental progression allows us to clearly identify how each new physical process modifies the behavior of the ensemble.

As with any simulation, since there are a number of choices which need to be made, we start with a discussion of motivation and strategy. The primary goal of the toy simulation is to build a qualitative intuition about how each effect will impact the charge transportation, but do so in a way that balances that with simplicity where possible. With this in mind, we note that we made the toy model unitless, which means the results from the toy simulation are not suitable for a quantitative

[1]There are no valleys to scatter between, so there is no intervalley scattering for isotropic scenarios.

comparison and can only be interpreted relative to each other qualitatively. Similarly, no attempt was made to fine-tune any of the values. The choice of parameter values for the charge energy, voltage, and scattering parameters include:

- Assume the initial conditions of the charge correspond to an energy of 1 eV, which is at the higher end of the energy spectrum for an ionized electron in CDMS. This ensures that all electrons will have at least one Luke emission before any effects due to the electric field.

- The step sizes within the simulation are chosen to be a small fraction of the trajectory to ensure a smooth path between scattering interactions and capture the curvature induced by the electric field. We choose step sizes to be around 10^{-5} times the detector size in the absence of voltage, and $\frac{10^{-7}}{Voltage}$ times the detector size in the presence of voltage.

- The value of the voltage was set to balance two competing effects: be large enough so that all electrons end up at the top surface, but not high enough that it obscures the other effects.

- The intravalley scattering rates were set so that the electron undergoes a Luke emission as soon as it reaches its critical wavevector magnitude. For simplicity, we implement this with characteristic length $l_0 = 0$ (defined in Equation 2.41). This reduces the scattering probability to a Dirac delta function, $\delta(k_{\text{threshold}} - |\vec{k}|)$, meaning scattering occurs immediately once the charge's wavevector exceeds a predefined threshold. The value of $k_{threshold}$ is set so that an electron would continue to undergo an intravalley scattering until its energy is just above 10^{-4} times its initial energy. Given the assumption that the initial electron energy is chosen to be $1\ \mathrm{eV}$, this corresponds to a typical electron energy of $0.1\ \mathrm{meV}$ during its path.

- While the rate of intervalley scatterings is expected to be small compared to Luke emission processes at these energies [33, 52, 64], our studies are only useful if there are occasional scatterings. To implement this, we use a simple stochastic model by rolling a uniform random number between 0 and 1 at each step. If the number falls below the threshold, the electron undergoes an intervalley transition where the threshold is set to produce about 0.5

scatterings on average along the full trajectory to the surface. Although this model is simplistic, it captures the essential voltage-dependent nature of intervalley scattering by tying the scattering frequency to the step size and thus indirectly to the electron's kinetic energy.

In Section 4.1, we examine electron transport in an idealized isotropic crystal to establish a baseline for comparison with anisotropic cases. In Section 4.2, we move to the case of electron transport in anisotropic crystals without any applied electric field or scattering effects. In Section 4.3, we study the behavior of the electron transport in anisotropic crystals under the influence of a uniform electric field, without including any scattering processes. In Section 4.4, we showcase how enabling intravalley scattering alters the electron transport and the arrival distributions, without including intervalley scattering. In Section 4.5, the electrons are allowed to change their valley through intervalley scattering, without intravalley scattering. In Section 4.6, we present the final results of the toy simulation when all the dominant effects are included, which will qualitatively be comparable to a realistic experiment.

Table 4.1: In this table, we list the configuration properties of the datasets simulated using our toy model with pointers to the figures that use them. We show it to list the set of configuration combinations that are used to help illustrate the crystal band structure, voltage, intravalley scattering, and intervalley scattering effects on how electrons move in a crystal. Note that all samples are generated with $1\ \mathrm{eV}$ monochromatic energy electrons emanating from the point $x = y = z = 0$ (center of the detector) uniformly in all directions. The details about the detectors used in these samples are described in Table 4.2

Simulated Datasets						
#	Crystal Type	Voltage	Intravalley Scattering	Intervalley Scattering	Trajectory Figures	Top Surface Arrival Distribution Figures
1	Isotropic	Disabled	Disabled	Disabled	Figure 4.1	Figure 4.2
2	Isotropic	Enabled	Disabled	Disabled	Figure 4.3	Figure 4.4
3	Isotropic	Enabled	Enabled	Disabled	Figure 4.5	Figure 4.6
4	Si(100)	Disabled	Disabled	Disabled	Figure 4.7	Figure 4.8
5	Ge(100)	Disabled	Disabled	Disabled	Figure 4.9	Figure 4.10
6	Si(100)	Enabled	Disabled	Disabled	Figure 4.11	Figure 4.12
7	Ge(100)	Enabled	Disabled	Disabled	Figure 4.13	Figure 4.14
8	Si(100)	Enabled	Enabled	Disabled	Figure 4.15	Figure 4.16
9	Ge(100)	Enabled	Enabled	Disabled	Figure 4.17	Figure 4.18
10	Si(100)	Enabled	Disabled	Enabled	Figure 4.19	Figure 4.20
11	Ge(100)	Enabled	Disabled	Enabled	Figure 4.21	Figure 4.22
12	Si(100)	Enabled	Enabled	Enabled	Figure 4.23	Figure 4.24
13	Ge(100)	Enabled	Enabled	Enabled	Figure 4.25	Figure 4.26

Table 4.2: In this table, we list the important geometric parameters for the three different detector types that are used in the toy simulations. We show it to specify the configuration details used to make the datasets. We note that while the orientations of the crystals described in Chapter 2 are chosen to be the same as used by the SuperCDMS experiment [65, 66], shown in Figures 1.6 and 1.7, the shape and size used in the simulations are kept identical for simplicity. The scattering and other parameter values and methods, selected for pedagogical instead of quantitative reasons, are described in the text.

Toy Simulation Detectors Information			
Crystal Type	Shape	Size	Valley Orientations
Isotropic	Rectangular	$80 \times 80 \times 24\ \mathrm{mm}^3$	None
Si(100)	Rectangular	$80 \times 80 \times 24\ \mathrm{mm}^3$	$[\pm 1, 0, 0]$, $[0, \pm 1, 0]$, $[0, 0, \pm 1]$
Ge(100)	Rectangular	$80 \times 80 \times 24\ \mathrm{mm}^3$	$[\pm 1, \pm 1, \pm 1]$

4.1 Toy Simulation Results: Isotropic Medium

In this section, we examine electron transport in an idealized isotropic crystal to establish a baseline for comparison with anisotropic cases. This configuration allows us to isolate the geometric and kinematic aspects of charge propagation without the complexities introduced by band anisotropy or scattering. By analyzing electron motion with no applied electric field, with an electric field, and then with intravalley scattering added, we develop intuition for how each effect shapes the trajectory arrival position and time distributions in the simplest case[2]. Additionally, as we assume a scalar effective mass for holes as described in Section 2.4.1, these results form our expectations of hole transportation. We also note that we do not include the case of intervalley scattering, as an isotropic medium can be thought of as having only one energy band extrema in the Brillouin zone at Γ-point ($\vec{k} = 0$), as discussed in Chapter 2. In the first paragraph, we describe the behavior of electrons propagating in an isotropic medium with no external electric field and no scattering effects. In the second paragraph, we introduce a uniform external electric field directed along the negative z-axis and describe its influence on electron motion in the isotropic crystal. In the third paragraph, we add intravalley scattering to observe its effect on electron trajectories.

We start with the behavior of electrons propagating in an isotropic medium with no external electric field and no scattering effects. Since the effective mass is scalar and direction-independent, as described in Equation 2.33, all electrons with the same energy propagate at the same speed regardless of their initial direction. Figure 4.1 shows that the electrons travel in straight lines outward from the origin, preserving the spherical symmetry of the initial conditions. The surface arrival points form an arc tangent distribution on the top face, as seen in Figure 4.2, and the arrival times depend only on the straight-line distance traveled. This configuration provides a clean benchmark for observing how additional physical effects break the spherical symmetry.

We now introduce a uniform external electric field directed along the negative z-axis and describe its influence on electron motion in an isotropic crystal. Since the band structure is isotropic,

[2]We also note that the isotropic case can also be used as a sanity check for the toy simulation, as it should behave like a free charge case.

using Equation 3.24, the acceleration vector is always aligned with the electric field. Figure 4.3 shows that with a high enough electric field, all electrons are deflected toward and reach the top surface, and their trajectories exhibit cylindrical symmetry around the field axis. This focusing effect results in a circular arrival pattern on the top surface, as seen in Figure 4.4, and reduces the average arrival time due to the accelerating force.

We next add intravalley scattering to observe its effect on electron trajectories. As described in Section 3.3, each scattering event reduces the kinetic energy and alters the velocity direction of the electron. It is worth noting that in the isotropic case there are no valleys so here each scattering only introduces a random component to the trajectory, thereby reducing the influence of the initial conditions. As shown in Figure 4.5, the trajectories become more compact. The arrival points in Figure 4.6 form a tighter circular pattern, while the arrival time distribution broadens and shifts to later times due to the reduced average speed caused by repeated energy loss.

Having concluded our examination of electron transport in an isotropic medium, we have established a clear baseline for understanding how geometry, acceleration, and scattering individually influence charge trajectories and surface arrival patterns. With this reference in hand, we now turn to anisotropic media, where valley-dependent effective masses break this symmetry and introduce new directional behaviors in the charge dynamics.

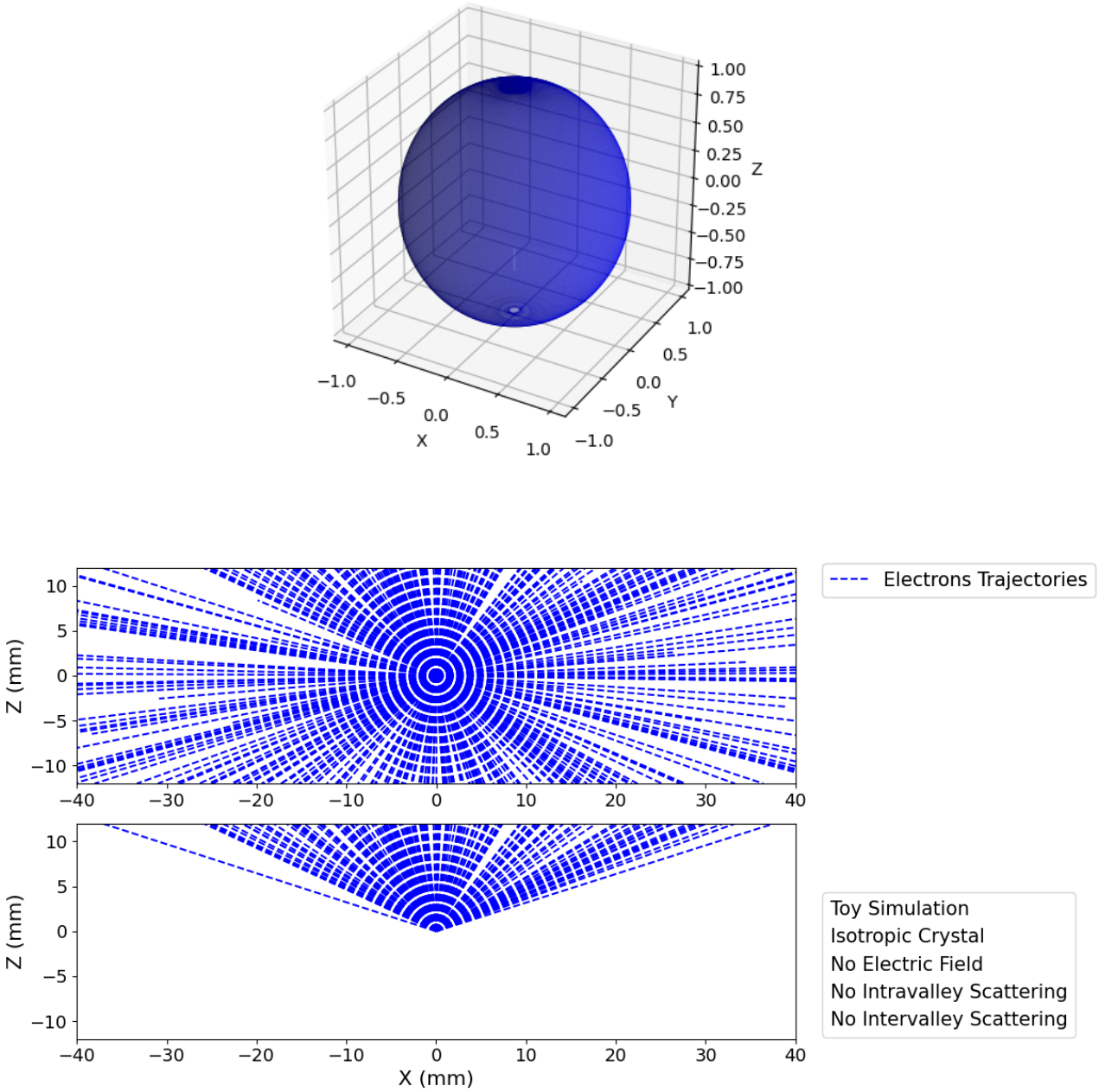

Figure 4.1: This figure shows three views of the simulated trajectories of a mono-energetic point source of electrons in the isotropic band structure crystal described in Table 4.1 with no electric field and no scattering effects. We show it because in the absence of the electric field and scattering effects, electrons move in a straight line, and we see spherical symmetry around the origin. The figure on the top shows the initial directions and velocities, which are uniformly distributed in all directions. The figure on the bottom shows two versions of the trajectories in the xz plane; the top version shows a subset of the trajectories in all directions, while the bottom shows a subset of those trajectories that hit the top surface.

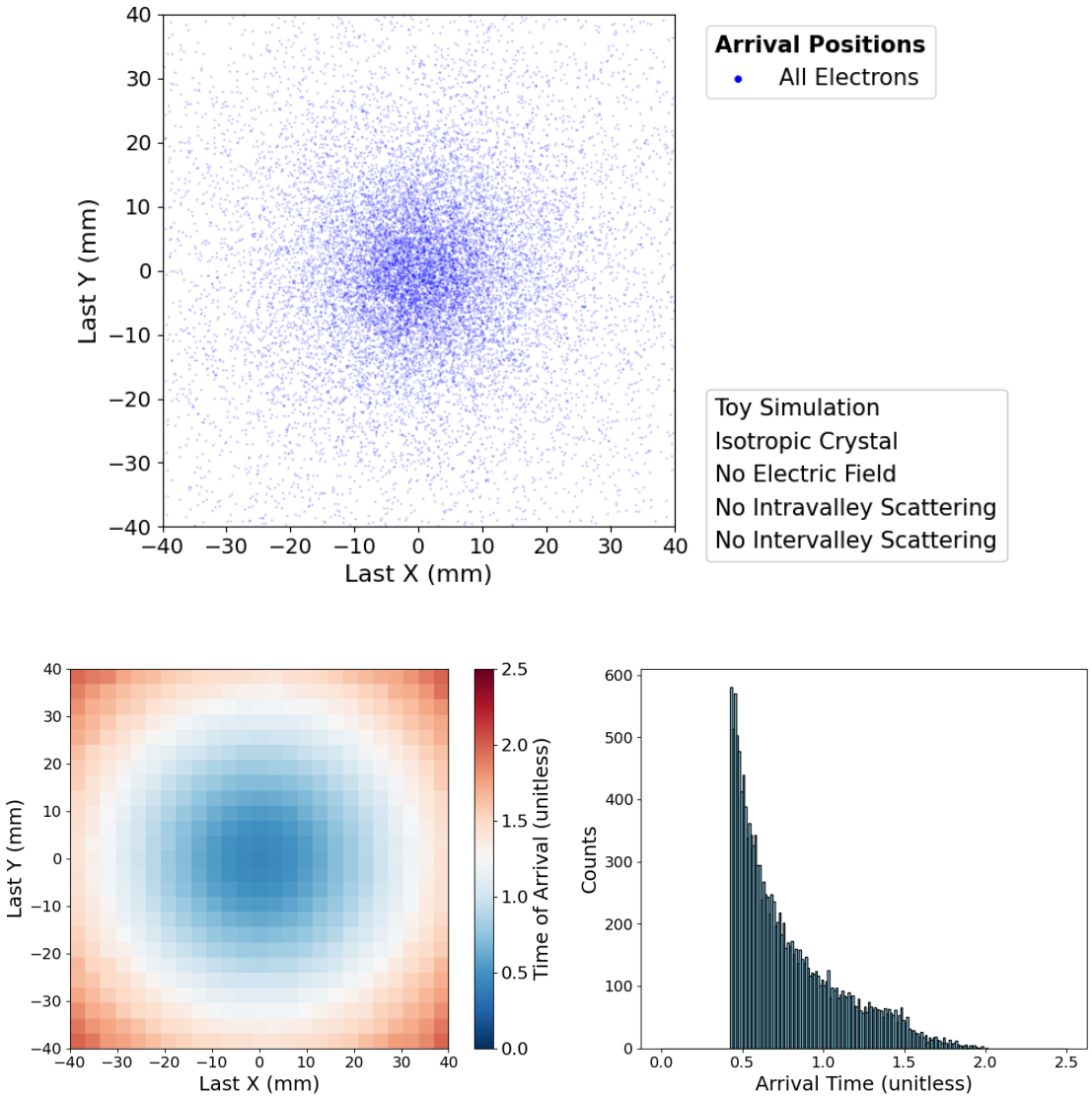

Figure 4.2: This figure shows the distribution of electron arrival positions and times on the top surface of an isotropic crystal for the same sample and configuration as the bottom portion of Figure 4.1. We show it because, in the absence of the electric field, the pattern on the surface can be easily understood as being from purely geometric effects. The top portion of the figure shows the density of arrival points, and is well described by an arc tangent pattern relative to the center. The bottom portion shows both the two-dimensional heat map of the arrival times and a one-dimensional histogram, which have the same distribution for the same reasons because the electrons are mono-energetic. Note that due to how we choose whether the trajectory hits the surface, some events will be chosen as if they hit the top surface, while in fact, they hit a sidewall. This will be true for all cases without voltage, but for the cases with voltage, we can choose the voltage to be large enough so that no event hits a sidewall. This artifact causes the abnormal distribution on the $x = \pm 40$ and $y = \pm 40$.

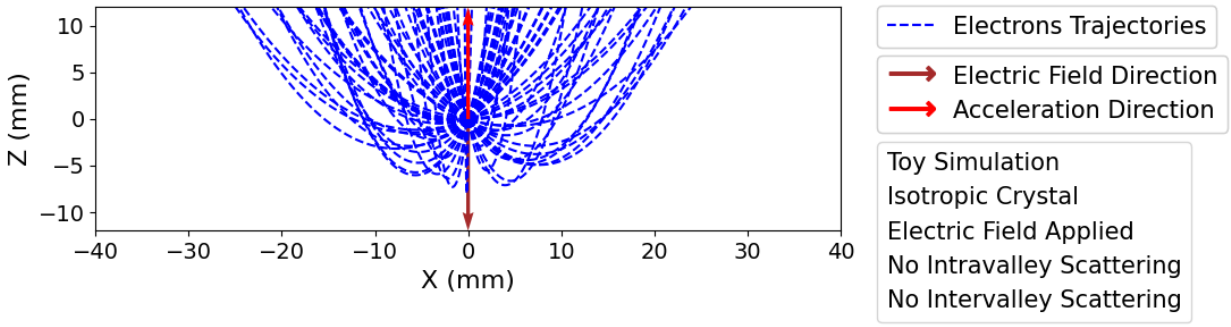

Figure 4.3: This figure shows the electron trajectories in the toy isotropic crystal simulation configuration with an electric field in the negative z direction that is large enough such that all electrons reach the top surface. We show it for comparison with Figure 4.1. We note that in an isotropic crystal, the acceleration caused by an electric field has the same axis as the electric field. This causes a symmetry of the trajectories around the electric field and acceleration axis for electron trajectories.

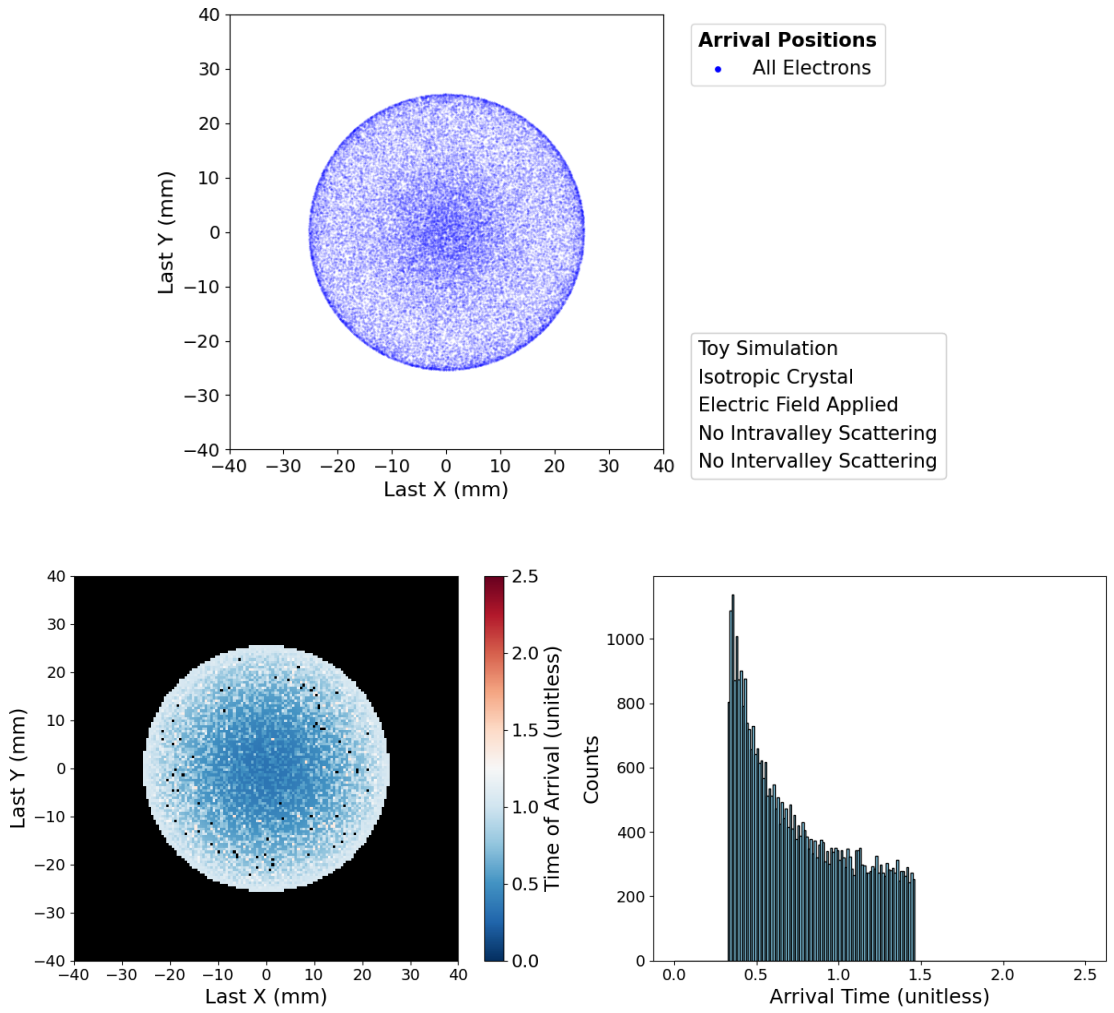

Figure 4.4: This figure shows the distribution of the arrival positions and times on the top surface of an isotropic crystal with an electric field but without scattering effects. We show it to illustrate the effect of the application of the electric field so that it can be compared to Figure 4.2. We note that the electric field and the symmetry mentioned in Figure 4.3 result in the top surface arrival points being tightly clustered around the acceleration and electric field axis, and the average arrival times are lower. This figure sets the baseline for future comparisons with the top of Figures 4.8 and 4.10 as other effects are added.

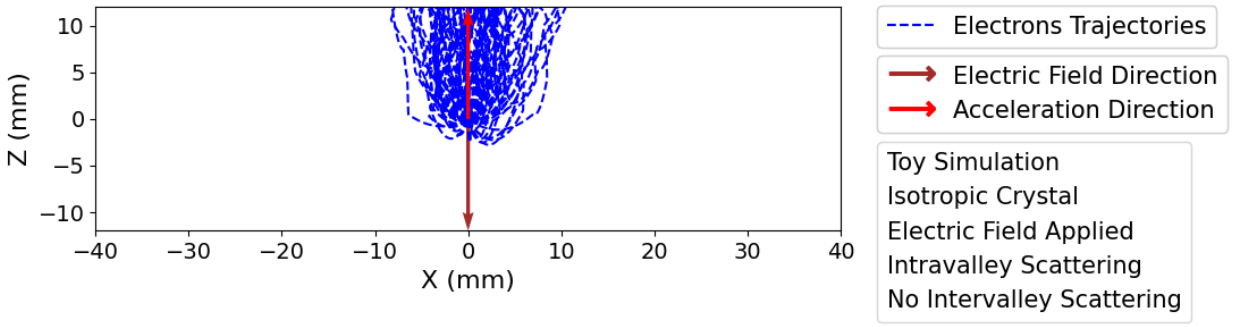

Figure 4.5: This figure shows the trajectories in an isotropic crystal with both a voltage and intravalley scattering but without intervalley scattering. We show it to illustrate the effect of the Luke scattering in the electrons' trajectories in an isotropic crystal. Comparing with Figure 4.4, we see that intravalley scattering causes electrons to lose their speed quickly and get scattered soon after they accelerate enough. This results in a smaller spread around the electric field axis.

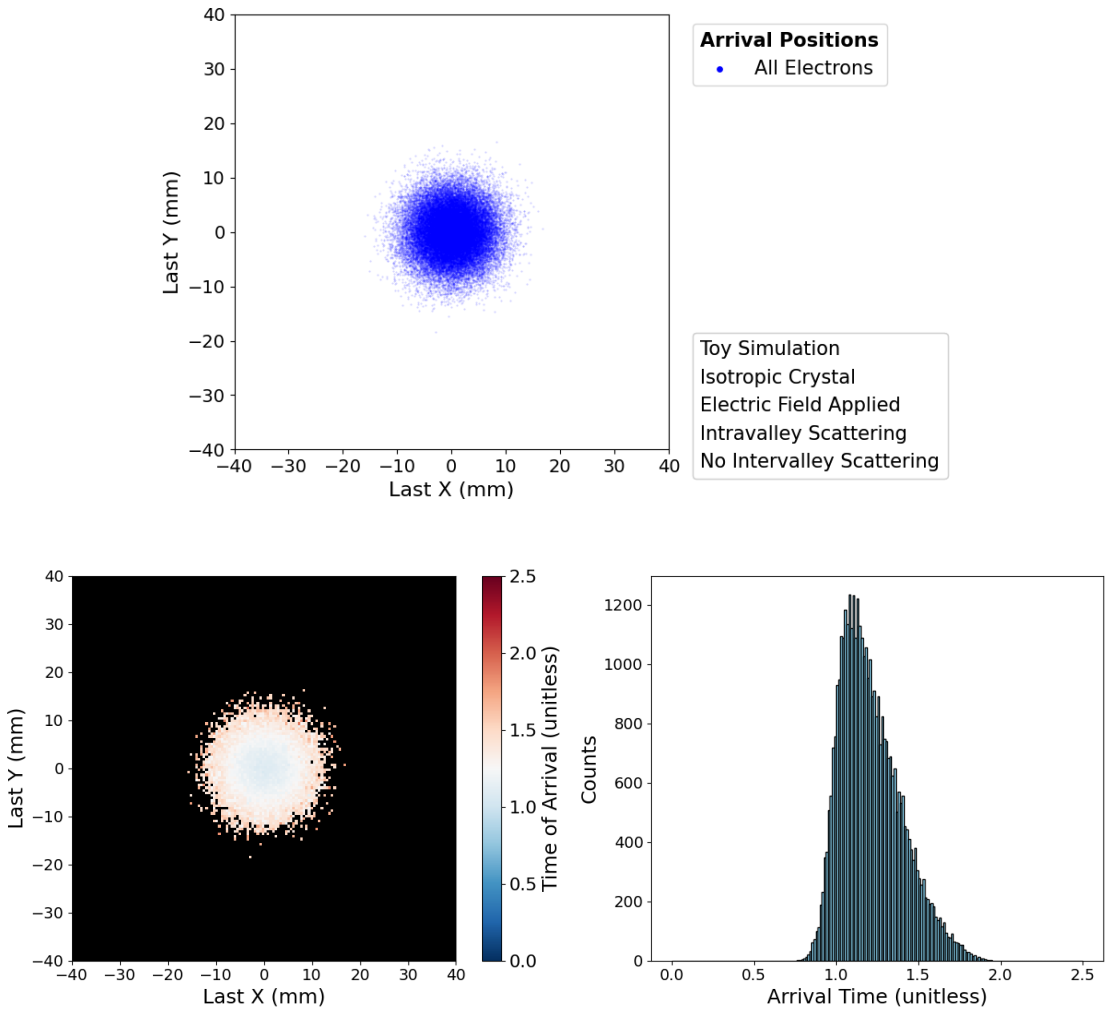

Figure 4.6: This figure shows the distribution of the arrival positions and times on the top surface of an isotropic crystal with both voltage and intravalley scattering but without intervalley scattering. We show it to highlight the impact of the intravalley scattering in the electrons' arrival position and time distributions in an isotropic crystal. Comparing with Figure 4.4, we see that the distribution is much tighter around the origin as the intravalley scattering causes electrons to remain at a low energy, and that the arrival times are significantly later due to slower average speeds. We also note that the arrival times distribution also changed from exponential-like to skew-Gaussian-like.

4.2 Toy Simulation Results: Anisotropic Medium Without Electric Field or Scattering

In this section, we present the toy simulation results for electron transport in anisotropic crystals without any applied electric field or scattering effects. As described in Section 3.1, in the absence of external forces and interactions, charge carriers move along straight-line paths. However, because of the anisotropic effective mass tensor associated with each valley, the velocity depends not only on the energy but also on the orientation of the initial wavevector with respect to the valley axis. As a result, monoenergetic electrons exhibit different velocity magnitudes for different directions, leading to anisotropic arrival-time distributions. In the first paragraph, we analyze the impact of anisotropy in silicon using the Si(100) configuration. In the second paragraph, we explore the corresponding behavior in germanium using the Ge(100) crystal orientation.

To include anisotropy, we now describe the results of the toy simulation in a silicon crystal with no applied electric field or scattering processes. As shown in Figure 4.7, the electrons again propagate in straight lines from the center of the crystal to the detector surfaces, and the spatial distribution of the arrival points is nearly identical to the isotropic case presented in Figure 4.1. However, as explained in Section 3.1, the electrons that have a smaller angle with a valley move more slowly for the same energy. Since all the electrons are moving in a straight line, the top surface only captures valley $[100]$ electrons. In this case, the electrons that are moving further from the xyz axes (the valleys in Si(100)) also have a greater angle with the valleys and hence move faster as described in Section 3.1, resulting in a square-like shape in the arrival-time distribution in Figure 4.8, even though they have the same arrival position distribution.

For a germanium crystal in a Ge(100) configuration, like the silicon case, all electrons travel in straight-line trajectories without acceleration or scattering, as shown in Figure 4.9. However, since in Ge(100) the valleys are along the $[\pm 1, \pm 1, \pm 1]$, the electrons that end up further away from the center of the top surface not only travel a longer distance, but also are closer to a valley and move slower. This results in the arrival time distribution shown in Figure 4.10.

Having concluded our study of transport without electric fields or scattering in anisotropic media, we next introduce an external electric field. This addition highlights the role of anisotropic

acceleration in shaping the electrons' trajectories and further distinguishes the behaviors of silicon and germanium under applied fields.

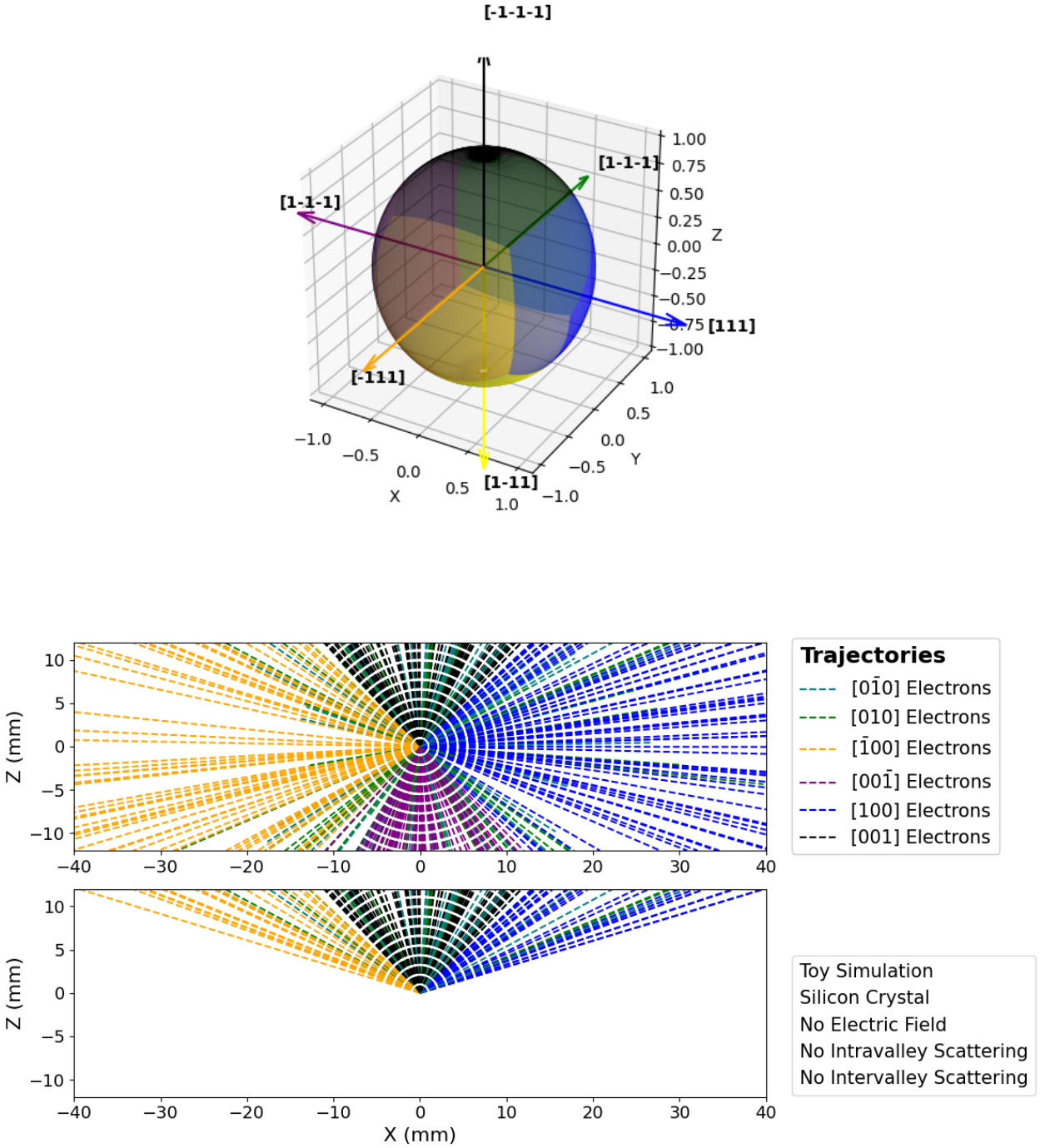

Figure 4.7: This figure shows three views of the simulated trajectories of a mono-energetic point source of electrons in the silicon band structure crystal described in Table 4.1 with no electric field and no scattering effects with colors added to indicate the different valleys each electron travels in. We show it to illustrate the effect of the silicon band structure on the electrons' trajectories in the absence of any complicating effects. Compared with the isotropic case shown in Figure 4.1, we note that while the electrons still move in a straight line and there is no difference in the electrons' path, the trajectories have different speeds.

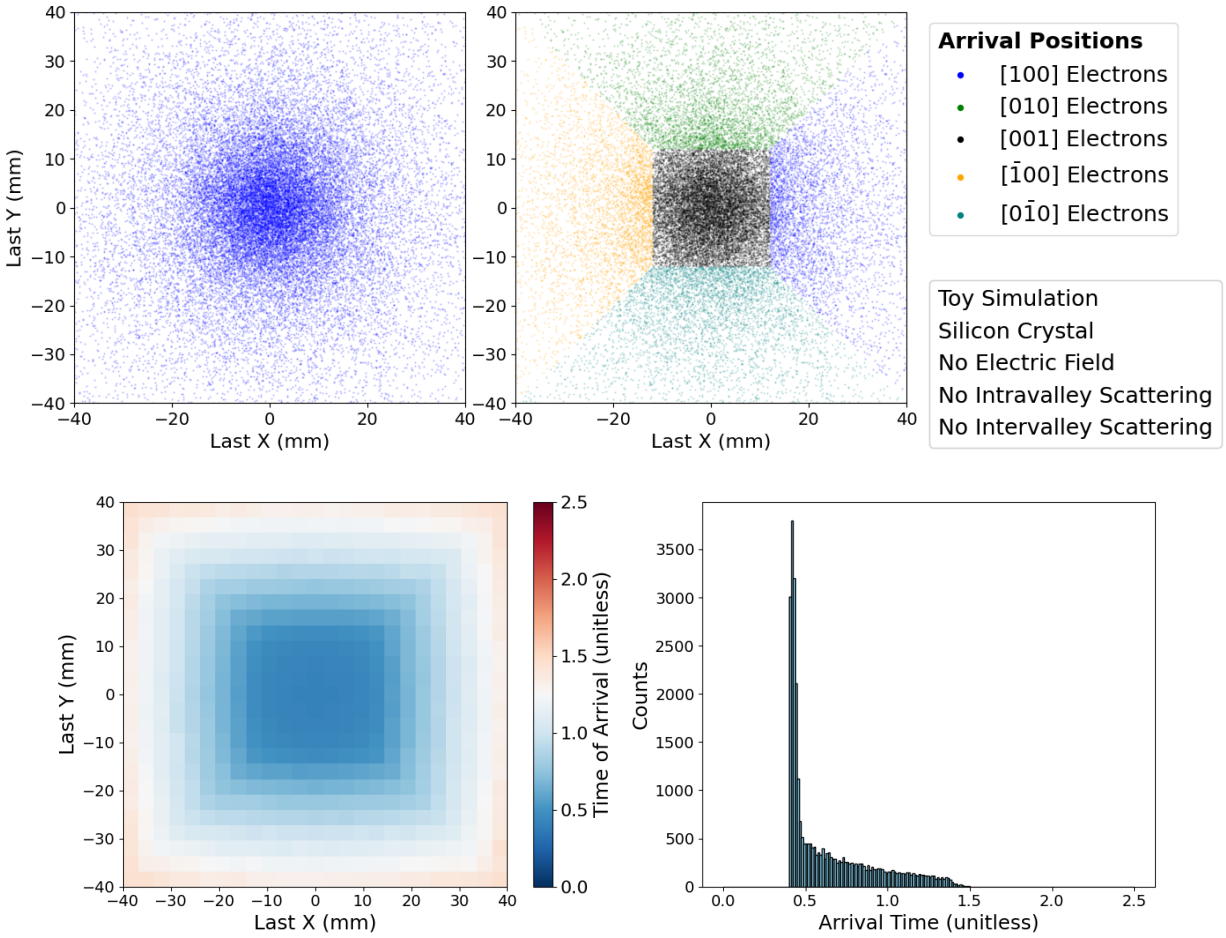

Figure 4.8: This figure shows the distribution of electron arrival positions and times on the top surface of a silicon crystal with no electric field and no scattering. We show it to highlight the effect of the anisotropic band structure of silicon on the electrons' speed distribution. Comparing to the isotropic case shown in Figure 4.2, we note that while the arrival positions are the same (the plot in the top right color codes the valleys for completeness), the electron arrival times are different in the bottom plots, due to the valleys effect on the speed distribution for the same energy electrons, and has a square heat map shape along with more tightly constrained arrival times.

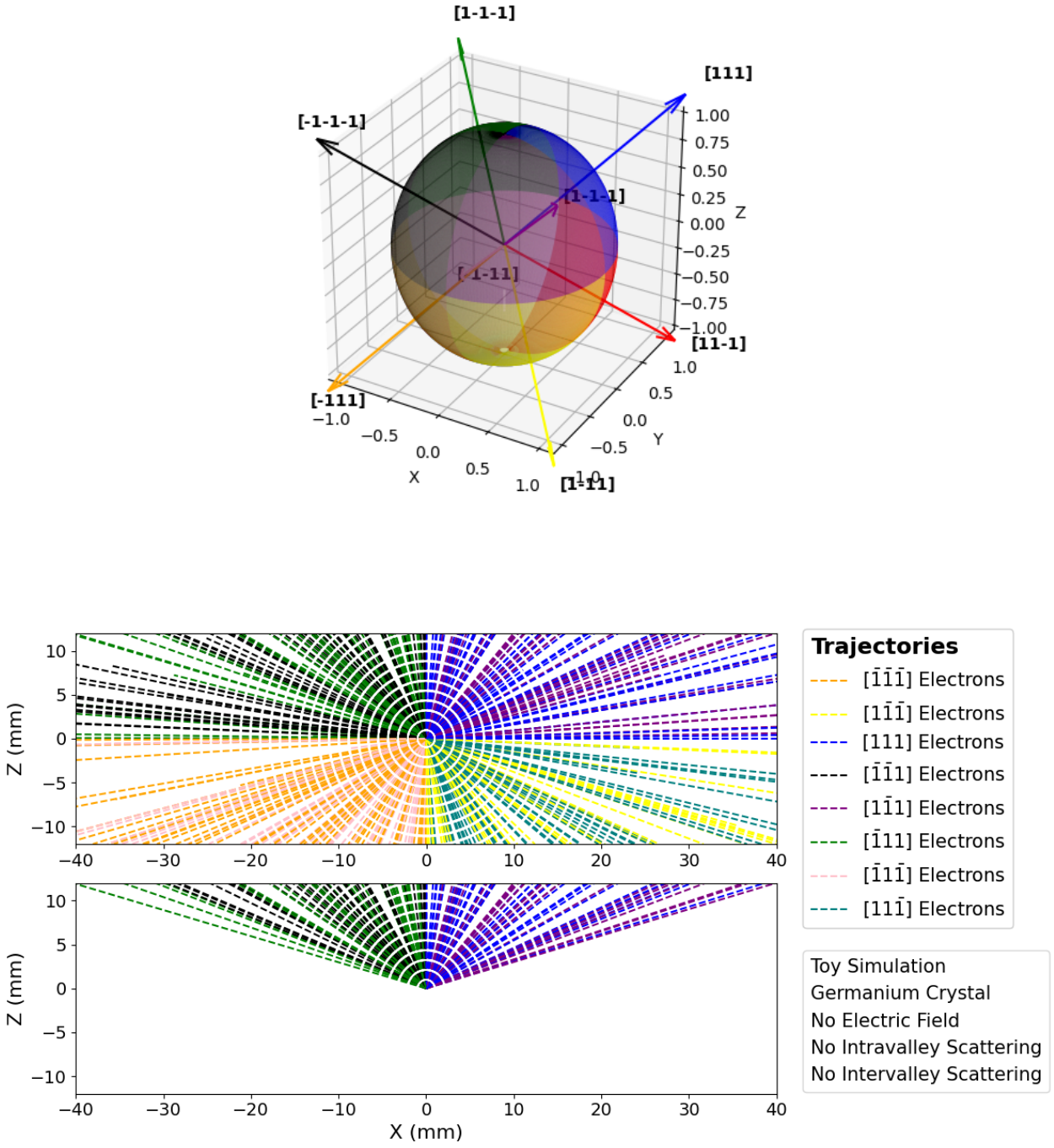

Figure 4.9: This figure shows four views of the simulated trajectories in a germanium crystal for the case where we have no electric field or scattering. We show it to illustrate the effect the band structure has in germanium compared to the silicon and isotropic crystal cases. Comparing with Figures 4.1 and 4.7, we note that changing only the band structure does not affect the electrons' paths. However, later in Figure 4.10, we see that changing the valleys affects the electrons' speeds, and thus time of arrivals.

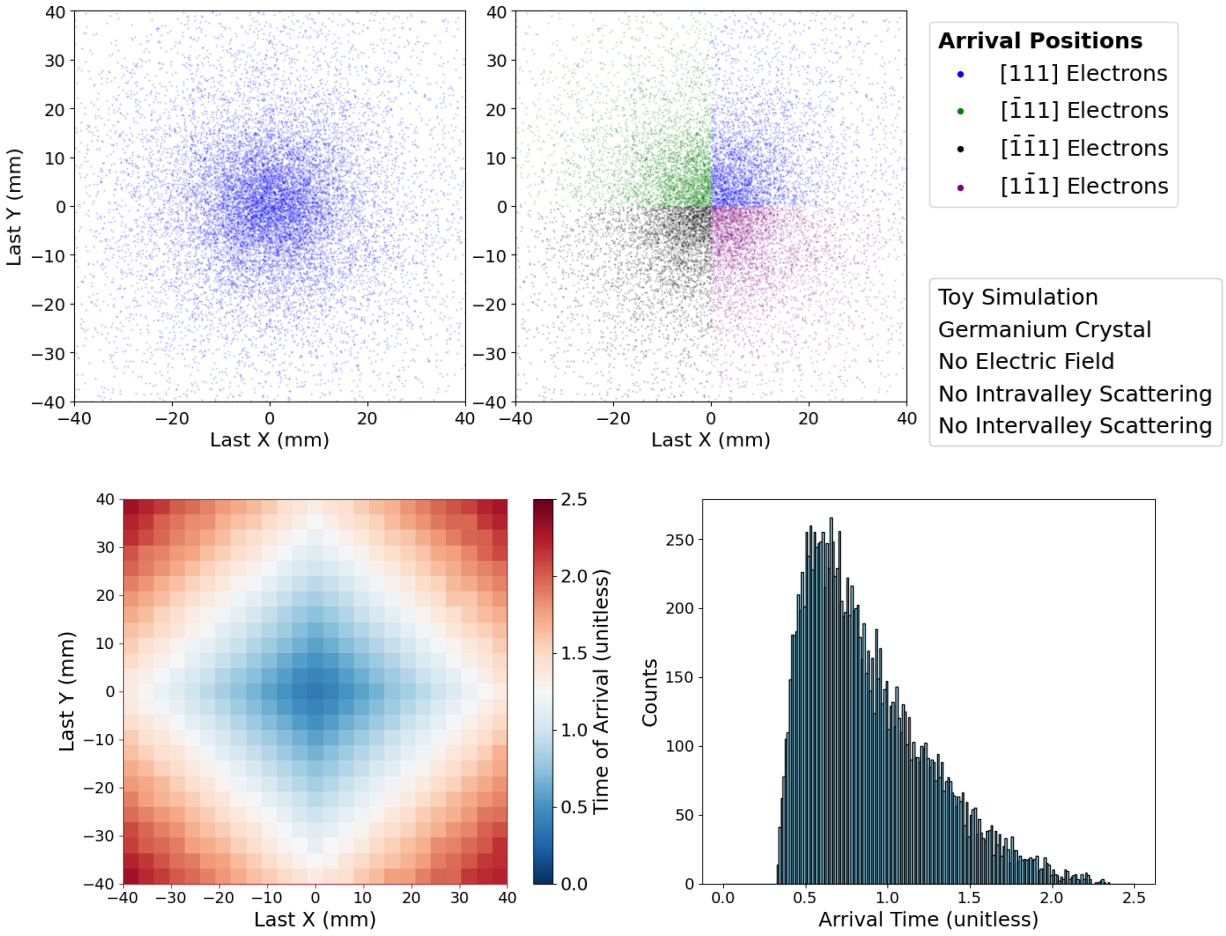

Figure 4.10: This figure shows the distribution of electron arrival positions and times on the top surface of a germanium crystal in the absence of voltage and scattering effects. We show it to highlight the difference in the arrival times as a function of crystal band structure. Compared with Figures 4.2 and 4.8, we note that because the valleys in germanium have different energy levels and directions than the silicon case, the same energy electrons have different speeds, producing a different shape of the arrival times.

4.3 Toy Simulation Results: Anisotropic Medium Under an External Electric Field

In this section, we study the behavior of electron transport in anisotropic crystals under the influence of a uniform electric field, without including any scattering processes. As described in Section 3.2, the acceleration of a charge carrier is governed by the anisotropic mass tensor, leading to directional dependencies in how the electric field alters the trajectory. Even though electrons still follow smooth paths without interruption, the anisotropy of the mass tensor causes the acceleration vectors to deviate from the direction of the electric field and vary in magnitude depending on the valley. In the first paragraph, we describe the toy simulation results for a silicon crystal in the Si(100) configuration under an applied electric field and without scattering. In the second paragraph, we describe the corresponding results for a germanium crystal in the Ge(100) configuration.

Following the format of the previous section, we first look at the toy simulation results for a silicon crystal under an applied electric field and without scattering. As shown in Figure 4.11, all electrons accelerate in the direction of the electric field, which is aligned with the negative z axis; again, the value of the electric field has been set so that all electrons reach the top surface. Because the Si(100) orientation has valleys aligned with the x, y, and z axes, all the valleys are either perpendicular or parallel to the electric field, and all motion can be considered as being in the longitudinal or transverse direction relative to it. Using Equation 3.25 and the notation there, we can see that the electrons in the $\pm z$ valleys, will experience an acceleration equal to $\vec{a} = \frac{\vec{F}}{m_L}$ as the electric field aligns with the longitudinal direction of the valley, while the electrons in the $\pm x$ and $\pm y$ valleys will experience an acceleration equal to $\vec{a} = \frac{\vec{F}}{m_T}$ as the electric field aligns with the transverse direction of the valleys. Since $m_L > m_T$ for both silicon and germanium, as described in Section 2.4.2, electrons in the $\pm x$ and $\pm y$ valleys accelerate faster compared to the $\pm z$ valleys electrons. As a result, the trajectories all curve toward the $+z$ direction, but electrons from different valleys accelerate differently. Additionally, electrons with an initial velocity direction further from the xyz axes have a higher initial velocity, which causes them to move farther in the xy plane. This produces a square-like spatial distribution with rounded edges in the arrival locations, as seen in

Figure 4.12. The arrival time histogram further reflects the two distinct acceleration regimes, with a clear separation between fast and slow populations corresponding to different valleys.

Next, we move to the corresponding results for a germanium crystal in the Ge(100) configuration. Unlike in silicon, the valleys in germanium are oriented along the $[\pm 1, \pm 1, \pm 1]$ directions. In this case, all valleys have the same angle with respect to the applied electric field in the negative z direction, meaning that the magnitude of the acceleration is the same for all electrons regardless of valley. However, because the direction of the acceleration vector depends on the direction of each valley, electrons in different valleys are deflected along different paths. As illustrated in Figure 4.13, electrons from opposite valleys pair together with matching acceleration vectors, resulting in four distinct propagation directions. Consequently, the top surface exhibits eight spatially separated arrival clusters that form symmetric groupings around the z axis, as shown in Figure 4.14. In each quadrant, the farther cluster relative to the origin is for the electrons with an initial velocity pointing downwards, and the closer cluster is for the electrons with an upward initial velocity. However, in contrast to silicon, the arrival time distribution is tightly clustered, since all electrons experience the same acceleration magnitude.

Having concluded our examination of transport in anisotropic media under an applied electric field, we now introduce intravalley scattering into the simulation. This effect disrupts smooth motion by introducing both energy loss and random angular deflections, and allows us to study how scattering reshapes electron distributions on the detector surface.

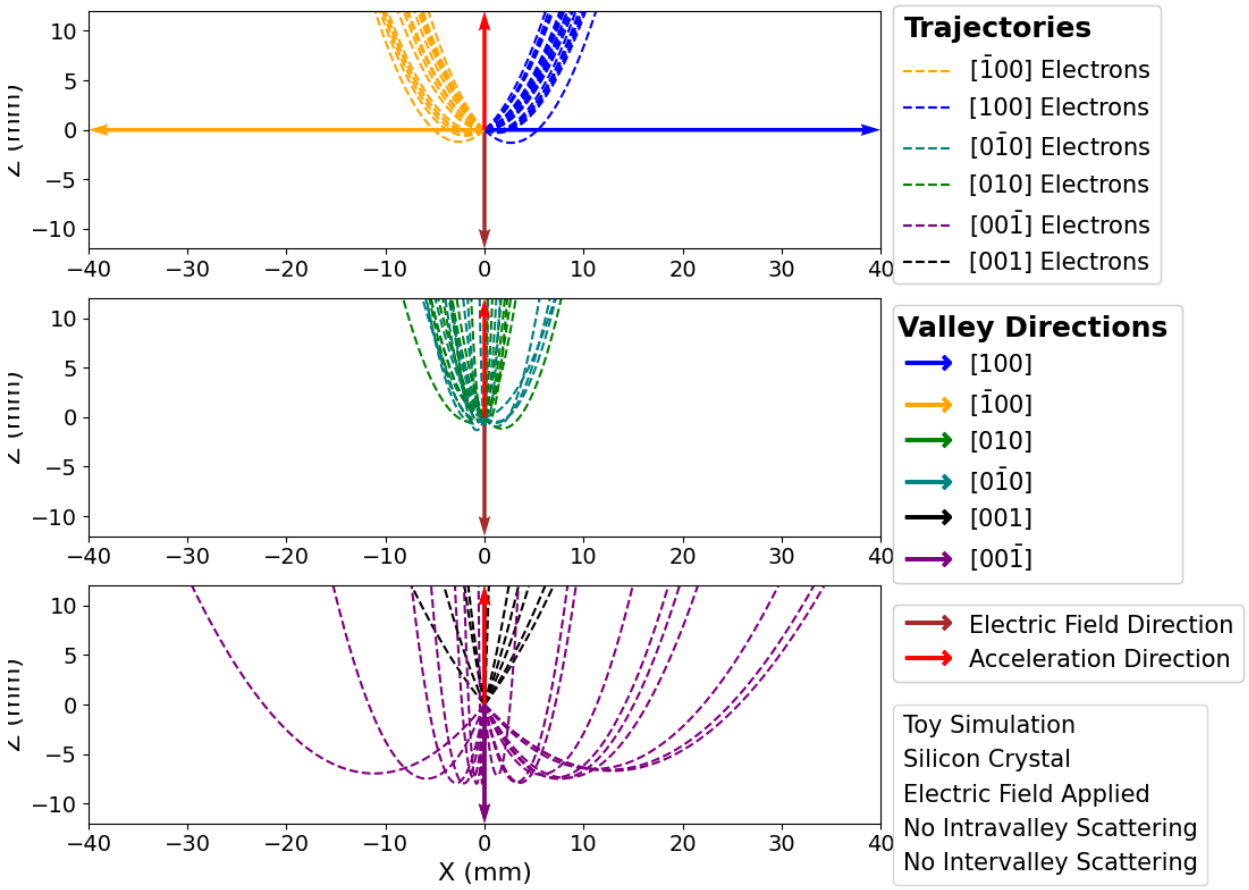

Figure 4.11: This figure shows three plots of the electron trajectories in a silicon crystal with an applied electric field, but where the trajectories are separated by their initial valley (pair of directions in each plot), and the voltage is aligned with one of the valleys in the negative z direction. We show it to highlight the effect of an electric field on electrons paths in an anisotropic crystal. Comparing to the isotropic case shown in Figure 4.3, we see that all the electrons share the same acceleration direction (which is the same as in the isotropic case), but the magnitude of the acceleration is dependent on the valley the electrons are traveling in.

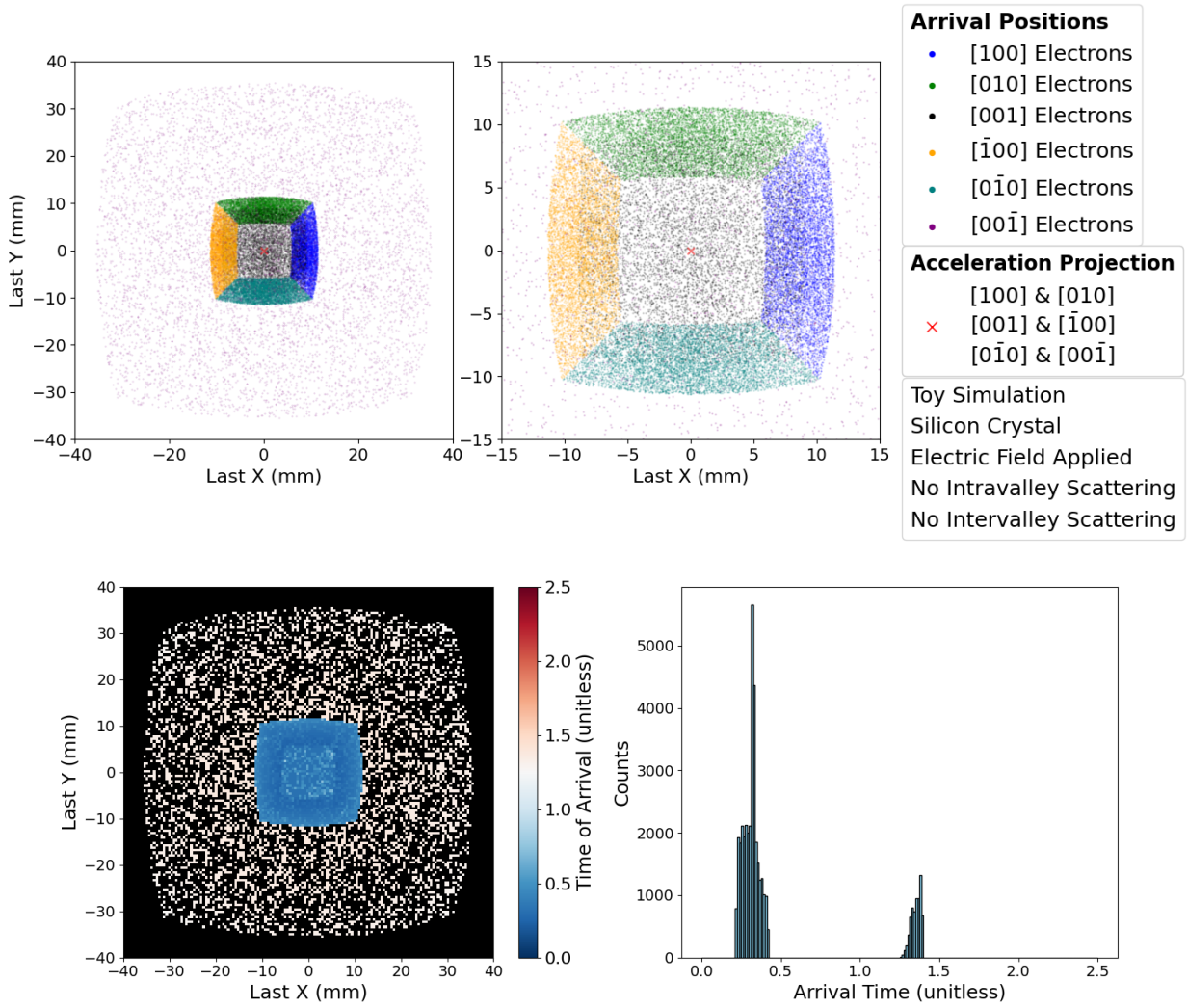

Figure 4.12: This figure shows the distribution of electron arrival positions and times on the top surface of a silicon crystal with an electric field but no scattering. We show it to illustrate the combined effects of the band structure and electric field on the electrons' arrival position patterns in silicon. Comparing to the isotropic case shown in Figure 4.4, we observe that the arrival position patterns are now square-like. Note that the top right plot is a zoomed-in version of the left plot. On the bottom right, we see that the arrival time distribution is now separated into early and late components; the later components are due to the electrons from the z valley having smaller acceleration from the bottom of Figure 4.11.

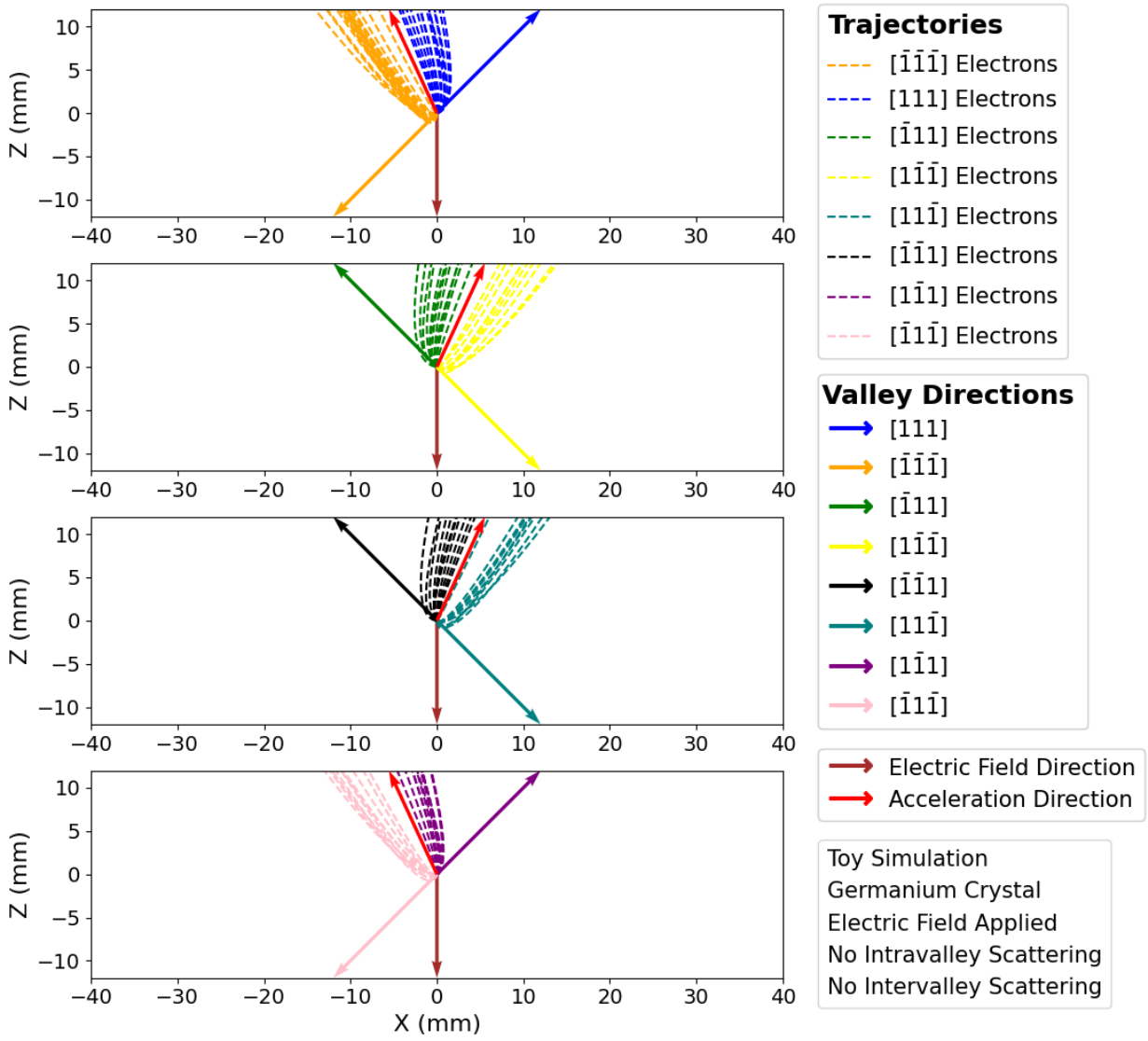

Figure 4.13: This figure shows four views of the simulated electron trajectories for the germanium configuration with an electric field but without scattering effects. We show it to highlight how changing the crystal and the angles between the electric field and the valleys can affect the electrons' trajectories. Comparing to the silicon case shown in Figure 4.11, we note that all the valleys in the $[\pm 1, \pm 1, \pm 1]$ directions have the same angle with the electric field pointing in the z direction, all the electrons share the same acceleration magnitude but in different directions. However, each valley and anti-valley pair shares the same acceleration vector.

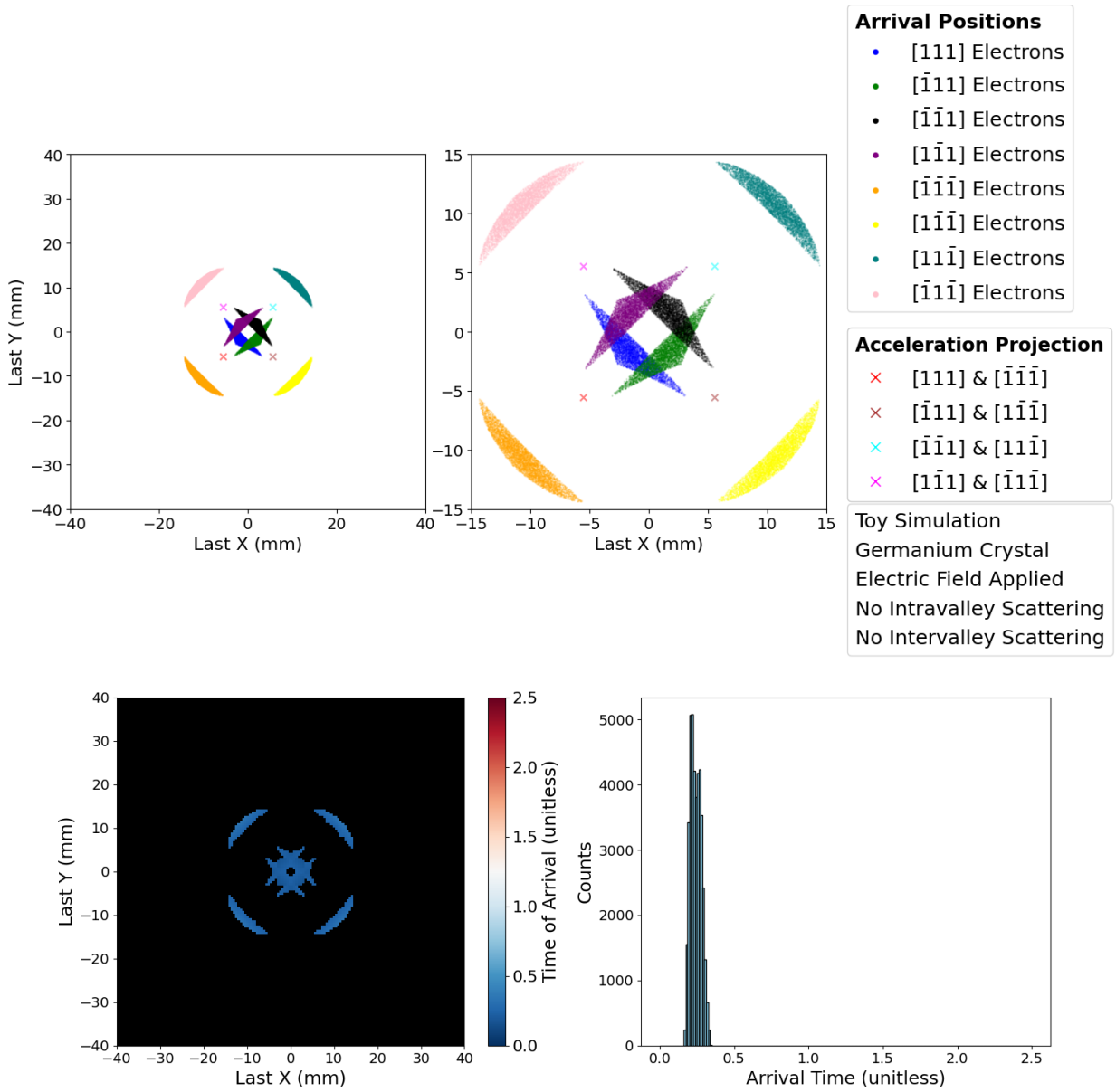

Figure 4.14: This figure shows the distribution of electron arrival positions and times on the top surface of a germanium crystal with an electric field but in the absence of scattering effects. We show it to illustrate how changing the crystal to the germanium configuration affects the electron arrival patterns. Compared to the silicon case shown in Figure 4.12, the valleys all share the same acceleration magnitude but not the same acceleration direction, forming distinct clustering in position at the top surface. We also note that each same-axis valley pair shares the same acceleration vector, forming four sets of two distributions around the four different acceleration directions (indicated with an x). On the other hand, the time of arrival for the electrons is very clustered, with very little variation, as all valleys share the same acceleration magnitude. Note that the top right-hand side plot is a zoomed-in version of the left-hand side plot.

4.4 Toy Simulation Results: Anisotropic Medium Under an External Electric Field Including Intravalley Scattering

In this section, we investigate the effect of intravalley scattering on electron transport in anisotropic crystals with an external electric field. As described in Section 3.3, while the electric field is increasing the kinetic energy, Luke scattering causes electrons to emit phonons and lose energy as they propagate. The rapid alternation of processes results in what can be considered to be an effective speed, or terminal velocity, but with frequent changes in velocity direction. The repeated energy losses also result in trajectories that increasingly align with the direction of acceleration, regardless of the initial velocity. By simulating the system with only intravalley scattering enabled, we isolate its impact on charge motion and surface arrival patterns; quantitative modeling is done in G4CMP in the next chapter. In the first paragraph, we analyze electron transport in a silicon crystal with the Si(100) and the same electric field orientation as Section 4.3. In the second paragraph, we present the corresponding results for a germanium crystal in the Ge(100) orientation.

Again, we start with silicon and describe the interplay between the electric field and scattering processes that produce the paths and arrival positions shown in Figures 4.15 and 4.16. The dominant issue is that the direction-based acceleration effectively conspires to bias the overall trajectory over multiple scatterings. As seen in Figure 4.15, electrons rapidly lose their initial kinetic energy due to repeated emission of phonons, which causes them to scatter frequently and become more strongly influenced by the electric field. As described in Section 4.3, electrons with velocity directions that have a larger angle with their valleys gain velocity faster as their acceleration magnitude is bigger, leading them to travel slightly farther between each scatter. This effect, in Si(100), causes the x and y valley electrons to be more focused on the top surface than the z valley electrons. Additionally, due to Equation 3.13, for electrons with the same velocity magnitude, those whose velocity vectors are more aligned with their valley direction must have a larger wavevector magnitude. As a result, based on the scattering rate model in Equation 2.39, they experience a higher probability of scattering (i.e., a shorter mean free path). This behavior is not limited to the initial motion; throughout the trajectory, electrons with a velocity direction closer to the valley

are more likely to scatter again. This means that, throughout the entire propagation, the electrons move further in the transverse direction than in the longitudinal direction. In the Si(100) configuration, this effect causes the x-valley electrons to spread more along the yz plane and the y-valley electrons to spread more in the xz plane. Consequently, the arrival points on the top surface form a characteristic '+' shaped distribution centered around the electric field axis, as shown in Figure 4.16. Compared to the no-scattering case, the spatial spread is reduced, and the arrival times are significantly delayed and more narrowly clustered, due to the electrons' lower average speeds because of continuous phonon emissions.

Moving to germanium, the paths and arrival positions are shown in Figures 4.17 and 4.18. As discussed in Section 4.3, in Ge(100), different valley electrons experience similar acceleration magnitudes but in different directions due to the valley orientations. However, as seen in the silicon case, with intravalley scattering enabled, electrons quickly lose their initial momentum, and their motion becomes dominated by the acceleration direction associated with the valley they are currently occupying. We note in advance that this effect holds regardless of when the valley was entered, and similarly applies in scenarios where intervalley scattering causes valley changes during transport, which will be discussed in Section 4.5. This results in electrons clustering along the direction of the acceleration vector, where the size of the clusters is dependent on the magnitude of the electric field compared to the initial energy. Additionally, as described for the Si(100) case, the electrons move further in the transverse direction than in the longitudinal direction. On the top surface, the eight distinct clusters observed without scattering, previously shown in Figure 4.14, merge into four elliptical clusters, as shown in Figure 4.18. The arrival time distribution remains tightly clustered but is delayed compared to the non-scattering case, consistent with reduced average velocities.

Having concluded our analysis of intravalley scattering effects, we next examine the impact of intervalley scattering on electron propagation. This additional mechanism alters the valley identity of electrons, affecting both their acceleration direction and overall trajectory, while leaving the total energy approximately unchanged.

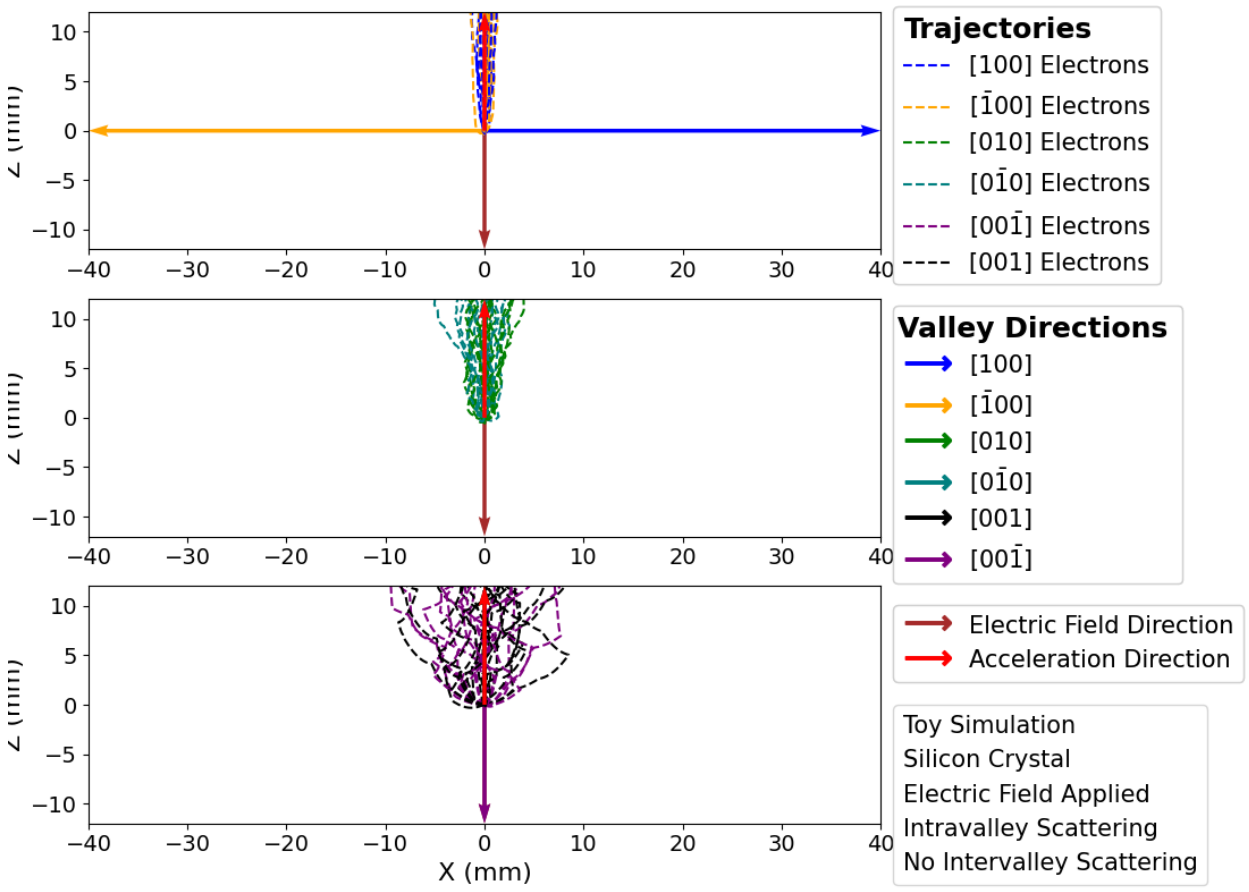

Figure 4.15: This figure shows three plots of the trajectories in an electric field for a silicon crystal with intravalley scattering, where the trajectories are separated by their initial valley (pair of directions in each plot), and the voltage is aligned with one of the valleys in the negative z direction. We show it to highlight the effect of Luke scattering on electrons paths in an anisotropic crystal. Comparing to Figure 4.11, we see a much tighter trajectory around the acceleration direction as the electrons quickly lose their initial speed and direction due to Luke scattering.

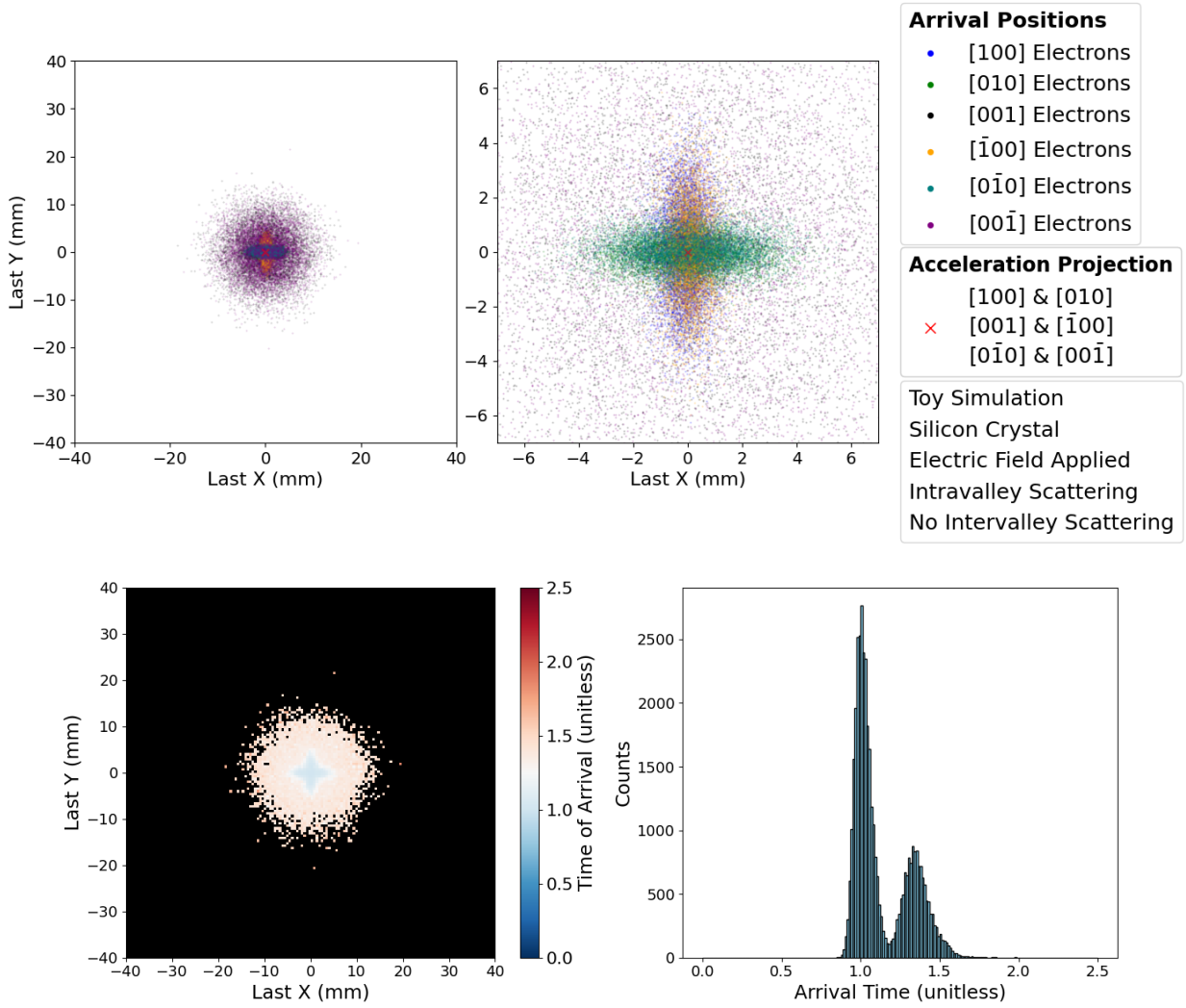

Figure 4.16: This figure shows the distribution of electron arrival positions and times on the top surface of a silicon crystal with an electric field and intravalley scattering but without intervalley scattering. We show it to illustrate the effect of the Luke scattering on the electrons' arrival position patterns in a silicon crystal. Compared to the no-Luke scattering case shown in Figure 4.12, the Luke scattering has both shrunk the arrival position and created a + sign, which is apparent in the zoomed-in distribution on the top right. We also note that there are again two different arrival clustering times, but that they have moved significantly closer to each other and to the later times due to Luke scattering keeping electrons at a lower average speed.

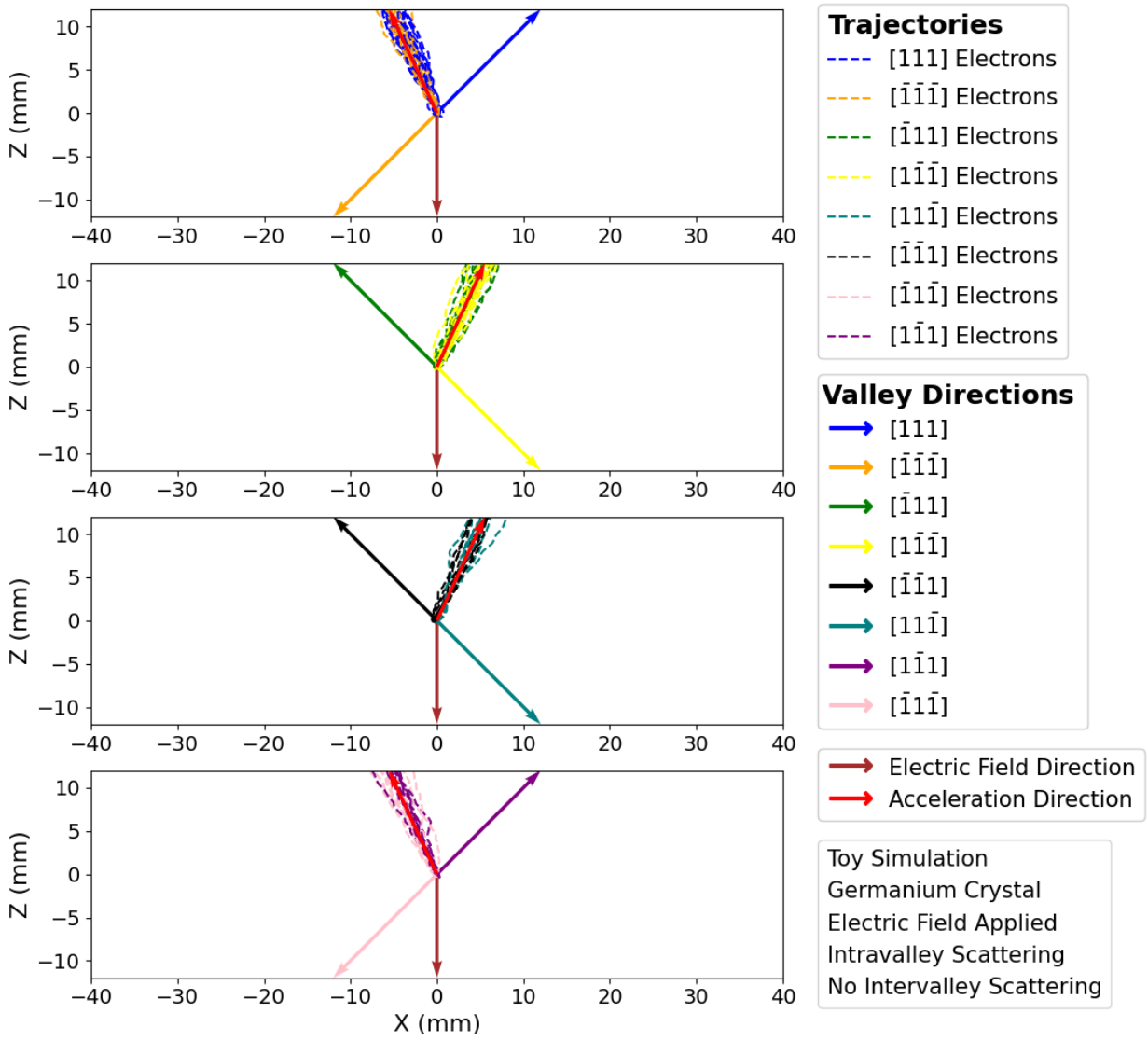

Figure 4.17: This figure shows four views of the simulated electron trajectories for the germanium configuration with an electric field and intravalley scattering but without intervalley scattering. We show it to highlight how Luke scattering affects electron tracks in germanium. Compared to the case without Luke scattering shown in Figure 4.13, we note that electrons quickly lose their initial speed and move around in the 4 different acceleration directions, which causes each valley and anti-valley pair electrons to end up in the same place at the top surface.

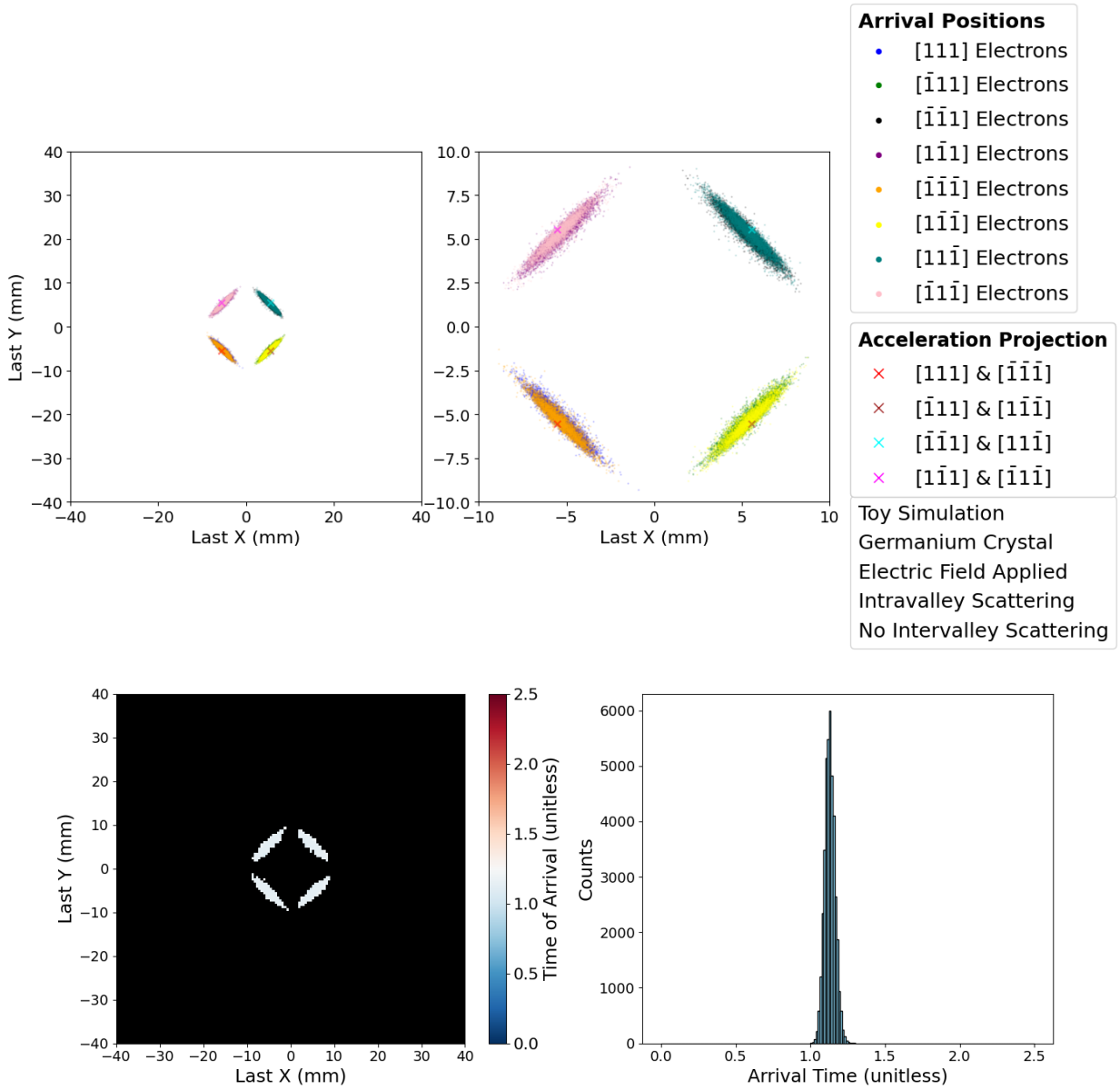

Figure 4.18: This figure shows the distribution of electron arrival positions and times on the top surface of a germanium crystal with voltage and intravalley scattering but in the absence of intervalley scattering. We show it to illustrate how Luke scattering affects the patterns on the top surface. Compared to the case without Luke scattering shown in Figure 4.14, we note that the eight distributions shown in Figure 4.14 effectively condense into four distributions as each of the valley and anti-valley distributions gets mixed up together; again, the top right plot is a zoomed-in version of the left plot. We also note that the distance of each distribution is velocity dependent; a smaller voltage would make the ellipses smaller and closer to the middle. We also point out that while the time of arrival distribution again only has small variation, it is shifted to later times due to the scattering lowering the average speed.

4.5 Toy Simulation Results: Anisotropic Medium Under an External Electric Field Including Intervalley Scattering

In this section, we isolate the impact of intervalley scattering on electron transport in anisotropic crystals with an external electric field. As described in Section 3.5, we model intervalley scattering so that it changes the electron's valley without changing its energy, but does so on an infrequent basis. While the direction of the wavevector with respect to the valley is preserved in our simplified toy model, the transition to a new valley alters the mass tensor and, consequently, the electron's acceleration. For pedagogical reasons, we start by considering the case where intravalley scattering is disabled, so the electrons retain their initial energy and velocity magnitude throughout their trajectories. While not physical, this configuration can give us an intuition about how intervalley scattering can mix the clusters in the arrival position distributions together. In the first paragraph, we examine the behavior of electrons in a silicon crystal under the influence of an electric field and intervalley scattering. In the second paragraph, we present the corresponding results for germanium.

The behavior of electrons in a silicon crystal under the influence of an electric field and intervalley scattering is shown in Figure 4.19. electrons begin their motion with deterministic valley-dependent acceleration, similar to the behavior described in Section 4.3. However, after undergoing one or more intervalley scattering events, electrons are reassigned to a new valley, potentially reassigning electrons from x or y valleys to z valleys or vice versa, thereby changing the magnitude of the electron's acceleration. Even though no energy is lost, the direction and magnitude of the acceleration are changed, resulting in nontrivial deviations from the initial paths. This leads to a visible mixing of trajectories among different valley groups. On the top surface, this effect slightly blurs the previously distinct square-like arrival pattern seen in the no-scattering case, as shown in Figure 4.20. The arrival time distribution also becomes smeared between the two peaks associated with different valley accelerations, due to the valley transitions mid-flight.

For the corresponding results for germanium, we note that we used a higher voltage to produce this sample compared to Section 4.3, to show the effect of intervalley scattering more clearly. As

shown in Figure 4.21, electrons begin in distinct valley states with unique acceleration directions determined by the Ge(100) valley configuration. After each intervalley scattering, as our intervalley scattering model does not change the energy of the electrons, they maintain their speed but shift to a different valley, resulting in a change in the direction of acceleration. On the top surface, this results in arrival points between the eight well-defined clusters observed in the non-scattering case, as shown in Figure 4.22; electrons that scatter only once appear between two clusters, connecting those clusters together, while electrons that scatter multiple times end up somewhere between those connections. The arrival time distribution remains tightly clustered because all electrons gain the same kinetic energy.

Having concluded our examination of intervalley scattering in isolation, we next enable both intravalley and intervalley scattering in the simulation. This final configuration captures the full set of dominant effects and provides a benchmark for interpreting the results of our more complex full detector simulations.

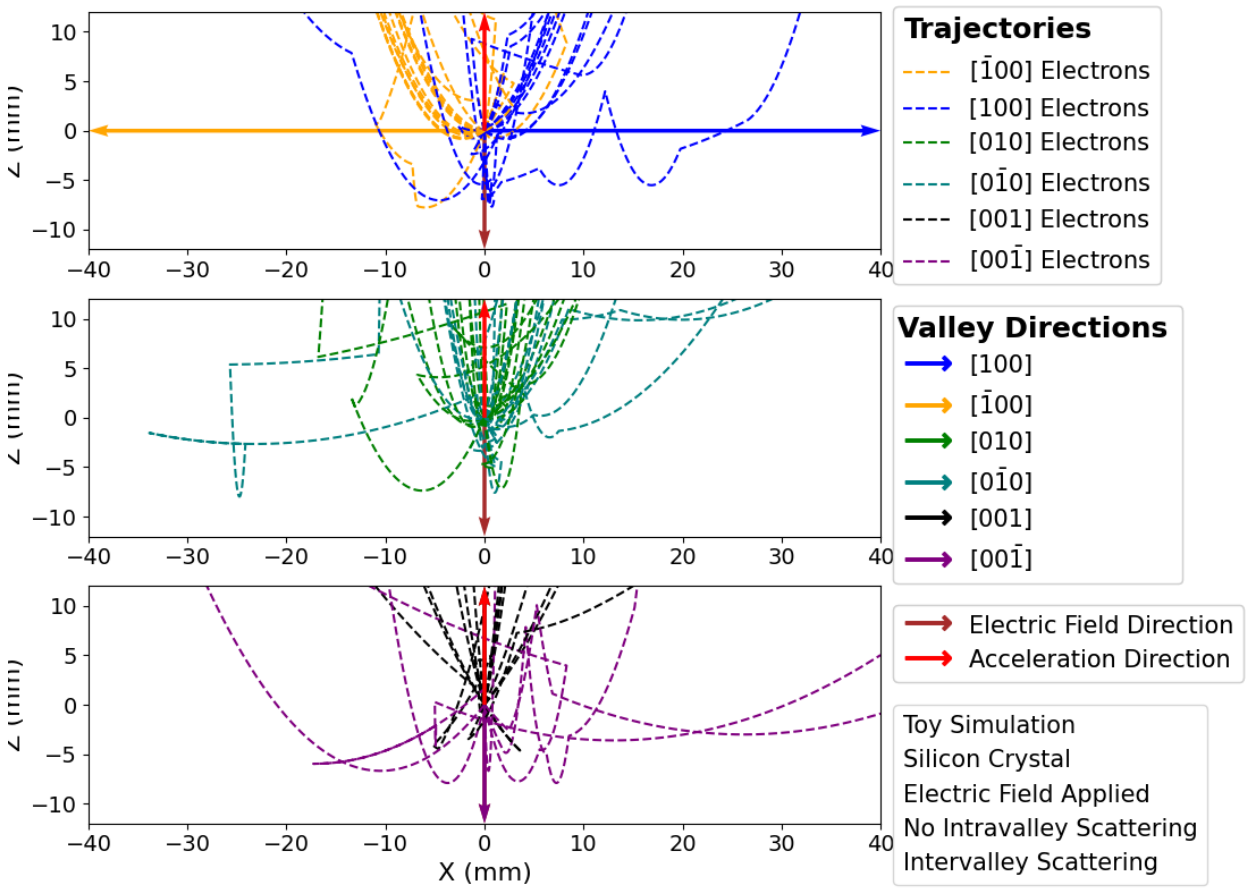

Figure 4.19: This figure shows three plots of the trajectories in a silicon crystal under a voltage with intervalley scattering but without intravalley scattering. We show it to highlight the effect of just changing the valley without emitting a phonon on electrons' paths in an anisotropic crystal. Comparing to the case without scattering effects shown in Figure 4.11, we see a few outlier tracks that are separated from the rest, which is because of two effects: intervalley scattering changes the direction of the momentum, and different valleys have different acceleration magnitudes.

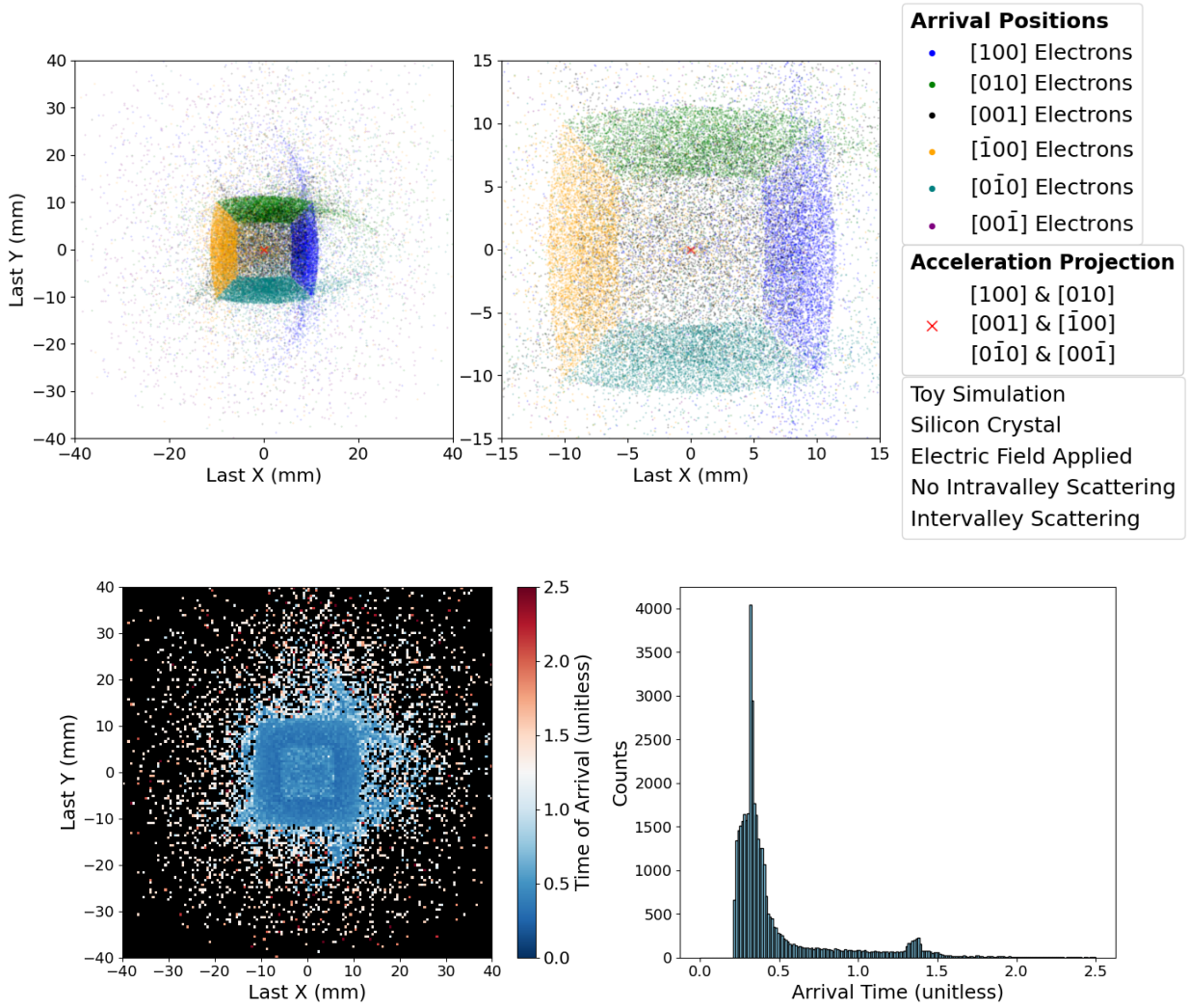

Figure 4.20: This figure shows the distribution of electron arrival positions and times on the top surface of a silicon crystal under a voltage with intervalley scattering but without intravalley scattering. We show it to illustrate how just changing the valley without emitting a phonon alters the electron distribution at the top surface in our silicon configuration. Compared to Figure 4.12, intervalley scattering slightly mixes the different valley clusters together. We note that there are arc-like patterns in the plots, which are due to the non-physical simplifying assumptions in the toy simulation to illustrate the case of intervalley scattering without phonon emission. Specifically, the electron's angle in the new valley is taken to be the same as the previous valley, which causes a slight asymmetry. In the full simulation, where phonons are emitted when scattered, we will not observe this effect. We also note that the arrival times still have the same two peaks as the no-scattering case, but there are now events in between due to some electrons changing valleys.

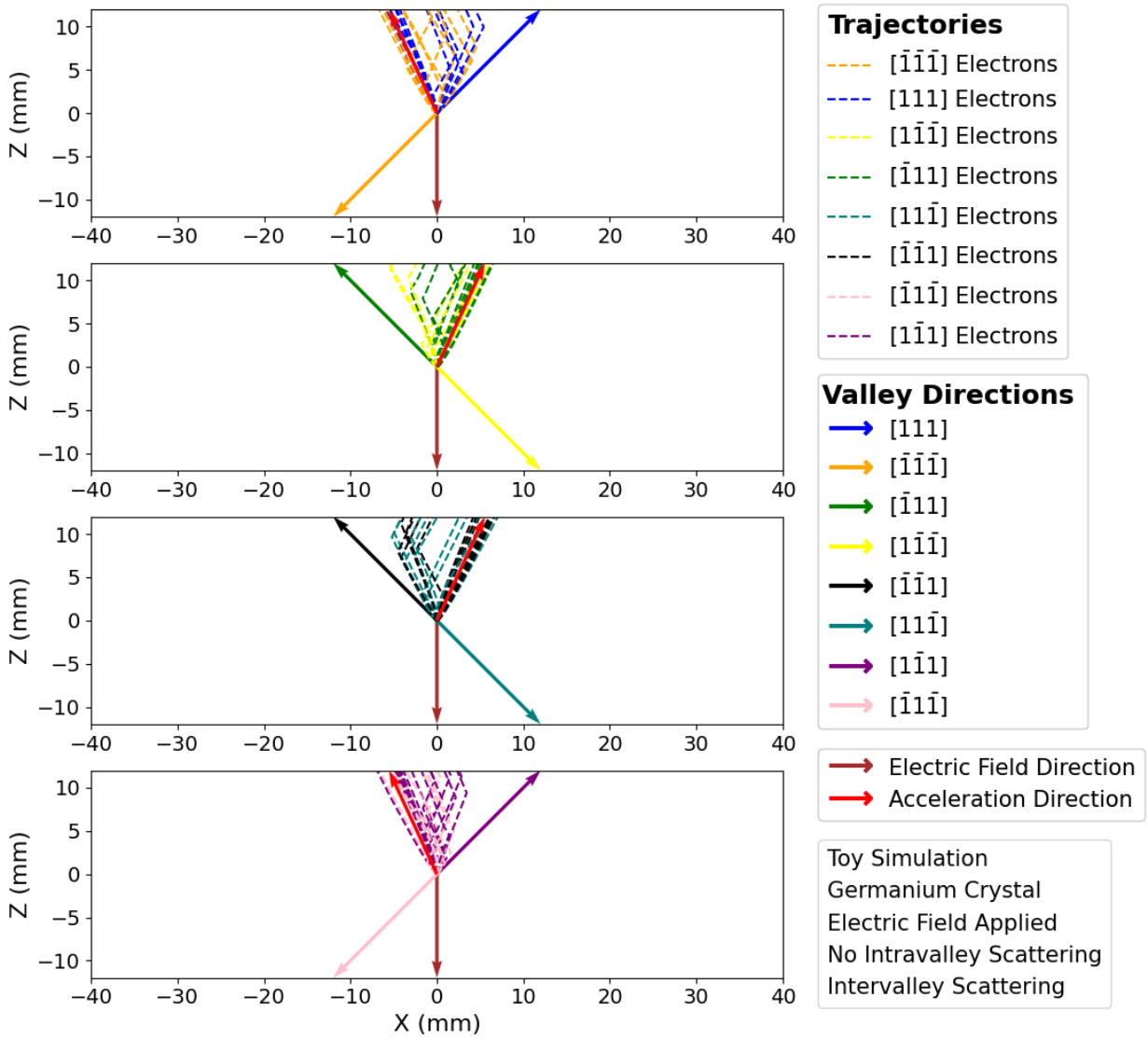

Figure 4.21: This figure shows three plots of the trajectories in a silicon crystal under a voltage with intervalley scattering but without intravalley scattering. We show it to highlight the effect of just changing the valley without emitting a phonon on electrons' paths in our germanium configuration. Compared to Figure 4.13, in each plot, we see some electrons get separated from the rest as intervalley scatterings change their valleys to a different axis, which changes their acceleration direction.

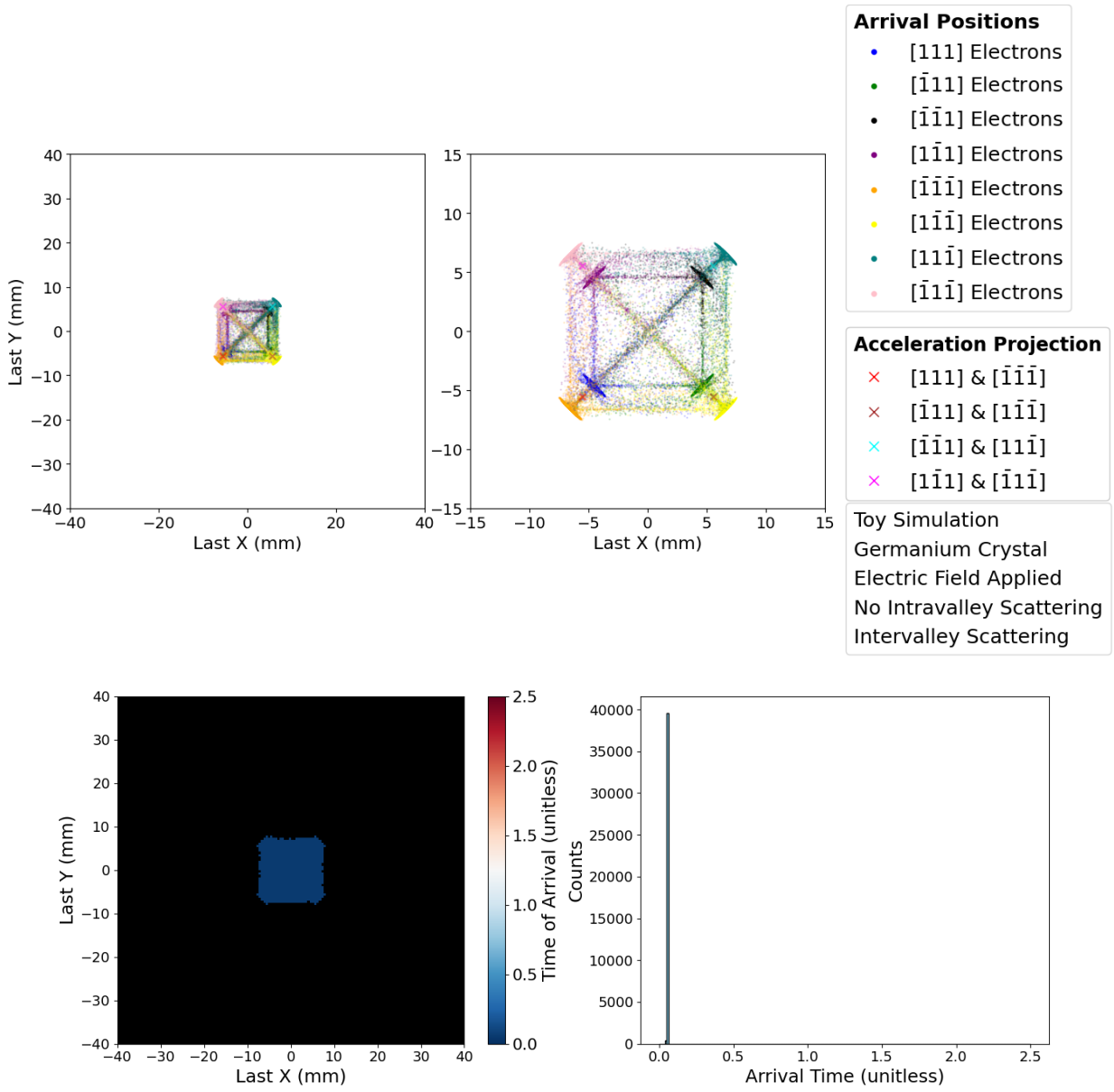

Figure 4.22: This figure shows the distribution of electron arrival positions and times on the top surface of a germanium crystal under a voltage with intervalley scattering but without intravalley scattering. We show it to illustrate how just changing the valley without emitting a phonon alters the electron distribution at the top surface. Compared to Figure 4.14, intervalley scattering causes electrons to change valleys and end up somewhere between the eight clusters in the no-intervalley case, depending on how many times they scatter before they reach the top surface. In this case, the time of arrival distribution is incredibly tight and is much lower due to the unphysical effect of not losing energy due to scattering.

4.6 Toy Simulation Results: Anisotropic Medium With All Dominant Effects Included

In this section, we present the results of the toy simulation with all dominant effects included. While each effect has been studied in isolation in the previous sections, combining them allows us to observe the interplay between scattering-induced momentum and energy changes, directionally dependent acceleration, and valley mixing. As a reminder, the values of parameters used in the toy simulation were not chosen to quantitatively mirror real crystal values, so all results should be taken with a grain of salt. For example, the intravalley scattering rate was selected to be small but nonzero, with no attempt to take into account the actual ratio of intervalley to intravalley scattering rates, like shown in Figure 2.10. As usual, we start with silicon and then move to germanium.

The results for electron transport in silicon with all effects included are shown in Figures 4.23 and 4.24. Electrons begin with randomly assigned initial directions, and, because the mean free path for intravalley scattering is smaller than intervalley scattering, quickly undergo intravalley scattering events that emit some of their energy as phonons and reorient their velocity vectors. As shown previously in Section 4.4, the emission of phonons causes electrons to lose energy rapidly, making their motion increasingly governed by the acceleration. Simultaneously, intervalley scattering, as explored in Section 4.5, allows some electrons to transition between valleys, thereby changing their effective mass and acceleration magnitude mid-flight. These two processes work together: intravalley scattering drives electrons to align with acceleration directions, while intervalley scattering redistributes electrons between valleys. The resulting arrival pattern on the top surface resembles a distorted version of the plus-shaped structure seen in the intravalley-only case (Figure 4.16), now blurred by valley mixing caused by the intervalley scatterings. The arrival time distribution continues to exhibit two dominant peaks corresponding to distinct valley groups, but the separation between them is reduced due to transitions across valley types caused by intervalley scattering. While quantitative results will be shown in the next chapter, for now, we note that the ratio of the peaks depends on the ratio of the intervalley and intravalley scattering rates.

The corresponding simulation results for electron transport in germanium with all dominant effects included, shown in Figures 4.25 and 4.26, are equally interesting. As in the silicon case, the

combination of intravalley and intervalley scattering fundamentally shapes the electrons' behavior. As in the silicon case, intravalley scattering rapidly emits the initial kinetic energy and redirects electrons toward valley-specific acceleration directions, effectively locking their motion into one of the four dominant accelerations shown in Section 4.4. At the same time, intervalley scattering causes electrons to transition between valley states, each associated with a distinct acceleration direction, resulting in branching or outlier trajectories, as described in Section 4.5. We again note the small number of tracks with outliers caused by the intervalley scatterings and that the arrival position distribution exhibits the four dominant elliptical clusters from same-axis valley pairs, like the intravalley-only case, but with some electrons ending up somewhere between the clusters due to intervalley scatterings. This result qualitatively matches the experimental results shown in Figure 1.13, whereas, again, the true scattering rates are needed for quantitative comparison. The arrival time distribution remains tightly clustered due to the energy-stabilizing effect of frequent phonon emissions.

Having completed our study of all dominant effects in isolation and in combination in our toy simulation, we next turn to the full simulation implementation described in Chapter 5, where these physical processes are applied in realistic detector geometries within G4CMP, and we utilize quantitative estimates of scattering parameters to more accurately model scattering rates. We can use the results from this chapter as a qualitative benchmark for comparisons with the G4CMP results.

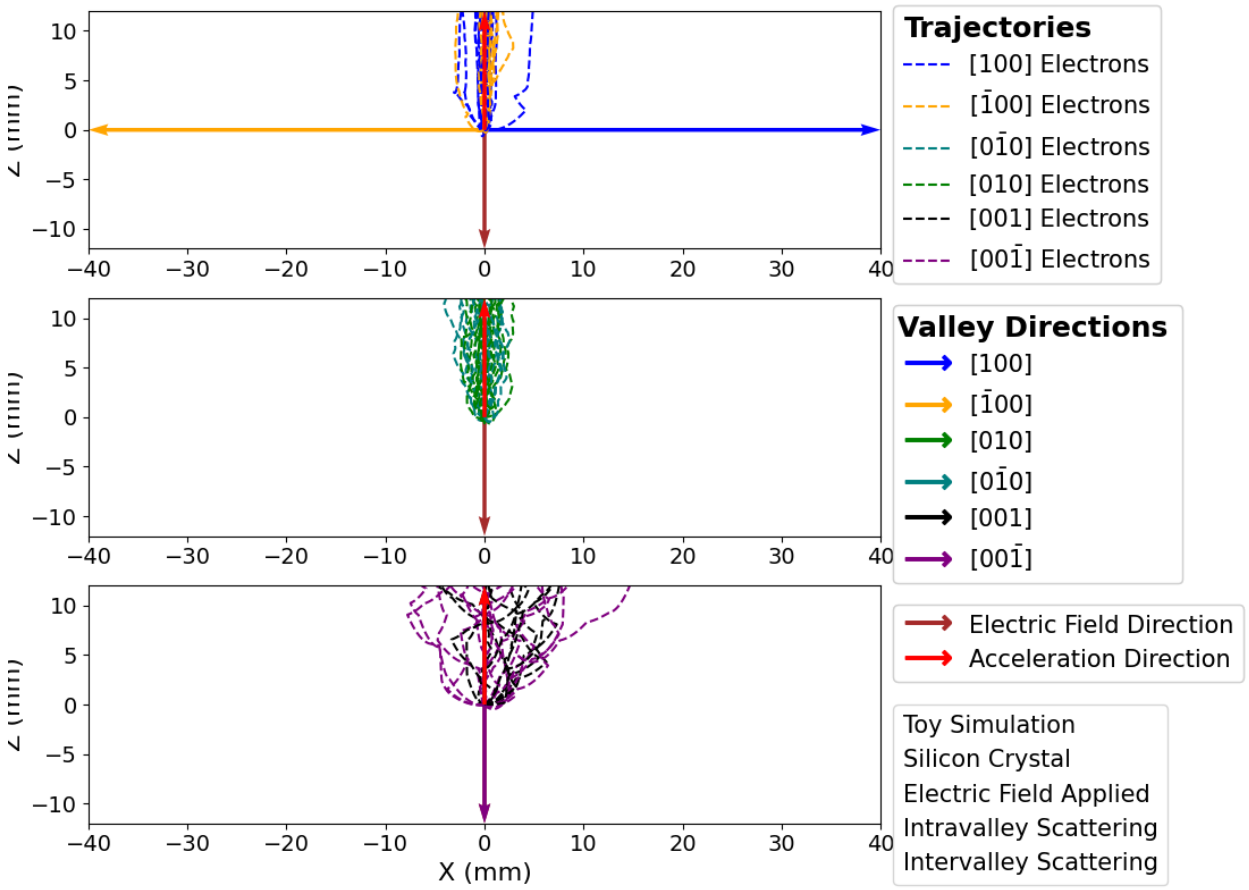

Figure 4.23: This figure shows three plots of the trajectories in a silicon crystal under a voltage with both scattering effects. We show it to demonstrate how electrons move in silicon with all the dominant effects included. Compared to the Figures 4.15 and 4.19, all electrons have the same direction and their trajectories are dominated by the electric field as intravalley scattering causes electrons to lose their initial energy quickly and move with a velocity close to a terminal speed while intervalley scattering causes some electrons to change their valley and scatter, and accelerate with a different magnitude.

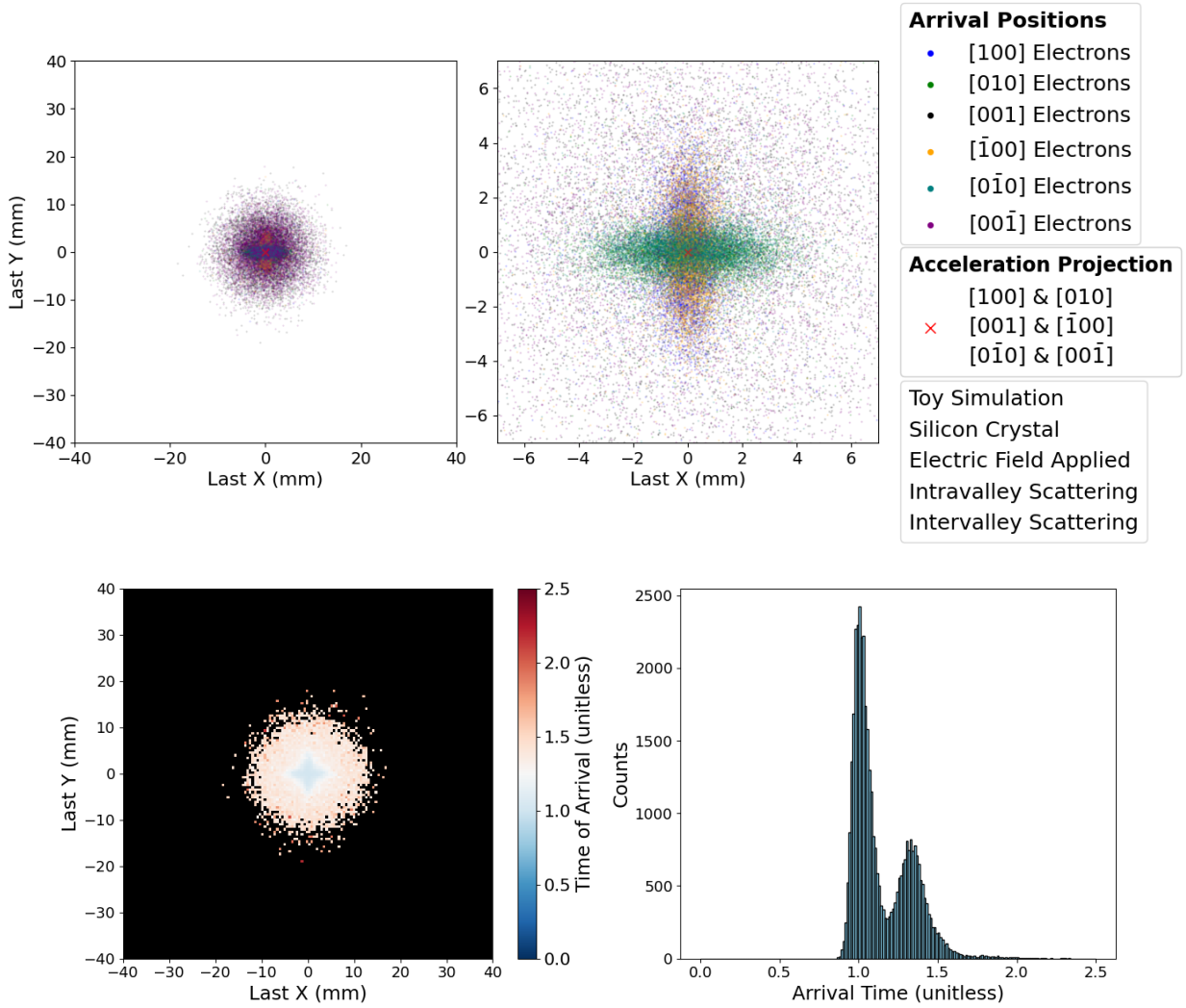

Figure 4.24: This figure shows the distribution of electron arrival positions and times on the top surface of a silicon crystal under a voltage with both scattering effects. We show it to set our expectation for the patterns we see in a silicon crystal with all the dominant effects included in the full simulation. Compared to Figures 4.16 and 4.20, intervalley causes electrons to change valleys, slightly mixing up the shapes that we saw in the intravalley-only case. Note that even with all effects included, we expect a double-peak arrival time.

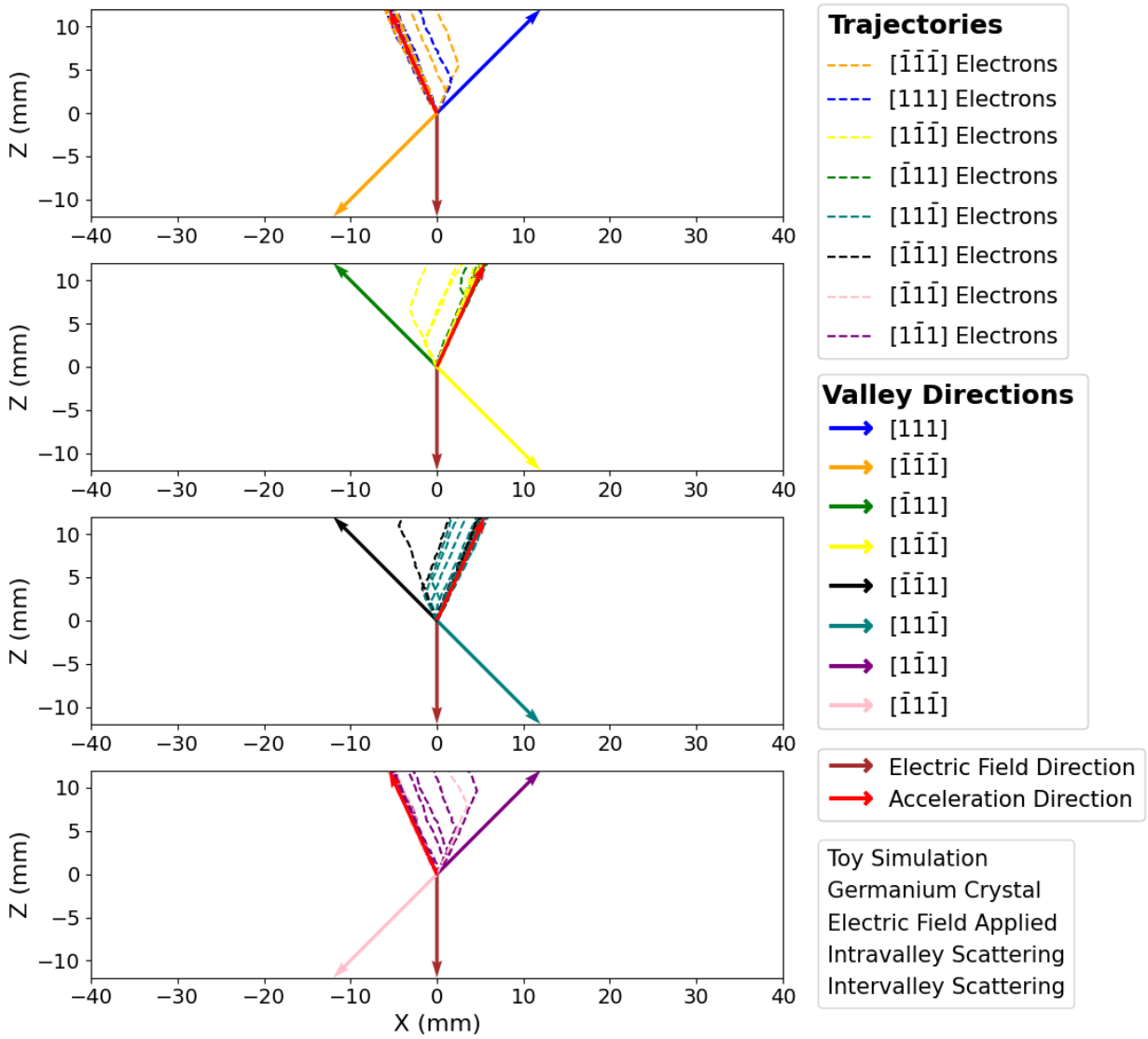

Figure 4.25: This figure shows four plots of the trajectories in a germanium crystal under a voltage with both scattering effects. We show it to demonstrate how electrons move in our germanium configuration with all the dominant effects included. Compared to the Figures 4.17 and 4.21, while all electrons have the same acceleration magnitude, and their movement is dominated by the electric field due to intravalley scattering, a fraction of the electrons scatter and accelerate in a different direction due to intervalley scattering changing their valleys.

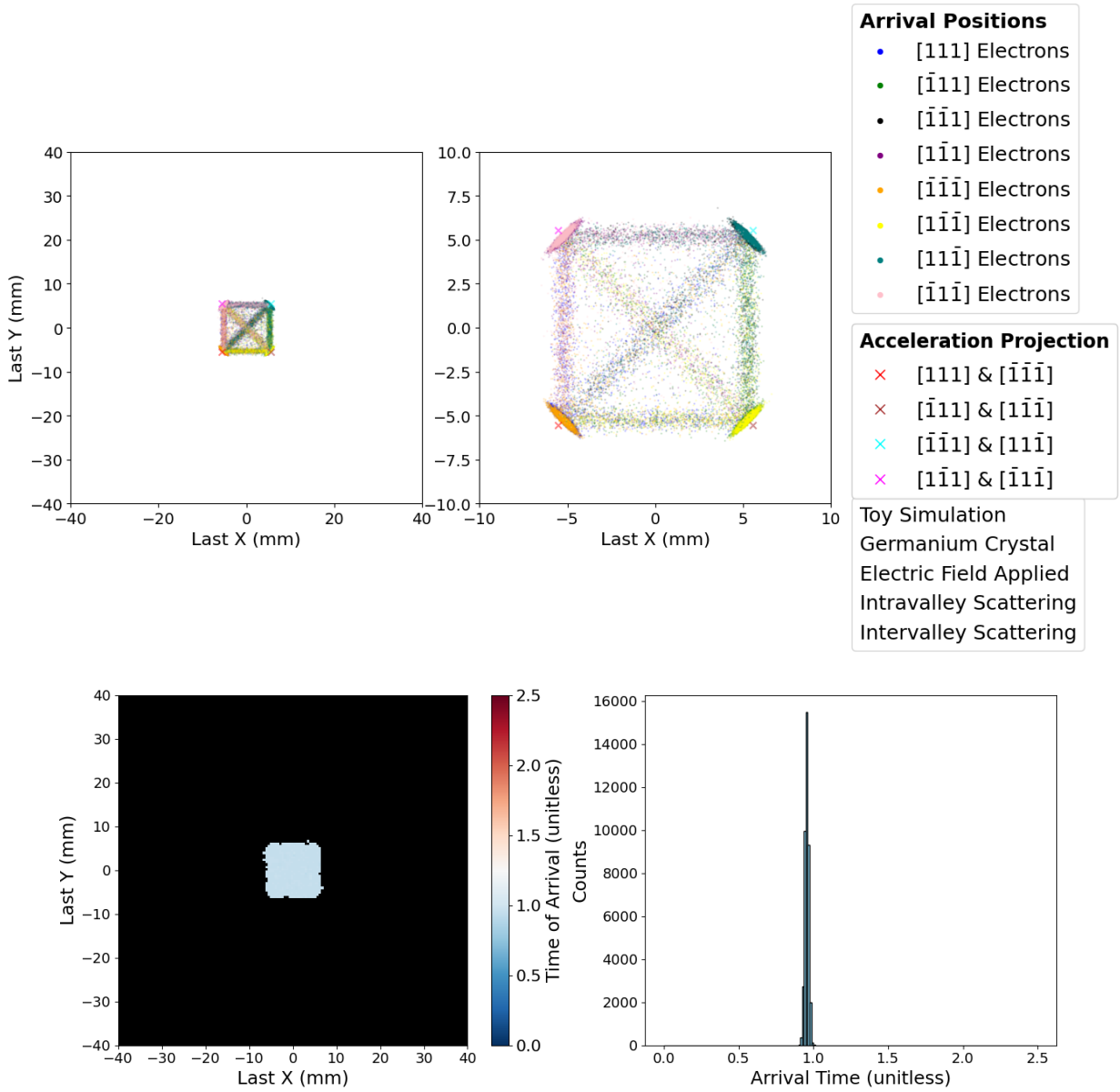

Figure 4.26: This figure shows the distribution of electron arrival positions and times on the top surface of a germanium crystal under a voltage with both scattering effects. We show it to set our expectation for the patterns we see in a germanium crystal with all the dominant effects included in the full simulation. Compared to Figures 4.18 and 4.22, intravalley scattering causes the same-axis valleys electrons to end up in the same clusters, effectively forming four clusters instead of eight, while the intervalley scattering causes electrons to end up between the four clusters. We continue to see the single, narrow time of arrival distribution.

5. RESULTS USING THE FULL GEANT4 CONDENSED MATTER PHYSICS SIMULATION AND COMPARISONS WITH EXPECTATIONS AND EXPERIMENTAL DATA

In this chapter, we present the results from realistic simulations of electron transport in semiconductors using the Geant4 Condensed Matter Physics (G4CMP) framework, focusing on the arrival distribution of electrons at the surface. While the toy simulations in Chapter 4 helped isolate and visualize individual transport effects in simplified geometries, the full complexity of real experimental setups necessitates a transition from qualitative to quantitative results, achieved through a fully integrated Monte Carlo approach. This includes effects from realistic detector geometries, numeric values of the effective masses, applied electric fields, and measured scattering rates for silicon and germanium. By reproducing both the SuperCDMS detectors and test stand setups, simulations enable direct comparisons with both our expectations and the toy model, as well as real experimental data.

The set of simulated configurations mirrors those in Chapter 4, allowing for comparisons between the idealized toy modeling and the full simulations. Table 5.1, following the order of the previous chapter, lists the samples made. The size, shape, and orientation of each crystal are detailed in Table 5.2, and the scattering parameters and models are given in Table 5.3. All other parameters are taken as the default values in G4CMP[1]. We note that while the bandgap values from Equations 2.28 and 2.29 are temperature dependent, we use the values for a temperature of $50\ \mathrm{mK}$. All other parameters and modeling are taken to be constant which is a good approximation for temperatures well less than $1\ \mathrm{K}$. To focus on the charge propagation, we skip the energy deposition and electron-hole pair creation process mentioned in Section 3.5, and again only consider electrons emitted from the detector center and uniformly distributed in all directions, but with a fixed energy of $1\ \mathrm{eV}$.

In Section 5.1, we start with an isotropic medium, both with and without voltage and scatter-

[1]Software version number V9.9.1.

Table 5.1: In this table, we list the datasets simulated using G4CMP, the configurations of each, and identify the figures that use them. We show it to list the set of configuration combinations that are used to help illustrate the effect that the crystal band structure, voltage, intravalley scattering, and intervalley scattering have on electrons as they move in a crystal. Note that all samples are generated with 1 eV monochromatic energy electrons emanating from the point $x = y = z = 0$ (center of the detector) and distributed uniformly in all directions. The details about the detectors and their crystal orientations used in these samples are included in Table 5.2.

Simulated Datasets					
#	Crystal Type	Voltage (Volts) in $-z$ Direction	Intravalley Scattering	Intervalley Scattering	Top Surface Arrival Distribution Figures
1	Isotropic	Disabled	Disabled	Disabled	Figure 5.1
2	Isotropic	1 and 30	Disabled	Disabled	Figure 5.2
3	Isotropic	1 and 30	Enabled	Disabled	Figure 5.3
4	Isotropic	1 and 30	Enabled	Enabled	Figure 5.4
5	Si(100)	Disabled	Disabled	Disabled	Figure 5.5
6	Ge(100)	Disabled	Disabled	Disabled	Figure 5.6
7	Si(100)	1 and 30	Disabled	Disabled	Figure 5.7
8	Ge(100)	1 and 30	Disabled	Disabled	Figure 5.8
9	Si(100)	1 and 30	Enabled	Disabled	Figure 5.9
10	Ge(100)	1 and 30	Enabled	Disabled	Figure 5.10
11	Si(100)	1 and 30	Enabled	Enabled	Figure 5.11
12	Ge(100)	1 and 30	Enabled	Enabled	Figure 5.12
13	Si(111)	20, 40, 75, and 100	Enabled	Enabled	Figure 5.14

ings, and compare the arrival distributions to the toy model results. In Section 5.2, we switch to silicon and germanium crystals with and without voltage and scatterings. In Section 5.3, we compare the simulation outputs to published experimental results. We note before beginning that only the arrival position results are presented, as there is limited value in presenting another version of the trajectories and arrival times.

Table 5.2: In this table, we list the size, shape, and orientations of the crystals used in the G4CMP simulations. We use the same configurations used by the SuperCDMS experiment, shown in Figures 1.6 and 1.7 [65, 66]. For simplicity, the isotropic detector is chosen to have the same geometry as the silicon detector. We also note that the name column is what we later refer to as each detector type. However, sometimes we refer to them by their crystal type, as both are unique.

G4CMP Detectors Information			
Crystal Type	Shape	Size	Valley Orientations
Isotropic	Rectangular	$10 \times 10 \times 4\ \mathrm{mm}^3$	None
Si(100) (HVeV)	Rectangular	$10 \times 10 \times 4\ \mathrm{mm}^3$	$[\pm 1, 0, 0]$, $[0, \pm 1, 0]$, $[0, 0, \pm 1]$
Ge(100) (iZIP)	Cylinder	Diameter: $76\ \mathrm{mm}$ Thickness: $25\ \mathrm{mm}$	$[\pm 1, \pm 1, \pm 1]$
Si(111)	Rectangular	$10 \times 10 \times 4\ \mathrm{mm}^3$	$\pm[-1, 0, 1]$, $\pm[1, \sqrt{2}, 1]$, $\pm[1, -\sqrt{2}, 1]$

Table 5.3: In this table, we list the parameters and values used in G4CMP for intravalley and intervalley scattering processes. The intravalley scattering rates are calculated using Equation 2.41 with the characteristic length values given here. The intervalley scattering rates are calculated using Equations 2.44 and 2.45 for germanium and silicon, respectively, with the coefficients given. We note that the intravalley characteristic length is calculated using the electron conductivity mass, where m_e is the mass of the electron. Finally, it's important to note that the parameters used in the simulation of the isotropic case are not based on any real crystal; rather, they have been set to have the same values as the silicon case, with the difference that there are no valleys.

G4CMP Scattering Parameters			
	Isotropic	Silicon	Germanium
Electron Conductivity Mass	$0.258\ m_e$	$0.258\ m_e$ [52]	$0.126\ m_e$ [52]
Hole Effective Mass	$0.5\ m_e$	$0.5\ m_e$ [52]	$0.35\ m_e$ [52]
Electron Intravalley Characteristic Length l_0	$16.5\ \mu\mathrm{m}$	$16.5\ \mu\mathrm{m}$ [52]	$257\ \mu\mathrm{m}$ [52]
Hole Intravalley Characteristic Length l_0	$7.5\ \mu\mathrm{m}$	$7.5\ \mu\mathrm{m}$ [52]	$108\ \mu\mathrm{m}$ [52]
Intervalley Rate Coefficients and Exponents	-	$b = 1.5\ \mathrm{MHz}$ $m = 1.5\ \mathrm{Hz}$ $\alpha_{\text{linear}} = 4$	$A = 6.72e^{-2}\ \mathrm{Hz}$ $E_0 = 217\ \frac{\mathrm{V}}{\mathrm{m}}$ $\alpha_{\text{quadratic}} = 3.24$

5.1 Results For Isotropic Medium

In this section, we present the G4CMP simulation results for an isotropic crystal. This configuration serves as our model for the propagation of holes. Because the effective mass is isotropic, at each point, the acceleration, energy loss, and scattering behavior are uniform in all directions, and the arrival distributions can be directly compared, albeit qualitatively, to the toy simulation results described in Section 4.1. In the first paragraph, we describe the G4CMP simulation of an isotropic crystal without electric fields or scattering. In the second paragraph, we show how an applied electric field modifies the arrival distribution results in the isotropic crystal for two different voltages. In the third paragraph, we present the impact of adding intravalley scattering to the isotropic crystal under an electric field. In the fourth paragraph, for pedagogical reasons, we investigate the effect of enabling intervalley scattering in the isotropic case, despite the fact that such scattering is physically unmotivated in a medium without distinct valleys.

As the simplest case, we describe the G4CMP simulation of an isotropic crystal without electric fields or scattering. As shown in Figure 5.1, because there is no field or scattering, the resulting arrival point distribution exhibits perfect radial symmetry and matches the toy simulation result shown in Figure 4.2. This confirms that the full simulation preserves the fundamental behavior expected from the isotropic model described in Section 3.1.

The electron arrival distribution significantly changes when the electric field is applied. Here we consider two different voltage and in each, the electric field accelerates all the electrons in the $+z$ direction with the same magnitude of $a = \frac{F}{m^*}$ as described in Section 3.2, causing them to move on a smooth curved path with the arrival distribution shown in Figure 5.2. Additionally, we observe that at lower voltage, not all electrons reach the top, while at higher voltage, all electrons cluster closer to the center. This is consistent with the expectations from the toy simulation in Figure 4.4.

Next, we present the impact of adding intravalley scattering within the isotropic crystal under an electric field. The simulation results in Figure 5.3 show that Luke scattering causes the electrons to rapidly emit phonons and lose energy, as described in Section 3.3, resulting in a smaller arrival

distribution, even at lower voltages. We also observe that increasing the voltage has minimal impact on the arrival distribution size, since any energy gained is quickly lost to phonon emission. These results match the toy simulation in Figure 4.6.

For pedagogical reasons, we investigate the effect of enabling intervalley scattering in the isotropic case, despite the fact that such scattering is physically unmotivated in a medium without distinct valleys. As shown in Figure 5.4, the arrival distributions remain identical to those in the previous case without intervalley scattering shown in Figure 5.3. This confirms that, in isotropic materials where all directions are equivalent and no valley-dependent acceleration exists, intervalley scattering has no measurable impact on the electron transport.

Having completed our presentation of the arrival distribution results in an isotropic medium using G4CMP, we confirm that the simulation results align with both our toy model expectations from Chapter 4 and the theoretical modeling developed in Chapters 2 and 3. We now move to the results in silicon and germanium, where anisotropic band structures, crystal orientations, and valley-dependent dynamics lead to different results.

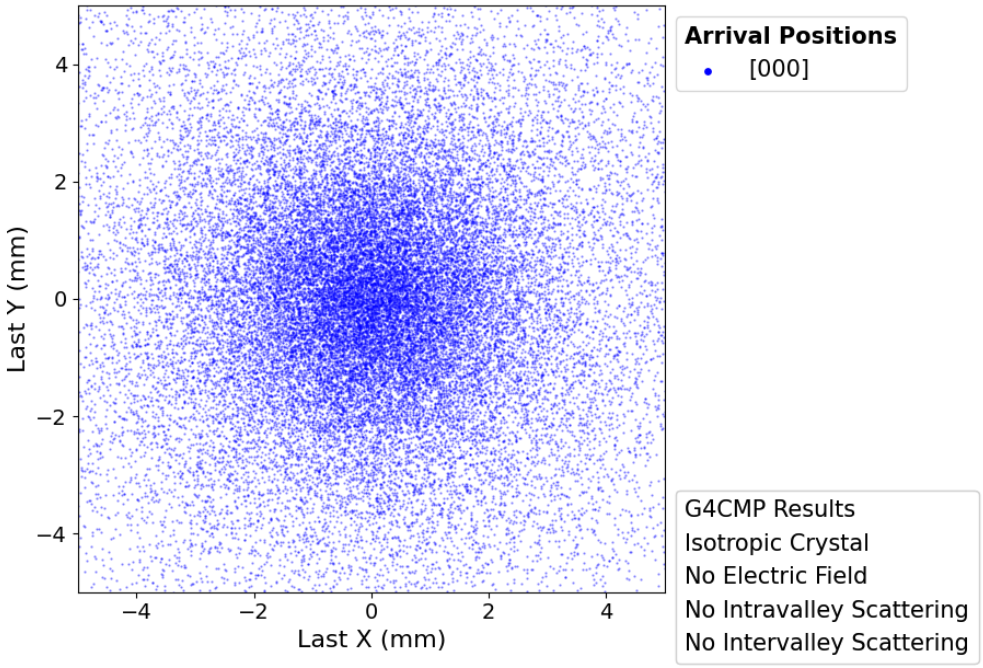

Figure 5.1: This figure shows the density of arrival points at the top surface of a hypothetical square isotropic material with a monoenergetic set of electrons emanating from the center using the full G4CMP simulation. We show it because this simulation is the simplest case that helps verify that the full simulation results qualitatively match our expectations in Figure 4.2. Note that electrons that do not reach the top surface are not included here.

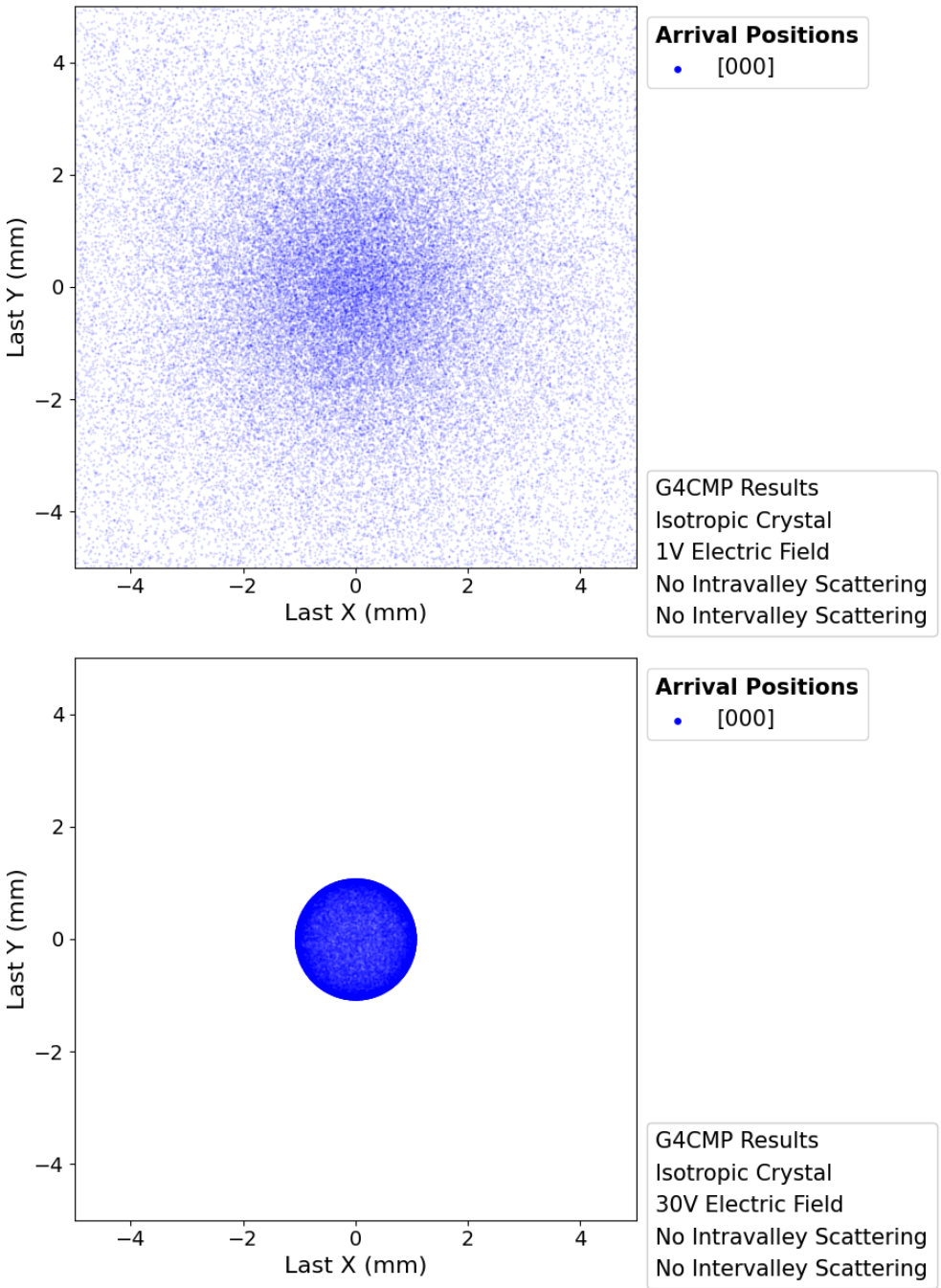

Figure 5.2: This figure shows the G4CMP results for the distribution of electron arrival positions on the top surface of a square isotropic crystal with two different voltages. We show it to illustrate how the full simulation results change when we add different voltages without any crystal effects included. Compared to Figure 4.4, we note that the full simulation results qualitatively match our expectations. We also note that at low voltages, not all electrons hit the top surface, but with the high voltage value choice, the electrons cluster into a small area on the top surface.

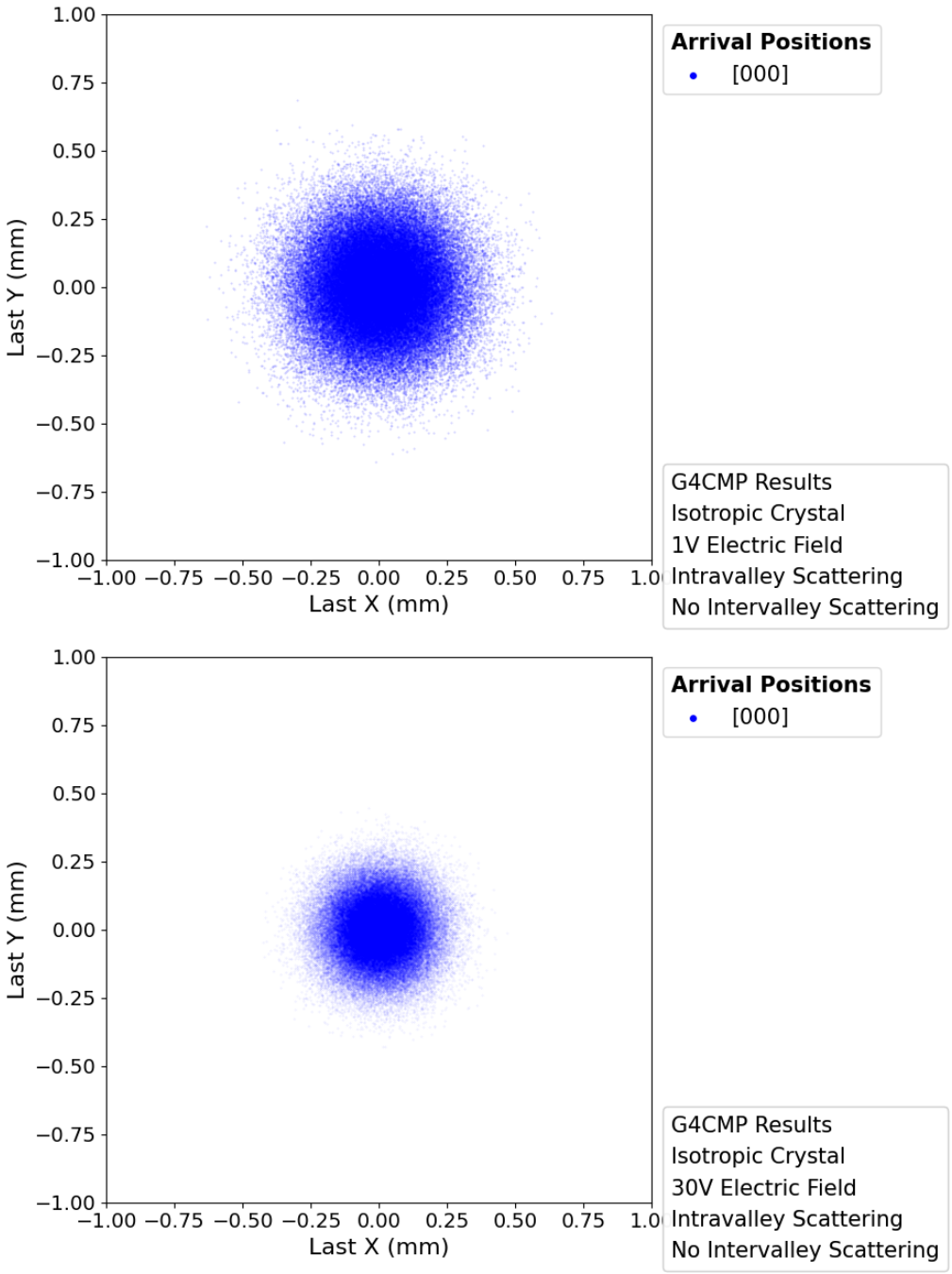

Figure 5.3: This figure shows the G4CMP results for the distribution of electron arrival positions on the top surface of an isotropic crystal for two different voltages with intravalley scattering, but without intravalley scattering. We show it to illustrate how the Luke scattering affects the results, independent of anisotropic crystal complications. Compared to the top part of Figure 5.2, we note that all electrons now reach the top surface and have results comparable to the high voltage case. We also note that increasing the voltage has little effect on reducing the cluster size as Luke scattering causes electrons to lose their initial energy rapidly and maintain a relatively constant average speed as the higher energy gain rate leads to a higher frequency of Luke scattering events. These results match the expectations shown in Figure 4.6.

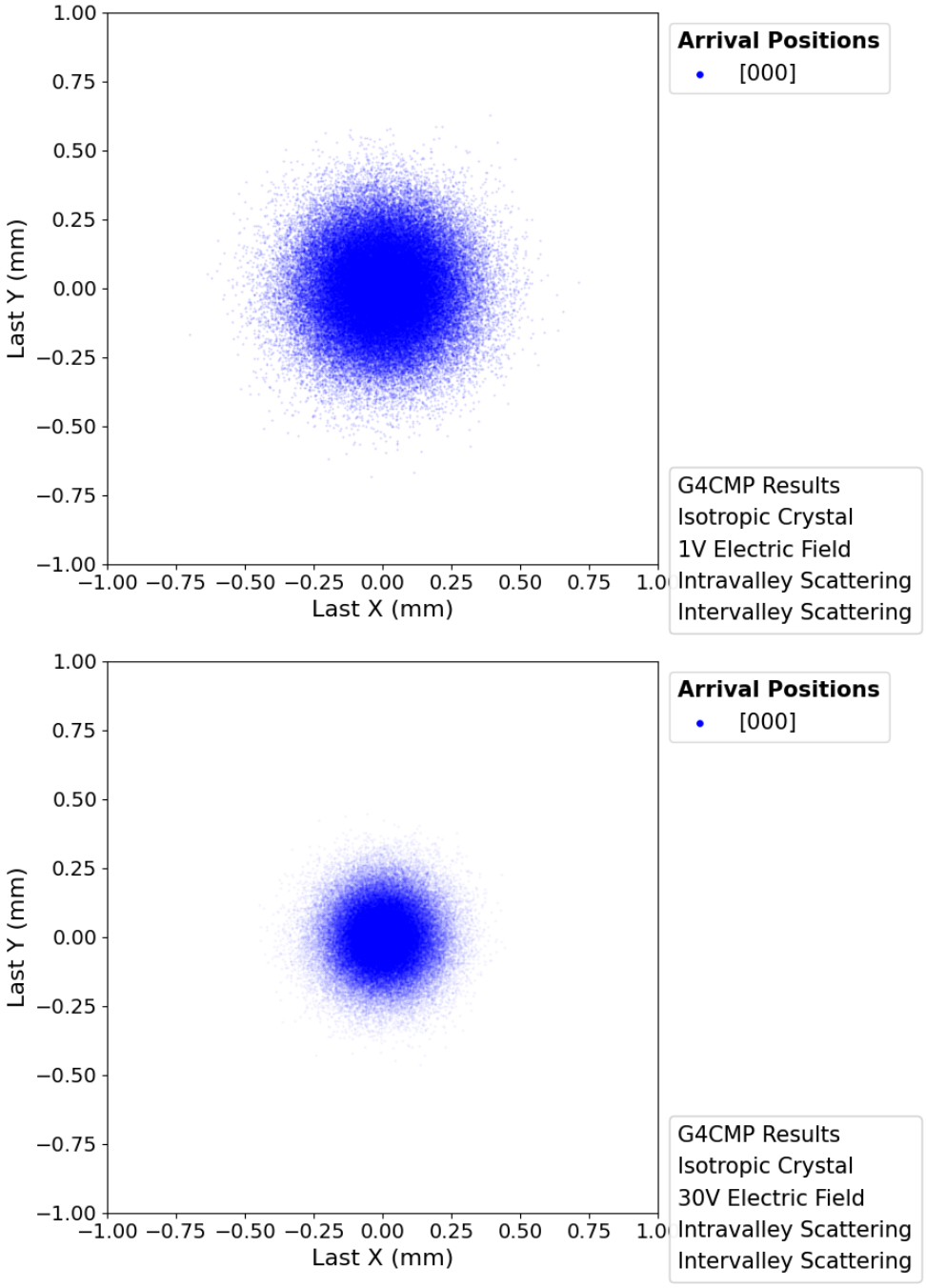

Figure 5.4: This figure shows the G4CMP results for the distribution of electron arrival positions on the top surface of an isotropic crystal with all dominant effects, including intervalley scattering, along with two different voltages. We show it to confirm that even when the unphysical intervalley processes are included in an isotropic crystal, the results are qualitatively the same as Figure 5.3, which matches our expectations.

5.2 Results for Silicon and Germanium

In this section, we present the G4CMP simulation results for charge transport in anisotropic crystals, specifically silicon and germanium detectors, under various electric field and scattering configurations. These results incorporate the full complexity of real detector geometries, realistic valley structures, and material-specific scattering models and are readily compared to the expectations of Chapters 3 and 2 as well as the results of the previous chapter. In the first paragraph, we describe the simulation results for silicon and germanium in the absence of both electric fields and scattering effects. In the second paragraph, we present the results from applying an external electric field in the negative z direction, which modifies the electron transport in silicon and germanium crystals in the absence of scattering. In the third paragraph, we examine the impact of enabling intravalley scattering with the scattering rates taken from Table 5.3. In the fourth paragraph, we present the results for electron transport in silicon and germanium detectors with both intravalley and intervalley scattering enabled.

Starting with the simplest anisotropic case, we describe the results for silicon and germanium in the absence of both electric fields and scattering effects. As discussed in Section 4.2, electrons in this case propagate in straight lines at constant energy, with their velocities determined by the angle between their initial wavevector and the axis of their valley. Although the speed varies with direction due to the anisotropic effective mass tensors, the electrons' arrival positions on the top surface remain unchanged compared to the isotropic case, forming a radially symmetric arctangent pattern. While Figure 5.5 for silicon has a square arrival pattern, we note that this is due to both the rectangular shape of the detector and the fact that most of the electrons do not reach the top surface. Similarly, Figure 5.6 for germanium has a circular pattern due to its cylindrical geometry. These results qualitatively match the toy model outputs in Figures 4.8 and 4.10, confirming that anisotropy in velocity alone does not break the symmetry of the arrival distribution in the absence of fields and scattering.

As expected from our discussion in previous chapters, applying an external electric field in the negative z direction modifies electron transport in silicon and germanium crystals even in

the absence of scattering. We note that in both cases the voltage used was selected so that all electrons reach the top surface as described in Section 4.3, the Si(100) crystal is oriented such that the $\pm z$ valleys are aligned with the field, while the $\pm x$ and $\pm y$ valleys are orthogonal to it. Electrons in the $\pm x$ and $\pm y$ valleys, therefore, experience greater acceleration. Additionally, electrons with an initial velocity direction further from the xyz axes move farther in the xy plane. These effects lead to a square-like arrival distribution as shown in Figure 5.7. In contrast, the Ge(100) crystal is configured such that all valleys have equal angles with the electric field. As a result, the acceleration magnitude is the same across all valleys, but the directions differ, producing eight distinct arrival clusters as shown in Figure 5.8. These results agree with the toy model predictions from Figures 4.12 and 4.14, and demonstrate the valley-dependent acceleration effects described in Section 3.2.

Including the intravalley scattering effects with the rates taken from Table 5.3 significantly affects the arrival points distributions. As discussed in Section 4.4, intravalley scattering causes electrons to rapidly lose their initial kinetic energy through the emission of Luke phonons, effectively making their motion more strongly governed by the applied electric field than their initial conditions. We observe that, as expected from the toy model, since the scattering rate is lower in the transverse direction, the same-energy electrons move further in that direction than in the longitudinal direction, causing each valley electron arrival distribution pattern to be more scattered in their transverse directions. Lastly, because the energy gained from the electric field is quickly radiated away, increasing the voltage has only a limited effect on the final spread of the arrival clusters. Figure 5.9 shows the results for Si(100). As predicted in Figure 4.16, the combination of effects results in the distinct '+' shaped pattern on the detector surface. In Ge(100), where valleys are oriented along the diagonals, the eight arrival clusters seen in the no-scattering case merge into the four elliptical groups shown in Figure 5.10. This follows the expectations from Figure 4.18. We also note that in both materials, the cluster size remains nearly constant with increasing voltage, reflecting the minimal effect of voltage increase on the cluster sizes as previously described.

Lastly, we present the results for electron transport in silicon and germanium detectors with

both intravalley and intervalley scattering enabled. As discussed in Section 3.3 and illustrated in the toy simulations of Section 4.5, the addition of intervalley scattering allows electrons to experience different accelerations during their propagation. Figure 5.11 shows the result in Si(100). This mixing causes the distinct valley-dependent clusters observed with only intravalley scattering to blur together, producing a smoother and more circular arrival distribution. Similarly, Figure 5.12 for Ge(100), the intervalley transitions fill the previously empty regions between the four main elliptical clusters. These patterns qualitatively match the toy simulation expectations shown in Figures 4.24 and 4.26, confirming that the underlying physical models behave as expected even in realistic scenarios. The other primary difference is that as the applied voltage increases, the number of intervalley scattering events also increases, consistent with the energy-dependent scattering rates listed in Table 5.3. This leads to greater valley mixing and further blurring of the arrival patterns, ultimately producing distributions that approach a circular symmetry as the effects of individual valley accelerations are averaged out.

Having established that the full G4CMP simulations qualitatively reproduce the expected behaviors of electron transport in both isotropic and anisotropic media, we now turn to a comparison with experimental data. In the next section, we compare the G4CMP simulated distributions with published results from silicon and germanium test devices under varying voltages. These comparisons provide critical validation for our modeling approach and highlight areas where further refinement of the simulation may be necessary to achieve quantitative agreement.

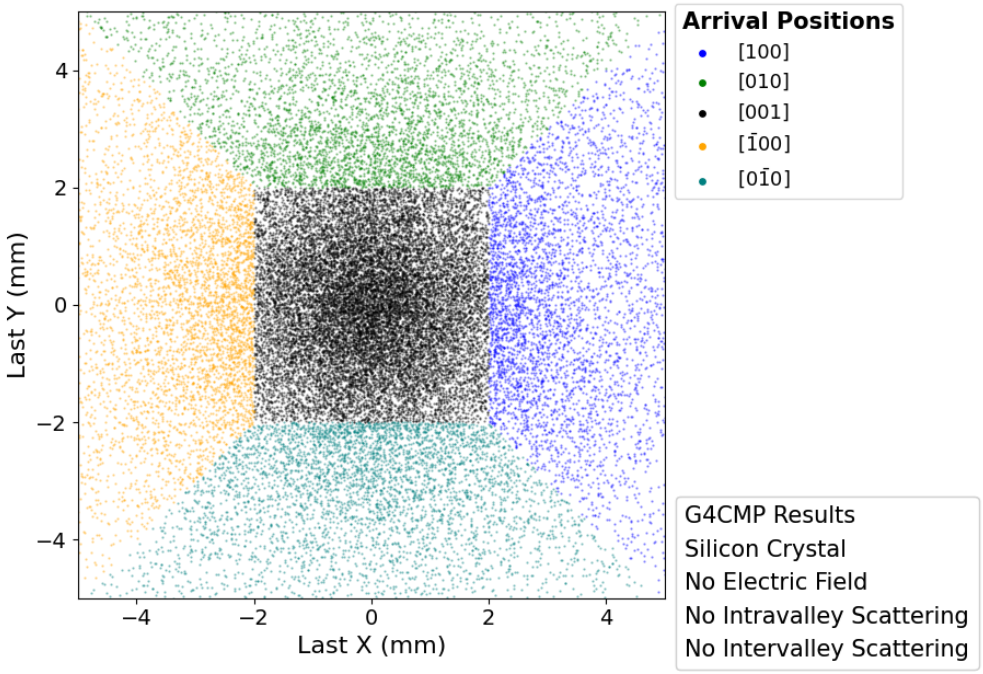

Figure 5.5: This figure shows the G4CMP results for the distribution of electron arrival positions on the top surface of a square-shaped silicon detector without an electric field or scattering. We show it to illustrate that the full simulation results for the silicon match the toy model expectations qualitatively and are basically identical to Figure 4.8. Note that the colors of the points represent the starting valley of the electrons and that not all electrons reach the top surface.

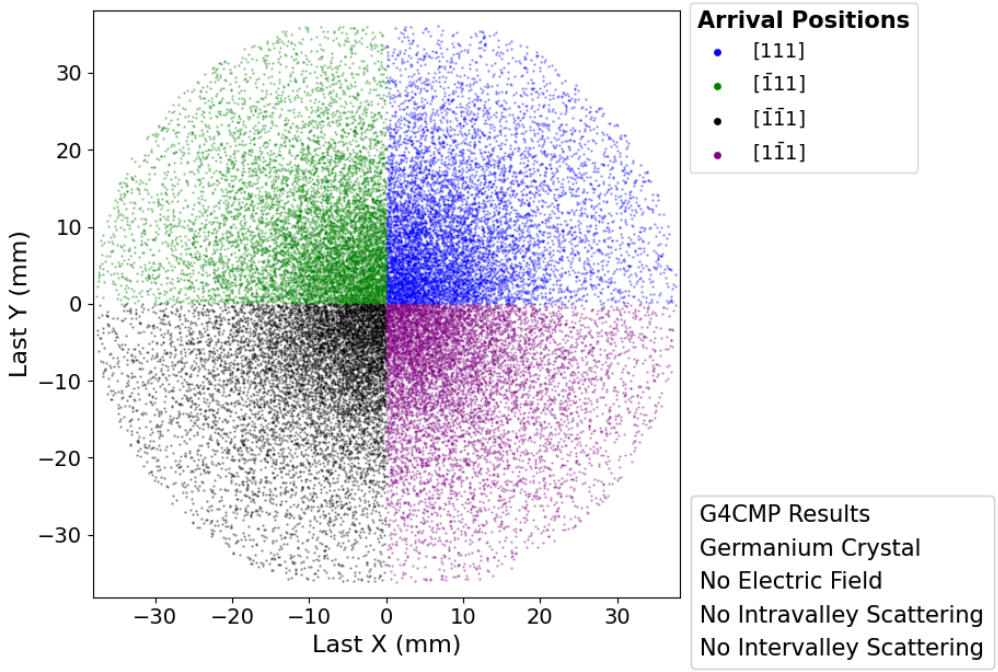

Figure 5.6: This figure shows the G4CMP results for the distribution of electron arrival positions on the top surface of a cylindrical germanium detector without an electric field or scattering. We show it to illustrate that changing the medium to any anisotropic crystal does not affect the arrival density in the absence of voltage or scattering effects. Compared to Figure 4.10, we note that our toy model expectations qualitatively match our full simulation result. We also note that, unlike Figures 5.2-5.4, the circular shape is due to the boundaries of the crystal, not the electric field or scattering effects. Here the colors of the points again represent the starting valley of the electrons, and not all electrons reach the top surface.

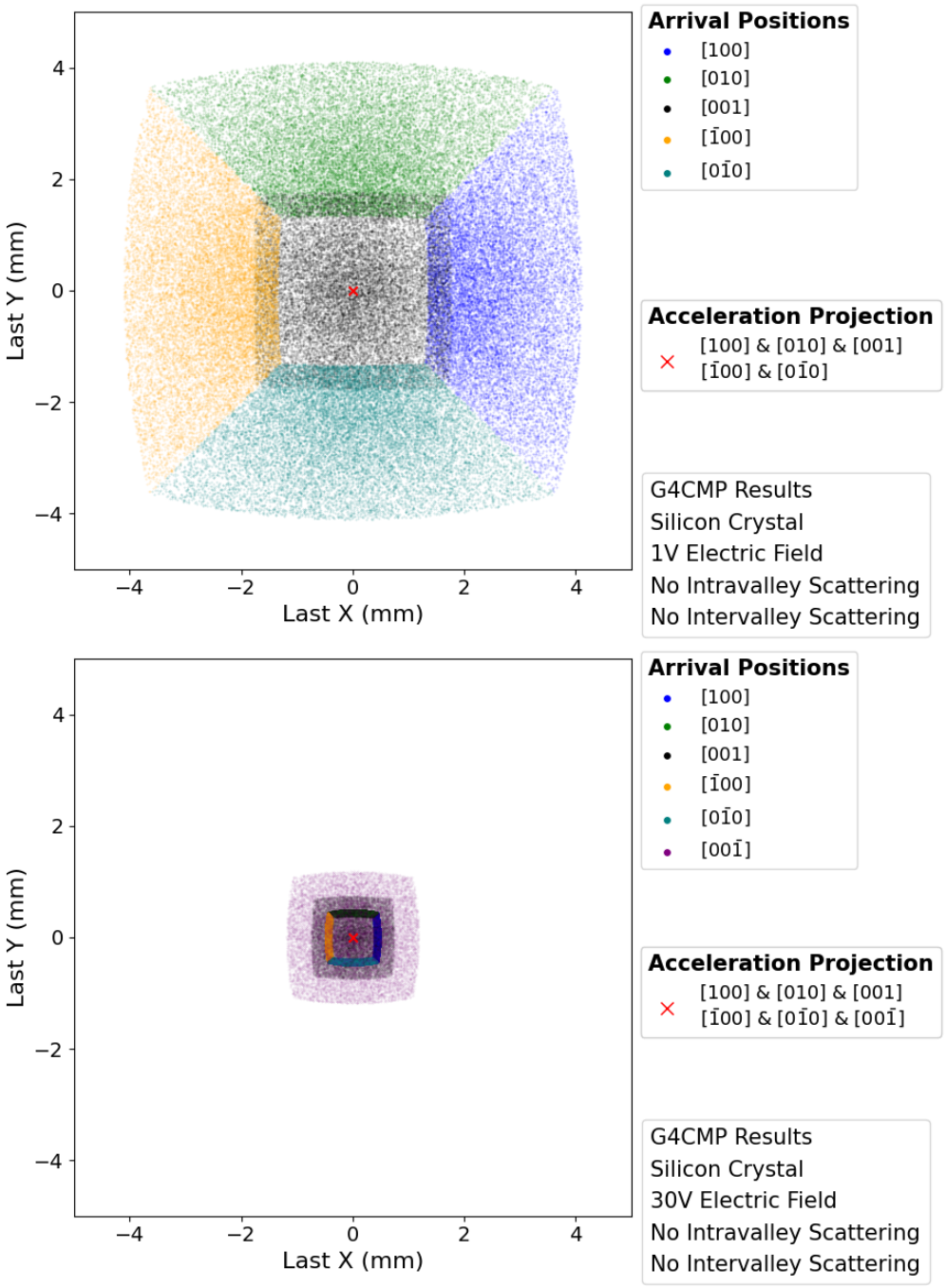

Figure 5.7: This figure shows the G4CMP results for the distribution of electron arrival positions on the top surface of a square-shaped silicon detector with two different voltages but no scattering. We show it to illustrate how, compared to Figure 5.5, the combination of an electric field and valleys causes electrons to end up in the square-like shape as predicted from the toy model, as was shown in Figure 4.12. We also note that in the top plot, the top surface is not fully populated, which is expected due to the fact that the $[00\bar{1}]$ valley electrons do not get accelerated enough to hit the top surface and instead hit the bottom or a side surface and are not shown. On the other hand, the higher-value voltage choice in the bottom plot causes all electrons to reach the top surface, since the $[00\bar{1}]$ valley electrons' acceleration is high enough, and the arrival point clusters become smaller while preserving the overall shape.

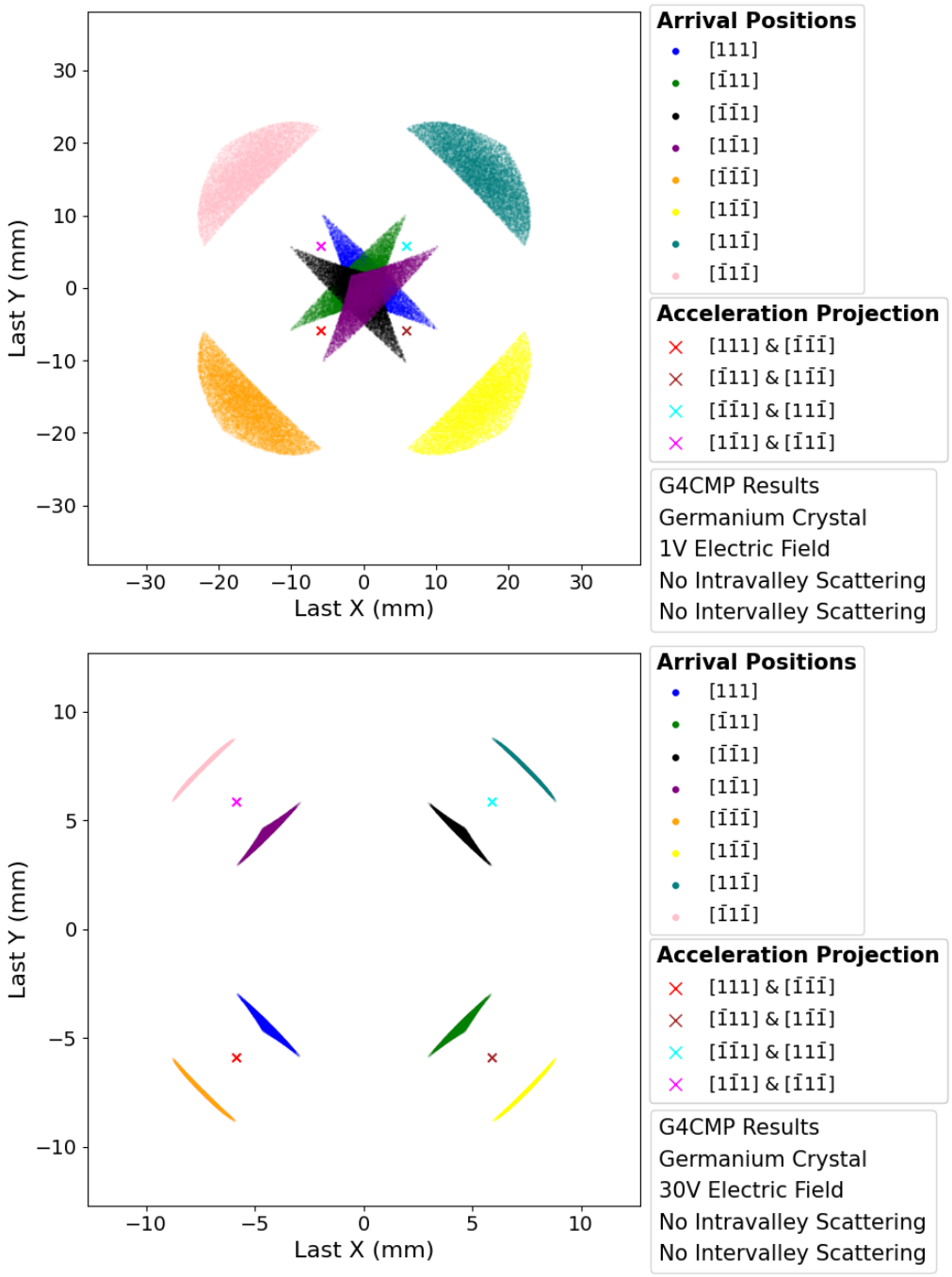

Figure 5.8: This figure shows the G4CMP results for the distribution of electron arrival positions on the top surface of a cylindrical germanium detector with two different voltages but no scattering. We show it to illustrate that, compared to Figure 5.6, the combination of an electric field and the different valley directions causes electrons to end up in 8 regions, the shape of which are determined by the voltage and the valley directions, which matches our expectations from the toy model shown in Figure 4.14. We also note that by increasing the voltage, the arrival point clusters become smaller and closer to the acceleration vector indicated with an x.

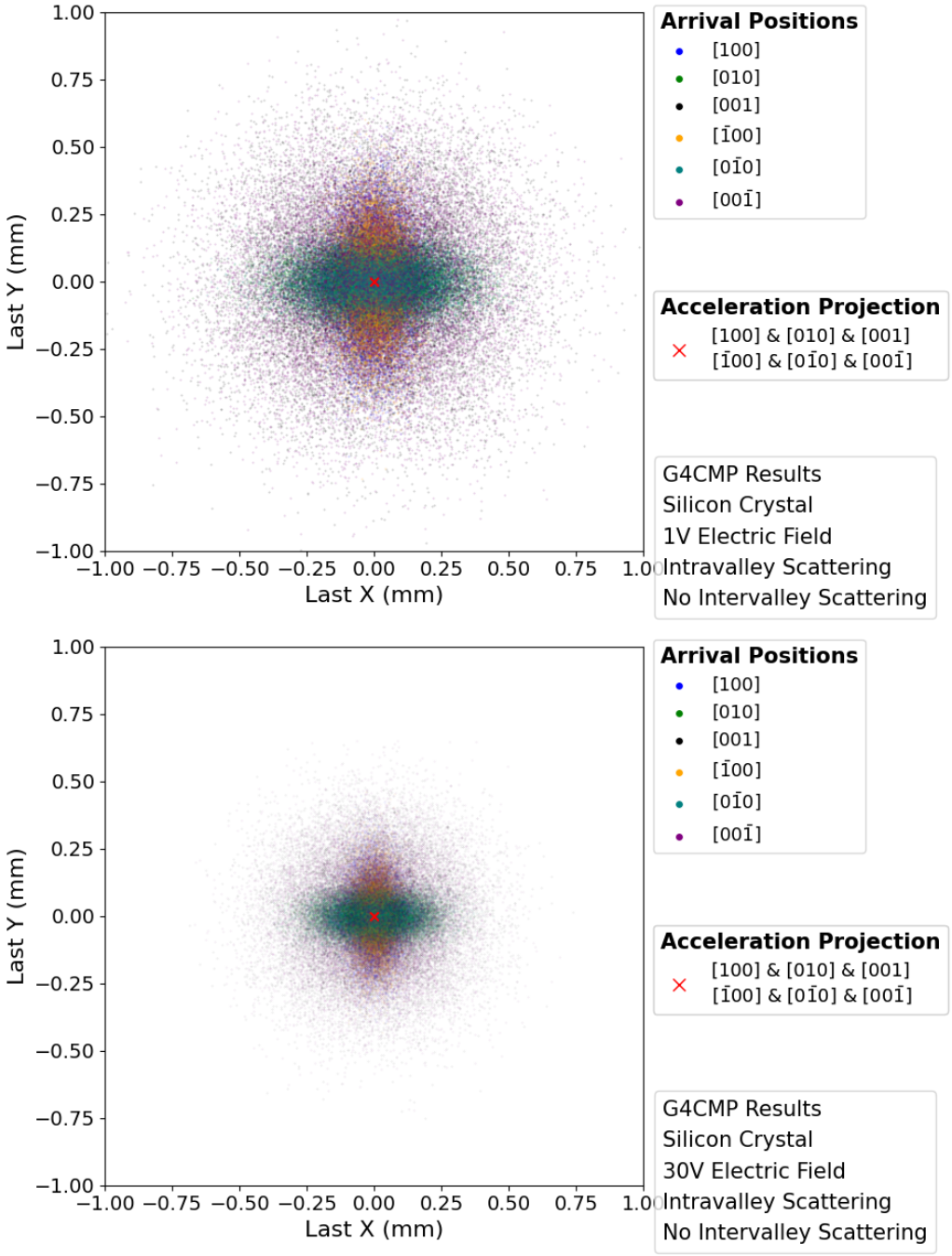

Figure 5.9: This figure shows the G4CMP results for the distribution of electron arrival positions on the top surface of a square-shaped silicon detector with two different voltages, both with intravalley scattering using the rates given in Table 5.3 but without intravalley scattering. We show it to illustrate that, compared to Figure 5.7, the Luke scattering causes all the electrons to end up in one cluster, making a + sign in the middle of the top surface. As shown in Figure 4.16, this is expected due to the fact that the electrons quickly lose their initial energy to Luke scattering events, and that increasing the voltage barely affects the size and shape of the clusters.

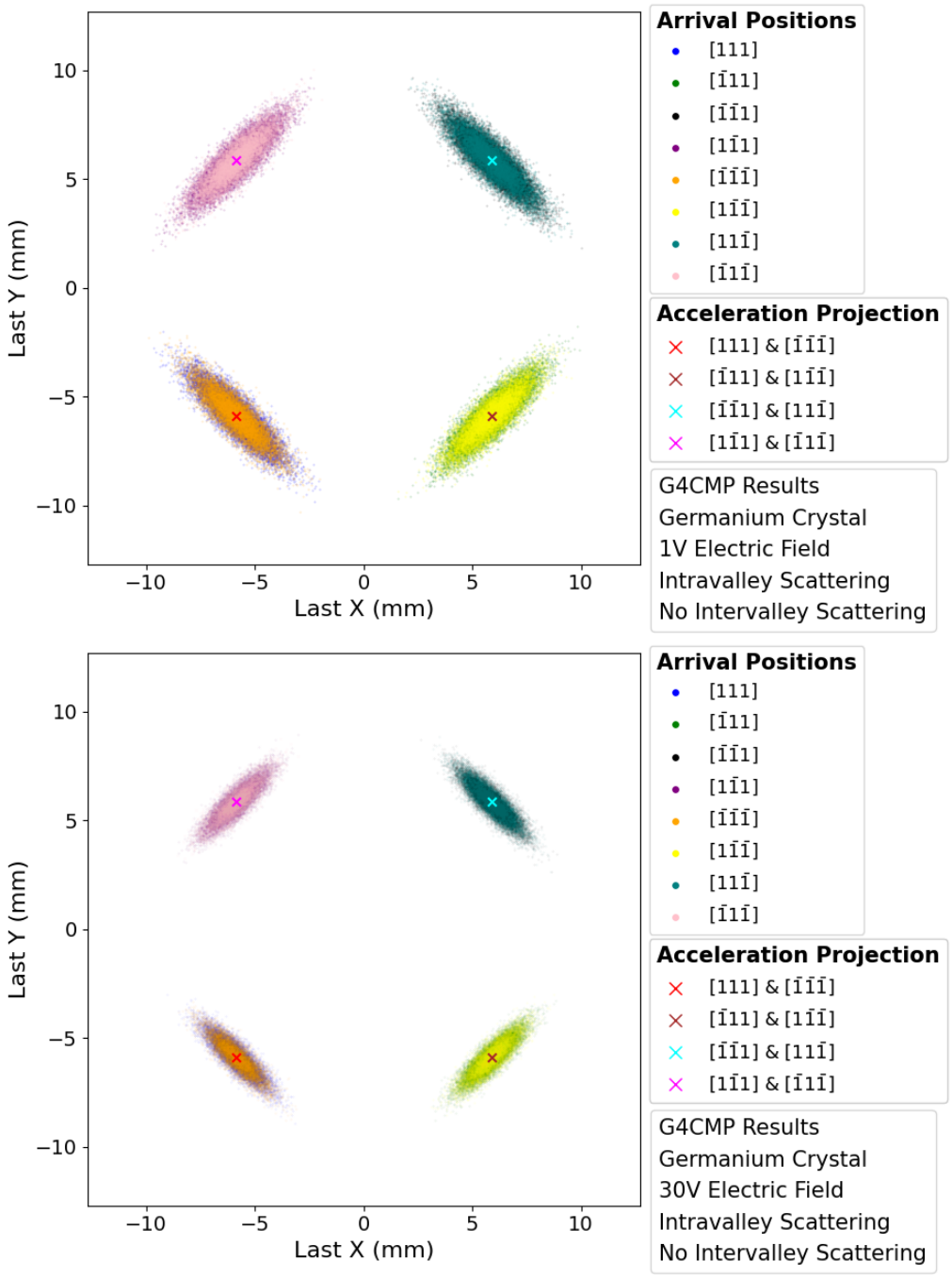

Figure 5.10: This figure shows the G4CMP results for the distribution of electron arrival positions on the top surface of a cylindrical germanium detector with two different voltages, with intravalley scattering but without intravalley scattering. We show it to illustrate that, compared to Figure 5.8, Luke scattering causes the same-axis valley electrons arrival points to merge and locate in an ellipsoidal shape with a center between the acceleration and the valley axis, as expected from our toy simulation results shown in Figure 4.18, and that increasing the voltage barely affects the size and shape of the clusters.

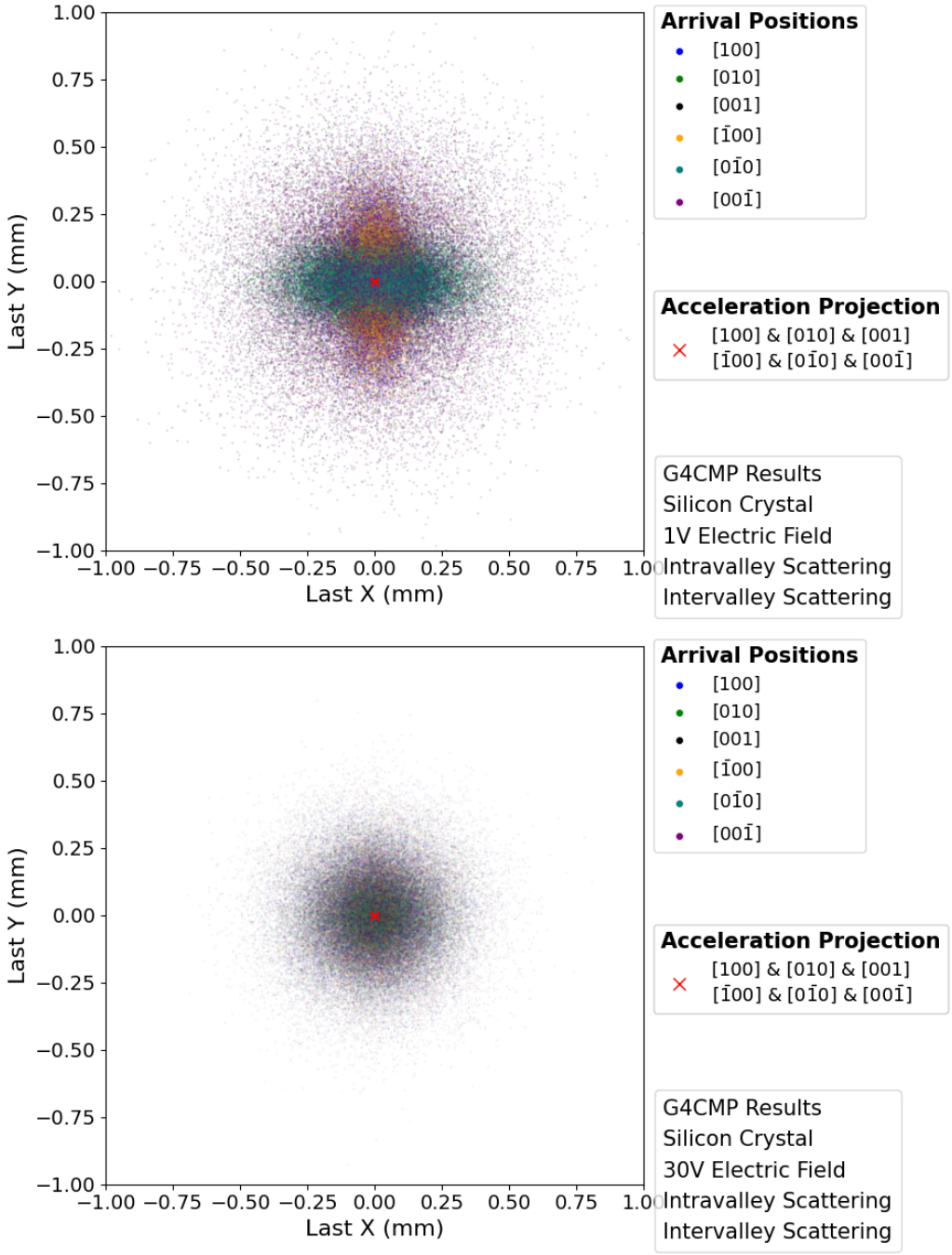

Figure 5.11: This figure shows the G4CMP results for the distribution of electron arrival positions on the top surface of a square-shaped silicon detector with all dominant effects included for two different voltages. We show it to present the full simulation results for the silicon detector, including all the effects. We note that compared to Figure 5.9, the intervalley scattering causes electrons to change valleys, effectively mixing the different valley clusters together, which results in the overall shape of the distribution gradually transforming into a circle as the voltage increases, which matches our toy simulation expectations shown in Figure 4.24.

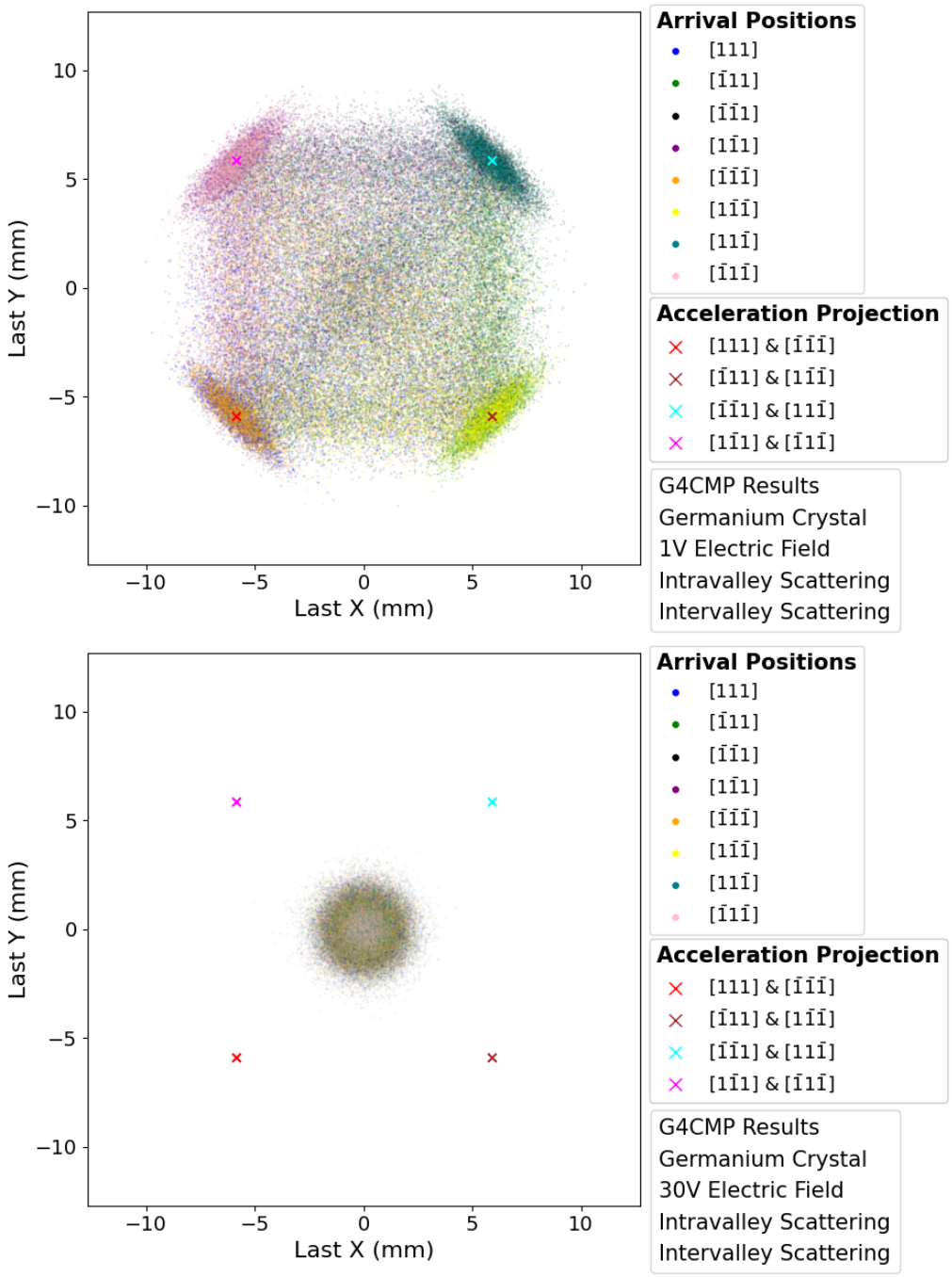

Figure 5.12: This figure shows the G4CMP results for the distribution of electron arrival positions on the top surface of a cylindrical germanium detector with all dominant effects included for two different voltages. We show it to present the full simulation results for the germanium detector, including all the effects. We note that compared to Figure 5.10, intervalley scattering causes some electrons to end up between the 4-cluster structure, which matches our toy simulation expectations shown in Figure 4.26. Additionally, we observe that as the intervalley scattering rate increases with voltage, at high enough voltages, the structure is effectively wiped out.

5.3 Comparison With Experiment

In this section, we compare the full G4CMP simulation results with experimental data from real silicon and germanium detectors. Such comparisons enable us to validate our physical models, test parameter value choices, and understand areas that require further development. Although the simulations and experiments differ slightly in geometry, crystal orientation, and operating conditions such as temperature, qualitative comparisons remain highly valuable. In the first paragraph, we discuss the temperature dependence of the experimental electron arrival distributions before turning to the detailed comparison with G4CMP. In the second paragraph, we compare the G4CMP simulation results for the electron arrival distributions in the Si(111) orientation to experimental data from a detector. In the third paragraph, we perform a similar comparison between the simulation results and experimental data obtained from a germanium detector.

It's important to discuss the temperature dependence of the experimental electron arrival distributions before turning to the detailed comparison with the G4CMP results. The experiments were done with $500\ \mathrm{mK}$ and $5\ \mathrm{K}$ for silicon and $1\ \mathrm{K}$ for germanium, which are different than the $50\ \mathrm{mK}$ assumption used to select the values given in Table 5.3. For the purposes of comparison, we assume that temperature-dependent changes to the electron band structure are small enough that the acceleration directions and the bandgap energies given in Equations 2.28 and 2.29 remain effectively unchanged. However, the scattering rates described in Table 5.3 have some temperature dependence. To a degree of approximation, the impact of a higher voltage mimics a rise in the scattering rates. For intravalley scattering, the results in Figures 5.9 and 5.10 suggest any impact on the primary shape is relatively small; the cluster positions should remain approximately the same. On the other hand, Figures 5.11 and 5.12 suggest significant changes for the arrival distributions within the cluster positions for different intervalley scattering rates. Given that even a qualitative comparison between G4CMP results and the experimental data is still useful, we use the experimental results as a guide to extrapolate the impact of temperature on the scattering rates for a given temperature [33, 34, 64].

The first comparisons are done with the results from a silicon detector with a Si(111) orien-

tation. Figure 5.13 presents the experimental arrival positions measured at various voltages and temperatures, while Figure 5.14 shows our corresponding G4CMP results using the parameter values in Table 5.3, which are the default G4CMP values. We observe that:

- As expected, the positions of the electrons that did not go through any intervalley scatterings (the triangle vertices) look the same, independent of the voltage and temperature.
- As the voltage increases, the ratio of the electron arrivals on the vertices to arrivals within them drops. This is as expected due to the rate of intervalley scattering, which can be thought of as voltage dependent as given in Equation 2.44.
- By increasing the voltage enough, all the electrons go through so many intervalley scatterings that they essentially end up on a circle around the center (average of the three valley vectors).

While the trend of the arrival distributions qualitatively matches the experiment, the results for the same voltages are quantitatively different, as G4CMP results seem to mimic the experimental results at much higher voltages. For example, the $-4\ \mathrm{V}$ results in data look like the $-20\ \mathrm{V}$ results in simulation and the $-20\ \mathrm{V}$ results in data look like the $-100\ \mathrm{V}$ results in simulation. This suggests that the discrepancy in density distribution arises from the values of the intervalley scattering rate parameters described in Table 5.3. We note that those parameters were tuned to the data, but done so with an older version of G4CMP, prior to our changes, and without any temperature dependence terms. This further suggests that, for quantitative predictions for this and other scenarios, improved, carefully calibrated intervalley scattering rates, such as those investigated in previous studies [33], will be necessary. Efforts in this area are beyond the scope of this work, but are expected to follow the approaches like those in Ref. [64] to both refine and accurately parameterize the intervalley scattering rates. Such efforts are in progress, and future students will re-run with similar geometric configurations when they are completed and quantitatively compared.

We perform a similar comparison between the G4CMP simulation results and the experimental data obtained from a germanium detector. Figure 5.15 shows the experimental arrival distributions for electrons at four different applied voltages at $1\ \mathrm{K}$ and can be compared to the G4CMP

results in Figure 5.12. We begin by noting the primary configuration differences, which include the temperature, the crystal orientations, and the electron path lengths. Still, a useful but qualitative comparison can be readily made using simple rotation and scaling adjustments, as the angles between the valleys and the electric field don't change, and there is clear qualitative agreement. Moving to a quantitative comparison, we note that the experimental geometry has electrons traveling approximately $3.89\ \mathrm{mm}$, whereas our simulation has the electrons traveling $12.7\ \mathrm{mm}$ to the top surface. In the G4CMP results, the clusters are centered around $x = \pm 5.88\ \mathrm{mm}$, $y = \pm 5.88\ \mathrm{mm}$. By rotating the G4CMP results by 45 degrees and applying a scaling of $\frac{3.89}{12.7}$, G4CMP predicts the clusters to be centered at $x = \pm 2.547\ \mathrm{mm}$, $y = 0$, and $x = 0$, $y = \pm 2.547\ \mathrm{mm}$, which is close to the experimental results for the cluster positions which have values of approximately $x = \pm 2.6\ \mathrm{mm}$, $y = 0$, and $x = 0$, $y = \pm 2.6\ \mathrm{mm}$ taken from the leftmost figure. As with silicon, the experimental data for electron arrivals between the clusters show the same trends as a function of voltage. This again suggests the need for improvement in the intervalley scattering rate calculations.

Having concluded our analysis, we have demonstrated qualitative agreement between the simulated results, simplified toy models, and experimental data. Between the valley-dependent propagation and the scattering models, the simulations successfully reproduced key experimental features, including cluster patterns and voltage-dependent sizes and patterns. Nonetheless, discrepancies between the data and simulation suggest that the intervalley scattering rate modeling or parameter values need further refinement in G4CMP. With these insights, in the next chapter, we highlight future directions to enhance G4CMP capabilities and discuss the broader applications of G4CMP in other fields.

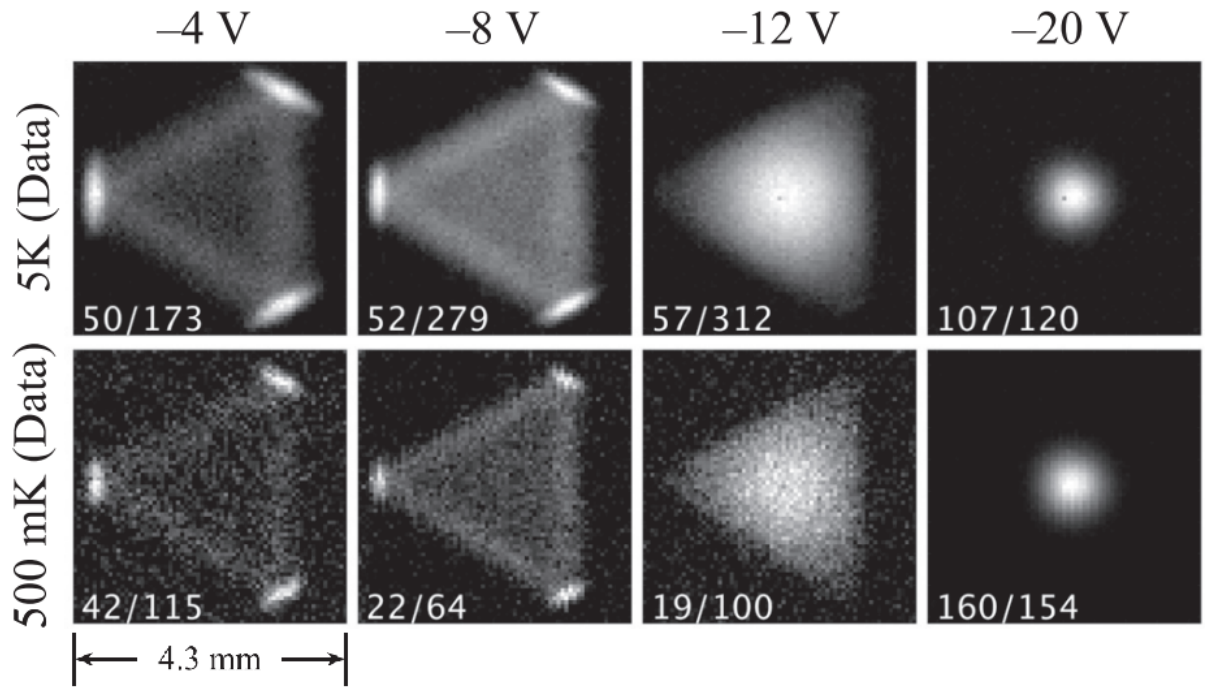

Figure 5.13: This figure, shows the same test device results as Figure 1.12 but for a number of additional voltages and temperatures. We show it because the set of results allows for comparison with the G4CMP results shown in Figure 5.14. We note that the points outside of the triangle are intrinsic noise in the analog readout. The numbers in the bottom left of each plot give the maximum pulse height (in mV) and the normalized integrated intensity (relative to -12 V, 500 mK), respectively [33].

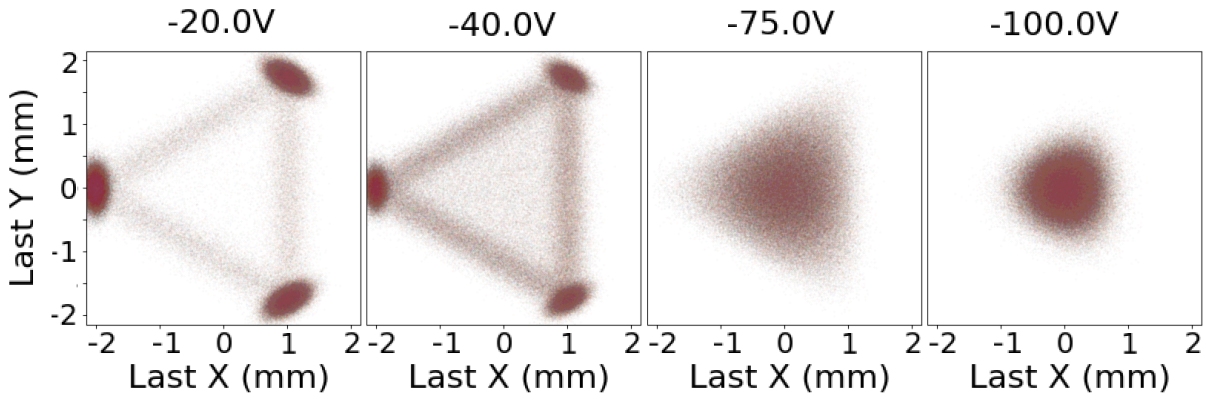

Figure 5.14: This figure shows the G4CMP results for the electron arrival positions in a silicon crystal in the Si(111) orientation for the case where we have all effects included and for 4 different voltages. We show it to compare with the experimental results in Figure 5.13. While there are clear similarities in the shapes in general, the density of arrival position points in-between the triangle edges (no intervalley scattering) at each voltage are qualitatively different. On the other hand, we notice that the trend as a function of voltage appears to be the same, but with different voltage values. This suggests that the values from the intervalley scattering rate calculations described in Table 5.3 are not correct.

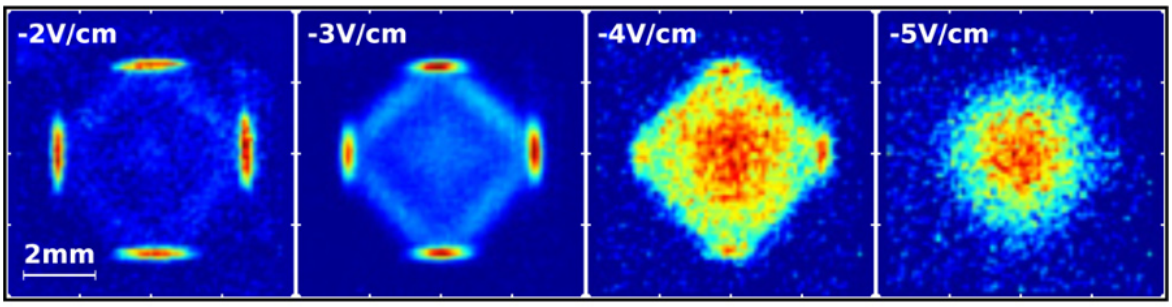

Figure 5.15: This figure shows a set of experimental results for the electrons' arrival positions in a high-purity germanium test device for four different voltages [34]. We show it because the set of results allows for a visual comparison with the case simulated in G4CMP shown in Figure 5.12, as well as provides multiple points so we can extrapolate. We note that there are configuration differences between the experimental results and those shown in Figure 5.12. Specifically, the crystal used here is $3.89\ \mathrm{mm}$ thick with $10\ \mathrm{mm} \times 10\ \mathrm{mm}$ top and bottom faces, operating at $1\ \mathrm{K}$ with the valleys located at $[\pm 1, \pm 1, 0]$, $[\pm 1, 0, \pm 1]$, and $[0, \pm 1, \pm 1]$. Comparisons can be made by scaling and simple rotations, and we observe that the arrival points, the position of the corners, and the size of the whole shape match qualitatively. On the other hand, again, the density of electrons in between the bands is not the same for the same voltage, and future work, like in Ref. [64], is required to better parameterize the intervalley scattering rates in G4CMP.

6. SUMMARY OF THE THESIS AND CONCLUSIONS

In this chapter, we summarize and conclude this thesis. We have completed our motivation for the need for improved descriptions of charge propagation in low-temperature, single-crystal semiconductors, presented a powerful semiclassical modeling, implemented it in a full Geant4 simulation tool-kit, and compared its results to data from experiment. Before concluding with our hopes for the upcoming SuperCDMS data-taking run, we mention one of the primary plans for improving the simulation and comment on the use of these tools for advancing quantum computing. In Section 6.1, we outline directions for improving the modeling of the intervalley scattering rates. In Section 6.2, we discuss how the modeling framework developed in this thesis may be applied beyond the SuperCDMS experiment for quantum computing, and conclude the thesis by commenting on our hopes for the upcoming SuperCDMS experiment at SNOLAB.

6.1 Plans for Enhancing the Intervalley Scattering Rate Modeling

In this section, we comment on two parallel activities in progress for improving the modeling of the intervalley scattering. While there is good reason to believe that the work presented in this thesis captures the dominant physical mechanisms governing electron transport in silicon and germanium detectors, given the disagreements we saw in the previous chapter we expect that refinements further refinements of the intervalley scattering process will likely both improve quantitative agreement with experimental data as well as expand the range of conditions over which the simulation remains predictive. In the first paragraph, we discuss improving the modeling of the intervalley scattering rates by re-tuning the parameters of the existing model. In the second paragraph, we outline a longer-term direction in which phenomenological intervalley scattering models are replaced or supplemented by more physically motivated microscopic descriptions.

As described in Section 5.2, the modeling of the intervalley scattering rates used in G4CMP followed the description in Table 5.3. However, since the parameter values used were taken from a tuning process based on an older version of G4CMP [33], they are no longer expected to re-

main the best fit within the updated framework. As argued in Section 5.3, incorrect intervalley parameters can affect the expected charge arrival distributions and their voltage dependence, and we hypothesized this was the cause of the observable difference between our full results and the test-bench data. This suggests that the simulation would be improved by following the procedures in Refs. [33] and [64], using our updated version. This work is in progress, and when completed, it will allow for more sophisticated comparisons of the data to see if we are missing anything that needs to be added.

A parallel direction is to replace the phenomenological intervalley scattering models or supplement them with more physically motivated microscopic descriptions. As described in Section 2.5.2, the models currently implemented in G4CMP are what we would call effective or phenomenological models, which means they are simply based on a reasonable parameterization that reproduces the observed data. A more physically motivated approach is to characterize the scattering rates based on the microphysics of the impurity and optical phonon scatterings at low temperatures. These should be energy dependent, and hopefully, not only improve the accuracy of the simulation but also reduce material-specific tunings. A more physical model, along with proper tuning after incorporation, would also allow us to see if there are additional effects that need to be included in our modeling.

Having concluded our discussion of the plans for intervalley scattering rate modeling, we next explore other applications of the framework. Specifically, we consider how G4CMP simulations could contribute to advancing quantum computing research and other dark matter detection experiments.

6.2 Other Applications of G4CMP and Usage in SuperCDMS-SNOLAB Experiment

In this section, we discuss how the modeling framework developed in this work may be applied beyond the SuperCDMS experiment, and we conclude the thesis by commenting on our hopes for the upcoming SuperCDMS experiment at SNOLAB. Although the primary motivation of this work is dark matter detection in the SuperCDMS experiment, the underlying description of charge transport in anisotropic semiconductor crystals is broadly relevant to future dark matter detection

experiments as well as quantum technologies. In the first paragraph, we outline how G4CMP's ability to model charge propagation at the microscopic level is directly applicable to quantum technologies. In the second paragraph, we discuss how G4CMP can play a crucial role in the next generation of direct dark matter detection experiments.

G4CMP's ability to model charge propagation at the microscopic level is directly applicable to quantum information science technologies. In many solid-state quantum platforms, such as semiconductor-based qubits and superconducting devices operated at cryogenic temperatures, the presence and motion of even a small number of unintended charge carriers can limit device performance [67, 68]. While these systems are typically operated without an applied bias and are designed to suppress thermal excitations, external energy deposits, such as those from cosmic rays or radioactive backgrounds, can liberate electrons into the conduction band of the substrate [69, 70]. Once created, these charges can drift through the crystal or become trapped near surfaces and interfaces, producing local electric fields that randomize qubit phases, alter energy levels of a two-level system (like a quantum dot), or induce false signals in sensitive readout elements. A detailed understanding of how charges propagate in anisotropic band structures, even in the zero-field or near-surface limit, is therefore essential for predicting these effects. As a result, the modeling framework developed in this thesis and the G4CMP simulation can be used for the design and optimization of quantum devices.

G4CMP can also play a crucial role in the next generation of direct dark matter detection experiments. As experiments push toward lower energy thresholds and increased sensitivity to lighter dark matter candidates, detector responses become increasingly more dependent on small microscopic charge transport effects. As shown in Figure 2.10, intervalley scattering events become rare at low energies, causing the detector response to depend more strongly on the underlying crystal structure at low voltages, as observed in Figures 5.13 and 5.15. In this regime, simplified descriptions, such as models based on a modified scalar effective mass, may no longer be sufficient to accurately interpret the observed data. The G4CMP framework, with its ability to simulate charge propagation, scattering, and phonon emission within realistic detector geometries, provides

a physics-based tool for making predictive comparisons with experimental measurements. As a result, the framework developed in this thesis makes G4CMP applicable not only to the SuperCDMS experiment, but also to future direct detection experiments through straightforward modifications of detector geometry and configuration. Additionally, by enabling detailed studies of how transport signatures depend on material choice, crystal orientation, electric field configuration, and detector geometry, G4CMP can directly inform both detector design and optimization for next-generation searches [32, 33].

Having completed our discussion of the improved charge transport modeling, we look forward to using it in the upcoming SuperCDMS-SNOLAB experiment. In that experiment, the modeling developed in this thesis will be incorporated into the SuperCDMS simulation and analysis workflow as a reference for interpreting the observed data. We hope that the additional understanding it provides can assist with background rejection, improve energy measurement resolutions, as well as play a central role in the overall search optimization. Such advances may well prove to be the linchpin that ties together a discovery of dark matter.

REFERENCES

[1] V. Trimble, "Existence and nature of dark matter in the universe," *Annual Review of Astronomy and Astrophysics*, vol. 25, no. 1, pp. 425–472, Sep. 1987. DOI: 10.1146/annurev.aa.25.090187.002233.

[2] F. Zwicky, "On the masses of nebulae and of clusters of nebulae," *The Astrophysical Journal*, vol. 86, p. 217, Oct. 1937. DOI: 10.1086/143864.

[3] G. W. Angus, H. Y. Shan, H. S. Zhao, and B. Famaey, "On the proof of dark matter, the law of gravity, and the mass of neutrinos," *The Astrophysical Journal*, vol. 654, no. 1, pp. L13–L16, Dec. 2006. DOI: 10.1086/510738.

[4] D. Clowe *et al.*, "A direct empirical proof of the existence of dark matter," *The Astrophysical Journal*, vol. 648, no. 2, pp. L109–L113, Aug. 2006. DOI: 10.1086/508162.

[5] G. Bertone, D. Hooper, and J. Silk, "Particle dark matter: Evidence, candidates and constraints," *Physics Reports*, vol. 405, no. 5–6, pp. 279–390, Jan. 2005. DOI: 10.1016/j.physrep.2004.08.031.

[6] A. Mitridate, T. Trickle, Z. Zhang, and K. M. Zurek, "Snowmass white paper: Light dark matter direct detection at the interface with condensed matter physics," *Physics of the Dark Universe*, vol. 40, p. 101 221, May 2023. DOI: 10.1016/j.dark.2023.101221.

[7] R. Agnese *et al.*, (SuperCDMS Collaboration), "Low-mass dark matter search with CDMSlite," *Physical Review D*, vol. 97, no. 2, p. 022 002, Jan. 2018. DOI: 10.1103/physrevd.97.022002.

[8] R. Agnese *et al.*, (SuperCDMS Collaboration), "Projected sensitivity of the SuperCDMS SNOLAB experiment," *Physical Review D*, vol. 95, no. 8, p. 082 002, Apr. 2017. DOI: 10.1103/physrevd.95.082002.

[9] E. Corbelli and P. Salucci, "The extended rotation curve and the dark matter halo of M33," *Monthly Notices of the Royal Astronomical Society*, vol. 311, no. 2, pp. 441–447, Jan. 2000. DOI: 10.1046/j.1365-8711.2000.03075.x.

[10] P. Schneider, J. Ehlers, and E. E. Falco, *Gravitational lenses*. Springer, 1992, ISBN: 9783662037584.

[11] V. Belokurov *et al.*, "The cosmic horseshoe: Discovery of an Einstein ring around a giant luminous red galaxy," *The Astrophysical Journal*, vol. 671, no. 1, pp. L9–L12, Nov. 2007. DOI: 10.1086/524948.

[12] "Einstein ring captured by the Hubble space telescope," NASA/ESA Hubble Space Telescope. (2011), [Online]. Available: https://esahubble.org/.

[13] T. M. Undagoitia and L. Rauch, "Dark matter direct-detection experiments," *Journal of Physics G: Nuclear and Particle Physics*, vol. 43, no. 1, p. 013 001, Dec. 2015. DOI: 10.1088/0954-3899/43/1/013001.

[14] G. F. Knoll, *Radiation detection and measurement*. Wiley, 2010, ISBN: 9780470131480.

[15] M. Schumann, "Direct detection of WIMP dark matter: Concepts and status," *Journal of Physics G: Nuclear and Particle Physics*, vol. 46, no. 10, p. 103 003, Aug. 2019. DOI: 10.1088/1361-6471/ab2ea5.

[16] A. Boveia and C. Doglioni, "Dark matter searches at colliders," *Annual Review of Nuclear and Particle Science*, vol. 68, no. 1, pp. 429–459, Oct. 2018. DOI: 10.1146/annurev-nucl-101917-021008.

[17] J. M. Gaskins, "A review of indirect searches for particle dark matter," *Contemporary Physics*, vol. 57, no. 4, pp. 496–525, Jun. 2016. DOI: 10.1080/00107514.2016.1175160.

[18] R. Essig *et al.*, "Snowmass2021 cosmic frontier: The landscape of low-threshold dark matter direct detection in the next decade," Apr. 2023. DOI: 10.48550/ARXIV.2203.08297.

[19] J. D. Winchell, "Characterizing photon and neutron responses in CDMS detectors using real and simulated Cf-252 data," Ph.D. dissertation, Texas A&M University, Dec. 2023. [Online]. Available: https://www.slac.stanford.edu/exp/cdms/ScienceResults/Theses/winchell.pdf.

[20] P. N. Luke, "Voltage-assisted calorimetric ionization detector," *Journal of Applied Physics*, vol. 64, no. 12, pp. 6858–6860, Dec. 1988. DOI: 10.1063/1.341976.

[21] E. Azadbakht, "Comparison of simulations and data from small high voltage single crystal detectors for dark matter searches," Ph.D. dissertation, Texas A&M University, Oct. 2022. [Online]. Available: https://www.slac.stanford.edu/exp/cdms/ScienceResults/Theses/azadbakht.pdf.

[22] "SuperCDMS SNOLAB prototype detector," Super Cryogenic Dark Matter Search Experiment. (2023), [Online]. Available: https://supercdms.slac.stanford.edu/overview/experiment-overview.

[23] A. J. Anderson, "A search for light weakly-interacting massive particles with SuperCDMS and applications to neutrino physics," Ph.D. dissertation, Massachusetts Institute of Technology, Jun. 2015. [Online]. Available: http://hdl.handle.net/1721.1/99316.

[24] G. Aad *et al.*, (ATLAS Collaboration), "The ATLAS simulation infrastructure," *The European Physical Journal C*, vol. 70, no. 3, pp. 823–874, Sep. 2010. DOI: 10.1140/epjc/s10052-010-1429-9.

[25] S. Abdoulline *et al.*, "The CMS simulation software," in *2006 IEEE Nuclear Science Symposium Conference Record*, IEEE, 2006, pp. 1655–1659. DOI: 10.1109/nssmic.2006.354216.

[26] C. Kittel, *Introduction to solid state physics*. Wiley, 2013, ISBN: 9780471415268.

[27] N. W. Ashcroft and N. D. Mermin, *Solid state physics*. Cengage Learning, 1976, ISBN: 9780030839931.

[28] N. Kurinsky, "The low-mass limit: Dark matter detectors with eV-scale energy resolution," Ph.D. dissertation, Stanford University, 2018. [Online]. Available: https://purl.stanford.edu/xh271zf3698.

[29] B. K. Ridley, *Quantum processes in semiconductors*. Clarendon Press, 1999, ISBN: 0191545007.

[30] K. Seeger, *Semiconductor physics*. Springer, 2004, ISBN: 9783662098554.

[31] S. Agostinelli *et al.*, "Geant4—a simulation toolkit," *Nuclear Instruments and Methods in Physics Research Section A: Accelerators, Spectrometers, Detectors and Associated Equipment*, vol. 506, no. 3, pp. 250–303, Jul. 2003. DOI: 10.1016/s0168-9002(03)01368-8.

[32] M. Kelsey *et al.*, "G4CMP: Condensed matter physics simulation using the Geant4 toolkit," *Nuclear Instruments and Methods in Physics Research Section A: Accelerators, Spectrometers, Detectors and Associated Equipment*, vol. 1055, p. 168 473, Oct. 2023. DOI: https://doi.org/10.1016/j.nima.2023.168473.

[33] R. A. Moffatt *et al.*, "Spatial imaging of charge transport in silicon at low temperature," *Applied Physics Letters*, vol. 114, no. 3, Jan. 2019. DOI: 10.1063/1.5049691.

[34] R. A. Moffatt *et al.*, "Imaging the oblique propagation of electrons in germanium crystals at low temperature and low electric field," *Applied Physics Letters*, vol. 108, no. 2, Jan. 2016. DOI: 10.1063/1.4939753.

[35] S. Smirnov, "Physical modeling of electron transport in strained silicon and silicon-germanium," Ph.D. dissertation, Technische Universität Wien, 2003. [Online]. Available: https://repositum.tuwien.at/handle/20.500.12708/12174.

[36] R. Winkler, *Spin-orbit coupling effects in two-dimensional electron and hole systems*. Springer, 2003, ISBN: 9783540366164.

[37] R. P. Feynman, R. B. Leighton, and M. L. Sands, *The Feynman lectures on physics, vol. 3*. Addison-Wesley, 1971, ISBN: 0201021188.

[38] T. Young, "The Bakerian Lecture. Experiments and calculations relative to physical optics," *Philosophical Transactions of the Royal Society of London*, vol. 94, pp. 1–16, Dec. 1804. DOI: 10.1098/rstl.1804.0001.

[39] D. J. Griffiths, *Introduction to quantum mechanics*. Cambridge University Press, 2017, ISBN: 9781107179868.

[40] A. Tonomura, J. Endo, T. Matsuda, T. Kawasaki, and H. Ezawa, "Demonstration of single-electron buildup of an interference pattern," *American Journal of Physics*, vol. 57, no. 2, pp. 117–120, Feb. 1989. DOI: 10.1119/1.16104.

[41] R. Bach, D. Pope, S.-H. Liou, and H. Batelaan, "Controlled double-slit electron diffraction," *New Journal of Physics*, vol. 15, no. 3, p. 033 018, Mar. 2013. DOI: 10.1088/1367-2630/15/3/033018.

[42] "Brillouin zone of a hexagonal reciprocal lattice," Wikimedia Commons. (2007), [Online]. Available: https://commons.wikimedia.org/wiki/File:Brillouin_zone.svg.

[43] Y. Varshni, "Temperature dependence of the energy gap in semiconductors," *Physica*, vol. 34, no. 1, pp. 149–154, Jan. 1967. DOI: 10.1016/0031-8914(67)90062-6.

[44] S. L. Chuang, *Physics of optoelectronic devices*. Wiley, 1995, ISBN: 0471109398.

[45] E. O. Kane, "Band structure of indium antimonide," *Journal of Physics and Chemistry of Solids*, vol. 1, no. 4, pp. 249–261, Jan. 1957. DOI: 10.1016/0022-3697(57)90013-6.

[46] J. M. Luttinger and W. Kohn, "Motion of electrons and holes in perturbed periodic fields," *Physical Review*, vol. 97, no. 4, pp. 869–883, Feb. 1955. DOI: 10.1103/physrev.97.869.

[47] C. Jacoboni and L. Reggiani, "The Monte Carlo method for the solution of charge transport in semiconductors with applications to covalent materials," *Reviews of Modern Physics*, vol. 55, no. 3, pp. 645–705, Jul. 1983. DOI: 10.1103/revmodphys.55.645.

[48] G. Dresselhaus, "Spin-orbit coupling effects in zinc blende structures," *Physical Review*, vol. 100, no. 2, pp. 580–586, Oct. 1955. DOI: 10.1103/physrev.100.580.

[49] G. Ottaviani, L. Reggiani, C. Canali, F. Nava, and A. Alberigi-Quaranta, "Hole drift velocity in silicon," *Physical Review B*, vol. 12, no. 8, pp. 3318–3329, Oct. 1975. DOI: 10.1103/physrevb.12.3318.

[50] D. S. Catherall and A. J. Minnich, "Hot-hole transport and noise phenomena in silicon at cryogenic temperatures from first principles," *Physical Review B*, vol. 108, no. 23, p. 235 207, Dec. 2023. DOI: 10.1103/physrevb.108.235207.

[51] B. Cabrera, M. Pyle, R. Moffatt, K. Sundqvist, and B. Sadoulet, "Oblique propagation of electrons in crystals of germanium and silicon at sub-kelvin temperature in low electric fields," Apr. 2010. DOI: 10.48550/ARXIV.1004.1233.

[52] S. W. Leman, "Invited review article: Physics and Monte Carlo techniques as relevant to cryogenic, phonon, and ionization readout of cryogenic dark matter search radiation detectors," *Review of Scientific Instruments*, vol. 83, no. 9, Sep. 2012. DOI: 10.1063/1.4747490.

[53] G. L. Bir and G. E. Pikus, *Symmetry and strain-induced effects in semiconductors*. Wiley, 1974, ISBN: 0470073217.

[54] S.-i. Tamura, "Spontaneous decay rates of LA phonons in quasi-isotropic solids," *Physical Review B*, vol. 31, no. 4, pp. 2574–2577, Feb. 1985. DOI: 10.1103/physrevb.31.2574.

[55] B. Neganov and V. Trofimov, "Otkrytia i izo-breteniya ussr patent no. 1037771," USSR Patent 1 037 771, 1985.

[56] M. V. Fischetti and S. E. Laux, "Band structure, deformation potentials, and carrier mobility in strained Si, Ge, and SiGe alloys," *Journal of Applied Physics*, vol. 80, no. 4, pp. 2234–2252, Aug. 1996. DOI: 10.1063/1.363052.

[57] K. Murase, K. Enjouji, and E. Otsuka, "Determination of deformation potential constants from the electron cyclotron resonance in germanium and silicon," *Journal of the Physical Society of Japan*, vol. 29, no. 5, pp. 1248–1257, Nov. 1970. DOI: 10.1143/jpsj.29.1248.

[58] N. Sclar, "Ionized impurity scattering in nondegenerate semiconductors," *Physical Review*, vol. 104, no. 6, pp. 1548–1558, Dec. 1956. DOI: 10.1103/physrev.104.1548.

[59] A. Broniatowski, "Carrier anisotropy and impurity scattering in Ge at mK temperatures: Modeling and comparison to experiment," *Journal of Low Temperature Physics*, vol. 167, no. 5–6, pp. 1069–1074, Feb. 2012. DOI: 10.1007/s10909-012-0543-5.

[60] A. Broniatowski, "Intervalley scattering of hot electrons in germanium at millikelvin temperatures," *Journal of Low Temperature Physics*, vol. 176, no. 5–6, pp. 860–869, Jan. 2014. DOI: 10.1007/s10909-014-1091-y.

[61] Wikipedia. "Divergence theorem." English, Wikipedia, The Free Encyclopedia. (May 2025), [Online]. Available: https://en.wikipedia.org/w/index.php?title=Divergence_theorem&oldid=1293087129.

[62] C. Herring and E. Vogt, "Transport and deformation-potential theory for many-valley semiconductors with anisotropic scattering," *Physical Review*, vol. 101, no. 3, pp. 944–961, Feb. 1956. DOI: 10.1103/physrev.101.944.

[63] J. Fang *et al.*, "Understanding the average electron–hole pair-creation energy in silicon and germanium based on full-band Monte Carlo simulations," *IEEE Transactions on Nuclear Science*, vol. 66, no. 1, pp. 444–451, Jan. 2019. DOI: 10.1109/tns.2018.2879593.

[64] A. Broniatowski *et al.*, "Cryogenic Ge detectors with interleaved electrodes: Design & modeling," *Journal of Low Temperature Physics*, vol. 151, no. 3–4, pp. 830–834, Jan. 2008. DOI: 10.1007/s10909-008-9754-1.

[65] D. Amaral *et al.*, (SuperCDMS Collaboration), "Constraints on low-mass, relic dark matter candidates from a surface-operated SuperCDMS single-charge sensitive detector," *Physical Review D*, vol. 102, no. 9, p. 091 101, Nov. 2020. DOI: 10.1103/physrevd.102.091101.

[66] R. Agnese *et al.*, (SuperCDMS Collaboration), "Results from the super cryogenic dark matter search experiment at Soudan," *Physical Review Letters*, vol. 120, no. 6, p. 061 802, Feb. 2018. DOI: 10.1103/physrevlett.120.061802.

[67] M. McEwen *et al.*, "Resisting high-energy impact events through gap engineering in superconducting qubit arrays," *Physical Review Letters*, vol. 133, no. 24, p. 240 601, Dec. 2024. DOI: 10.1103/physrevlett.133.240601.

[68] E. Yelton *et al.*, "Modeling phonon-mediated quasiparticle poisoning in superconducting qubit arrays," *Physical Review B 110, 024519 (2024)*, vol. 110, no. 2, p. 024 519, Feb. 23, 2024. DOI: 10.1103/physrevb.110.024519.

[69] C. Larson *et al.*, "Quasiparticle poisoning of superconducting qubits with active gamma irradiation," *PRX Quantum*, vol. 6, no. 3, Sep. 2025. DOI: 10.1103/2lyd-8swv.

[70] X. Li *et al.*, "Cosmic-ray-induced correlated errors in superconducting qubit array," *Nature Communications*, vol. 16, no. 1, May 2025. DOI: 10.1038/s41467-025-59778-z.